

**DEVELOPMENTS IN AMBIENT MASS SPECTROMETRY IMAGING
FOR IN-DEPTH SPATIALLY RESOLVED ANALYSIS OF COMPLEX
BIOLOGICAL TISSUES**

by

Daisy Melina Unsihuay Vila

A Dissertation

Submitted to the Faculty of Purdue University

In Partial Fulfillment of the Requirements for the degree of

Doctor of Philosophy



Department of Chemistry

West Lafayette, Indiana

August 2022

THE PURDUE UNIVERSITY GRADUATE SCHOOL
STATEMENT OF COMMITTEE APPROVAL

Dr. Julia Laskin, Chair

Department of Chemistry

Dr. Scott McLuckey

Department of Chemistry

Dr. Robert Stahelin

Department of Medicinal Chemistry and Molecular Pharmacology

Dr. Chi Zhang

Department of Chemistry

Approved by:

Dr. Christine Hrycyna

Dedicated to my husband, my parents, and siblings

ACKNOWLEDGMENTS

These last five years have been an amazing journey that I could have ever dream about. I am aware that my accomplishments are not only mine but a result of the supportive environment that I have been surrounded by which provided me with all the tools to succeed. In the next paragraphs, I will write thanks to all the people that helped me along the way to reach the end line.

Julia Laskin. I am honored to be one of your first graduate students. Since that moment I heard about nano-DESI, I knew that it was what I wanted to explore during these years of graduate school. Thank you for giving me the chance to work and learn from you. Your mentoring has been paramount for my development as a scientist. I am grateful for all the support that you gave me in my academic and personal life. You always supported me to any opportunity that I was interested in applying and never clipped my wings. Thanks for all the time that you dedicated to me and your willingness to help me.

Laskin lab members. Thank you for making the lab a second home for me. I might not be the most social person when I am working, but whenever I was taking breaks, it was always nice having someone to talk to and share how my day was going. I will miss you all. For the new members: Emerson, Mushfeqa, Sarah and Nazifa: you are joining a great family.

Ruichuan Yin. Thanks for the mentorship provided during your time at the Laskin lab and give me the courage to carry out those challenging high-resolution experiments by myself.

Hugo Samayoa-Oviedo. Your friendship is one of the best gifts that I take with me from my time at Purdue. Thank you for the great moments that we spent together. Although you broke my heart when you joined the soft-landing team, it was pleasant to have someone that speaks the same language that I can connect with and share jokes that nobody else would understand.

Pei Su. Your passion for science was always invigorating for me to keep working hard to someday be as good as you are. I am grateful for all the help and mentoring that you provided me, but I am beyond grateful for our friendship that will last forever.

Hang Hu. I admire your intelligence and dedication to your work. Thank you for all your help and patience to teach me your intricate tools. It was nice sharing all these years together in the lab and see your growth as a scientist.

Xiantang Li. You were like a dad for me in the lab. It was always nice having someone that treats you with coffee and food.

Solita Wilson. Your bubbly personality was always contagious, and it energized me to continue my day specially during those Orbitrap times. Thank you for all the great conversations that we share.

Kuang lab. It has been a pleasure working with you. Thank you for your willingness to help me with any experimental work that I needed and the nice treatment that I received whenever I visited your lab.

My mentees: Manxi, Sneha, Alessandra, Sarah and Nazifa. It has been a great adventure being your mentor. I learned a lot about myself along the way which made me a better person. It is exciting to see your progress and all your accomplishments.

Peruvian community at Purdue. I am grateful for the great moments we spent together that made me feel like I was in Peru again. Whenever I felt homesick, you were the ones that help me to feel better. Victor, Maybe, Romina and Andres, you will be in my heart forever.

Amy and Kevin. Thank you for ‘adopting’ me as your daughter and made me part of your lives during my time at Purdue. It was always nice to experience a sense of home whenever I visited you to receive all that love that only parents can provide.

Saayak Halder. I am blessed that life gave me a second brother like you. Your company all these years have been a great emotional support for me, especially during those times when my medical situation was unclear, you kept me grounded and motivated me to focus on the good things of life.

Myra Flores. I will never be able to retribute everything that you have done for me. Thank you for believing in me and give me the chance to have my first internship abroad. That opportunity opened me the doors to so many others that enabled me to grow as a scientist and as a person.

My parents, Franklin and Melina. I have been always grateful to have you as my parents, but it is not until I left home that I realized how privileged I was. All these years, you have provided me with incommensurate love and caring. You made home a peaceful place where I could freely express my ideas, where I could always find support and be happy. Thank you for all your efforts to raise a strong and resilient woman, confident about herself and without fear of jumping into a whole new adventure away from you. Thank you for allowing me to dream big and always be there whenever I failed. You are amazing.

My husband, Kevin. What a lucky person that I am to have you in my life. I admire you intelligence both: academic and emotionally. I admire your kindness. I admire your discipline, and above all, I admire your heart. You always inspire me to be a better person. Thank you, my dear.

TABLE OF CONTENTS

LIST OF TABLES	10
LIST OF FIGURES	11
LIST OF ABBREVIATIONS	17
ABSTRACT.....	20
CHAPTER 1. INTRODUCTION	22
1.1 Mass spectrometry imaging	22
1.2 Nano-DESI overview	22
1.2.1 Improvements in the nano-DESI platform	24
1.2.2 Improvements in the spatial resolution.....	24
1.2.3 Nano-DESI applications	26
1.2.4 Overview of the thesis	27
CHAPTER 2. IMAGING OF TRIGLYCERIDES IN TISSUES USING NANOSPRAY DESORPTION ELECTROSPRAY IONIZATION (nano-DESI) MASS SPECTROMETRY ...	32
2.1 Introduction.....	32
2.2 Materials and methods	34
2.2.1 Chemicals and solutions	34
2.2.2 Tissue collection and handling	34
2.2.3 Nano-DESI experiments	35
2.2.4 Data processing.....	36
2.3 Results and discussions.....	36
2.3.1 Effect of solvent composition on the extraction of TGs.....	37
2.3.2 Effect of ionization on the detection of TGs	39
2.3.3 Nano-DESI MSI of gastrocnemius tissues	42
2.4 Conclusions.....	46
CHAPTER 3. IMAGING AND ANALYSIS OF ISOMERIC UNSATURATED LIPIDS THROUGH ONLINE PHOTOCHEMICAL DERIVATIZATION OF C=C BONDS	48
3.1 Introduction.....	48
3.2 Materials and methods	49
3.2.1 Nomenclature.....	49

3.2.2	Chemicals and Solutions.....	49
3.2.3	Tissue collection and handling	50
3.2.4	Optics.....	51
3.2.5	ESI platform.....	51
3.2.6	Nano-DESI platform.....	52
3.2.7	Profiling and nano-DESI MSI experiments.....	53
3.2.8	Data processing.....	54
3.3	Results and discussions.....	55
3.4	Conclusions.....	70
CHAPTER 4. HIGH-RESOLUTION IMAGING AND IDENTIFICATION OF BIOMOLECULES USING NANO-DESI COUPLED TO ION MOBILITY SPECTROMETRY.		
	76
4.1	Introduction.....	76
4.2	Materials and methods	78
4.2.1	Chemicals	78
4.2.2	Tissue sectioning and handling.....	78
4.2.3	Nano-DESI platform.....	78
4.2.4	Nano-DESI MSI experiments.....	80
4.2.5	Data processing.....	81
4.3	Results and discussion	82
4.3.1	Nano-DESI imaging of drift time separated ions	82
4.3.2	Separation of isomeric species.....	87
4.3.3	IM-MSI eliminates interferences from isobaric peaks	90
4.4	Conclusions.....	93
CHAPTER 5. MULTIMODAL WORKFLOW FOR HIGH-RESOLUTION IMAGING OF INDIVIDUAL SKELETAL MUSCLE FIBERS USING NANO-DESI MSI.....		103
5.1	Introduction.....	103
5.2	Materials and methods	105
5.2.1	Chemicals	105
5.2.2	Tissue sectioning and handling.....	105
5.2.3	Immunofluorescence staining.....	106

5.2.4	Nano-DESI experiments	106
5.2.5	Data processing.....	107
5.2.6	Image registration	107
5.2.7	Statistical analysis.....	108
5.3	Results.....	108
5.4	Discussion.....	119
5.4.1	Phospholipid acyl chain composition differences in muscle fibers.....	120
5.4.2	Metabolomic fingerprints linked to energy metabolism.....	124
5.5	Conclusions.....	126
CHAPTER 6. CONCLUSIONS AND PERSPECTIVES.....		127
APPENDIX A. Identification of metabolites using MS/MS databases.....		130
APPENDIX B. Annotated species with their relative abundances extracted per each fiber type with their classification based on the pattern distribution and metabolism depicted across all the replicates.		132
REFERENCES		145
VITA.....		166
LIST OF PUBLICATIONS		168

LIST OF TABLES

Table 3.1. Twelve unsaturated lipid species identified in the lipid extract of the gastrocnemius muscle tissue using the ESI setup coupled to the QTOF instrument. The diagnostic fragments used to identify the C=C bond location in the acyl chains are highlighted in bold. The order of the acyl chain does not indicate the sn-position. Only the peaks corresponding to the product A are shown.	72
Table 3.2. Fourteen unsaturated lipid species directly extracted from a mouse uterine tissue using the nano-DESI coupled to the Orbitrap instrument. The diagnostic fragments used to identify the C=C bond location in the acyl chains are highlighted in bold. The order of the acyl chain does not indicate the sn-position. Only the peaks corresponding to the product A are shown.	74
Table 4.1. Front Funnel Settings for the QTOF and IM-QTOF Mode experiments in Positive Mode	80
Table 4.2. Front Funnel Settings for the QTOF and IM-QTOF Mode experiments in Negative Mode	80
Table 4.3. Drift Tube Settings for the IM-QTOF in Positive Mode/Negative Mode	80
Table 4.4. List of annotations in negative mode nano-DESI-IM-MSI	95
Table 4.5. List of annotations in positive mode nano-DESI-IM-MSI	98

LIST OF FIGURES

Figure 1.1. Schematic diagram of the nanospray desorption electrospray ionization (nano-DESI). Figure reproduced with permission from reference 1, Copyright © 2012, American Chemical Society.....	23
Figure 1.2 Data acquisition in nano-DESI MSI experiments. Modified from reference 14. Copyright © 2019, Springer Nature.....	25
Figure 1.3 Solvent optimization for improved molecular coverage	28
Figure 1.4. Photochemical derivatization of C=C bond in lipids using singlet oxygen reaction .	29
Figure 1.5. Coupling of Nano-DESI MSI with ion mobility	30
Figure 1.6. High-spatial resolution imaging of skeletal muscle fibers	31
Figure 2.1. Lipid profiles obtained from a region of the line scan where TGs are abundant using a) MeOH:H ₂ O (9:1), b) MeOH:DCM (4:6), and c) MeOH:AcN:tol (5:3.5:1.5) under the same experimental conditions. An optical image showing the region where the line scans were acquired on the tissue is displayed on the left side of panel a). Normalization factors (NL) are displayed in each panel.....	38
Figure 2.2. a) Optical image of a liver tissue showing regions where different line scans were collected. b) Representative mass spectra obtained for line scans acquired using MeOH:H ₂ O, MeOH:DCM and MeOH:AcN:tol solvent mixtures.....	39
Figure 2.3. Average mass spectra of the TG-rich region displaying lipid signals obtained a) using MeOH:AcN:tol (5:3.5:1.5) and by doping MeOH:AcN:tol (5:3.5:1.5) with b) 0.1 mM and c) 2 mM of ammonium formate. Black and red asterisks highlight the same TG species detected as [M+K] ⁺ and [M+NH ₄] ⁺ adducts, respectively. NL values are displayed in each panel.	41
Figure 2.4. Reactive nano-DESI mass spectrum obtained using MeOH:AcN:tol doped with 100 μM of GT. GT in the solvent produces a strong peak at <i>m/z</i> 132.11 that dominates the spectrum. A closer look into the phospholipids region shows the presence of GT adducts with PC species extracted from the tissue.	42
Figure 2.5. Nano-DESI images acquired using MeOH:H ₂ O (9:1) and MeOH:AcN:tol (5:3.5:1.5) solvents in positive mode. a) Optical images of gastrocnemius tissue sections and ion images of [M+H] ⁺ ion of CAR(14:0) and carnosine, LPC (16:0), PC (36:1) and PC(40:6) detected as [M+K] ⁺ adducts. b) Ion images of TG(46:0), TG(48:0), TG(50:2), TG(50:1), TG(52:3) and TG(54:4) detected as [M+K] ⁺ adducts. Scale bar is 7 mm. All ion images are normalized to the TIC and the corresponding normalized ion abundance scales are shown in the color bars located next to each ion image.....	43
Figure 2.6. Positive mode ion images of other TGs detected as [M+K] ⁺ adducts in gastrocnemius tissue using MeOH:H ₂ O (9:1) and MeOH:AcN:tol (5:3.5:1.5) solvents. Scale bars are 7 mm. All ion images are normalized to the TIC and the corresponding normalized ion abundance scales are shown in the color bars located next to each ion image	44

Figure 2.7. a) Ion images of TG(52:4) obtained using MeOH:H₂O (9:1) and MeOH:ACN:tol (5:3.5:1.5) solvents illustrating the region of interest (ROI) analysis. Dashed green lines outline the ROI selected in each image. Color bars show the normalized ion abundance scale for each ion image. b) Bar graphs show normalized ion abundances of TGs detected as [M+K]⁺ adducts (left axis) calculated from the average ROI spectra obtained for both images. A scatter plot shows the ratio of the abundances (right axis), Int_{MeOH:H₂O}/ Int_{MeOH:AcN:tol}, observed for different TG species. 45

Figure 3.1. Experimental setup for the online singlet oxygen reaction with lipids coupled to a) ESI on a QTOF MS and b) nano-DESI on a QE-Orbitrap. 1 – laser pointer with an ND filter and lens attached; 2 – micropositioners; 3 – Dino-lite cameras; 4 – sample holder; 5 – Zaber ZYX stage. Inserts show a photograph of the irradiated ESI tip positioned at a mass spectrometer inlet (panel a, 6) and nano-DESI probe (panel b). The photograph shows the tip of the primary capillary (7) interfaces with the sampling side of the nanospray capillary (8) irradiated by the laser at another end (9). The shear force probe (10) controls the distance between the sample and the nano-DESI probe. 52

Figure 3.2. a) Schematic representation of the oxidation of the C=C bonds in lipids by singlet oxygen and fragmentation via CID that yields unique neutral losses. Experimental setup for the online singlet oxygen reaction with lipids coupled to b) ESI and c) nano-DESI. 56

Figure 3.3. Positive mode ESI-MS of LPE 17:1, PC 36:2 and TG 48:3 and their (LOOH)_n products generated by the reaction with ¹O₂. The [M+Na]⁺ ions of (LOOH)_n where **n** indicates the number of O₂ additions are highlighted in blue. 57

Figure 3.4. Light on and light off positive mode ESI mass spectra of the LPE 17:1 standard at *m/z* 488. 27. Several features near *m/z* 550 correspond to solvent peaks that are unaffected by laser irradiation. The RB-related peaks are observed at *m/z*>850. An expanded view of the *m/z* 460-560 region is shown in the red box where the arrow indicates the hydroperoxide product. Only one product of the photochemical derivatization of LPE 17:1 is observed in the spectrum. 57

Figure 3.5. b) Structures of PC 18:1(9Z)/18:1(9Z) (left) and PC 18:1(6Z)/18:1(6Z) (right) showing the cleavage sites. c) LTQ-CID and d) HCD spectra of the isomeric LOOH products at *m/z* 840.5. 59

Figure 3.6. MS² spectra of the hydroperoxide product of PC-d5 17:0_22:4 (7Z, 10Z, 13Z, 16Z) obtained using an a) LTQ and b) Orbitrap. Chemical structure of PC-d5 17:0_22:4 showing the cleavage sites. The diagnostic peaks corresponding to the position of the double bond at C7, C10, C13 and C16 are highlighted in pink, blue, green and orange, respectively. The shorter arrow corresponds to product A and the longer arrow corresponds to product B. 60

Figure 3.7. MS² spectra of the hydroperoxide product of PC-d5 17:0_20:3 (8Z, 11Z, 14Z) obtained using an a) LTQ and b) Orbitrap. Chemical structure of PC-d5 17:0_20:3 showing the cleavage sites. The diagnostic peaks corresponding to the position of the double bond at C8, C11, C14 are highlighted in pink, blue, and green, respectively. The shorter arrow corresponds to product A and the longer arrow corresponds to product B. 61

Figure 3.8. HCD spectra of unreacted LPE 17:1 (top panel) and LPE 17:1(LOOH) (bottom panel). Chemical structures of both molecules showing the cleavage sites are shown in the insets. The diagnostic peaks are highlighted in pink. 62

Figure 3.9. HCD spectra of unreacted TG 48:3 (top panel) and TG 48:3(LOOH) (bottom panel). Chemical structures of both molecules showing the cleavage sites are illustrated in the insets. The diagnostic peaks are highlighted in pink..... 62

Figure 3.10. Fragmentation of lipid species ionized in negative mode. a) Chemical structure of a phospholipid containing FA 14:1 and FA 17:0. The structure along with the cleavage sites are shown for the unreacted lipids (left side) and LOOH (right side). b) HCD spectra of PS 31:1, PG 31:1 and PI 31:1 along with MS/MS of their corresponding hydroperoxide. The diagnostic peaks are highlighted in pink. We note that negative mode experiments suffer from ion suppression due to abundant RB-related peaks observed near the lipid region. In negative mode, we estimated the yield of the LOOHs products to be around 5% with respect to the unreacted lipid. Other photosensitizers may be used to improve the reaction yield and sensitivity in negative mode.... 63

Figure 3.11. Positive mode ESI-MS spectra of the mouse gastrocnemius muscle tissue extract obtained using the $^1\text{O}_2$ reaction in a solution containing RB at a) 5 μM b) 50 μM c) 100 μM and d) 500 μM concentrations. The reaction products are highlighted in blue and RB peaks are highlighted in pink. 64

Figure 3.12. a) ESI-MS of a mouse gastrocnemius muscle tissue extract obtained using the $^1\text{O}_2$ reaction; the LOOH products are shown in blue. b) Ion chromatograms of the endogenous PC 38:6 at m/z 828.55 (left) and PC 36:4 m/z 804.55 (right) and their corresponding reaction products at m/z 860.54 and m/z 836.54, respectively, obtained with and without laser excitation. 65

Figure 3.13. Ion chromatograms of the LPE 17:1 standard at m/z 488.3 and its hydroperoxide product, LPE 17:1(LOOH) at m/z 520.3, collected with the ESI setup. Light on and light off profiles are highlighted in blue and black, respectively..... 66

Figure 3.14. Line scan profiles of a mouse uterine tissue collected using the nano-DESI probe. The traces from top to bottom correspond to LPE 17:1 standard, LPE 17:1(LOOH), the endogenous PC 34:1, and its hydroperoxide product PC 34:1(LOOH). When the nano-DESI probe is on the glass slide, we only observe the signal of the LPE 17:1 standard. After the light is turned on, the ion signal of the LPE 17:1(LOOH) appears while the signal of the unreacted LPE 17:1 drops. The signals of the endogenous PC 34:1 and its product, PC 34:1(LOOH), are observed when the nano-DESI probe is on the tissue. At 1 min, the light is turned off, which causes the signals of the reaction products LPE 17:1(LOOH) and PC 34:1(LOOH) to immediately disappear. The signal of the standard 67

Figure 3.15. CID spectra of PC 34:1(LOOH) at m/z 814.5573 showing the presence of 9 Δ and 11 Δ isomers labeled in pink and blue, respectively. Fragment ions of the isobaric PE 40:6 (Na^+) and PE 42:9 (H^+) are labeled in green and yellow, respectively. 68

Figure 3.16. a) Optical image of rat cerebellum. b) Nano-DESI MS¹I of PC 34:1(LOOH). FDIIs of positional isomers corresponding to c) 11 Δ /(9 Δ +11 Δ) and d) 9 Δ /(9 Δ +11 Δ). Nano-DESI MS² images of the fragments at e) m/z 771.5 and f) m/z 673.5 corresponding to PE 40:6 and PE 42:9, respectively. 69

Figure 3.17. a) Nano-DESI MS¹ image of PC 36:1(LOOH) at m/z 842.5881 in the mouse brain tissue. b) An FDI image of the 11 Δ isomer of PC 36:1(LOOH). 70

Figure 3.18. Nano-DESI imaging experiments coupled to the $^1\text{O}_2$ reaction. a) An optical image of the mouse uterine tissue showing the area scanned by the nano-DESI probe. b) An MS¹ image of PC 16:0_18:1(LOOH) at m/z 814.5573. c) An FDI image of the 11 Δ isomer of PC 16:0_18:1(LOOH). The FDI calculation excludes the pixels outside of the tissue boundary highlighted in blue. 70

Figure 4.1. a) A schematic drawing of the high-resolution nano-DESI MSI source. b) A photograph of the imaging platform, showing the custom-designed cart (1); vibrationally insulated platform (2); lock-in amplifier (3), and computer that controls the XYZ stage (4). c) A zoomed-in photograph corresponding to the red dashed box in panel b. The XYZ stage (5), micro positioners (6), Dino-Lite microscope (7), capillary extension (8), primary capillary (9), nanospray capillary (10) and shear force probe (11) are also highlighted. 79

Figure 4.2 Pie chart showing the total number of species detected from the molecular profiling in a) positive mode and b) negative mode with the nano-DESI IM-MSI platform. 82

Figure 4.3. Averaged mass spectra and CCS vs. m/z plots of the species identified in the nano-DESI-IM-MSI of a mouse uterine tissue in a) positive mode and b) negative mode. c) Phospholipids separated by drift time in the m/z 720–890 region highlighted with the dashed box in panel a. Triangles and circles denote [M+Na]⁺ and [M+K]⁺ ions, respectively, and the symbol colors indicate the lipid class of the molecule as indicated in the legend. The nomenclature used to indicate the individual species is AA:X, where AA denotes the acyl chain length and X denotes the number of double bonds. The dotted lines highlight the series of homologous species differing by the number of double bonds; the number of double bonds for each species is indicated inside the corresponding marker. d) Fatty acids and oxidized fatty acids separated by drift time in the m/z 250–400 region highlighted with the dashed box in panel b. Nomenclature used to indicate individual species is the same as described earlier. 83

Figure 4.4. A 2D-IM-MS plot obtained for m/z 111.0202..... 85

Figure 4.5. Optical images of the mouse uterine tissue sections (left column) highlighting their main components including myometrium (myo) composed of longitudinal (L) and circular (C) muscle layers, stroma (S), luminal epithelium (LE) and glandular epithelium (GE) are included on the left side. Representative nano-DESI ion images of the tissue sections collected using the new nano-DESI-IM-QTOF platform in positive mode (top row) and negative mode (bottom row) using 1 Hz acquisition rate. The intensity scale changes from black (low) to yellow (high)..... 87

Figure 4.6 a) The experimental and deconvoluted arrival time distribution (ATD) of m/z 343.2272. The experimental ATD (dotted line) is overlaid on top of the best fit profile (solid green line). ATD profiles of isomers 1 and 2 are shown as blue and pink lines, respectively. Colored bars indicate the region selected for image generation. b) An optical image of the mouse uterine tissue section c) A composite ion image generated at DT 24.91 ms. Ion images of d) isomer 1 at DT 24.52 ms and e) isomer 2 at DT 25.52 ms. d) An FDI image showing that the relative abundance of isomer 1 is decreased in the LE region. 88

Figure 4.7. Ion images generated from the deconvoluted drift time peak corresponding to a) m/z 345.2422 and b) m/z 347.2585. The FDI images showing the relative abundance of isomer 1 are depicted on the right side 90

Figure 4.8. a) A 2D-IM-MS plot of the m/z range of 304.5–307.5 showing the isotopic distributions of GSH (orange line) and GSSG (purple line). Ion images of closely-spaced isobaric peaks at b) m/z 306.0748, DT 17.85 ms and c) m/z 306.0758, DT 21.29 ms. d) An ion image obtained without IM separation, in which the contribution of the M+2 isotopic peak of GSSG is indicated in purple and the contribution of the monoisotopic peak of GSH is indicated in yellow..... 91

Figure 4.9. Separation of isobaric PE (40:4) from PC (P-38:3) in the 2D IM-MS plot. Drift time-selected ion images generated for each molecule are depicted on the right side..... 93

Figure 4.10. 2D IM-MS plot showing the isobaric separation of a solvent peak at DT 30.62 from the endogenous molecule LPC(18:2) at DT 32.16 ms. The ion image corresponding to LPC (18:2) without drift time separation is included on the left side for comparison. 94

Figure 5.1. Multimodal imaging of skeletal muscle fibers which combines IF imaging with MSI in a) positive mode and b) negative mode. The results are shown for three biological replicates examined in this study. IF images are displayed on the left of ion images showing the distribution of type I (green), type IIa (red), type IIx (black) and type IIb (blue) fibers in GAS. Ion images selected for visualization of fiber patterns are PC 40:6 observed as a $[M+Na]^+$ adduct at m/z 856. 5830 and $[M-H]^-$ ion of PC 22:1;O2 at m/z 622. 3716 for positive and negative mode nano-DESI MSI, respectively. Scale bars are displayed inside each ion image The color bar is displayed on the right side indicating that the intensity scale changes from black (low) to yellow (high). 109

Figure 5.2. Calculation of the spatial registration of the imaging of individual muscle fibers. We use variations on the chemical gradient of a molecule using the 80/20 rule. 110

Figure 5.3. Multimodal workflow for nano-DESI MSI of skeletal muscle fibers. a) Optical image of a GAS tissue section. Yellow square indicates the region of the tissue analyzed in the MSI experiment. b) Ion images of tissue-related peaks. c) IF image acquired using an adjacent tissue section cropped to the region analyzed by MSI. d) RGB representation of all ion images using PCA analysis. e) ROI image created from IF segmentation. f) Registration of segmented image to RGB images yields ROI fiber-specific masks that enable feature extraction for each fiber type. g) Data analysis using extracted ion abundances enables comparison of the chemical composition of different fiber types..... 111

Figure 5.4 Affine registration process. a) Ion image that serves as a fixed image, b) gray scale of an IF image which serves as a moving image. c) The result of the affine registration of the IF image to the ion image..... 112

Figure 5.5. a) Segmented IF image. b) Eroded image of a) to eliminate surrounding pixels that might overlap with other fiber types. Fiber-specific mask generated for c) type I, d) type IIa, e) type IIx and f) type IIb are displayed overlapping a representative ion image to show the good match between the mask and fiber pattern..... 112

Figure 5.6. a) LDA analysis of all the features identified in GAS tissue in positive mode. Green circles correspond to type I fibers, red circles correspond to type IIa fibers, black circles correspond to type IIx, and blue circles correspond to type IIb fibers. b) Bar graph showing the sorting of species based on their spatial localization. Red-green (RG) corresponds to a molecular distribution enhanced in type I and type IIa fibers. Red-green-black (RGBK) corresponds to a distribution enhanced in type I, type IIa, and type IIx fibers. Blue (BL) corresponds to a distribution enhanced

in type IIb fibers. Everywhere pattern indicates a uniform molecular distribution across the tissue.	113
Figure 5.7. a) MS/MS spectrum of m/z 175.0245 identified as ascorbic acid. b) IF and TIC normalized ion images of m/z 175.0245.	114
Figure 5.8. Volcano plots showing a direct comparison of a) type I and type IIa fibers, b) type I and type IIa fibers, and c) type IIa and type IIx fibers. Purple circles indicate molecules significantly different displaying a $\log_2(FC)$ less than -0.5 or greater than 0.5 and p -value <0.05 in a) and b), and $\log_2(FC)$ less than -0.3 or greater than 0.3 and p -value <0.05 in c).	117
Figure 5.9. a) Heatmap of all the molecules identified in GAS tissue. Abundances are shown in a z-score scale using the blue-white-red color bar which indicates z-values ranging from -1.5 to 1.5. TIC normalized ion images of b) $[M+H]^+$ adduct of PC 36:2 at m/z 786.6007, c) $[M-H]^-$ adduct of PE 40:6 at m/z 790.5787, d) $[M+Na]^+$ adduct of PC 34:0 at m/z 784.5850, e) $[M+Na]^+$ adduct of SM d36:1 at m/z 753.5894 and f) $[M-H]^-$ adduct of PC 16:0_5:0(COOH) at m/z 608.3565. Scale bars are displayed inside each ion image. The color bar is displayed on the right side indicating that the intensity scale changes from black (low) to yellow (high).	121
Figure 5.10. Acyl chain composition of all the phospholipids detected in GAS tissue with a carbon length ranging from 12C to 24C. Length of the bars indicates the number of species containing a specific acyl chain. Red bars indicate oxidative species whereas blue bars indicate glycolytic species.	123
Figure 5.11. MS/MS spectrum of m/z 636.3862 showing the presence of multiple isomers. Orange arrows indicate the truncated oxidized acyl chains whereas the green circles indicate the presence of multiple fatty acid chains.	124

LIST OF ABBREVIATIONS

AA	Arachidonic Acid
AAc	Ammonium Acetate
AcN	Acetonitrile
AF	Ammonium Formate
AGC	Automatic Gain Control
AMP	Adenosine Monophosphate
ATD	Arrival Time Distribution
ATGL	Adipose Triglyceride Lipase
CAR	Carnitine
CCS	Collision Cross Section
CHCl₃	Chloroform
CID	Collision Induced Dissociation
CL	Cardiolipin
DCM	Dichloromethane
DG	Diacylglyceride
dGMP	Deoxyguanosine Monophosphate
DHA	Docosahexaenoic Acid
DMF	Dimethylformamide
DPA	Docosapentaenoic Acid
DT	Drift Time
DTIMS	Drift Tube Ion Mobility Spectrometer
ESI	Electrospray Ionization
FA	Fatty Acid
FC	Fold change
GAS	Gastrocnemius muscle
GE	Glandular Epithelium
GSH	Glutathione
GSSG	Oxidized Glutathione

GT	Girard T
HCD	High-energy Collision Dissociation
HDoHE	Hydroxydocosaheanoic Acid
HSL	Hormone Sensitive Lipase
IF	Immunofluorescence
iMFP	Integrated Microfluidic Probe
IMP	Inosine Monophosphate
IMS	Ion Mobility Spectrometry
iMSI	Isomer-resolved Mass Spectrometry Imaging
IT	Injection Time
LAESI	Laser Desorption Electrospray Ionization
LC-MS	Liquid Chromatography-Mass Spectrometry
LDA	Linear Discriminant Analysis
LDs	Lipid Droplets
LE	Luminal Epithelium
LESA	Liquid Extraction Surface Analysis
LL	Longitudinal Layer
LOOH	Lipid Hydroperoxide
LPC	Lysophosphatidylcholine
LPE	Lysophosphatidylethanolamine
LTQ	Linear Ion Trap Mass Spectrometer
MALDI	Matrix Assisted Laser Desorption Ionization
MeOH	Methanol
MG	Monoacylglyceride
MGL	Monoacylglycerol Lipase
MS/MS	Tandem Mass Spectrometry
MSI	Mass Spectrometry Imaging
MUFA	Monounsaturated Fatty Acid
MyHC	Myosin Heavy Chain
Myo	Myometrium
Nano-DESI	Nanospray Desorption Electrospray Ionization

NCE	Normalized Collision Energy
OCT	Optical Cutting Temperature
OD	Outer Diameter
OzID	Ozone-induced dissociation
PA	Palmitic Acid
PC	Phosphatidylcholine
PCA	Principal Component Analysis
PE	Phosphatidylethanolamine
PG	Phosphatidylglycerol
PS	Phosphatidylserine
PUFA	Polyunsaturated Fatty Acid
QqQ	Triple Quadruple Mass Spectrometer
RB	Rose Bengal
ROI	Region of Interest
ROS	Reactive Oxygen Species
SA	Stearic Acid
SFA	Saturated Fatty Acid
SM	Sphingomyelin
TG	Triacylglyceride
TIC	Total Ion Current
Tol	Toluene
UVPD	Ultraviolet Photodissociation

ABSTRACT

Ambient Mass Spectrometry Imaging (MSI) is a powerful analytical tool in biomedical research that enables simultaneous label-free spatial mapping of hundreds of molecules in biological samples under native conditions. Nanospray desorption electrospray ionization (nano-DESI) is an emergent ambient MSI technique developed in 2010 that uses localized liquid extraction of molecules directly from surfaces. Like other liquid-extraction based techniques, nano-DESI relies on gentle removal of molecules from surfaces and soft ionization. High sensitivity and spatial resolution, versatility of the solvent composition, which may be used to tailor the extraction and ionization of selected molecules, quantification capabilities at the single-pixel level as well as compensation for matrix effects by adding a known standard to the solvent, and online derivatization are key features of nano-DESI MSI that position it as a unique analytical tool for studying biological systems.

Despite the advantages that nano-DESI provides, there are still challenges associated with the structural characterization, extraction, and detection of certain molecular classes. Therefore, my dissertation research has focused on addressing these analytical challenges by developing innovative approaches that substantially enhance the performance of the nano-DESI technique in the study of complex biological systems.

In this thesis, a systematic study of the solvent composition is carried out to aid in the detection of neutral lipids such as triglycerides thereby expanding the molecular coverage of nano-DESI experiments. Taking advantage of the versatility of the solvent composition, I developed an approach for the online derivatization of unsaturated lipids into lipid hydroperoxides using the reaction of singlet oxygen with C=C bonds. This method further expands the specificity of nano-DESI MSI by enabling the detection and imaging of positional lipid isomers. To aid in the analysis of complex mixtures and provide additional structural information in the form of collision cross sections, coupling of nano-DESI with a drift-tube ion mobility spectrometry is also reported along with examples of the powerful capabilities of this platform. Lastly, nano-DESI MSI is used to address the complexity in the analysis of individual skeletal muscle fibers. This collaborative project involves the development of a robust image registration approach of immunofluorescence imaging and high-spatial resolution nano-DESI MSI to obtain accurate chemical maps specific to

each fiber type. The developments described in this thesis are key to understanding the dynamic metabolic processes on a molecular level with an unprecedented specificity and sensitivity.

CHAPTER 1. INTRODUCTION

1.1 Mass spectrometry imaging

Mass spectrometry (MS) is a powerful analytical technique, which enables sensitive detection and identification of molecules in complex mixtures. With the advent of soft ionization techniques such as electrospray (ESI)¹ and matrix-assisted laser desorption ionization (MALDI),² MS became an indispensable tool for the label-free detection of intact biomolecules in biological samples. Dramatic improvements in sensitivity, quantification, and identification capabilities of the MS instrumentation have uniquely positioned it at the forefront of biological research, clinical studies, drug discovery, forensics, and environmental sciences. Meanwhile, the development of approaches for the spatial localization of molecules using MS imaging (MSI) has extended these strengths of the analytical MS to the cellular and sub-cellular scale, and enabled detailed molecular mapping of hundreds of molecules in biological tissues.³⁻⁹

Since the initial demonstration of MSI by the Caprioli group,¹⁰ MALDI has become the most widely used soft ionization technique in MSI experiments with several commercial platforms available to the scientific community.^{8,9,11,12} Recent developments of ambient ionization techniques, in which samples are analyzed without special pre-treatment, have expanded the range of MSI applications.¹³⁻¹⁵ These ionization techniques can be classified into laser-based and liquid extraction-based approaches.¹⁶ Laser ablation (LA) and LA coupled with ESI (LAESI)¹⁷ along with matrix-assisted laser desorption ESI (MALDESI)¹⁸ are among the most widely used laser-based ionization techniques in MSI. Meanwhile, a majority of MSI experiments involving liquid extraction-based techniques have relied on desorption electrospray ionization (DESI)^{19,20} and its variants along with nanospray desorption electrospray ionization (nano-DESI),²¹ liquid microjunction surface sampling probe (LMJ-SSP),²² and liquid extraction surface analysis (LESA).²³

1.2 Nano-DESI overview

Nano-DESI, is a relatively new ambient ionization technique developed by the Laskin group at the Pacific Northwestern National Laboratory.²⁴ A nano-DESI probe is comprised of two capillaries forming a liquid bridge (Figure 1.1). The primary capillary supplies the solvent from a

syringe to the nanospray capillary forming a 90° angle at their intersection point. The nanospray capillary transfers the solvent to the MS inlet. In the presence of the high voltage, ionization takes place at the tip of the nanospray capillary. A micrometer droplet is formed after the nano-DESI probe is landed on the surface thereby enabling localized extraction of molecules from surfaces which are then transported through the nanospray capillary.

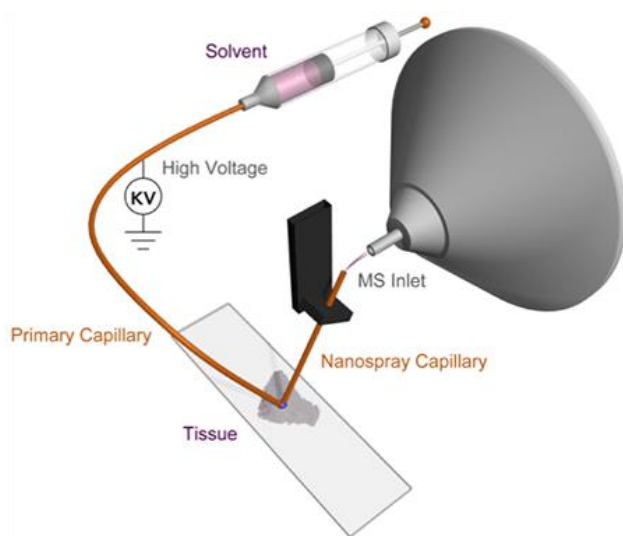


Figure 1.1. Schematic diagram of the nanospray desorption electrospray ionization (nano-DESI). Figure reproduced with permission from reference 1, Copyright © 2012, American Chemical Society.

The versatility of nano-DESI relies on the flexibility in the solvent composition, which may be modified to target the extraction or ionization of selected molecules. In a traditional nano-DESI experiment, a polar mixture comprised of methanol: water (MeOH:H₂O) is used as the working solvent. This mixture is compatible with ESI resulting in efficient ionization of a wide variety of polar molecules. A comparison of lipids observed in nano-DESI and LC-MS/MS experiments using this solvent composition revealed good coverage of many lipid classes²⁵ except triglycerides (TGs), which are not efficiently extracted because of their low polarity.

Online chemical derivatization taking advantage of the accelerated reactions in microdroplets is another important capability of nano-DESI. Implementation of this approach only requires the addition of the reagent to the nano-DESI solvent. For example, evaluation of the presence of carbonyl groups contained in secondary organic aerosols was reported using a reaction with Girard T reagent.²⁶ Alternatively, the addition of different ionization enhancers have also proven to be effective at improving the detection of some classes molecules.^{27,28}

Similar to other imaging techniques, nano-DESI is subject to matrix effects. Matrix effects originate from the competition of analyte molecules for charge resulting in signal suppression during ionization. The composition of the extracted analyte mixture and variations in alkali metal concentration across the sample are two key factors determining the severity of matrix effects.²⁹ It has been demonstrated that normalization of the signals of endogenous molecules extracted from sample to the signal of the corresponding adduct of a standard with similar structural characteristics efficiently compensates for signal suppression in ionization. This approach is implemented by adding one or more standards to the nano-DESI solvent thereby revealing accurate concentration gradients by normalizing ion signals at the single-pixel level.

1.2.1 Improvements in the nano-DESI platform

Since the initial report in 2010,²¹ there have been many developments aiming at enhancing the performance and expanding the application of nano-DESI for imaging of biological samples. Initially, assembling of the nano-DESI platform involved mounting the sample holder onto an automated XYZ stage that uses a three-point plane method to define the tilt of the sample plane and recalculate the vertical position of the stage at each point.³⁰ Using this approach, imaging of relatively flat samples was accomplished. Moreover, the development of the data analysis software, MSI QuickView, was reported that enabled data visualization and normalization. Improvements of the setup described above aimed at extending the imaging capabilities of nano-DESI to uneven surfaces which represents a more realistic scenario. Integration of a shear-force probe with the nano-DESI probe enabled constant-distance mode imaging thereby accounting for height variations in samples with complex topographies.^{31,32} This development that combines surface probe microscopy and MSI permits accurate control of the distance between the nano-DESI probe and the sample which also helps maintaining a constant droplet size across the scanned area.

1.2.2 Improvements in the spatial resolution

In nano-DESI MSI data are acquired by scanning the tissue under the nano-DESI probe in lines shown as orange highlights in the inset of Figure 1.2. A sample is positioned on a motorized XYZ stage controlled by a custom-designed Labview program. A typical experiment involves

scanning of the sample along the X direction in a line with constant velocity and stepping between the lines in the Y direction.

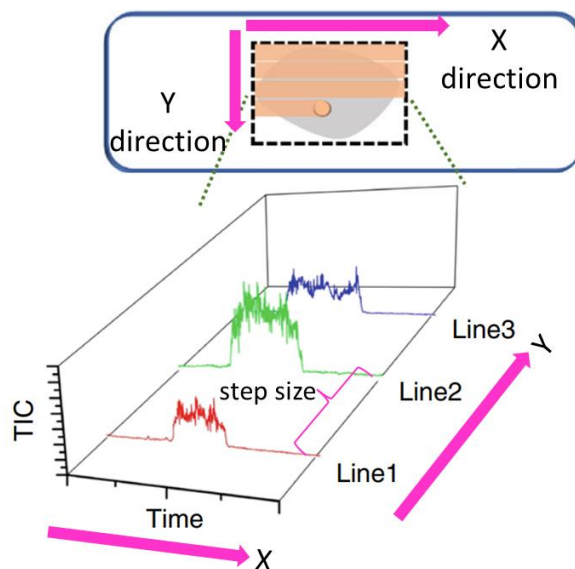


Figure 1.2 Data acquisition in nano-DESI MSI experiments. Modified from reference 14. Copyright © 2019, Springer Nature

In liquid-extraction techniques like nano-DESI, the spatial resolution is determined mainly by three factors: 1) a combination of the acquisition speed of the instrument and velocity of the stage which defines pixel size in the X direction, 2) line spacing which defines pixel size in the Y direction and 3) the size of droplet formed between the nano-DESI probe and the sample.³³ The size of the droplet determines the ultimate spatial resolution. The acquisition speed of the instrument (1) becomes important only when the scan rate is high. Finally, the spacing between the lines is a user's choice.

In order to obtain the best possible resolution, the acquisition parameters 1) and 2) are selected to ensure that the spatial resolution is not limited by the acquisition settings. For example, more pixels in the X-direction can be collected by either lowering the velocity of the stage or increasing the acquisition speed (number of scans/seconds) or both. In contrast, the pixel size in the Y direction is more constrained because of the step size between the line scans which is selected to be equal or greater than the droplet size. For example, when the outer diameter (OD) of the capillaries comprising the nano-DESI probe is around 150 μm , the step size (pixel size in the Y direction) ranges from 150-200 μm . This spacing was selected to ensure that the same region is

not scanned more than once which might affect analyte localization in the tissues. However, a recent study using oversampling demonstrated that it is possible to use step sizes smaller than the droplet size to improve the resolution in the Y direction.³³ In that study, the step size was reduced by a factor of three thereby notably improving the quality of the overall image and enabling the visualization of features that were not observed in a lower resolution experiment.

Improvement of the spatial resolution related to the droplet size involves the modification of the nano-DESI probe. Given that smaller droplet sizes yield better spatial resolution, the primary and secondary capillaries are pulled down to ODs ranging from 15 to 25 μm . Although the fabrication of the two finely pulled capillaries is somewhat more complex, these capillaries operate similar as the ones described earlier. High-spatial resolution nano-DESI MSI experiments require a precise control of the sampling distance to avoid damaging the delicate pulled capillaries. Therefore, it is vital that the high-resolution nano-DESI probe operates in combination with a shear probe, which is positioned in close proximity to the liquid bridge formed between the two capillaries. A detailed protocol providing the details of the fabrication and assembling of the high-resolution nano-DESI probe has been recently published.³⁴ Using this approach, the spatial resolution of nano-DESI experiments is improved from 100 μm to better than 10 μm .

1.2.3 Nano-DESI applications

Nano-DESI has proven to be a versatile technique in the analysis and profiling of many classes of molecules. For example, nano-DESI was initially used for the molecular characterization of secondary organic compounds collected on substrates thereby providing a better platform for soft ionization of complex mixtures and enabling the preservation of chemically labile species.^{35,36} In combination with high-resolution MS, nano-DESI was also successfully used for the analysis of both polar and non-polar constituents of petroleum, one of the most complex systems available in nature.³⁷

Microbiology has been another important area of research that benefited from the capabilities of nano-DESI that enabled *in vivo* imaging of living microbial, fungi, and yeast colonies. Nano-DESI has been used for the spatial profiling of chemical gradients generated by living microbial communities grown on agar plates.^{38–41} Because nano-DESI enables localized analysis of living colonies directly from the Petri dish, the viability of the colonies is not

compromised. Moreover, this type of sampling is advantageous for detecting unique molecules like glycolipids that are generally not detected with other extraction methods.³⁸

Mapping of intricate metabolic pathways in mammalian tissues has been by far the most prominent area of nano-DESI applications. For example, nano-DESI has been used to examine molecular alterations associated with disease progression like diabetes⁴² and ischemic stroke²⁹ or organ development like lung⁴³ and uterus.^{44,45} Moreover, it has also been used to address sample heterogeneity thereby providing unique insights into the metabolic transformations at a single cell level. Examples of these systems include pancreatic islets⁴⁶ and human cheek cells.⁴⁷

1.2.4 Overview of the thesis

Despite the exciting developments in nano-DESI MSI in the last decade, there are still significant challenges related to the structural characterization of lipids and metabolites, molecular coverage of the method, and comprehensive understanding of the chemical information obtained from MSI and its relevance to health and disease.

Thus, the aim of my PhD was to expand the capabilities of nano-DESI MSI to make it a powerful technique for molecular mapping of complex biological systems. I have developed analytical methods that substantially improve molecular coverage, specificity, and sensitivity of nano-DESI MSI experiments. These developments are key to understanding molecular localizations and their relevance to health and disease. Although the methods described herein are primarily developed using nano-DESI, they can readily be implemented in any liquid-extraction based technique.

Chapter 2 demonstrates the versatility of liquid-extraction based techniques in providing a simple means of improving the molecular coverage of MSI experiments via the optimization of the solvent composition. Traditionally, nano-DESI MSI experiments are performed using a solvent comprised of MeOH:H₂O 9:1 (v/v), which provides good coverage of most lipids classes except for neutral lipids like triglycerides (TGs). These lipids are rarely detected in MSI experiments unless they are abundant in the sample. The effect of the solvent on the extraction and ionization efficiency of TGs is examined using different nonpolar solvents and ionic dopants. It is found that the addition of ionic compounds does not improve the ionization of TGs which can readily form adducts with salts available in the tissue. In contrast, the use of nonpolar solvents dramatically improves the extraction of the hydrophobic TGs. Most importantly, the presence of a non-polar

component in the solvent does not have degrade the overall signal. With the method described in this chapter, imaging of TGs is accomplished thereby expanding the molecular coverage of nano-DESI MSI experiments (Figure 1.3).

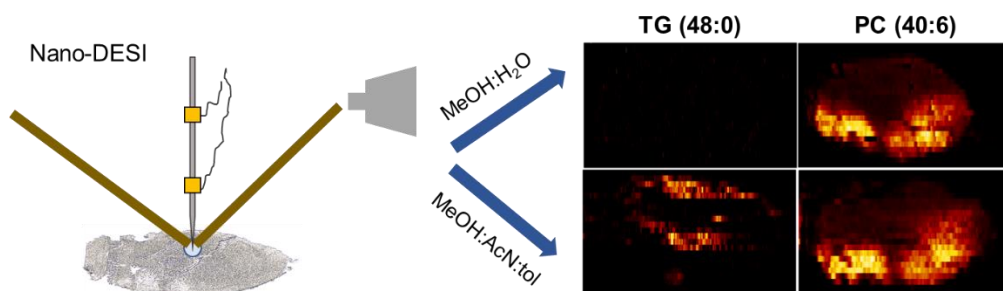


Figure 1.3 Solvent optimization for improved molecular coverage

Chapter 3 focuses on improving the specificity of nano-DESI imaging experiments by providing isomer level discrimination. This chapter describes the development of a powerful method for locating the double bond ($C=C$) position in lipids using reaction with singlet oxygen and collision-induced dissociation (CID). When combined with nano-DESI MSI, this method enables imaging of positional lipid isomers. These isomeric species are observed as a mixture in conventional MSI. The method described herein is versatile and inexpensive. Proof-of-concept experiments were initially performed using an ESI setup which demonstrated the feasibility of the approach. Next, this method is coupled with nano-DESI MSI. Lipids are extracted from the sample into a flowing solvent containing a photosensitizer. the solution is irradiated using a green laser pointer to generate singlet oxygen, which selectively reacts with $C=C$ in lipids to form lipid hydroperoxides. CID of the hydroperoxide products in a mass spectrometer reveals the position of the $C=C$ in the original lipid (Figure 1.4). Imaging experiments using this new method are performed for the first time revealing substantial changes in the isomeric composition of the white and gray matter in mouse cerebellum tissue.

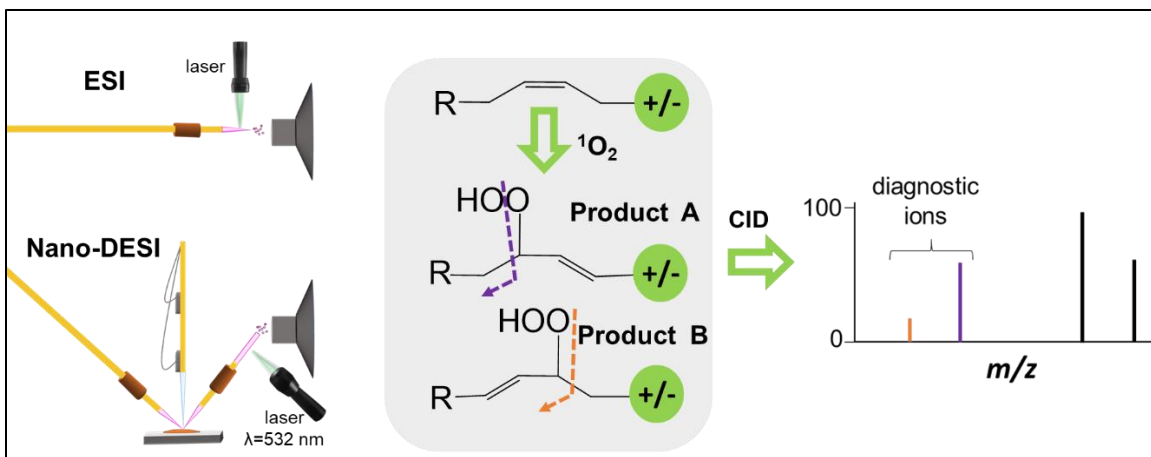


Figure 1.4. Photochemical derivatization of C=C bond in lipids using singlet oxygen reaction

Chapter 4 describes another important development of imaging experiments which involves the implementation of a nano-DESI source on a state-of-the-art ion mobility system for improved specificity of imaging experiments (Figure 1.5). Drift-time selected ion images with high spatial resolution are reported for the first time, which is not currently accessible using commercial platforms. This newly developed platform provides another dimension for separation of biomolecules based on their drift time, which facilitates rapid isobaric and isomeric separation, reduces chemical noise, and substantially improves the molecular specificity of imaging experiments. Examples of these new advantages are provided in this chapter. Moreover, collision cross section (CCS) measurements of different molecules are reported which can serve as additional molecular descriptors for molecular identification after comparison with open CCS libraries.

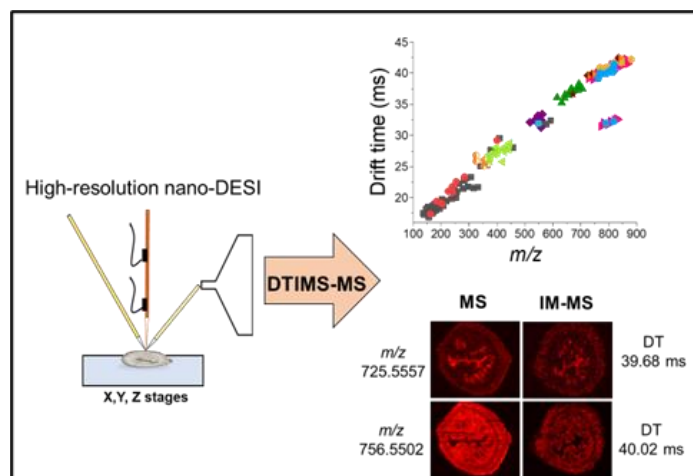


Figure 1.5. Coupling of Nano-DESI MSI with ion mobility

Chapter 5 provides an example of the power of high-spatial resolution nano-DESI MSI for mapping of the chemical composition of one of the most challenging systems, skeletal muscle fibers. These fibers are 30 μm in diameter and are arranged in a mosaic-like pattern, which complicates their characterization using both bulk analysis and lower-spatial resolution MSI approaches. In addition, shallow chemical gradients make it difficult to assign different molecular patterns to individual fibers. A multimodal approach is developed in which immunofluorescence (IF) imaging is used to guide MSI experiments (Figure 1.6). Given the challenges associated with correlating the observed spatial patterns in ion images to specific fiber types, a robust registration and segmentation approach has been developed in collaboration with Hang Hu, another graduate student in the Julia Laskin lab. In this approach, principal component analysis (PCA) is used to reduce data dimensionality of ion images and generate an RGB representation of the chemical gradients in the sample. Next, segmentation of the IF image is performed to obtain fiber type-specific region of interest (ROI) masks. Finally, the segmented image is registered to the RGB representation image and ion abundances in well-defined ROIs are obtained. Using this approach, the chemical composition of each fiber type was accurately determined and unique insights about their biological role were derived from the multimodal imaging data.

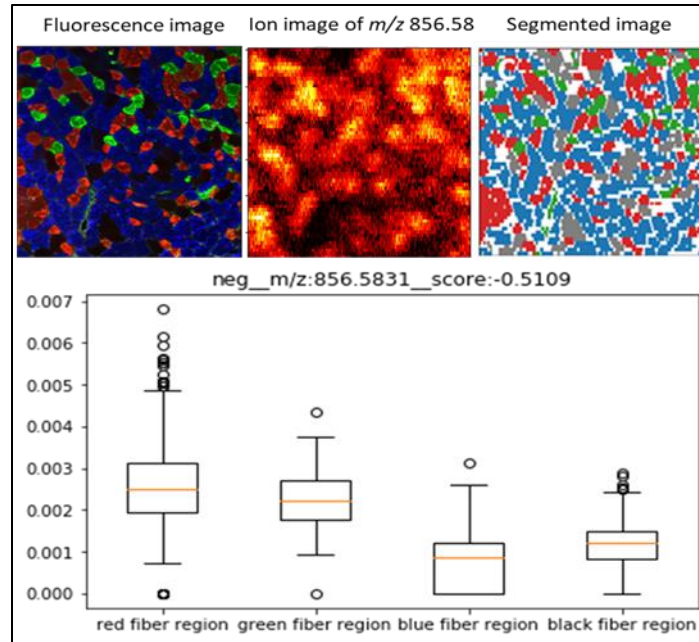


Figure 1.6. High-spatial resolution imaging of skeletal muscle fibers

Chapter 6 provides a general discussion of the results and future directions of this research.

CHAPTER 2. IMAGING OF TRIGLYCERIDES IN TISSUES USING NANOSPRAY DESORPTION ELECTROSPRAY IONIZATION (NANO-DESI) MASS SPECTROMETRY

2.1 Introduction

Lipids play an important role in biological systems by participating in signaling and energy storage and serving as cell membrane components.⁴⁸ Their complexity and structural diversity have always presented a challenge for both qualitative and quantitative analysis. At present, liquid chromatography coupled to mass spectrometry (LC-MS) is by far the most common platform used in lipidomics studies.^{49,50} LC-MS approaches have enabled confident identification and detection of both high- and low-abundance analytes in complex lipid mixtures. Alternatively, shotgun lipidomics approaches have been developed in an effort to improve the analysis throughput.^{51–53}

Mass spectrometry imaging (MSI) also has emerged as a powerful tool for the spatial mapping of molecules in biological samples.^{9,54,55} MSI is a label-free technology, which simultaneously provides chemical and spatial information in the form of molecular images. When used for lipid imaging, MSI experiments may be described as spatially-resolved shotgun lipidomics. Matrix assisted laser desorption/ionization (MALDI) is the most common ionization technique used for the imaging of a broad range of analytes ranging from small lipids and metabolites⁵⁶ to large biomolecules such as intact proteins.¹¹ Ambient liquid extraction ionization techniques including desorption electrospray ionization (DESI) and nanospray desorption electrospray ionization (nano-DESI) are gaining popularity in MSI because they operate under open-air conditions and do not require sample preparation.^{4,14,57,58} The application of these techniques to tissue imaging provides insights into the specific functions of lipids and metabolites in biological systems and helps identify potential biomarkers for the study of disease mechanisms.^{42,44,59,60} One of the advantages of ambient liquid extraction techniques is that solvent composition can be tailored to either enable selective extraction of the analytes of interest or provide broad coverage of molecules in the sample.¹⁴ Moreover, the addition of dopants to the working solvent has proven to be successful to improve the extraction of low-solubility species⁶¹ or enhance the ionization by changing the polarity of the analyte.^{27,62} In DESI experiments, binary mixtures of water with methanol (MeOH) at different ratios were reported to be suitable for the analysis of different phospholipid classes and sphingolipids.⁶³ A mixture of dimethylformamide

(DMF) with water or acetonitrile (AcN) has been used in DESI MSI experiments as a less destructive and tissue friendly solvent, which helped improved the sensitivity of the technique towards small metabolites.⁶⁴

In nano-DESI, molecules from the sample are extracted into a liquid bridge formed between two glass capillaries,^{21,24} transferred to a mass spectrometer inlet, and ionized by electrospray ionization. A majority of nano-DESI MSI experiments reported so far have been performed using a solvent composed of MeOH:H₂O (9:1) (v/v), which provides good coverage for most of lipid classes.^{44,65} It is not surprising that due to the polar nature of these traditionally used solvents, polar lipids were predominately observed in these studies. However, triglycerides (TGs) are detected with low efficiency using this solvent composition. Indeed, direct comparison between nano-DESI MSI and LC-MS/MS lipidomics analysis performed using MeOH:H₂O (9:1) revealed good coverage of a majority of lipid classes except for TGs in nano-DESI MSI.⁶⁶

TGs are neutral lipids consisting of a glycerol backbone and three fatty acyl chains. In mammals, TGs serve as the main source of energy for the body. Indeed, oxidation of TGs releases more than twice as much energy per gram than other biomolecules such as carbohydrates and proteins.⁶⁷ Accumulation of TGs in non-adipose tissues is associated with the development of insulin resistance⁶⁸ as well as other pathologies.^{69,70} Therefore, the ability to explore the localization of TGs in tissue sections is important for understanding of their role in complex biological processes. Nonpolar TGs are not readily extracted and ionized, which presents a challenge for imaging experiments utilizing liquid extraction-based ionization techniques. Therefore, it is important to develop approaches to improve their detection in these experiments. DESI analysis of TGs using 1:1 water/methanol (v/v) was performed for samples rich in TGs including edible oils and margarines.⁷¹ However, DESI imaging of TGs was reported for the first time after their complexation with Ag⁺ ions which improved the detection of olefinic lipids.⁷² This method allowed the detection of unsaturated but not of saturated TGs, which do not contain double bonds known to interact with Ag⁺ ions.

In this work, we aim to address the limitation of the 9:1 (v/v) MeOH:H₂O system,⁶⁶ which shows low sensitivity towards neutral TG species. In particular, we explore the effect of solvent composition on the extraction and ionization of TGs using gastrocnemius muscle tissue as a model system. We hypothesized that extraction of TGs may be improved using non-polar organic solvents and compared the detection efficiency of TGs using three solvent mixtures containing

nonpolar components. Furthermore, we examined the effect of ionic and reactive dopants on the ionization efficiency of TGs. Our results demonstrate substantial improvement in the detection of TGs as $[M+K]^+$ species using less polar solvents. However, we did not observe an improvement in the ionization efficiency using ionic dopants in the solvent. This is attributed to the high content of K^+ ions in tissue samples and favorable cationization of TGs via potassium cation complexation making $[M+K]^+$ adducts of TGs the most abundant species in the spectrum. On-line chemical derivatization with Girard T (GT) performed on the tissue did not produce reaction products with TGs on the timescale of nano-DESI analysis. Nano-DESI MSI experiments carried out using methanol:acetonitrile:toluene mixture enabled imaging of at least fourteen TG species in the tissue without noticeably affecting the detection efficiency of other analytes in the tissue. This result suggests that the detection of TGs in tissue sections using liquid extraction techniques is mainly determined by their solubility in the extraction solvent.

2.2 Materials and methods

2.2.1 Chemicals and solutions

Ammonium formate (AF) and HPLC plus toluene (tol) were acquired from Sigma-Aldrich. Omnisolv LC-MS grade water, methanol (MeOH), and acetonitrile (AcN) were purchased from Millipore Sigma's (Burlington, MA). Dichloromethane (DCM) ($\geq 99.5\%$ purity) was purchased from Avantor (Radnor, PA). Solvent mixtures used in this study are comprised of: (1) a 9:1 (v/v) MeOH:H₂O mixture, (2) a 5:3.5:1.5 (v/v/v) MeOH:AcN:tol and (3) a 6:4 (v/v) MeOH:DCM mixture. A 100 μ M solution of Girard T and AF solutions with concentrations ranging from 0.1 to 10 mM were also prepared using MeOH:AcN:tol.

2.2.2 Tissue collection and handling

Adult (3-month old) C57BL/6 mice used in this study were originally obtained from Jackson Laboratory (Bar Harbor, ME) and maintained in the animal facility with free access to standard rodent chow and water. All the procedures involving mice were approved by the Purdue University Animal Care and Use Committee (Protocol# 1112000440). Gastrocnemius muscles were collected as previously described.⁷³ Samples were flash frozen in liquid nitrogen, embedded using the optimal cutting temperature compound (OCT compound) with 1/2 of tissue devoid of OCT, and

stored in a -80°C freezer. Regions of the frozen muscle tissues remote from the OCT embedding were cross sectioned serially into 10 µm-thick sections using a Leica CM1850 cryostat. Adjacent sections were attached onto glass slides and stored in a slide storage box at -80°C. Tissue sections were allowed to thaw at room temperature prior running nano-DESI MSI experiments.

2.2.3 Nano-DESI experiments

Individual line scans using different solvent compositions were acquired using an Agilent 6560 IM-QTOF MS (Agilent Technologies, Santa Clara) whereas imaging experiments were performed on a Q-Exactive HF-X Orbitrap mass spectrometer (Thermo Fisher Scientific, Waltham, MA) using a custom designed nano-DESI source.^{32,65} The nano-DESI probe was assembled by forming a liquid bridge between the primary and nanospray fused silica capillaries (OD 150µm x ID 50µm). The nanospray capillary delivered the extracted analytes to the mass spectrometer inlet where they were ionized using electrospray ionization. A detailed description of this custom-designed shear force measurement unit can be found in our previous papers^{32,46}. Briefly, a third fused silica capillary (200 µm ID, 790 µm OD) was pulled to ~20 µm OD using a P-2000 puller (Sutter instrument, Novato, CA) to serve as a shear force probe. Pulling parameters: Line 1, Heat 650, Fil 4, Vel 80, Del 130, Pull 60; Line 2, Heat 650, Fil 4, Vel 50, Del 130, Pull 60. Two piezoelectric ceramic plates (3.8 MHz, Steiner & Martins, Inc., Doral, FL) were attached to the shear force probe: the upper plate induced the probe oscillation using a function generator and the bottom plate positioned closer to the sample, detected the amplitude of the shear force vibration through a lock-in amplifier (Stanford Research Systems, Sunnyvale, CA). The shear force probe was positioned next to the nano-DESI probe to maintain a constant distance between the sample and the nano-DESI probe and therefore, the same extraction efficiency throughout the experiment. All capillaries were positioned in front of the mass spectrometer inlet using high-resolution micromanipulators (5, XYZ500TIM, Quater Research and Development, Bend, OR). Two Dino-Lite microscope cameras were used to guide the assembly of the nano-DESI and shear force probes.

Two solvent compositions were used in imaging experiments: (1) MeOH:H₂O (9:1) (v/v) and (2) MeOH:AcN:tol (5:3.5:1.5) (v/v/v) and were infused using a syringe pump at 0.5 µL/min. Ionization was achieved by applying a 3.5 kV potential to the syringe needle. The heated capillary inlet was held at 30 V and 250 °C. Imaging data were acquired at a scan rate of 40 µm/s and a step between the lines of 175 µm. Mass spectra were acquired in positive mode in the range of m/z

133–2000. The spatial resolution was kept at ~200 μm . Data-dependent MS/MS experiments of molecules extracted from the tissue sections were performed using a mass resolution ($m/\Delta m$) of 60,000 at m/z 200, mass isolation window of 0.5 m/z , and HCD energy of 25 arbitrary units specific to the instrument.

2.2.4 Data processing

Each line scan was collected as an individual file (reduced profile, .RAW file format). Data processing was performed using Peak-by-Peak software (Spectroswiss, Lausanne, Switzerland). Ion images were generated using parallel (multi-core) calculations. First, peaks were extracted from mass spectra using a three-point quadratic interpolation to determine the apex of the peak. Second, peak abundances in each pixel of the image were normalized to the total ion current (TIC = sum of intensities): $Int_{\text{norm}} = (Int_i / \sum Int_i) * 100\%$. We note that normalization to the abundance of a specified m/z in the spectrum also is enabled by the software. Finally, ion images were constructed by plotting normalized abundances of targeted m/z features in each mass spectrum (pixel) within the mass tolerance window of ± 10 ppm as a function of location on the tissue sample. Initial lipid identification was performed using LIPID MAPS (www.lipidmaps.org) and metabolite identification was performed using METLIN database (<https://metlin.scripps.edu>). Final assignments were performed based on the MS/MS analysis.

Region of interest (ROI) analyses were performed on the regions where TGs were abundant in the tissue. Averaged mass spectra were obtained by spectral averaging over the ROIs and normalized to the TIC obtained over the ROI. The effect of the solvent composition was assessed by comparing the average intensities of TGs normalized to the TIC.

2.3 Results and discussions

In this study, we examined the effect of the solvent composition on the extraction and ionization of TGs in nano-DESI experiments. First, the molecular coverage of the commonly used nano-DESI solvent, MeOH:H₂O 9:1 (v/v), was compared against two alternative solvents MeOH:AcN:tol 5:3.5:1.5 (v/v/v) and MeOH:DCM 6:4 (v/v). Second, adduct formation and chemical derivatization with Girard T approaches were explored for improving the ionization of

TGs. Finally, nano-DESI imaging experiments were performed using MeOH:H₂O and MeOH:AcN:tol to test the imaging capabilities of these solvents.

2.3.1 Effect of solvent composition on the extraction of TGs

Two alternative solvents were examined for the analysis of TGs using nano-DESI MSI: MeOH:DCM 4:6 (v/v) and MeOH:AcN:tol 5:3.5:1.5 (v/v/v). The first solvent has been previously used in lipidomics analysis of plant and animal tissue samples and provided good coverage of both polar and nonpolar lipids including TGs.⁷⁴ The second solvent has been used for the detection of hydrophobic compounds in biological samples.^{24,75} However, no systematic study has been reported on the solvent optimization for tissue imaging experiments. Figure 2.1 a-c shows average mass spectra obtained for each solvent by acquiring line scans over the central region of the gastrocnemius muscle tissue as illustrated in Figure 2.1a. The results indicate that regardless of the solvent composition, PC species detected in muscle tissue in the mass range of m/z 740-860 as $[M+H]^+$, $[M+Na]^+$ and $[M+K]^+$ adducts are the dominant peaks in positive mode nano-DESI. This observation may be attributed to the polarity of PC species, which facilitates their detection in a mass spectrometer as compared to TGs that are neutral molecules. Moreover, PCs are mainly membrane lipids and therefore are present in high abundance in tissue samples making them relatively easy to detect.

Although the overall appearance of mass spectra obtained using three different solvents is similar, we observed interesting differences at $m/z > 840$ (Figure 2.1c). Specifically, the signals of TGs observed using MeOH:DCM and MeOH:AcN:tol showed an increase in abundance by at least an order of magnitude in comparison with the signals obtained using MeOH:H₂O. In the spectra, TGs were mainly detected as $[M+K]^+$ ions while the corresponding $[M+Na]^+$ adducts were much less abundant. This result reflects the important role that the solvent composition plays in ambient ionization techniques based on liquid extraction, in which the solubility of the analyte in the extraction solvent determines how effectively it is partitioned into the solvent. We have previously demonstrated that a 70:30 mixture of acetonitrile and toluene facilitates the extraction and ionization of nonpolar analytes from crude oil samples in nano-DESI experiments³⁷. It is reasonable to assume that the nonpolar components such as toluene and DCM improve the extraction efficiency of nonpolar molecules such TGs of interest to this study. Meanwhile, the presence of polar solvents such as MeOH and AcN promotes the extraction of polar lipids and

provides a stable electrospray signal.⁷⁶ In summary, we observed a comparable performance of the toluene and DCM mixtures in the analysis of muscle tissue sections. In contrast, analysis of mouse liver tissue sections indicated clear differences between these two solvent mixtures.

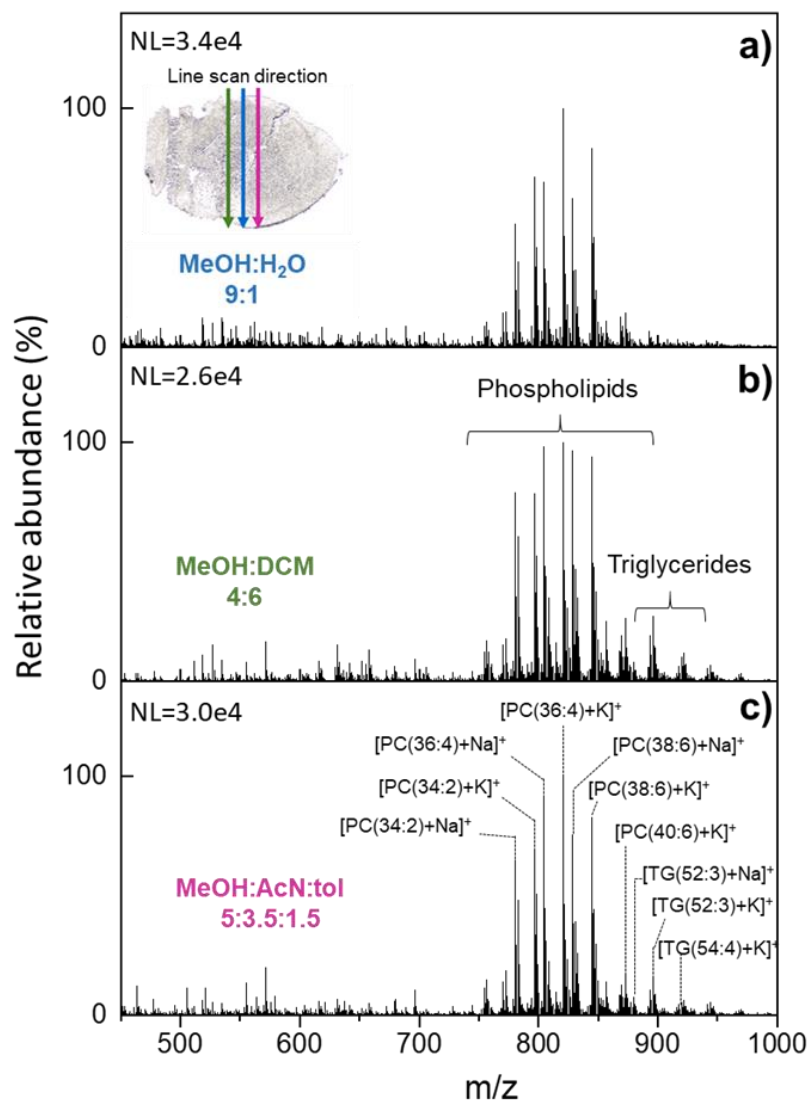


Figure 2.1. Lipid profiles obtained from a region of the line scan where TGs are abundant using a) MeOH:H₂O (9:1), b) MeOH:DCM (4:6), and c) MeOH:AcN:tol (5:3.5:1.5) under the same experimental conditions. An optical image showing the region where the line scans were acquired on the tissue is displayed on the left side of panel a). Normalization factors (NL) are displayed in each panel.

Figure 2.2a shows regions of the tissue that were sampled using different solvent mixtures by acquiring one line scan for each solvent in each region; Figure 2.2b shows representative average mass spectra obtained in the adjacent line scans. The MeOH:AcN:tol clearly outperformed MeOH:DCM in all the acquired line scans. Based on these results and safety concerns associated with DCM due to its carcinogenic properties, we chose MeOH:AcN:tol as the working solvent for the following experiments.

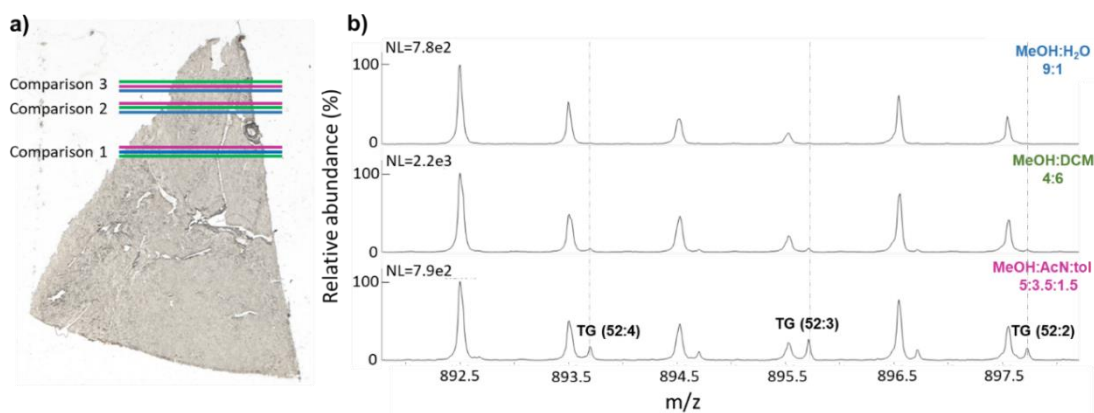


Figure 2.2. a) Optical image of a liver tissue showing regions where different line scans were collected. b) Representative mass spectra obtained for line scans acquired using MeOH:H₂O, MeOH:DCM and MeOH:AcN:tol solvent mixtures.

2.3.2 Effect of ionization on the detection of TGs

In addition to improving the extraction efficiency of TGs in nano-DESI experiments by optimizing the solvent composition, we explored the effect of different dopants in the solvent on the ionization efficiency of these lipids. Cationization of TG species with ammonium acetate (AAc) is a common strategy used in many lipidomics studies to enhance the ionization efficiency of neutral lipids.^{77,78} In this study, nano-DESI spectra were acquired using MeOH:AcN:tol solvent containing ammonium formate (AF) at different concentrations in a range of 0.1-10 mM. Representative mass spectra obtained using 0, 0.1 and 2 mM concentration of AF are shown in Figure 2.3. We observe that the signals corresponding to $[M+Na]^+$ and $[M+K]^+$ adducts of PC species are largely unaffected by the presence of AF in the solvent. The abundance of protonated PC species increases in the presence of AF (Figure 2.3b). This is the only substantial difference between mass spectra obtained at 0 and 0.1 mM AF concentrations (Figures 2.3a-b). Ammonium adducts of TGs appear as low-abundance species at low AF concentration (Figure 2.3b) and

increase in abundance at higher AF concentration (Figure 2.3c). However, the abundance of $[M+NH_4]^+$ ions of TGs at 2 mM AF concentration is still lower than the abundance of the corresponding $[M+K]^+$ species. Interestingly, the abundance of $[M+K]^+$ adducts of TGs increases with an increase in AF concentration. The relatively inefficient ionization of TGs as $[M+NH_4]^+$ ions observed in this study may be attributed to the high concentration of potassium ions in the tissue that leads to the preferred formation of $[M+K]^+$ adducts. Compared with LC-MS analysis where high concentrations of AAc are commonly used for lipid profiling, we found that at high concentrations of AF (~10 mM) all the signals were substantially suppressed. Similarly, we did not observe any measurable improvement in the signal of TGs by adding either $LiNO_3$ or KNO_3 to the solvent. Collectively, these results indicate that the addition of salts to the nano-DESI solvent does not improve the ionization of TGs extracted from muscle tissues.

We also examined whether reactive nano-DESI could be used for the analysis of TGs. On-line chemical derivatization is one of the common strategies used to improve the ionization of neutral molecules.⁷⁹ For example, reactive DESI employing betaine aldehyde (BA) as a reagent has been successfully used to improve the detection of cholesterol in brain.⁷⁹ This method exploited the reaction between the alcohol group of cholesterol with BA to produce a positively charged hemiacetal. Meanwhile, Girard T (GT) reagent has been used for reactive DESI analysis of ketosteroids⁸⁰ and nano-DESI analysis of aldehydes and ketones in organic aerosols³⁵. Unlike cholesterol, TGs do not have any functional groups specific to their structure that can be targeted by reactive analysis. However, like phospholipids, the carbonyl group of the glycerol backbone can serve as a possible target. Herein, we used GT dissolved in the MeOH:AcN:tol mixture to explore whether reactive nano-DESI analysis will enhance the detection efficiency of TGs in complex mixtures. GT converts aldehydes and ketones into hydrazines by reacting with carbonyl groups.⁸⁰ In our experiments, we varied the concentration of GT in the solvent and examined the distribution of m/z features observed in nano-DESI spectra of tissue samples. Although we did not observe any products of reaction between GT and TGs, formation of GT adducts of PC species with ~10% reaction efficiency was observed at GT concentrations above 100 μM . As shown in Figure 2.4, at this concentration the ion at m/z 132.11 corresponding to the unreacted GT dominates the spectrum obscuring the detection of lower abundance species.

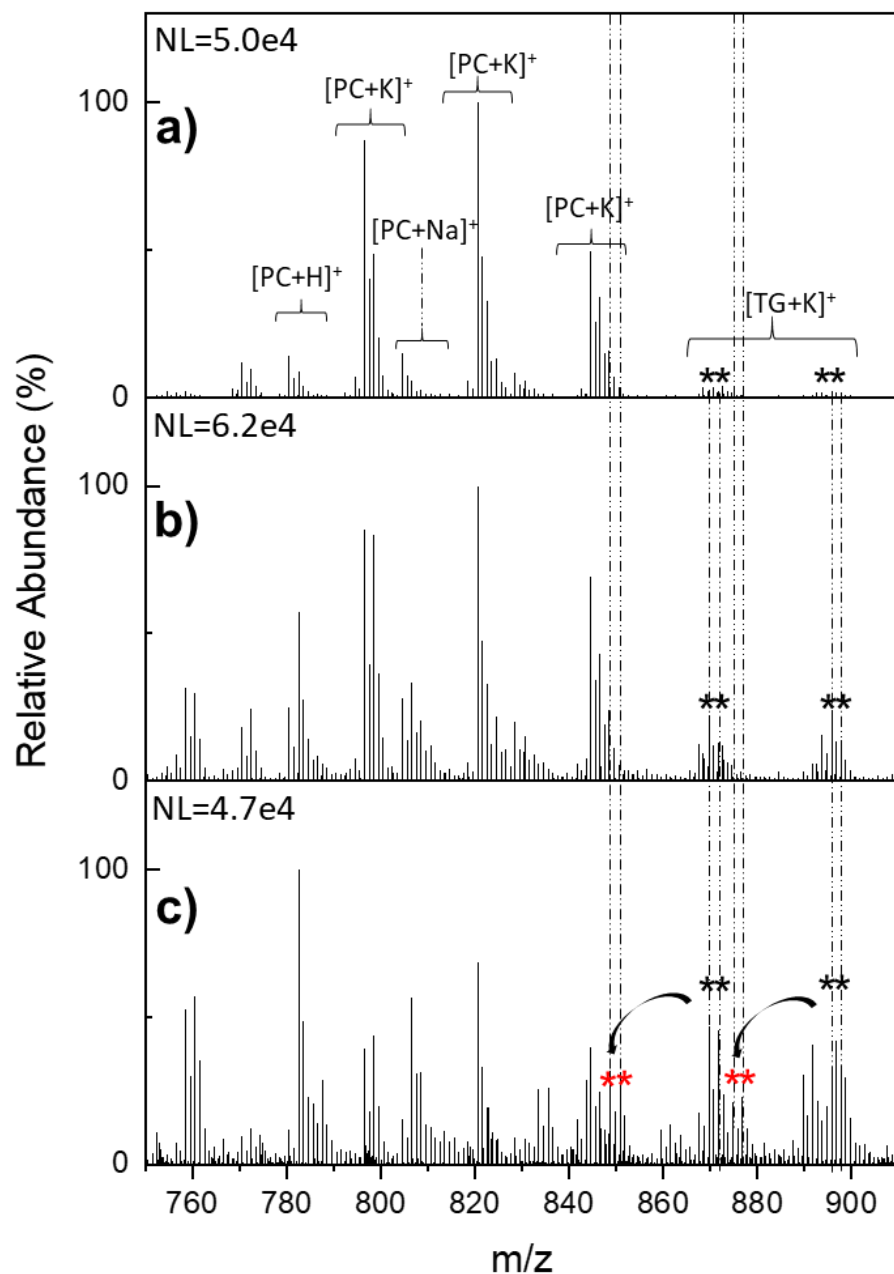


Figure 2.3. Average mass spectra of the TG-rich region displaying lipid signals obtained a) using MeOH:AcN:tol (5:3.5:1.5) and by doping MeOH:AcN:tol (5:3.5:1.5) with b) 0.1 mM and c) 2 mM of ammonium formate. Black and red asterisks highlight the same TG species detected as $[M+K]^+$ and $[M+NH_4]^+$ adducts, respectively. NL values are displayed in each panel.

Furthermore, the incomplete conversion of PCs into their corresponding hydrazine products generates a more complicated spectrum, which is not desirable for imaging experiments. In conclusion, neither cationization nor on-line chemical derivatization improved the sensitivity of TG detection in nano-DESI analysis of tissue sections. We conclude that high affinity of TGs

towards K^+ ions present in the tissue promotes their ionization and detection in nano-DESI MSI experiments. As a result, no ionization enhancers were used in the imaging experiments described in the next section.

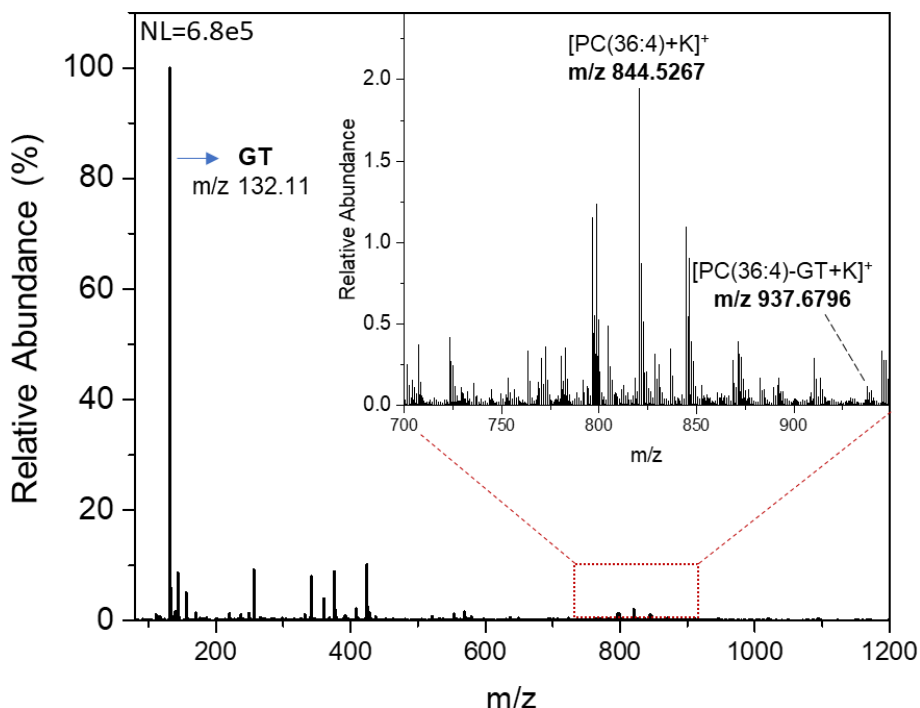


Figure 2.4. Reactive nano-DESI mass spectrum obtained using MeOH:AcN:tol doped with 100 μ M of GT. GT in the solvent produces a strong peak at m/z 132.11 that dominates the spectrum. A closer look into the phospholipids region shows the presence of GT adducts with PC species extracted from the tissue.

2.3.3 Nano-DESI MSI of gastrocnemius tissues

Two solvents, MeOH:H₂O and MeOH:AcN:tol, were used to image two adjacent gastrocnemius tissue sections to compare TG detection in nano-DESI MSI experiments. Figure 2.5a shows optical images of the sections along with ion images of $[M+K]^+$ ions of endogenous phospholipids including LPC(16:0), PC(36:1) and PC(40:6). Ion images corresponding to small metabolites including carnosine and miristoylcarnitine, CAR(14:0), are displayed as $[M+K]^+$ and $[M+H]^+$ ions respectively. All ion images are normalized to the total ion current (TIC). In both solvents, the distribution of a majority of phospholipids and metabolites detected in nano-DESI MSI experiments exhibit the same localization and similar abundance. Signaling molecules including LPC(16:0) are evenly distributed across the tissue whereas CAR(14:0), PC(36:1) and

PC(40:6) are observed in higher abundance in the deep region of gastrocnemius muscle tissue. Although correlating the localization of these molecules to different types of fibers is out of the scope of this work, it can be suggested that this region is enhanced in oxidative fibers (type I and IIa) based on similar results reported in previous studies using MALDI imaging.^{81,82} In contrast, the ion image corresponding to carnosine displayed higher abundance in regions where CAR(14:0), PC(36:1) and PC(40:6) are depleted, suggesting that carnosine may be used as a molecular marker of a different fiber type.

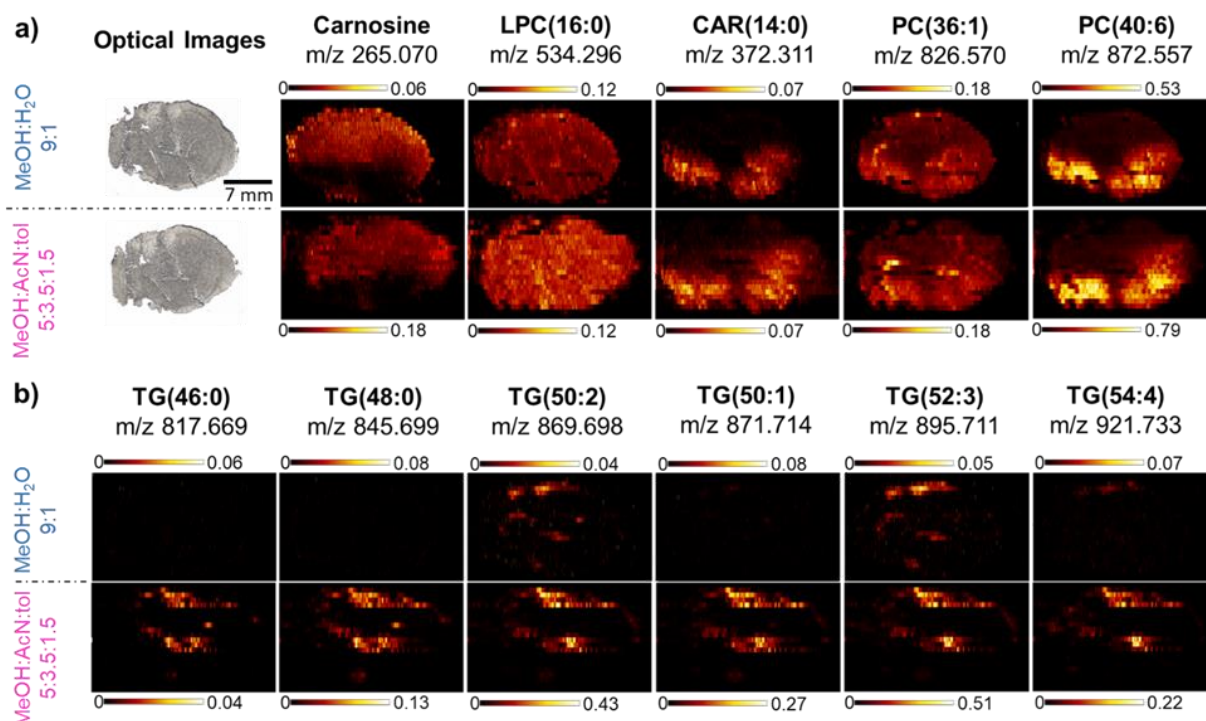


Figure 2.5. Nano-DESI images acquired using MeOH:H₂O (9:1) and MeOH:AcN:tol (5:3.5:1.5) solvents in positive mode. a) Optical images of gastrocnemius tissue sections and ion images of [M+H]⁺ ion of CAR(14:0) and carnosine, LPC (16:0), PC (36:1) and PC(40:6) detected as [M+K]⁺ adducts. b) Ion images of TG(46:0), TG(48:0), TG(50:2), TG(50:1), TG(52:3) and TG(54:4) detected as [M+K]⁺ adducts. Scale bar is 7 mm. All ion images are normalized to the TIC and the corresponding normalized ion abundance scales are shown in the color bars located next to each ion image.

Figure 2.5b shows ion images of representative [M+K]⁺ ions of TG species normalized to the TIC. Ion images of other TGs identified in this experiment are shown in Figure 2.6. We note that MS/MS spectra of the [M+K]⁺ adducts of TGs did not provide any structural information most likely because of the loss of K⁺ ion, which cannot be detected in these experiments. Acyl chain

information could only be obtained from the corresponding $[M+Na]^+$ adducts. Fragmentation of $[M+Na]^+$ ions suggested the presence of multiple isomers. For example, the MS/MS spectrum of TG(52:4) at m/z 877.725 contained fragment ions corresponding to the loss of the fatty acyl chains FA(18:1), FA(18:2), FA(18:3) and FA(16:0), indicating that the ion image of TG(52:4) is a combination of TG(18:2/18:2/16:0), TG(18:2/18:1/16:1), and TG(18:3/18:1/16:0) isomers. Since the signals of the $[M+Na]^+$ adducts were not as abundant as the $[M+K]^+$ adducts, we could not obtain MS/MS of the less abundant TG(46:0), TG(46:1) and TG(48:0) species. Overall, we estimate that we were able to detect 22 different TG species (including possible isomers) using MeOH:AcN:tol. In the future, we will use MS/MS imaging to examine the spatial localization of isomeric TG species.⁸³

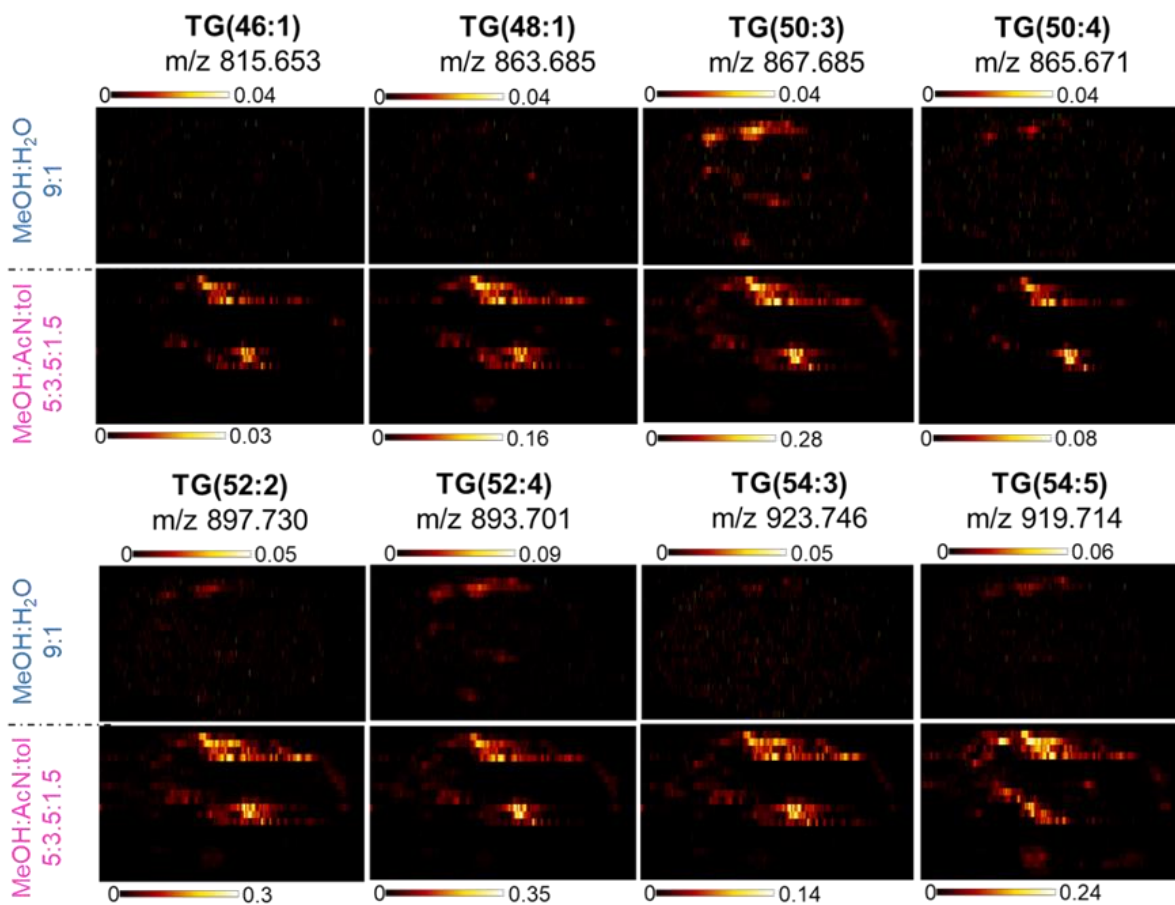


Figure 2.6. Positive mode ion images of other TGs detected as $[M+K]^+$ adducts in gastrocnemius tissue using MeOH:H₂O (9:1) and MeOH:AcN:tol (5:3.5:1.5) solvents. Scale bars are 7 mm. All ion images are normalized to the TIC and the corresponding normalized ion abundance scales are shown in the color bars located next to each ion image

It can be observed in Figure 2.5b that ion signals of all the TGs are notably higher when MeOH:AcN:tol is used as a working solvent. Polyunsaturated species such as TG(50:2) and TG(52:3) are detected using both solvents. In contrast, the detection of monounsaturated and saturated species such as TG(46:0), TG(48:0) and TG(50:1) and species with longer acyl chains such as TG(54:4) is substantially improved using MeOH:AcN:tol. These results demonstrate better performance of MeOH:AcN:tol solvent for imaging of hydrophobic molecules in tissues.

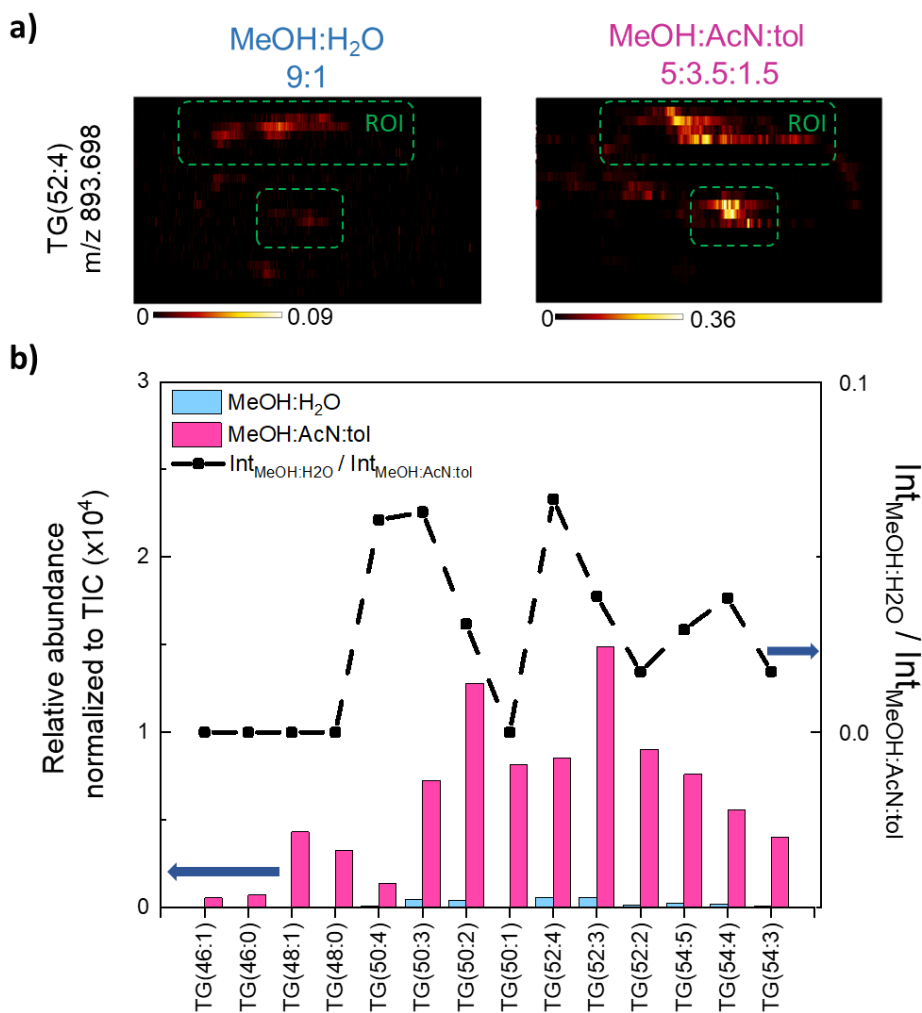


Figure 2.7. a) Ion images of TG(52:4) obtained using MeOH:H₂O (9:1) and MeOH:ACN:tol (5:3.5:1.5) solvents illustrating the region of interest (ROI) analysis. Dashed green lines outline the ROI selected in each image. Color bars show the normalized ion abundance scale for each ion image. b) Bar graphs show normalized ion abundances of TGs detected as [M+K]⁺ adducts (left axis) calculated from the average ROI spectra obtained for both images. A scatter plot shows the ratio of the abundances (right axis), $\text{Int}_{\text{MeOH:H}_2\text{O}} / \text{Int}_{\text{MeOH:AcN:tol}}$, observed for different TG species.

Region of interest (ROI) analysis was carried out to assess the extraction efficiency of TGs from tissue samples using MeOH:AcN:tol and MeOH:H₂O. Figure 2.7a displays ion images of TG(52:4) obtained using both solvents showing the regions selected for the ROI analysis. The relative abundance of all TG species obtained from the average spectra of the ROI is reported for both solvents in Figure 2.7b (left axis) along with the ratio of signal intensities, $\text{Int}_{\text{MeOH:H}_2\text{O}}/\text{Int}_{\text{MeOH:AcN:tol}}$, which is plotted against the right axis. We observed higher signals of the more polar unsaturated species in comparison to less polar saturated species. Moreover, higher signals were generally observed for unsaturated TG species with 50 and 52 carbons than for unsaturated TG with 54 carbons (Figure 2.7b). This observation is consistent with a previous study that discussed the effect of the polarity of acylglycerols on the signals of TGs electrosprayed using nonpolar solvents.⁸⁴ Specifically, that study reported higher MS signals of the more polar acylglycerols. Interestingly, less polar TGs are more strongly suppressed in the polar MeOH:H₂O solvent. For example, we observed similar abundances for TG(50:1) and TG(52:4) in MeOH:AcN:tol. However, TG(50:1) completely disappears when MeOH:H₂O is used as a working solvent. The intensity ratio, $\text{Int}_{\text{MeOH:H}_2\text{O}}/\text{Int}_{\text{MeOH:AcN:tol}}$, shown in Figure 2.7b indicates that this trend is consistent across all the TG species observed in this study. This result demonstrates the strong influence of the number of double bonds on the extraction efficiency of TG species from tissues in nano-DESI MSI experiments. In particular, the more polar compounds such as TG(52:3) can be extracted using both solvents and more hydrophobic compounds such as TG(46:1) are better extracted using the more hydrophobic solvent. In summary, we obtained good-quality images for 14 distinct m/z of TG species corresponding to at least 22 unique TGs using MeOH:AcN:tol solvent as compared to only four TG images obtained using MeOH:H₂O. Moreover, the signal intensity of all the TGs was enhanced by at least a factor of 16 in MeOH:AcN:tol.

2.4 Conclusions

In this study, we examined the effect of extraction and ionization on the detection of TGs in tissue imaging experiments using nano-DESI. We conclude that the detection of TGs in these experiments is mainly determined by the extraction efficiency from the sample. Subsequent ionization of TG species is promoted by alkali metal cations that are abundant in biological tissues. The presence of a small fraction of a nonpolar solvent in the solvent mixture has no measurable effect on the signal stability and total ion signal. However, an improved lipid coverage is observed

using solvents containing non-polar components, which enable the simultaneous detection of polar and nonpolar lipids in the same experiment. We note that the addition of salts or the GT reagent does not improve the detection of TG species. Imaging experiments confirm that the 5:3.5:1.5 MeOH:AcN:tol mixture provides a substantially better coverage of TGs in muscle tissue samples in comparison with the more polar 9:1 MeOH:H₂O mixture. Ion signals of TGs are improved by at least a factor of 16 allowing imaging of 14 TG species using this solvent in comparison with only four TG species imaged generated using MeOH:H₂O. Meanwhile, similar spatial distributions of metabolites including acylcarnitines, carnosine and PC species were observed using MeOH:H₂O and MeOH:AcN:tol. Collectively, these results indicate the superior performance of MeOH:AcN:tol in nano-DESI MSI experiments.

CHAPTER 3. IMAGING AND ANALYSIS OF ISOMERIC UNSATURATED LIPIDS THROUGH ONLINE PHOTOCHEMICAL DERIVATIZATION OF C=C BONDS

3.1 Introduction

Lipids are essential biomolecules acting as structural components of membranes, energy reservoirs, or signaling molecules in biological systems.⁸⁵ Multiple biochemical transformations that lipids undergo during their biosynthesis generate diverse lipid structures, which complicates their structural characterization.⁸⁶ Mass spectrometry (MS) has been extensively used to identify lipid classes, acyl chain composition, and degree of unsaturation.⁸⁷ However, the differentiation of isomers that vary only by the position of C=C double bonds critical to understanding their role in key metabolic processes remains challenging.

Isomer-resolved mass spectrometry imaging (iMSI) is an emerging technique that enables spatial-resolved analysis of molecules across samples with isomeric resolution.^{88–90} The development of novel mass spectrometry (MS) approaches with high structural specificity capabilities has led to the rapid growth of iMSI placing it as a potential analytical tool for diagnostic pathology. As a result, a direct link between lipid isomeric composition and disease progression has been suggested in several pathologies including diverse types of cancer,^{91–93} obesity,^{94,95} diabetes⁹⁶ and Alzheimer disease.⁹⁷

The most successful MS-based strategies for identifying C=C bond positions can be grouped into condense-phase and gas-phase approaches. Condense-phase approaches like Paternò-Büchi,⁹⁸ ozonolysis,⁹⁹ epoxidation¹⁰⁰ and thiol-ene¹⁰¹ reactions selectively derivatize C=C bonds before lipids are sent the mass spectrometer, where they undergo fragmentation to reveal the C=C location. Successful implementation of these methods for iMSI has only been possible through on-tissue deposition of the derivatizing agents because of the relative long reaction times which are in the order of minutes.^{102–104} Gas-phase approaches like ultraviolet photodissociation (UVPD),¹⁰⁵ ozone induced dissociation (OzID)¹⁰⁶ and ion-ion reactions¹⁰⁷ modify or dissociate the lipid structure to provide informative fragments of the C=C location within a mass spectrometer previously modified to perform the desired reaction. In the context of iMSI, these methods have successfully uncovered the distribution of a great variety of lipid C=C isomers.^{91,108–110} In these experiments,

each specie is isolated to undergo the reaction of interest thereby enabling the imaging of a small number of molecules per experiment.

Despite the significant progress in this field, spatially-resolved isomer-selected lipidomics experiments are still challenging. Herein, we introduce an online derivatization approach, that 1) enables fast photooxidation and profiling of C=C locations in lipids, 2) uses an inexpensive visible light source which can be easily focused, 3) does not require any instrument modification, and 4) is compatible with both the electrospray ionization (ESI)-based shotgun lipidomics workflow for the analysis of lipid extracts and mass spectrometry imaging (MSI) of biological samples using nanospray desorption electrospray ionization (nano-DESI).

3.2 Materials and methods

3.2.1 Nomenclature

Lipid nomenclature is as follows: LPE 17:1(10 Δ) denotes a 17-carbon fatty acid with one degree of unsaturation. The position of the C=C bond is indicated by 10 Δ , where the carbon atom is counted from the carboxylic end. For lipid standards with known geometry, Δ is replaced with either Z (cis) or E (trans).

3.2.2 Chemicals and Solutions

Rose bengal (RB, C₂₀H₂Cl₄I₄Na₂O₅), chloroform (CHCl₃), methanol (MeOH) and omnisolv LC-MS grade water were purchased from Millipore Sigma (Burlington, MA). LPE 17:1(10Z), PC 18:1(9Z)_{18:1(9Z)}, PC 18:1(6Z)_{18:1(6Z)}, PC 17:0_{22:4-d5}, PC 17:0_{20:3-d5}, PI 17:0_{14:1(9Z)}, PS 17:0_{14:1(9Z)} and PG 17:0_{14:1(9Z)} were purchased from Avanti Polar Lipid (Alabaster, AL). TG 16:1(9Z)_{16:1(9Z)}_{16:1(9Z)} was purchased from Larodan (Monroe, MI).

An RB stock solution was always freshly prepared using MeOH and was kept away from light. RB was added from a stock solution to the solvent or any analyzed solution right before each experiment. In all the experiments, the syringe containing the solution was covered with aluminum foil to avoid decomposition of the photosensitizer. 1 μ M solutions of the following standards were prepared in MeOH:H₂O (9:1)(v/v) containing 50 μ M RB: LPE 17:1(10Z), PC 17:0_{22:4-d5}, PC 17:0_{20:3-d5}, PC 18:1(9Z)_{18:1(9Z)}, PC 18:1(6Z)_{18:1(6Z)}, PI 17:0_{14:1(9Z)}, PS17:0_{14:1(9Z)} and PG 17:0_{14:1(9Z)} AL). TG 16:1(9Z)_{16:1(9Z)}_{16:1(9Z)}.

Lipid extract of gastrocnemius muscle tissue was prepared using a modified Bligh and Dyer method. First, ~50 mg of tissue was homogenized with 300 μ L of pure water and 200 μ L of tissue homogenate was transferred into a clean microcentrifuge tube. Next, 250 μ L of CHCl_3 and 450 μ L of MeOH were added to obtain a monophasic mixture. Subsequently, 250 μ L of CHCl_3 and 250 μ L of pure H_2O were added to induce phase separation into an organic and aqueous phase. Finally, the organic phase (lipid phase) was split into two tubes containing 150 μ L of the extract each and the solvent was evaporated using a speed vac chamber. The concentrated lipid extracts were stored at -80°C until ready to use.

A stock solution was prepared from concentrated lipid extracts which was resuspended in 200 μ L solution containing 175 μ L MeOH: H_2O (9:1) (v/v) and 25 μ L of CHCl_3 . The stock solution was immediately transferred to a glass vial. A 40-fold dilution was prepared using 10 μ L of stock solution and 390 μ L of MeOH: H_2O (9:1) (v/v). This extract was freshly prepared and stored at -20°C prior to analysis. For the $^1\text{O}_2$ reaction, 10 μ L of the 40-fold diluted lipid extract was added to MeOH: H_2O (9:1)(v/v) to produce 400 μ L of a solution containing 5 μM , 50 μM , 100 μM , or 200 μM RB.

For nano-DESI experiments, a solution containing 200 nM LPE 17:1 and 50 μM RB in MeOH: H_2O (9:1)(v/v) was used as the extraction solvent.

3.2.3 Tissue collection and handling

Gastrocnemius muscles were collected from adult (3-month old) C57BL/6 mice that were maintained in the animal facility with free access to standard rodent chow and water. All the procedures involving mice were approved by the Purdue University Animal Care and Use Committee (Protocol# 1112000440). Uterine tissues on day 4 of pregnancy were collected from the C57/BL6 mixed background mice using procedures described in our previous studies.³⁴ The mice were housed in the Cincinnati Children's Hospital Medical Center Animal Care Facility according to National Institutes of Health and institutional guidelines for the use of laboratory animals and animal handling protocols of the approved by Cincinnati Children's Hospital Research Foundation Institutional Animal Care and Use Committee. Both types of tissues were snap-frozen and sectioned using a cryostat. Sections of 12 μm thickness were mounted onto glass slides and stored in a -80°C freezer prior to analysis.

Wistar han rat was sacrificed after 30 minutes by CO₂ asphyxiation. These experiments were performed according to the institutional guidelines of Merck & Co. Brain was snap frozen in hexane/dry ice bath and stored in a -80 °C freezer. Tissues were sectioned (thickness = 12 μm) using a Leica CM3050 S cryostat (Leica Biosystems, Buffalo Grove, IL). Sections were thaw-mounted onto glass slides for the imaging experiments, shipped on dry ice, and stored in a -80 °C freezer until the analysis.

3.2.4 Optics

A battery-operated TS-002 1000 mW 532 nm green laser pointer pen (Lasepointerpro.com, North Brunswick, NJ) was modified to be operated in a continuous mode using a DC power supply. Warning: the laser pointer is a class 4 laser and should be operated using appropriate laser safety protocols. A reflective ND filter ND505A (Thorlabs, NJ) was placed in front of the laser to allow 32% of the light to be transmitted. A plano-convex lens Ø1" N-BK7 (Thorlabs, NJ) with a focal distance of 15 cm was used to focus the beam to a ~1 mm diameter. A beam block (400 - 700 nm, 10 W Max Avg) (Thorlabs, NJ) was placed on the opposite side of the laser to absorb the transmitted light.

3.2.5 ESI platform

ESI experiments were performed using a fused-silica capillary (100 μm ID, 375 μm OD) pulled to ~25 μm OD, which was positioned in front of the MS inlet using a micropositioner. Preparation of the capillary is detailed in our previous publication.³⁴ The laser assembly described earlier was mounted as shown in Figure 3.1a. In the ESI setup, a solvent containing RB and the lipids is continuously infused using a syringe pump at a flow rate of 0.5 μL/min. The syringe needle is connected either to the high voltage cable (LTQ and Orbitrap) or ground potential (QTOF). A 10-MΩ resistor is integrated into the high-voltage cable to avoid potential electric shock induced by the high voltage. Although RB is deposited onto the surfaces of the inlet, no contamination peaks were observed after spraying RB solutions for an extended period of time.

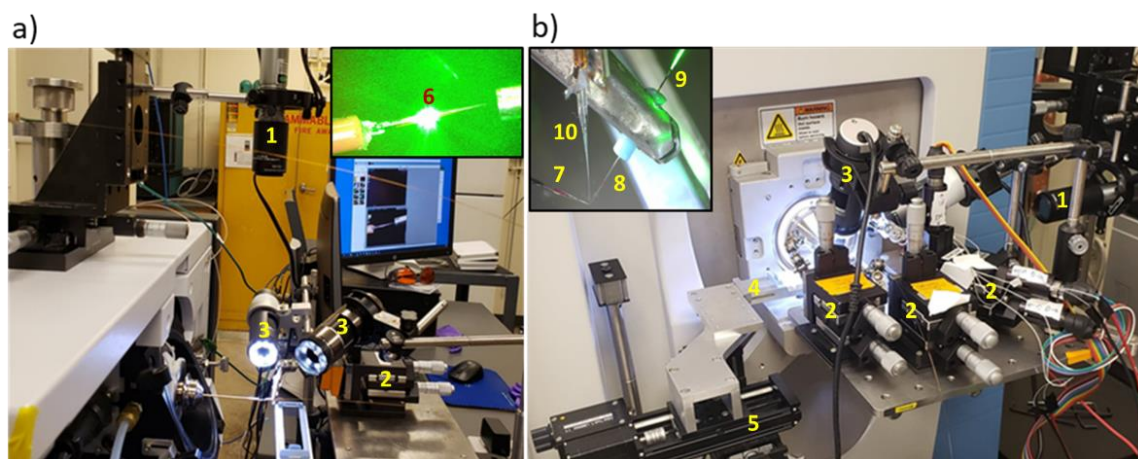


Figure 3.1. Experimental setup for the online singlet oxygen reaction with lipids coupled to a) ESI on a QTOF MS and b) nano-DESI on a QE-Orbitrap. 1 – laser pointer with an ND filter and lens attached; 2 – micropositioners; 3 – Dino-lite cameras; 4 – sample holder; 5 – Zaber ZYX stage. Inserts show a photograph of the irradiated ESI tip positioned at a mass spectrometer inlet (panel a, 6) and nano-DESI probe (panel b). The photograph shows the tip of the primary capillary (7) interfaces with the sampling side of the nanospray capillary (8) irradiated by the laser at another end (9). The shear force probe (10) controls the distance between the sample and the nano-DESI probe.

3.2.6 Nano-DESI platform

The nano-DESI platform was comprised of two micropositioners (Quarter Ressearch, XYZ 500 MIM) used for mounting the nano-DESI probe and placed it in front of the MS inlet. The sample was placed on a custom-made sample holder mounted onto a Zaber XYZ stage, which is controlled by a custom Labview program. A third micropositioner was used to hold the shear-force probe positioned next to the nano-DESI probe. Preparation of the primary capillary, spray capillary and shear force probes can be found in our previous work.³⁴ Two Dino-Lite digital microscopes were used to aid in the alignment of the two capillaries. One of the microscopes was placed above the capillaries and the other was placed laterally. In nano-DESI experiments, the extraction solvent containing 50 μM RB and 200 nM of standard LPE 17:1 is continuously infused through the primary capillary using a syringe pump at a flow rate of 0.5 $\mu\text{L}/\text{min}$. The liquid bridge formed between the primary and spray capillaries is used to extract endogenous species directly from a tissue section; the solvent and extracted analytes are transported via the spray capillary to the MS inlet. The capillary coating of the spray capillary was removed for performing online singlet oxygen reaction. The same laser setup described earlier for the ESI experiments is used in nano-DESI experiments (Figure 3.1b). The green laser is placed 15 cm away from the nano-DESI probe and focused onto the side of the spray capillary closest to the MS inlet. Because ESI and

nano-DESI experiments are performed using a very similar approach, in which the capillary is irradiated close to the ESI tip, we expect comparable reaction times and yields in these experiments. Before the nano-DESI probe is landed on the tissue, the standard is used to optimize the position and focusing of the laser by examining the yield of the hydroperoxide product, LPE 17:1(LOOH). For the 50 μm ID capillary, 1 mm spot size, and 0.5 $\mu\text{L}/\text{min}$ flow rate, the time to clear the irradiated volume is $(\pi \cdot (0.025 \text{ mm})^2 \cdot 1 \text{ mm}) / 0.5 \text{ } \mu\text{L}/\text{min} = 250 \text{ ms}$. Because the lifetime of singlet oxygen is in microseconds, it is unlikely that the reaction continues after the analyte leaves the irradiated volume. As a result, the upper limit estimate of the reaction time is 250 ms.

3.2.7 Profiling and nano-DESI MSI experiments

Experiments using gastrocnemius muscle tissue lipid extract were carried out using an Agilent 6560 IM-QTOF MS (Agilent Technologies, Santa Clara). Typical source parameters are as follows: ESI voltage of +4.5 kV, capillary temperature of 300 $^{\circ}\text{C}$. Mass spectra were acquired in the range of m/z 133–1000 operated in the 2GHz mode. MS/MS conditions are as follows: isolation window of 2 Da, acquisition rate of 1 Hz, nominal collision energy (NCE) of 30 units. An LTQ XL (Thermo Fisher Scientific GmbH, Bremen, Germany) ion trap mass spectrometer was used to perform low-energy ion-trap CID experiments of lipid standards under the following conditions: electrospray voltage of 3 kV, capillary temperature of 200 $^{\circ}\text{C}$, isolation window of 2 Da, automated gain control (AGC) on, maximum injection time (IT) of 250 ms, 1 microscans, and NCE of 25 units.

Profiling experiments with mouse uterine tissue were performed on a Q-Exactive HF-X Orbitrap mass spectrometer. A voltage of +3.0 kV and an RF Funnel voltage of +100 V were used in these experiments. Mass spectra were acquired in the range of m/z 133–2000 with a mass resolution ($m/\Delta m$) of 60,000 at m/z 200; the AGC target was set at 1×10^6 and the maximum IT was 200 ms; the heated capillary was held at 250 $^{\circ}\text{C}$. The sample was moved under the nano-DESI probe at a scan rate of 20 $\mu\text{m}/\text{s}$ and either MS or MS² spectra were acquired during the scan. MS² spectra were acquired using higher-energy collision-induced dissociation (HCD) using the isolation window of 2 Da, mass resolution of 45 000, AGC target of 2×10^5 , maximum IT of 80 ms, 1 microscan, and NCE of 22 and 30 for glycerophospholipids and glycerolipids, respectively. HCD experiments using lipid standards were carried out under the same conditions.

Imaging experiments of tissue sections were performed in both the MS¹ (MS¹I) and MS² (MS²I) modes using the following conditions. For imaging of a mouse uterine tissue, 46 lines were acquired over an area of 2.20 mm × 1.63 mm with an acquisition time of 4.56 min/line and total analysis time of ~3.5 h. Images were acquired in lines by a continuous motion of the stage in the x-direction at 8 µm/s and with spacing between the individual lines of 36 µm in the y-direction. In this experiment, a full MS and MS² of two m/z isolation windows centered at 814.53 and 411.27 were collected in a sequence in which the full MS alternated between each targeted ion. The full MS was collected with a mass resolution of 120,000 ($m/\Delta m$ at m/z 200) with one microscan. The AGC target was set to 1×10^6 , and maximum IT was 200 ms. HCD spectra were acquired with a mass isolation window of 2 Da, mass resolution of 15,000 ($m/\Delta m$ at m/z 200), and a 10 microscans. The AGC target was set to 2×10^4 ions and maximum IT was 200 ms. Each MS² spectrum was acquired with an NCE of 20 V.

For mouse brain tissue, 42 lines were acquired over an area of 4.05 mm × 1.80 mm with a scan rate of 15 µm/s, acquisition time of 4.5 min/line, and a total analysis time of ~3.2 h. The spacing between the individual lines was 43 µm. In this experiment, a full MS and MS² of three m/z isolation windows centered at 814.53, 840.57, and 842.56 were collected in a sequence in which the full MS alternated in between each targeted ion. The full MS was collected with a mass resolution of 60 000 ($m/\Delta m$ at m/z 200) and one microscan. The AGC target was set to 1×10^6 ions, and maximum IT was 200 ms. HCD spectra were acquired with a mass isolation window of 2 Da, mass resolution of 30,000 ($m/\Delta m$ at m/z 200), and 5 microscans. The AGC target was set to 2×10^4 ions and maximum IT was 200 ms. Each MS² spectrum was acquired with an NCE of 20V.

3.2.8 Data processing

Image generation was performed using a custom Python script, which uses pymzmlreader package to convert .RAW data files into a readable format. Since a constant AGC target was used in both MS and MS² experiments the number of spectra varied from line to line. To align the spatial positions of MS and MS² spectra, we used the acquisition time of each spectrum to perform a linear interpolation of line scan data. A mass window of 20 ppm was used to extract intensity values for selected m/z , which were used to generate ion images.

3.3 Results and discussions

In this work, we introduce an online strategy for iMSI using nanospray desorption electrospray ionization (nano-DESI) and online reaction of singlet oxygen ($^1\text{O}_2$) with C=C bonds in lipids. $^1\text{O}_2$ is the excited state of molecular oxygen containing one empty orbital, which reacts with electron-rich double bonds to produce hydroperoxides (Figure 3.2).^{111,112} Photochemical generation of $^1\text{O}_2$ is achieved using a photosensitizer, which is excited to a triplet state upon exposure to light and subsequently transfers its excitation energy to molecular oxygen present in solution. $^1\text{O}_2$ reacts with lipids to form lipid hydroperoxides (LOOHs).^{113–115} When subjected to collision-induced dissociation (CID), LOOHs undergo a bond cleavage at the location of the hydroperoxide group (Figure 3.2a) thereby revealing the double bond position. Herein, we use the online reaction of unsaturated lipids with $^1\text{O}_2$ followed by CID of the resulting LOOH to obtain diagnostic peaks that provide insights into the C=C bond location.

In ESI experiments (Figure 3.2b), a mixture of MeOH:H₂O (9/1, v/v) containing rose bengal (RB) as a photosensitizer and lipids is propelled through a fused silica capillary at 0.5 $\mu\text{L}/\text{min}$, ionized by ESI, and analyzed using MS. For the online derivatization, the capillary tip pulled to $\sim 25\ \mu\text{m}$ OD is illuminated with a green laser pointer (532 nm) positioned 15 cm away from the tip and focused using a convex lens. This configuration, which can be readily adapted to lipidomics experiments was used to test the feasibility of the online derivatization of C=C bonds in fatty acyl chains using the $^1\text{O}_2$ reaction. In another experiment (Figure 3.2c), the $^1\text{O}_2$ reaction is coupled to a high-resolution nano-DESI probe to perform an online derivatization and C=C profiling of analytes in complex lipid mixtures extracted from tissue sections. Here, the solvent containing RB is propelled through the nano-DESI probe, which extracts analytes from a specific location on the sample into a dynamic liquid bridge shown in the inset. The spray capillary transfers the extracted lipids and metabolites to a mass spectrometer inlet. The laser light is focused onto the tip of the spray capillary. A shear force probe is placed next to the nano-DESI probe to maintain a constant distance to the sample.^{31,32,34}

The reaction between $^1\text{O}_2$ and unsaturated lipids generates an allylic hydroperoxide at either end of the double bond accompanied by a shift in the double bond position to the adjacent carbon.^{114,115} The reaction results in a mass shift of 32 Da corresponding to the net addition of O_2 . Lipid nomenclature is as follows: LPE 17:1(10 Δ) denotes a 17-carbon fatty acid with one degree of unsaturation and the C=C bond on the 10th carbon atom from the carboxylic end (10 Δ). For

lipid standards with known geometry, Δ is replaced with either Z (cis) or E (trans). We selected RB as a photosensitizer due to its high quantum yield.¹¹⁶

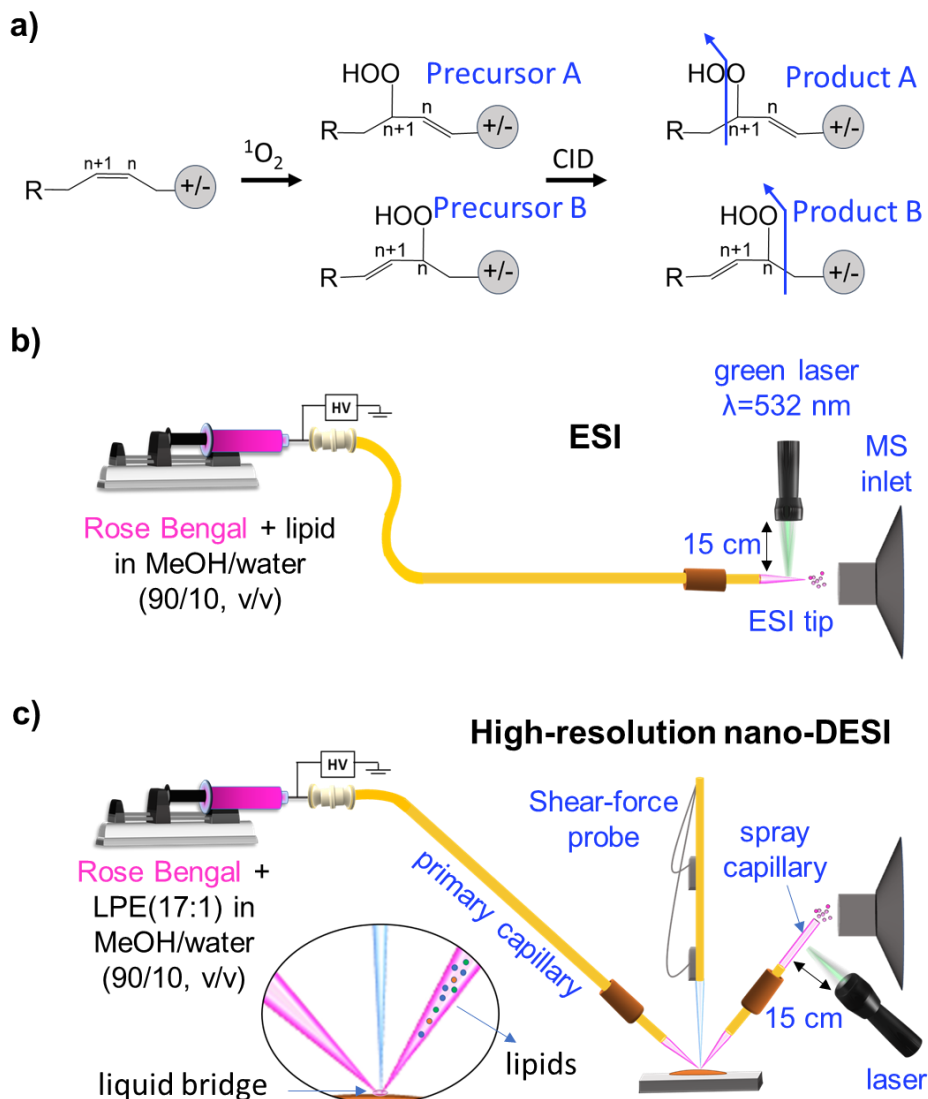


Figure 3.2. a) Schematic representation of the oxidation of the C=C bonds in lipids by singlet oxygen and fragmentation via CID that yields unique neutral losses. Experimental setup for the online singlet oxygen reaction with lipids coupled to b) ESI and c) nano-DESI.

Figure 3.3 shows ESI-MS of a standard mixture containing LPE 17:1, PC 36:2, and TG 48:3 obtained upon irradiation. Although the dominant product corresponds to the addition of one O_2 , other LOOH products observed in the spectrum confirm that the reaction occurs at each double bond. No other side products such as aldehydes, alcohols or ketones were observed in these experiments (Figure 3.4). The absence of side products commonly observed in the bulk

experiments may be attributed to the lack of direct interaction between RB and lipids in the relatively dilute solutions analyzed in this study.

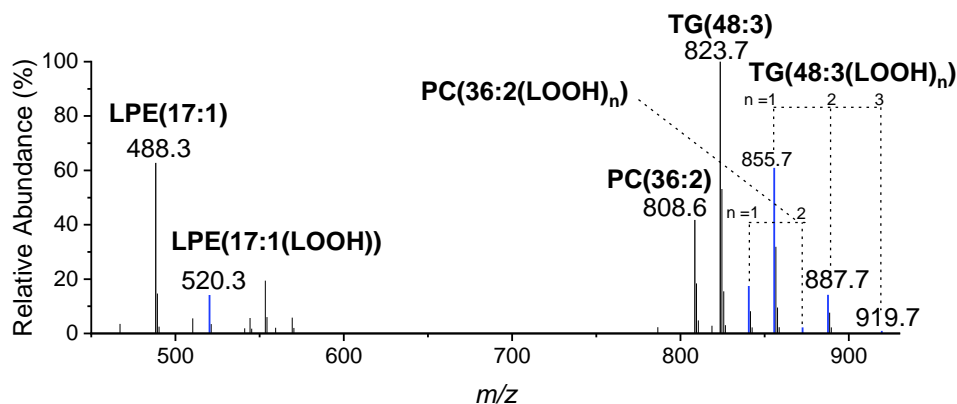


Figure 3.3. Positive mode ESI-MS of LPE 17:1, PC 36:2 and TG 48:3 and their (LOOH)_n products generated by the reaction with ¹O₂. The [M+Na]⁺ ions of (LOOH)_n where **n** indicates the number of O₂ additions are highlighted in blue.

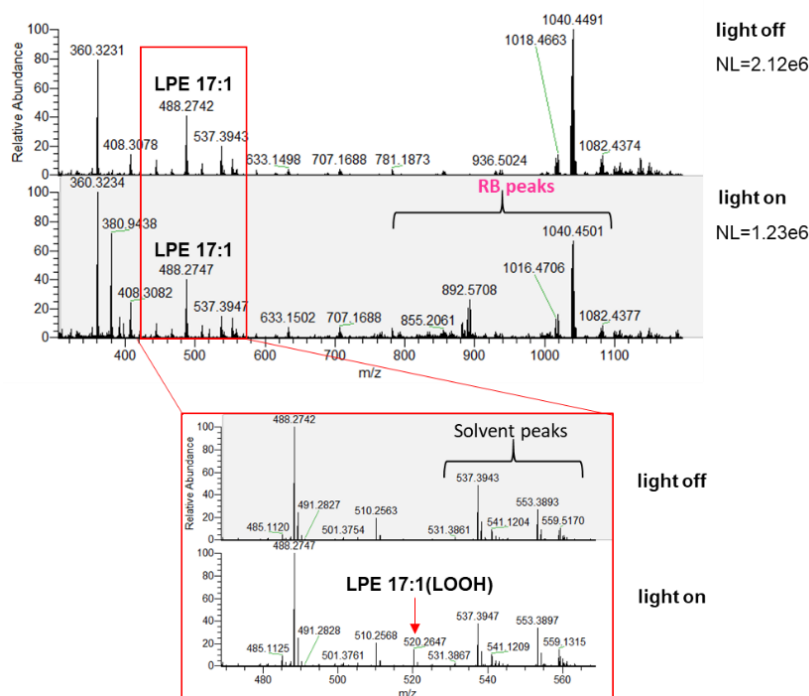


Figure 3.4. Light on and light off positive mode ESI mass spectra of the LPE 17:1 standard at m/z 488.27. Several features near m/z 550 correspond to solvent peaks that are unaffected by laser irradiation. The RB-related peaks are observed at $m/z > 850$. An expanded view of the m/z 460-560 region is shown in the red box where the arrow indicates the hydroperoxide product. Only one product of the photochemical derivatization of LPE 17:1 is observed in the spectrum.

CID of LOOHs generates unique neutral losses (NL) directly from the precursor ion, which reveal the position of the hydroperoxide group and hence C=C bond in the unreacted lipid. This is illustrated using two isomeric LOOH species generated from two positional isomers: PC 18:1(9Z)/18:1(9Z) and PC 18:1(6Z)/18:1(6Z) (Figure 3.5a). In this experiment, 1 μ M solutions of each standard containing 50 μ M RB were analyzed individually using ESI coupled with laser excitation. For both isomers, CID spectra (Figures 3.5b-c) contain fragments at m/z 781.4 and 657.5 corresponding to head group losses from m/z 840.5. Meanwhile, fragmentation at the hydroperoxide generates different fragments for the two isomers. For the 9Z isomer, a primary fragment ion corresponding to the loss of $C_8H_{18}O$ due to the cleavage at C10 of precursor A (Figure 3.5b) is observed at m/z 710.4. This fragment undergoes subsequent NL of 59 and 183 generating peaks at m/z 651.3 and 527.3, respectively confirming that LOOH is a PC species. The corresponding loss of $C_{11}H_{24}O$ due to cleavage at C7 is observed for the 6Z isomer generating a fragment at m/z 668.4 along with the head group losses at m/z 609.3 and 485.3. Fragment ions corresponding to precursor B (Figure 3.5c) are not observed in the higher energy collision-induced dissociation (HCD) spectra but are observed as minor peaks in the LTQ-CID spectrum (Figure 3.5b). This effect is more pronounced for polyunsaturated LOOHs (Figures 3.6-3.7), for which the diagnostic fragments of product B are observed in LTQ-CID but not in HCD spectra. We propose that differences in the energetics and kinetics of fragmentation of the two LOOH products affect their branching ratio on different MS timescales and levels of internal excitation. Importantly, a fragment corresponding to product A is observed on all the instruments and can be used to identify the C=C location of multiple lipid classes as shown in Figures 3.8-3.10.

Figure 3.11 shows mass spectra obtained for a mouse gastrocnemius muscle tissue extract containing different concentrations of RB (5, 50, 100, and 200 μ M). The 50 μ M RB solution provided good yields of LOOH products without producing dominant RB-related peaks that suppress the ionization of lipids at higher RB concentrations. Figure 3.12a shows part of a mass spectrum obtained under the optimized conditions, in which the LOOH products exhibit a 32 Da mass shift from their precursor lipids. Ion chromatograms of the endogenous PC 38:6 at m/z 828.6 and PC 36:4 at m/z 804.6 and the corresponding LOOH products are depicted in Figure 3.11b. The signals of PC 38:6(LOOH) at m/z 860.5 and PC 36:4(LOOH) at m/z 836.5 appear once the light is turned on showing a 30-40% LOOH yield relative to the unreacted lipid. LOOH signals remain stable over time demonstrating the feasibility of this approach for the online chemical

derivatization of C=C bonds. As described in the SI, we estimate that the reaction time is shorter than 250 ms.

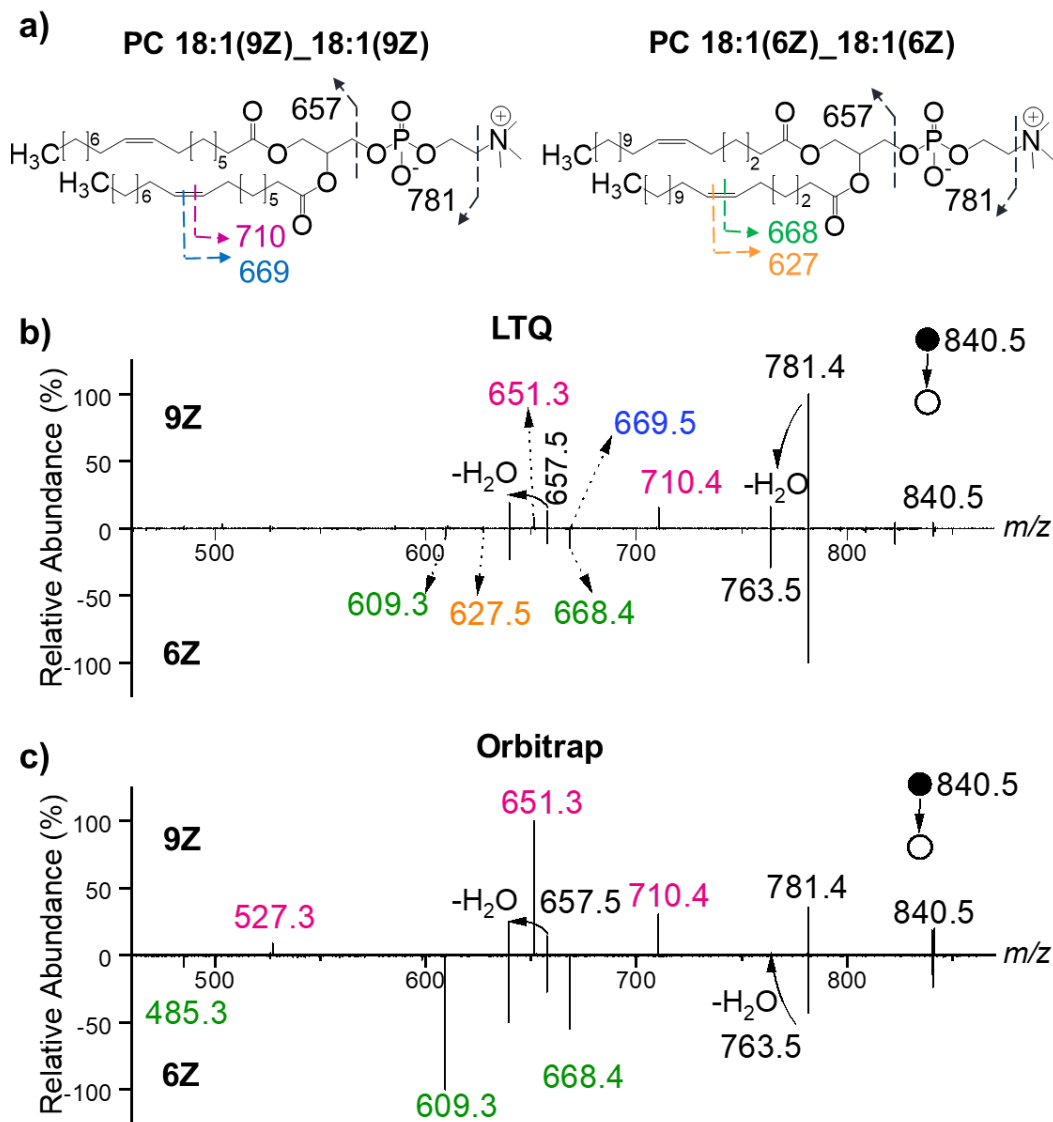


Figure 3.5. b) Structures of PC 18:1(9Z)/18:1(9Z) (left) and PC 18:1(6Z)/18:1(6Z) (right) showing the cleavage sites. c) LTQ-CID and d) HCD spectra of the isomeric LOOH products at m/z 840.5.

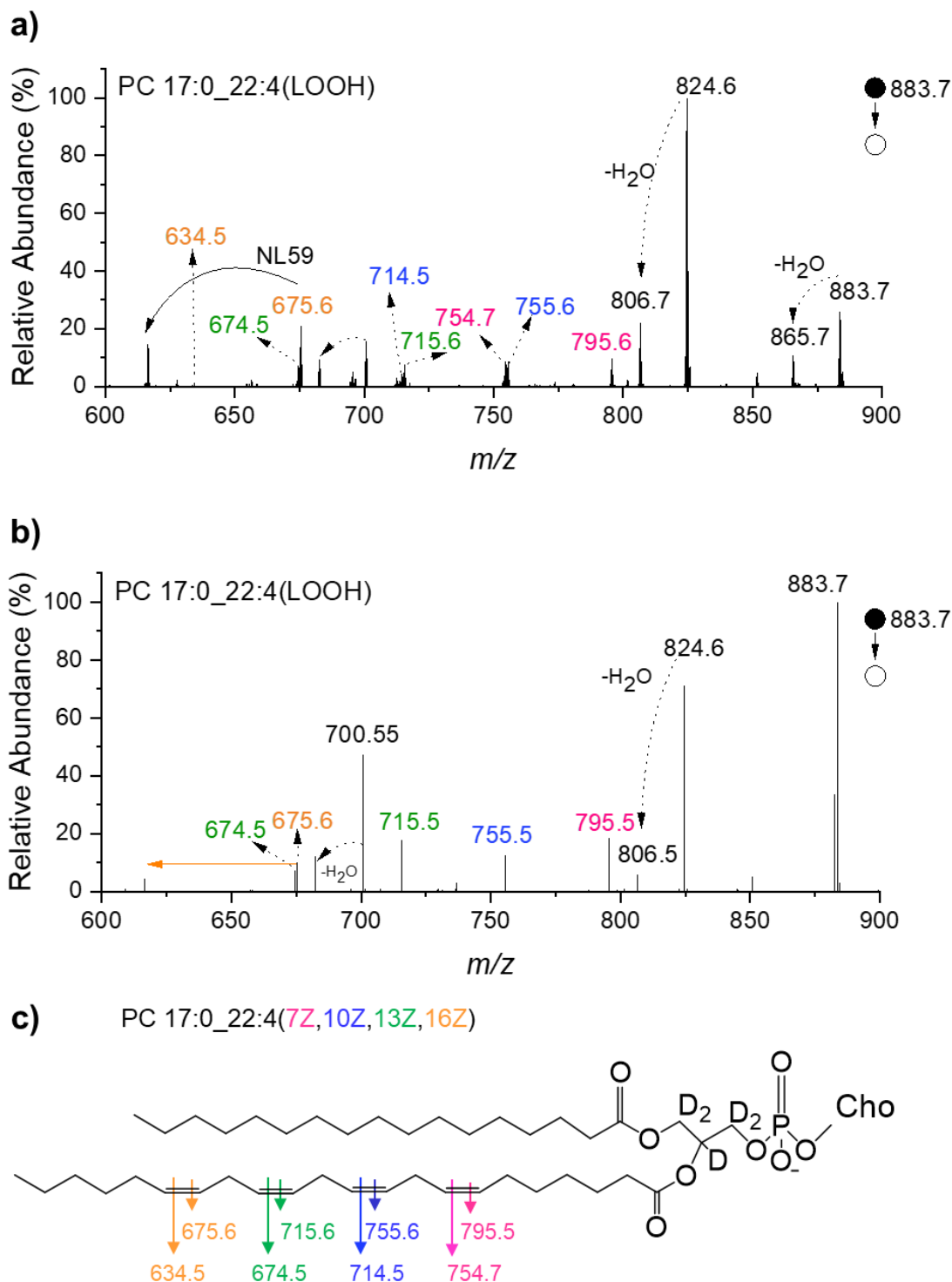


Figure 3.6. MS² spectra of the hydroperoxide product of PC-d5 17:0_22:4 (7Z, 10Z, 13Z, 16Z) obtained using an a) LTQ and b) Orbitrap. Chemical structure of PC-d5 17:0_22:4 showing the cleavage sites. The diagnostic peaks corresponding to the position of the double bond at C7, C10, C13 and C16 are highlighted in pink, blue, green and orange, respectively. The shorter arrow corresponds to product A and the longer arrow corresponds to product B.

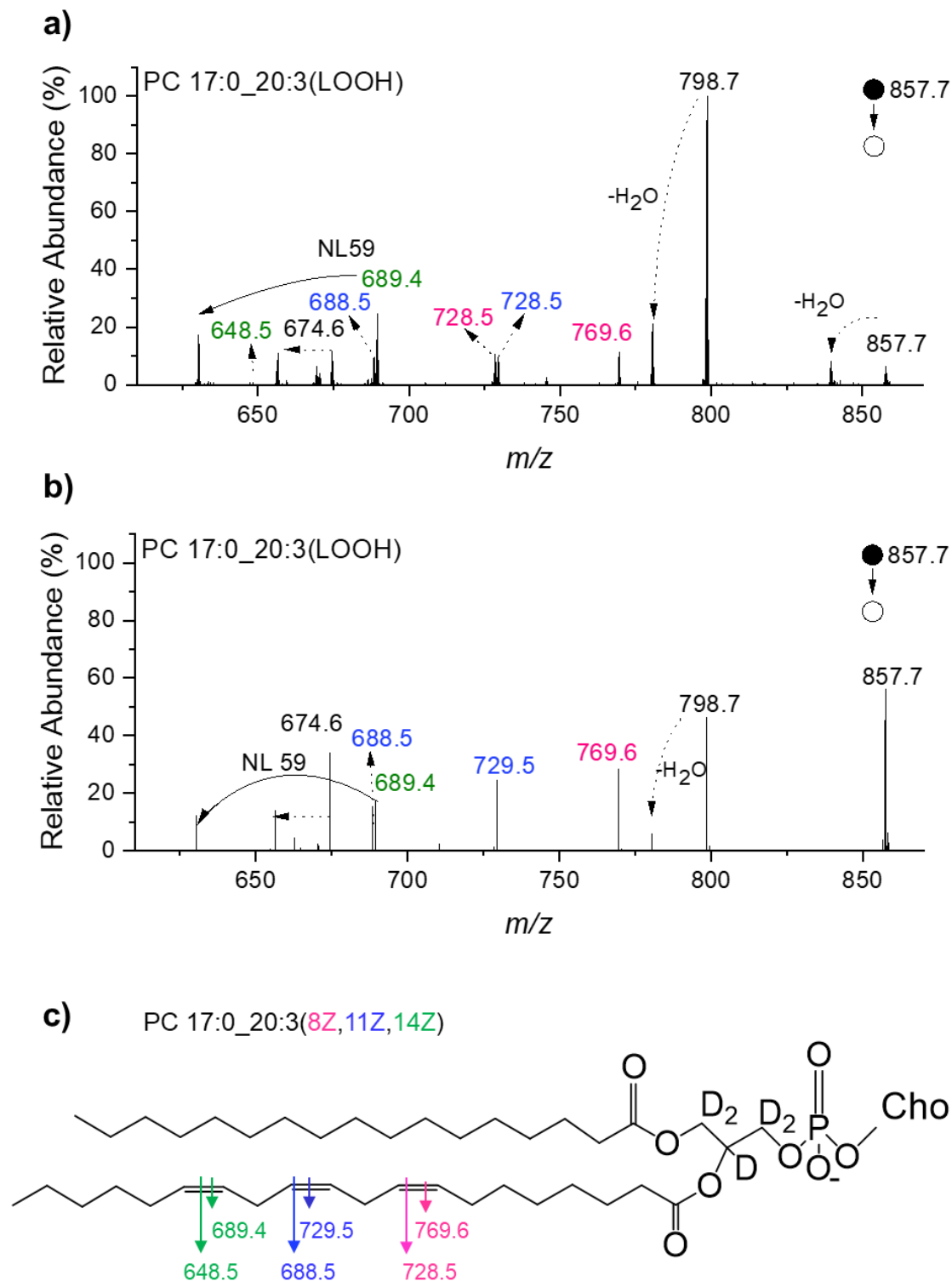


Figure 3.7. MS² spectra of the hydroperoxide product of PC-d5 17:0_20:3 (8Z, 11Z, 14Z) obtained using a) LTQ and b) Orbitrap. Chemical structure of PC-d5 17:0_20:3 showing the cleavage sites. The diagnostic peaks corresponding to the position of the double bond at C8, C11, C14 are highlighted in pink, blue, and green, respectively. The shorter arrow corresponds to product A and the longer arrow corresponds to product B.

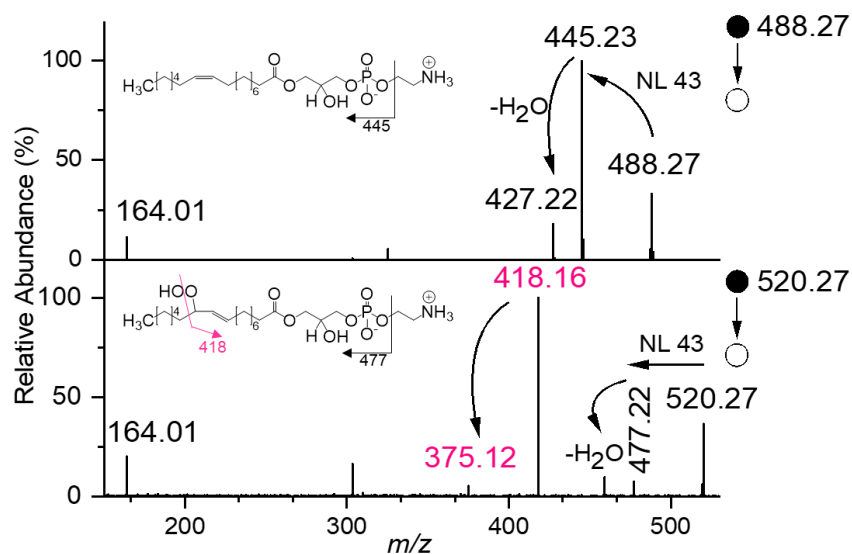


Figure 3.8. HCD spectra of unreacted LPE 17:1 (top panel) and LPE 17:1(LOOH) (bottom panel). Chemical structures of both molecules showing the cleavage sites are shown in the insets. The diagnostic peaks are highlighted in pink.

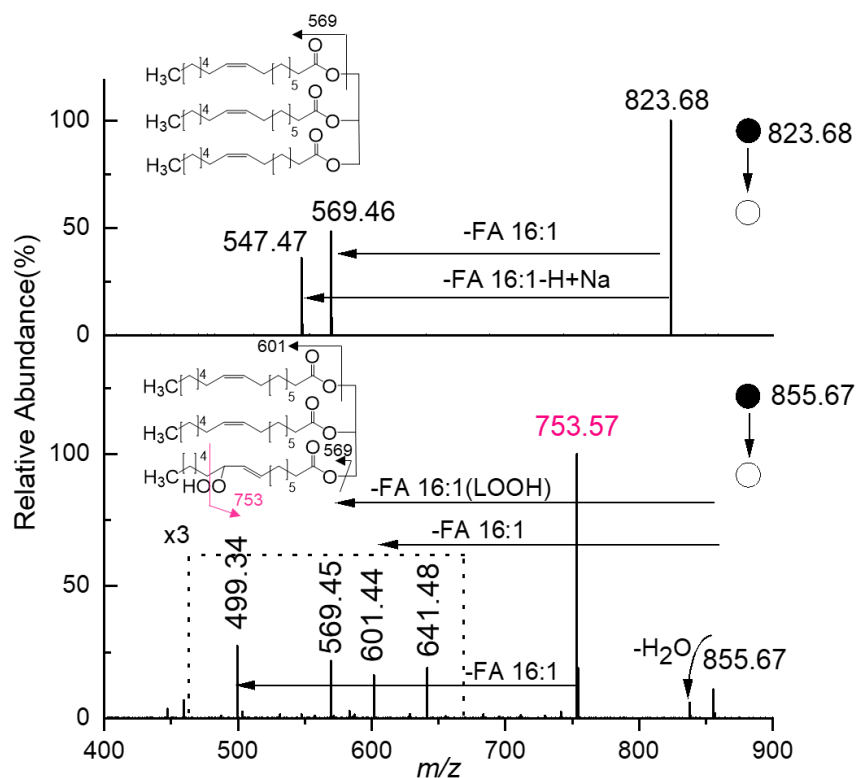


Figure 3.9. HCD spectra of unreacted TG 48:3 (top panel) and TG 48:3(LOOH) (bottom panel). Chemical structures of both molecules showing the cleavage sites are illustrated in the insets. The diagnostic peaks are highlighted in pink.

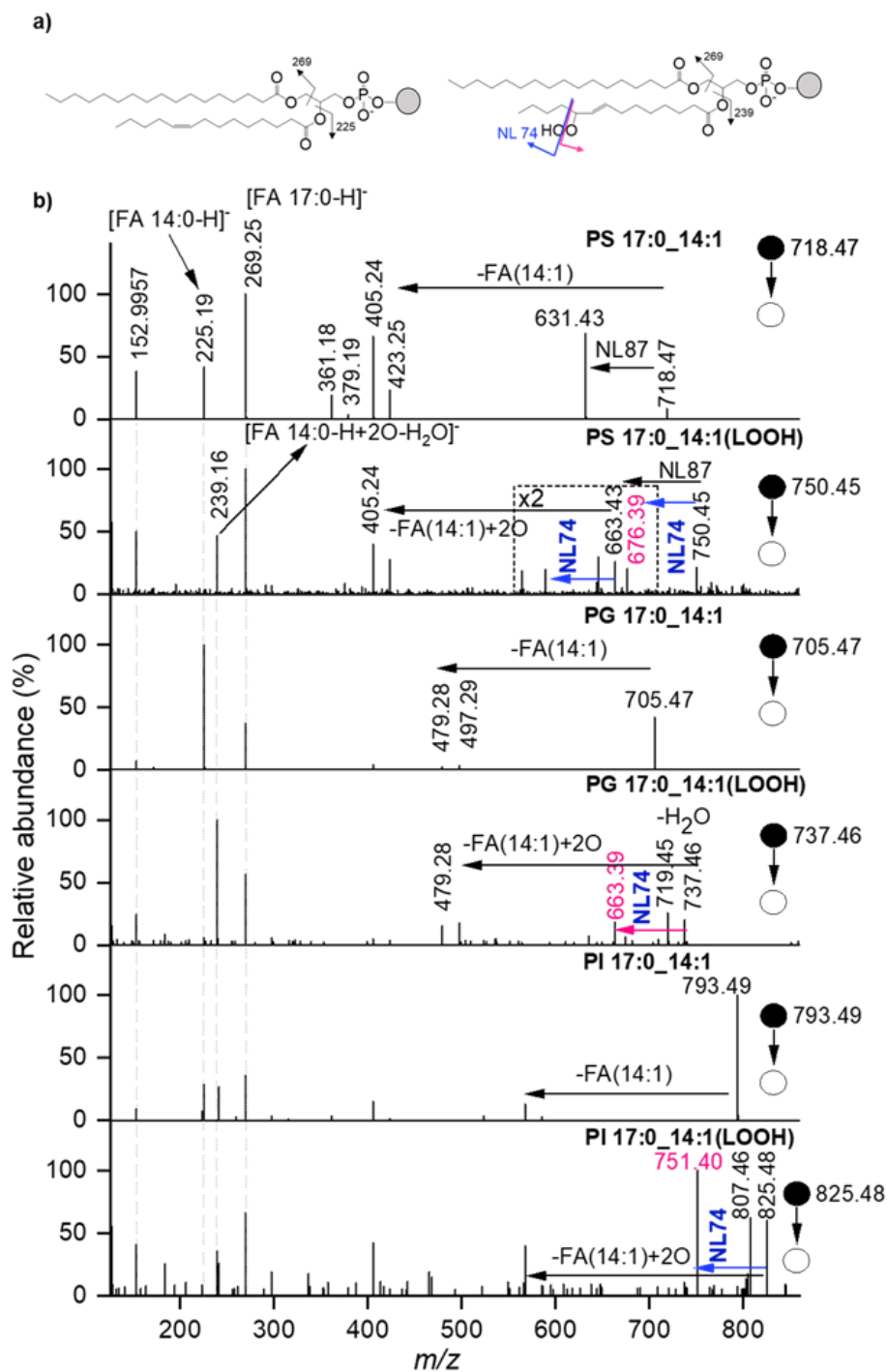


Figure 3.10. Fragmentation of lipid species ionized in negative mode. a) Chemical structure of a phospholipid containing FA 14:1 and FA 17:0. The structure along with the cleavage sites are shown for the unreacted lipids (left side) and LOOH (right side). b) HCD spectra of PS 31:1, PG 31:1 and PI 31:1 along with MS/MS of their corresponding hydroperoxide. The diagnostic peaks are highlighted in pink. We note that negative mode experiments suffer from ion suppression due to abundant RB-related peaks observed near the lipid region. In negative mode, we estimated the yield of the LOOHs products to be around 5% with respect to the unreacted lipid. Other photosensitizers may be used to improve the reaction yield and sensitivity in negative mode.

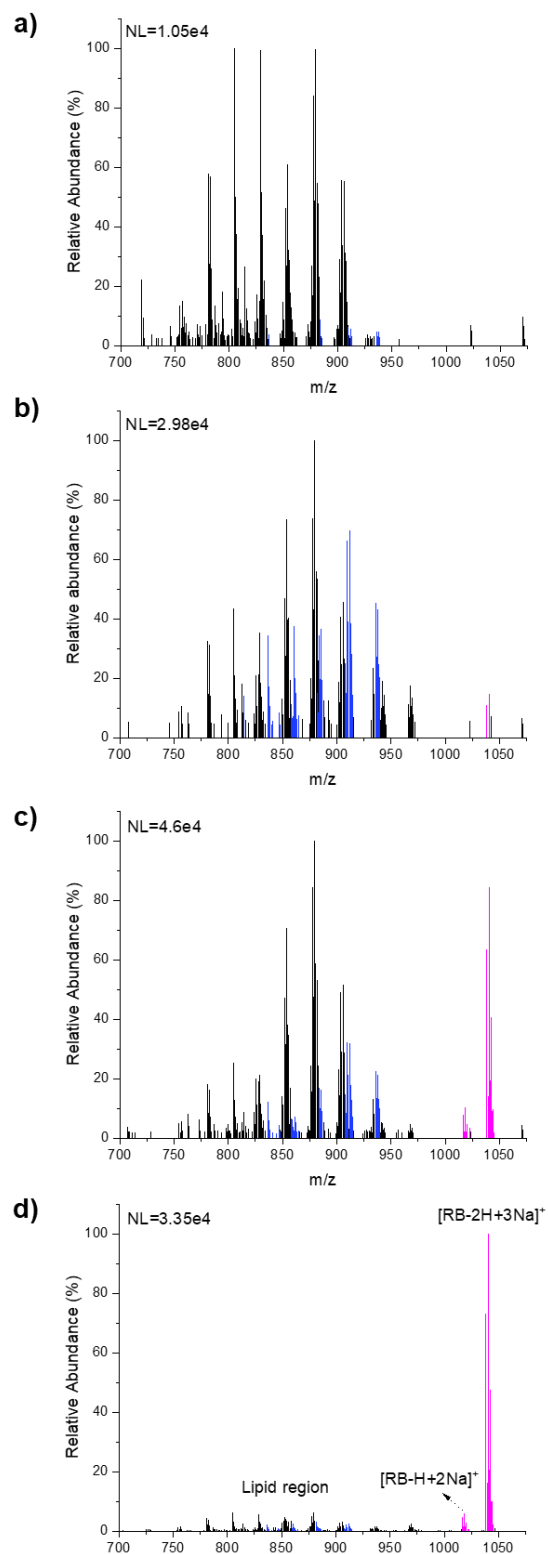


Figure 3.11. Positive mode ESI-MS spectra of the mouse gastrocnemius muscle tissue extract obtained using the $^1\text{O}_2$ reaction in a solution containing RB at a) 5 μM b) 50 μM c) 100 μM and d) 500 μM concentrations. The reaction products are highlighted in blue and RB peaks are highlighted in pink.

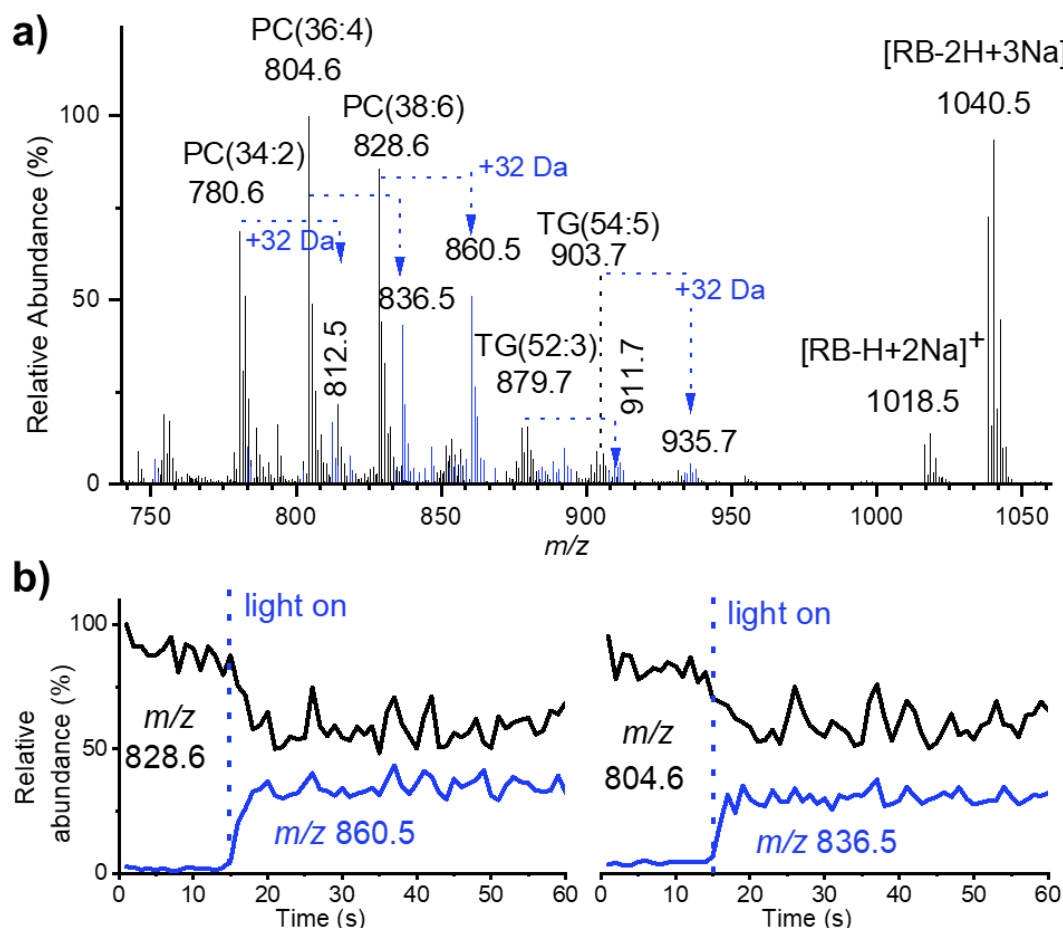


Figure 3.12. a) ESI-MS of a mouse gastrocnemius muscle tissue extract obtained using the $^1\text{O}_2$ reaction; the LOOH products are shown in blue. b) Ion chronograms of the endogenous PC 38:6 at m/z 828.55 (left) and PC 36:4 m/z 804.55 (right) and their corresponding reaction products at m/z 860.54 and m/z 836.54, respectively, obtained with and without laser excitation.

The rapid and efficient LOOH formation makes the $^1\text{O}_2$ reaction compatible with nano-DESI MSI experiments. To demonstrate the feasibility of isomer-specific profiling and imaging of lipids in tissues, we coupled the $^1\text{O}_2$ reaction with a high-resolution nano-DESI probe. The details of these experiments conducted in both MS^1 (MS^1I) and MS^2 (MS^2I) modes are provided in the SI. We used MeOH:H₂O (9/1, v/v) containing 50 μM RB and 200 nM LPE 17:1 as the extraction solvent. Figure 3.13 demonstrates the rapid response of the LPE 17:1 LOOH formation in the nano-DESI probe to laser excitation, which is similar to that observed using ESI.

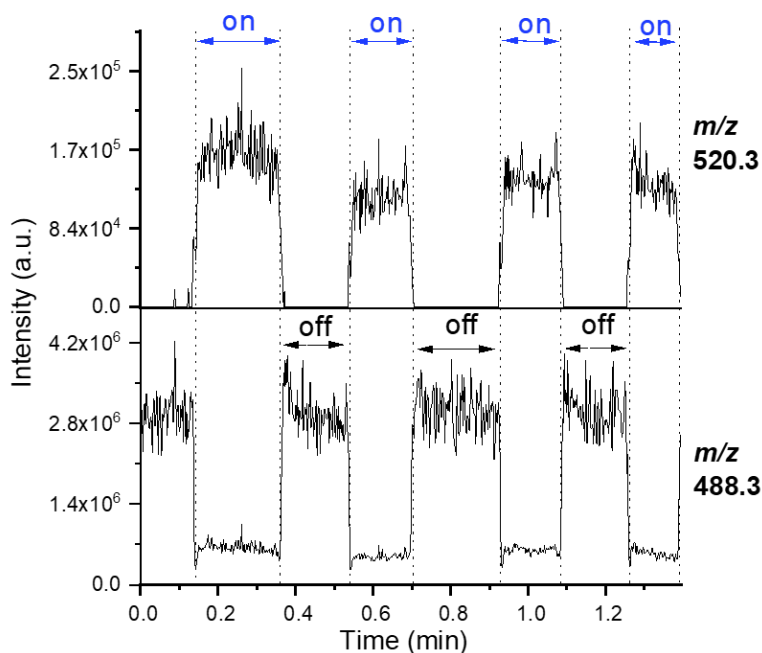


Figure 3.13. Ion chromatograms of the LPE 17:1 standard at m/z 488.3 and its hydroperoxide product, LPE 17:1(LOOH) at m/z 520.3, collected with the ESI setup. Light on and light off profiles are highlighted in blue and black, respectively.

Line profiles obtained for the LPE 17:1 standard, an endogenous PC 34:1, and their LOOH products by scanning the nano-DESI probe over a mouse uterine tissue are shown in Figure 3.14. Only LPE 17:1 is observed when the probe is positioned on the glass slide. After the light is turned on, the ion signal of LPE 17:1(LOOH) appears while the signal of LPE 17:1 decreases. The signals of the endogenous PC 34:1 and its product, PC 34:1(LOOH), are observed when the nano-DESI probe is on the tissue indicating that PC 34:1(LOOH) is generated with substantial yield on a timescale compatible with nano-DESI MSI. When the light is turned off, the signals of the reaction products LPE 17:1(LOOH) and PC 34:1(LOOH) disappear. Meanwhile, the signals of the corresponding precursor lipids remain. When the nano-DESI probe gets off the tissue, the signal of PC 34:1 disappears. This experiment establishes the utility of the $^1\text{O}_2$ reaction for imaging experiments.

We identified several isomeric lipids sampled directly from tissues by the nano-DESI probe using CID on a targeted list of LOOH products. Tables 3.1 and Table 3.2 report unsaturated lipid species in mouse muscle and uterine tissues, for which C=C locations were successfully identified. Lipids containing FA 18:1 showed diagnostic fragments indicative of the presence of isomeric 9 Δ

and 11 Δ pairs. Due to the complexity of the lipidome, some acyl chain combinations may yield ambiguous identifications in MS². For example, the same neutral losses are expected for FA 16:1(Δ 7) and FA 18:1(Δ 9) or for FA 16:1(Δ 9) and FA 18:1(Δ 11). Therefore, unambiguous identification of isomeric lipids containing both FA 16:1 and FA 18:1 requires MS³. Furthermore, some LOOHs overlap with endogenous lipids. Nevertheless, due to a very specific fragmentation, a majority of LOOHs and hence positional isomers are readily identified using MS²

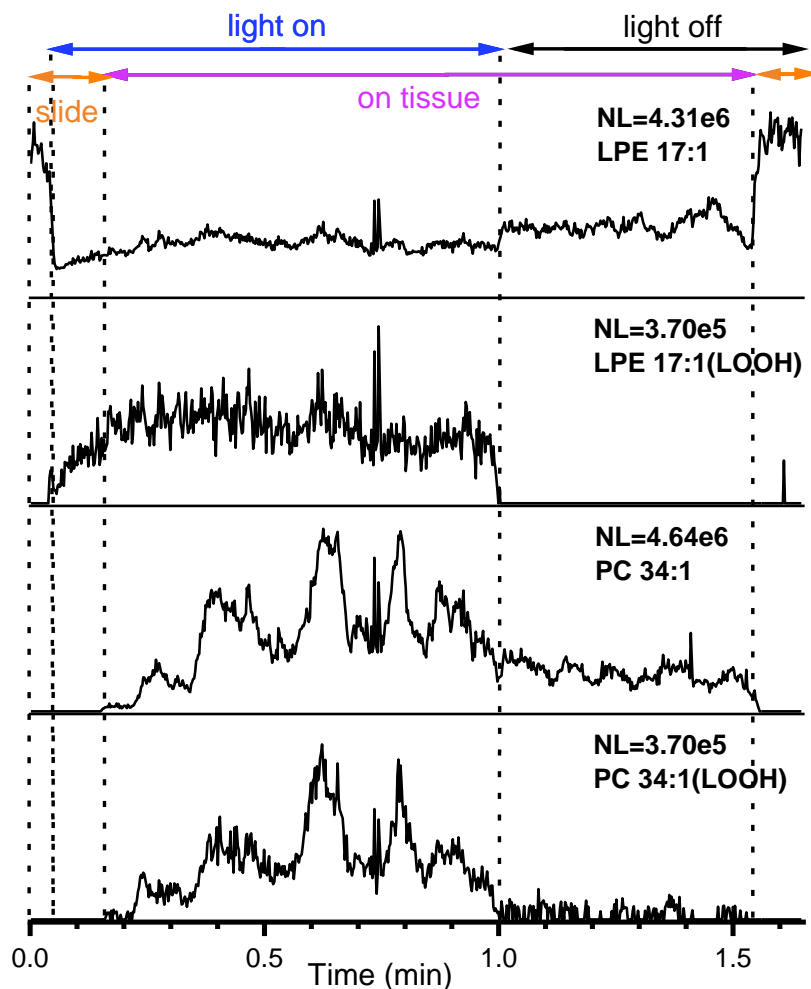


Figure 3.14. Line scan profiles of a mouse uterine tissue collected using the nano-DESI probe. The traces from top to bottom correspond to LPE 17:1 standard, LPE 17:1(LOOH), the endogenous PC 34:1, and its hydroperoxide product PC 34:1(LOOH). When the nano-DESI probe is on the glass slide, we only observe the signal of the LPE 17:1 standard. After the light is turned on, the ion signal of the LPE 17:1(LOOH) appears while the signal of the unreacted LPE 17:1 drops. The signals of the endogenous PC 34:1 and its product, PC 34:1(LOOH), are observed when the nano-DESI probe is on the tissue. At 1 min, the light is turned off, which causes the signals of the reaction products LPE 17:1(LOOH) and PC 34:1(LOOH) to immediately disappear. The signal of the standard

MS²I experiments focused on the localization of 9Δ and 11Δ isomers in rat brain and mouse uterine tissue. Figure 3.15 shows a representative HCD spectrum of m/z 814.5 ± 1 in rat brain tissue. The spectrum contains product ions of different phospholipids present in this m/z window. PC 34:1(LOOH) at m/z 814.5573 shows product ions corresponding to 9Δ (684.4, 625.3 and 501.3) and 11Δ (712.5, 653.4 and 529.4) isomers. We also observed fragment ions of the isobaric species including the [M+Na]⁺ ion of PE 40:6 (m/z 814.5362) and [M+H]⁺ ion of PE 42:9 (m/z 814.5387) at m/z 771.5 and 673.5, respectively. Although the mass shift of 32 Da generated by the ¹O₂ reaction is rather small, which complicates MS¹ spectra, product ions of different isomeric and isobaric species are readily distinguished in the MS² spectrum.

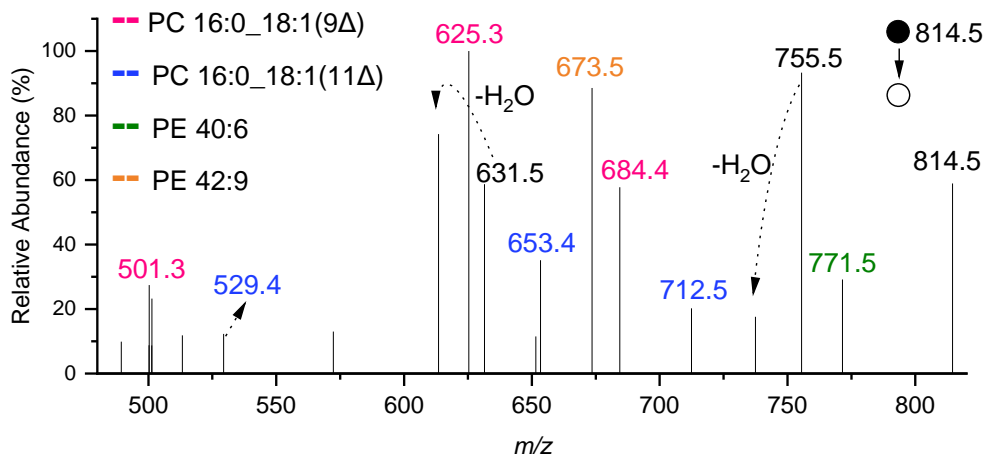


Figure 3.15. CID spectra of PC 34:1(LOOH) at m/z 814.5573 showing the presence of 9Δ and 11Δ isomers labeled in pink and blue, respectively. Fragment ions of the isobaric PE 40:6 (Na⁺) and PE 42:9 (H⁺) are labeled in green and yellow, respectively.

Next, we examined the spatial localization of the isomeric species using fractional distribution images (FDI). FDIs were generated by plotting the ratio of the summed intensities of all the fragments of the 11Δ isomer to the summed intensities of all the fragments of 11Δ and 9Δ isomers as a function of location on the tissue. Figure 3.16a shows an optical image of the rat tissue analyzed in MSI experiments. An MS¹ image of PC 34:1(LOOH) (Figure 3.16b) indicates that this molecule is enhanced in the gray matter. In contrast, FDI of 11Δ (Figure 3.16c) indicates the lower abundance of 11Δ in comparison with the 9Δ isomer in the white matter. A complementary distribution of the 9Δ isomer is shown in Figure 3.16d. These results are consistent with previous studies.^{103,104,109,117} MS²I of the characteristic fragments of the isobaric PE 40:6 at m/z 771.5 and

PE 42:9 at m/z 673.5 present in the same isolation window are shown in Figure 3.16e and Figure 3.16f, respectively. We note that it is impossible to identify C=C bond positions in PE 40:6 and PE 42:9 because CID of non-oxidized species does not provide this information. The results shown in Figure 3.16 indicate that both species are enhanced in the gray matter. FDI of the 11 Δ isomer of PC 18:0_18:1(LOOH) at m/z 842.5881 obtained in the same experiment is shown in Figure 3.17. Meanwhile, MS²I of mouse uterine tissue indicates that PC 16:0_18:1(LOOH) is evenly distributed across the tissue (Figure 3.18). These results indicate that the localization of isomeric lipids is strongly dependent on tissue type.

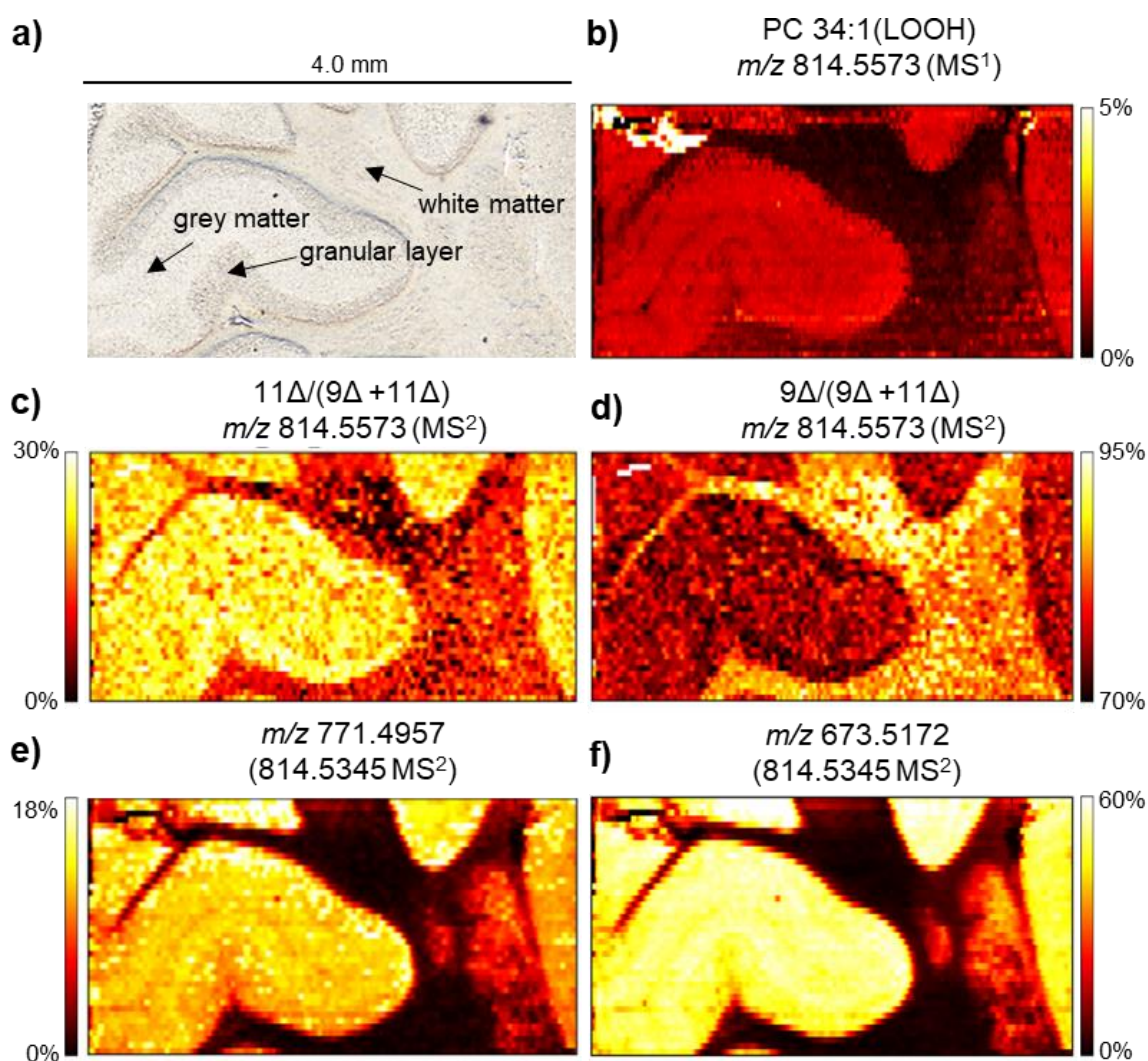


Figure 3.16. a) Optical image of rat cerebellum. b) Nano-DESI MS¹I of PC 34:1(LOOH). FDI of positional isomers corresponding to c) 11 Δ /(9 Δ +11 Δ) and d) 9 Δ /(9 Δ +11 Δ). Nano-DESI MS² images of the fragments at e) m/z 771.5 and f) m/z 673.5 corresponding to PE 40:6 and PE 42:9, respectively.

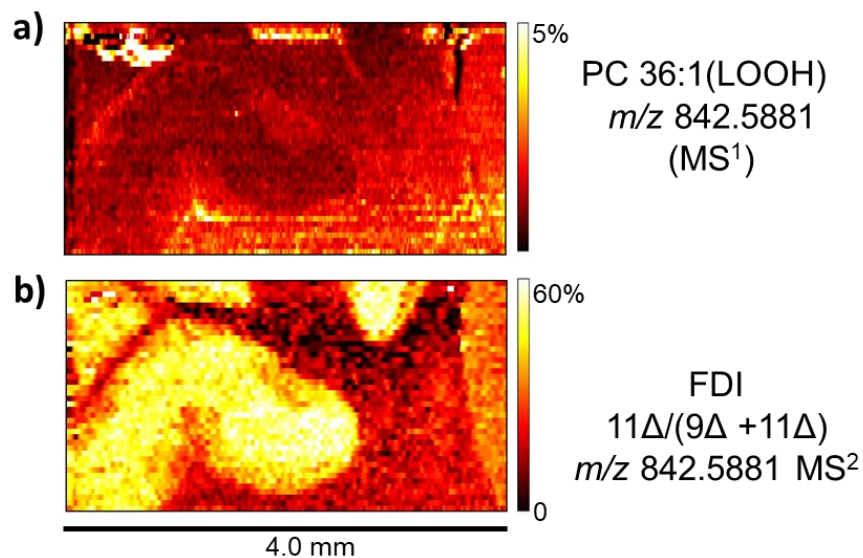


Figure 3.17. a) Nano-DESI MS¹ image of PC 36:1(LOOH) at m/z 842.5881 in the mouse brain tissue. b) An FDI image of the 11 Δ isomer of PC 36:1(LOOH).

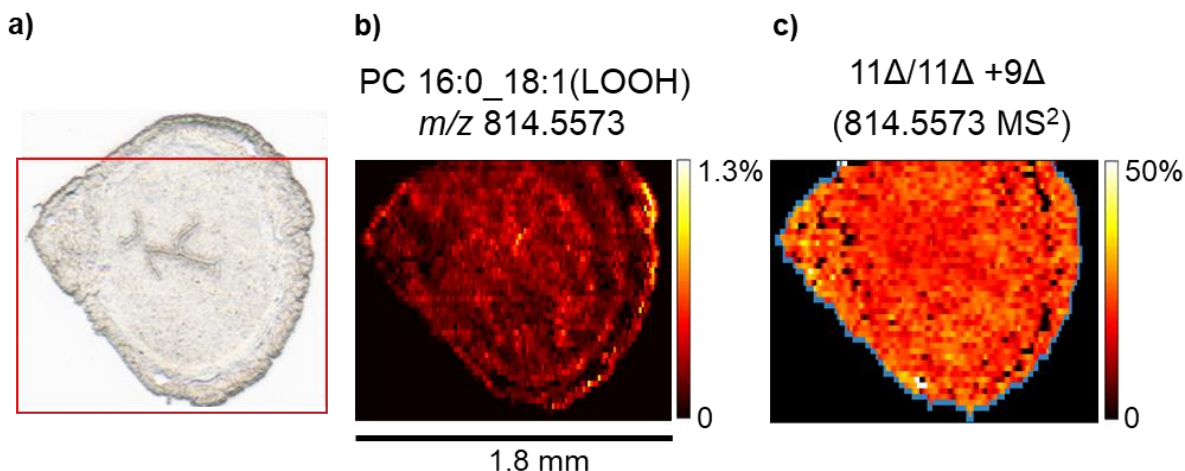


Figure 3.18. Nano-DESI imaging experiments coupled to the ¹O₂ reaction. a) An optical image of the mouse uterine tissue showing the area scanned by the nano-DESI probe. b) An MS¹ image of PC 16:0_18:1(LOOH) at m/z 814.5573. c) An FDI image of the 11 Δ isomer of PC 16:0_18:1(LOOH). The FDI calculation excludes the pixels outside of the tissue boundary highlighted in blue.

3.4 Conclusions

In summary, we have developed an online chemical derivatization method based on the ¹O₂ reaction for identifying C=C positions in different lipid classes. Rapid reaction rates enable on-the-fly photooxidation of lipids into their corresponding LOOH products. CID of LOOHs produces unique fragments revealing the C=C bond positions. This approach relies on an inexpensive light

source and photosensitizer added to the solvent or analyte mixture and can be readily implemented on any mass spectrometer. As a result, it is compatible both with lipidomics workflows and liquid extraction-based ambient ionization techniques. The small mass shift of 32 Da between the reactants and products may complicate MS¹ spectra but does not affect MS² experiments. We also note that RB generates abundant peaks in negative mode, which interfere with analyte signals. A different photosensitizer may be used in negative mode to alleviate this problem. Coupling of the ¹O₂ reaction with nano-DESI MS²I enables spatial localization of positional isomers, which cannot be achieved in the MS¹I mode. This capability will facilitate understanding of the role of isomeric C=C lipids in biological processes and exploit their potential as lipid biomarkers.

Table 3.1. Twelve unsaturated lipid species identified in the lipid extract of the gastrocnemius muscle tissue using the ESI setup coupled to the QTOF instrument. The diagnostic fragments used to identify the C=C bond location in the acyl chains are highlighted in bold. The order of the acyl chain does not indicate the sn-position. Only the peaks corresponding to the product A are shown.

#	name	Precursor ion	C=C location	fragment loss	m/z of fragment loss	m/z of ion predicted	m/z of ion observed	NL 59 from PCs
1	TG 18:2 _18:2_16:0	909.7139	$\Delta 9$	C8H16O	128.1201	781.5938	781.5972	does not apply
			$\Delta 12$	C5H12O	88.08881	821.6251	821.6300	does not apply
2	TG 18:2_ 18:1 _16:1	909.7139	$\Delta 9$	C8H18O	130.1358	779.5781	779.5791	does not apply
			$\Delta 11$	C6H14O	102.1045	807.6094	807.611	does not apply
3	TG 18:2 _18:1_16:0	911.7294	$\Delta 9$	C8H16O	128.1201	783.6093	783.6108	does not apply
			$\Delta 12$	C5H12O	88.08881	823.6406	823.6405	does not apply
	TG 18:2_ 18:1 _16:0	911.7294	$\Delta 9$	C8H18O	130.1358	781.5936	781.5946	does not apply
			$\Delta 11$	C6H14O	102.1045	809.6249	809.6225	does not apply
4	TG 18:2 _18:2_18:1	935.7326	$\Delta 9$	C8H16O	128.1201	807.6125	807.6131	does not apply
			$\Delta 12$	C5H12O	88.08881	847.6438	847.6448	does not apply
5	TG 18:2_ 18:1 _18:1	937.7439	$\Delta 9$	C8H18O	130.1358	807.6081	807.6081	does not apply
			$\Delta 11$	C6H14O	102.1045	835.6394	835.6041	does not apply
	TG 18:2 _18:1_18:1	937.7439	$\Delta 9$	C8H16O	128.1201	809.6238	809.6232	does not apply
			$\Delta 12$	C5H12O	88.08881	849.6551	849.657	does not apply
6	PC 18:1 _16:0	814.5494	$\Delta 9$	C8H18O	130.1358	684.4136	684.4241	625.346
			$\Delta 11$	C6H14O	102.1045	712.4449	712.4514	653.379
7	PC 18:2 _16:0	812.5403	$\Delta 9$	C8H16O	128.1201	684.4202	684.4215	625.348
			$\Delta 12$	C5H12O	88.08881	724.4515	724.4519	665.379

Table 3.1 continued

8	PC 20:4_16:0	836.5409	$\Delta 5$	C14H24O	208.1827	628.358	628.3574	569.287
			$\Delta 8$	C11H20O	168.1514	668.389	668.3903	609.316
			$\Delta 11$	C8H16O	128.1201	708.421	708.4211	649.349
			$\Delta 14$	C5H12O	88.08881	748.452	748.4521	689.376
9	PC 20:3_16:0	838.5531	$\Delta 8$	C11H20O	168.1514	670.402	670.4044	611.326
			$\Delta 11$	C8H16O	128.1201	710.433	710.429	651.361
			$\Delta 14$	C5H12O	88.08881	750.464	750.4665	691.392
10	PC 18:2_18:0	840.5779	$\Delta 9$	C8H16O	128.1201	712.4578	712.4507	653.378
			$\Delta 12$	C5H12O	88.08881	752.4891	752.4845	693.414
11	PC 22:6_16:0	860.5389	$\Delta 4$	C17H26O	246.1984	614.341	614.3444	555.266
			$\Delta 7$	C14H22O	206.1671	654.372	654.3716	595.302
			$\Delta 10$	C11H18O	166.1358	694.403	694.4053	635.332
			$\Delta 13$	C8H14O	126.1045	734.434	734.4381	675.364
			$\Delta 16$	C5H10O	86.07316	774.466	774.4672	715.395
			$\Delta 19$	C2H6O	46.04186	814.497	814.4995	755.426
12	PC 22:5_16:0	862.5539	$\Delta 7$	C14H22O	206.1671	656.387	656.3912	597.316
			$\Delta 10$	C11H18O	166.1358	696.418	696.4213	637.347
			$\Delta 13$	C8H14O	126.1045	736.449	736.4472	677.376
			$\Delta 16$	C5H10O	86.07316	776.481	776.4802	717.406
			$\Delta 19$	C2H6O	46.04186	816.512	816.5114	757.441

Table 3.2. Fourteen unsaturated lipid species directly extracted from a mouse uterine tissue using the nano-DESI coupled to the Orbitrap instrument. The diagnostic fragments used to identify the C=C bond location in the acyl chains are highlighted in bold. The order of the acyl chain does not indicate the sn-position. Only the peaks corresponding to the product A are shown.

#	name	Precursor ion	C=C location	Fragment loss	<i>m/z</i> of fragment loss	<i>m/z</i> of ion predicted	<i>m/z</i> of ion observed	NL 59 from PCs
1	MG 18:2	409.2581	Δ9	C8H16O	128.1201	281.138	281.1337	does not apply
			Δ12	C5H12O	88.08881	321.1693	321.1648	does not apply
2	MG 18:1	411.2676	Δ9	C8H18O	130.1358	281.1318	281.1341	does not apply
			Δ11	C6H14O	102.1045	309.1631	309.1649	does not apply
3	DG 18:2_16:0	647.4839	Δ9	C8H16O	128.1201	519.3638	519.3627	does not apply
			Δ12	C5H12O	88.08881	559.3951	559.3948	does not apply
4	DG 18:1_16:0	649.4976	Δ9	C8H18O	130.1358	519.3618	519.3633	does not apply
			Δ11	C6H14O	102.1045	547.3931	547.403	does not apply
5	DG 18:2_18:1	673.4995	Δ9	C8H16O	128.1201	545.3794	545.3802	does not apply
			Δ12	C5H12O	88.08881	585.4107	585.4121	does not apply
	DG 18:2_18:1	673.4995	Δ9	C8H18O	130.1358	543.3637	543.3661	does not apply
			Δ11	C6H14O	102.1045	571.395	571.3971	does not apply
6	DG 18:1_18:1	675.5139	Δ9	C8H18O	130.1358	545.3781	545.3742	does not apply
			Δ11	C6H14O	102.1045	573.4094	573.419	does not apply
7	PC 18:1_16:0	814.5573	Δ9	C8H18O	130.1358	684.4215	684.4205	625.3482
			Δ11	C6H14O	102.1045	712.4528	712.454	653.3806
8	PC 18:2_16:0	812.5402	Δ9	C8H16O	128.1201	684.4201	684.4228	625.3475
			Δ12	C5H12O	88.08881	724.4514	724.451	665.3789
9	PC 20:4_16:0	836.5409	Δ5	C14H24O	208.1827	628.358	628.3596	569.2839
			Δ8	C11H20O	168.1514	668.389	668.3882	609.317
			Δ11	C8H16O	128.1201	708.421	708.4233	649.3472
			Δ14	C5H12O	88.08881	748.452	748.448	689.3808

Table 3.2 continued

10	PC 20:3 _{16:0}	838.5579	Δ8	C11H20O	168.1514	670.406	not observed	611.3326
			Δ11	C8H16O	128.1201	710.438	710.4369	651.3639
			Δ14	C5H12O	88.08881	750.469	750.4636	not observed
11	PC 18:2 _{18:0}	840.5779	Δ9	C8H16O	128.1201	712.4578	712.454	653.381
			Δ12	C5H12O	88.08881	752.4891	752.4819	693.4116
12	PC 18:1 _{18:0}	842.5894	Δ9	C8H18O	130.1358	712.4536	712.4543	653.3808
			Δ11	C6H14O	102.1045	740.4849	not observed	681.4097
13	PC 20:4 _{18:0}	864.5681	Δ5	C14H24O	208.1827	656.385	656.3905	not observed
			Δ8	C11H20O	168.1514	696.417	696.4209	not observed
			Δ11	C8H16O	128.1201	736.448	736.453	not observed
			Δ14	C5H12O	88.08881	776.479	776.4838	not observed
14	PC 20:3 _{18:0}	866.5911	Δ8	C11H20O	168.1514	698.44	698.4344	not observed
			Δ11	C8H16O	128.1201	738.471	738.4644	not observed
			Δ14	C5H12O	88.08881	778.502	778.5033	not observed

CHAPTER 4. HIGH-RESOLUTION IMAGING AND IDENTIFICATION OF BIOMOLECULES USING NANO-DESI COUPLED TO ION MOBILITY SPECTROMETRY

4.1 Introduction

Mass spectrometry imaging (MSI) is ideally suited for the simultaneous mapping of the spatial distributions of hundreds of molecules directly from tissues in a label-free fashion.^{4,7,9,118–120} MSI is widely used in biomedical research and drug discovery to obtain a better understanding of the molecular-level response of biological systems to different conditions. A majority of MSI applications are focused on the identification of biomarkers and monitoring disease progression,^{44,121,122} understanding molecular alterations associated with organ development,^{43,123} visualizing drug distributions in tissues to identify the mechanisms of their action,^{124,125} and mapping the biological activity of enzymes by detecting their catalytic products¹²⁶. Desorption electrospray ionization (DESI)¹²⁷ and matrix-assisted laser desorption ionization (MALDI)^{11,55,128} are the two most common soft ionization techniques used in MSI. Ambient ionization techniques such as DESI have been employed in MSI experiments to eliminate sample pre-treatment prior to analysis and enable imaging of biological samples in their native state. Nanospray desorption electrospray ionization (nano-DESI) developed by our group²¹ is an ambient liquid extraction-based ionization technique, which has been used for imaging of biological tissues with high sensitivity and high spatial resolution of $\sim 10\ \mu\text{m}$.²⁴ Furthermore, we and others have demonstrated the quantitative capabilities of nano-DESI MSI and its ability to measure accurate concentration gradients in biological samples by normalizing the signals of endogenous molecules to the signals of internal standards added to the extraction solvent.^{29,129,130}

In the past two decades, substantial efforts have been dedicated to improving the spatial resolution, data processing, and speed of analysis of MSI.⁷ However, on-the-fly identification of molecules in MSI experiments is challenging. Furthermore, the presence of some isobaric and isomeric species, which cannot be separated by m/z alone complicates the interpretation of MSI data necessary for the molecular-level description of complex biological systems. Some of these challenges have been addressed using tandem mass spectrometry (MS/MS) imaging experiments, which enable simultaneous imaging and identification of molecules in biological samples.^{83,131} In addition, derivatization approaches including online singlet oxygen reaction¹³² and on-tissue

Paternò-Büchi¹⁰³ or ozonolysis reactions¹³³ have been coupled with MSI for studying the localization of positional isomers of phospholipids. However, these experiments are typically limited to a targeted list of m/z windows. Therefore, coupling MSI with structurally sensitive techniques is a promising approach for the untargeted analysis with improved coverage and structural characterization of molecules in biological samples.

Ion mobility spectrometry (IMS) separates molecules based on their size, shape, and charge^{134,135} and operates on a millisecond time scale, which facilitates its integration into MSI experiments.^{136,137} Furthermore, drift tube ion mobility spectrometry (DTIMS) provides structural information in the form of collision cross sections (CCS) of the separated ions.^{138–140} An interlaboratory study has demonstrated that CCS values are reproducible across different experimental platforms,¹⁴¹ which makes them excellent molecular descriptors and enables confident annotations of numerous biomolecules using open-source databases.^{142–144}

Several ion mobility instruments have been successfully coupled with MSI techniques including MALDI,^{145,146} DESI,^{147,148} liquid extraction surface analysis (LESA),¹⁴⁹ laser desorption electrospray ionization (LAESI),¹⁵⁰ and infrared matrix-assisted laser desorption electrospray ionization (IR-MALDESI).¹⁵¹ The advantages of such coupling include improved molecular coverage, the ability to generate background-free images, and rapid isomeric separation.^{136,152} Herein, we describe for the first time the design and performance of a portable high-resolution nano-DESI MSI platform coupled to a linear ion mobility quadrupole time-of-flight mass spectrometer (IM-QTOF MS), which combines the sensitivity, quantitative capability, and high spatial resolution of nano-DESI MSI with on-the-fly separation of isomeric analytes and their structural characterization using CCS measurements. In comparison with other ion mobility systems, DTIMS provides direct structural information without the need for external calibration, which facilitates the identification of biomolecules observed in nano-DESI MSI experiments. Proof-of-concept IM-MSI experiments using sections of mouse uteri on day 4 of pregnancy prior to embryo implantation demonstrate the capabilities of this newly-developed platform for imaging of drift time-selected biomolecules with a spatial resolution better than 25 μm . We demonstrate that ion mobility (IM) separation relaxes the requirement imposed on the mass resolving power of a mass analyzer by separating isobaric species along the drift time axis, enables separation of isomeric species, facilitates the identification of biomolecules observed in MSI experiments, and eliminates interferences from solvent-related peaks and peaks resulting from gas-phase

fragmentation of chemically labile endogenous molecules. In combination with the previously reported quantitative capabilities of nano-DESI MSI,¹⁵³ this platform opens up new research directions focused on isomer-selected quantitative imaging of complex biological samples. Furthermore, the newly developed versatile platform can be coupled to any mass spectrometer making it broadly applicable to a variety of applications.

4.2 Materials and methods

4.2.1 Chemicals

LC-MS grade methanol (MeOH) and LC-MS water were purchased from Sigma-Aldrich (St. Louis, MO).

4.2.2 Tissue sectioning and handling

Uterine tissues on day 4 of pregnancy were retrieved from the C57BL/6 mixed background pregnant mice on day 4 morning as described in our previous studies^{83,154}. The mice were housed in the Cincinnati Children's Hospital Medical Center Animal Care Facility according to National Institutes of Health and institutional guidelines for the use of laboratory animals and animal handling protocols of the approved by Cincinnati Children's Hospital Research Foundation Institutional Animal Care and Use Committee. Pieces of mouse uteri on day 4 of pregnancy were snap-frozen and sectioned using a cryostat. Sections of 12 μm thickness were mounted onto glass slides and stored in a -80 °C freezer prior to analysis.

4.2.3 Nano-DESI platform

Nano-DESI MSI experiments were performed on an Agilent 6560 IM-QTOF MS (Agilent Technologies, Santa Clara, CA). A schematic of the nano-DESI source is shown in Figure 4.1a. Figures 4.1b and 4.1c show the nano-DESI imaging system developed in this study which is assembled on a portable cart (1) that can be readily deployed in combination with any mass spectrometer. The cart houses all the components including a vibrationally insulated platform (2) (Newport, Irvine, CA), a lock-in amplifier (3) (Stanford Research Systems, Sunnyvale, CA) and a computer that controls the system (4). The XYZ stage (5) and sample holder are mounted on the vibrationally insulated platform, along with the micro-positioners (6) and Dino-Lite cameras (7).

A stainless steel capillary extension (8) is attached to the mass spectrometer inlet as shown in Figure 1c.

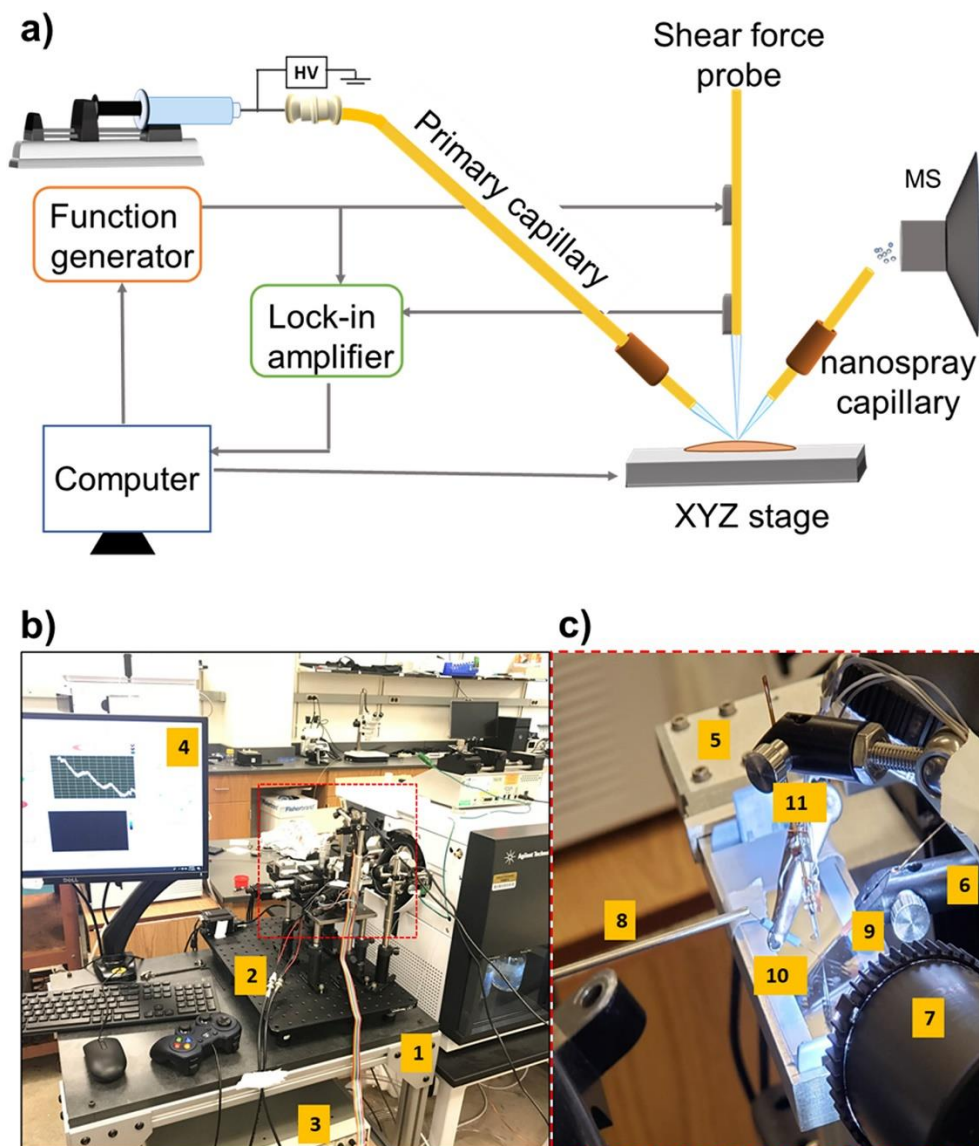


Figure 4.1. a) A schematic drawing of the high-resolution nano-DESI MSI source. b) A photograph of the imaging platform, showing the custom-designed cart (1); vibrationally insulated platform (2); lock-in amplifier (3), and computer that controls the XYZ stage (4). c) A zoomed-in photograph corresponding to the red dashed box in panel b. The XYZ stage (5), micro positioners (6), Dino-Lite microscope (7), capillary extension (8), primary capillary (9), nanospray capillary (10) and shear force probe (11) are also highlighted.

The nano-DESI probe is described in the next section. A pulse of 5V to 0V provided by the LabView program is used to synchronize the XYZ stage and Agilent's acquisition software.

Typical source parameters are as follows: capillary temperature of 300 °C, ESI voltage of +4.5 kV for positive mode and -4.0 kV for negative mode. Manual tuning was carried out to optimize most of the internal voltages and trapping and release times. Briefly, we use a mixture of standards covering the m/z range of 100-1500 which is used in our imaging experiments. We optimize the front funnel settings to minimize in-source fragmentation and improve signals at the low and high mass range in both modes. These parameters can be found in Tables 4.1-4.2.

Table 4.1. Front Funnel Settings for the QTOF and IM-QTOF Mode experiments in Positive Mode

High Pressure funnel delta (V)	High Pressure funnel RF (V)	Trap funnel delta (V)	Trap funnel RF (V)	Trap funnel Exit (V)
150	120	180	120	10

Table 4.2. Front Funnel Settings for the QTOF and IM-QTOF Mode experiments in Negative Mode

High Pressure funnel delta (V)	High Pressure funnel RF (V)	Trap funnel delta (V)	Trap funnel RF (V)	Trap funnel Exit (V)
-150	-100	-180	-100	-10

We reproduced the drift tube parameters reported previously in the inter-laboratory study,¹⁴¹ which uses the same DTIMS instrument used in this work. The detailed drift-tube settings can be found in Table 4.3. Finally, we evaluated the signal response to different trapping and release times and selected the parameters that enabled the best transmission of most of the standards without saturating the detector. A trapping time of 15 ms and a release time of 150 μ s were selected for positive mode experiments. Meanwhile, a trapping time of 15 ms and a release time of 300 μ s were selected for negative mode experiments.

Table 4.3. Drift Tube Settings for the IM-QTOF in Positive Mode/Negative Mode

Drift Tube Entrance (V)	Drift Tube Exit (V)	Rear Funnel Entrance (V)	Rear Funnel Exit (V)
1571.9/-1571.9	224.1/-224.1	218.2/-218.2	30/-30

4.2.4 Nano-DESI MSI experiments

Imaging experiments of uterine tissue sections were performed in triplicate using a mixture of MeOH:H₂O (9:1) (v/v), which was infused using a syringe pump (KD Scientific, Holliston, MA)

at 0.5 $\mu\text{L}/\text{min}$. The high-resolution nano-DESI probe is assembled in front of the mass spectrometer inlet as shown in Figure 1 and described in our previous studies.^{31,34} Briefly, the finely pulled primary (9) and nanospray (10) capillaries with OD of 15-25 μm are aligned to form a liquid bridge. Analyte molecules are extracted into the liquid bridge directly from the tissue and transferred to a mass spectrometer inlet through the nanospray capillary. A third capillary (11), that serves as a shear-force probe,³¹ is positioned in close proximity to the nano-DESI probe to maintain a constant distance between the sample and the nano-DESI probe. Imaging data are acquired in lines by scanning the sample under the nano-DESI probe in one direction and stepping between the lines in another direction. For all the data reported in this study, we used a scan rate of 20 $\mu\text{m}/\text{s}$ and a step between the lines of 29 μm resulting in a total analysis time of ~ 3 h per tissue section ($\sim 4 \text{ mm}^2$). Experiments were performed using an acquisition rate of 1 Hz resulting in an average pixel size of $20 \times 29 \mu\text{m}^2$. MS/MS data for most of the endogenous species observed in nano-DESI MSI experiments were acquired directly from tissue sections using the auto MS/MS mode at a collision energy of 20 V.

4.2.5 Data processing

The initial lipid and metabolite annotation is performed based on the accurate mass measurements using LIPID MAPS (www.lipidmaps.org) and METLIN (<https://metlin.scripps.edu>). Then, the CCS values are calculated for each molecule from the raw drift time values obtained using the single-field method. Next, the initial annotations are verified by comparing the measured CCS values with the values from the CCS compendium¹⁴². Finally, the assignments are confirmed using the MS/MS data acquired as described earlier. Distribution of molecular classes in both modes can be found in Figure 4.2. The full list of molecular annotations is summarized in Tables 4.4-4.5.

Analysis of the QTOF data is performed using the Ion Mobility-Mass Spectrometry Image Creator script developed by our group.¹⁵⁵ In brief, the script interfaces with Skyline's¹⁵⁶ command line to input experimental .d data files and export a chronogram summary of targeted masses. The script then reconstructs those chronograms into individual ion images. The resulting images are displayed using a self-normalized heat map color scale. Intensity values for each pixel are normalized to the TIC. For data with drift time information, Agilent's MassHunter Mass Profiler

software is used to extract a feature list, i.e. a list containing m/z , drift time, and charge information of recurring peaks among all the experimental lines.

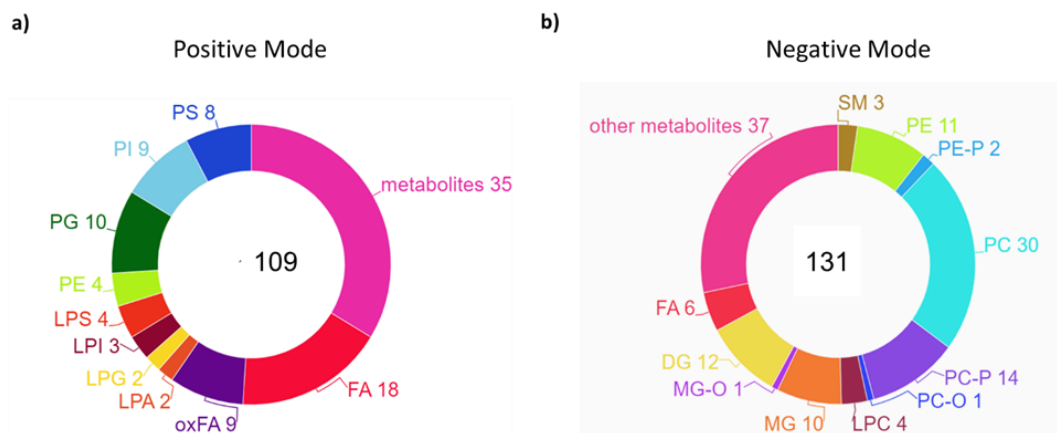


Figure 4.2 Pie chart showing the total number of species detected from the molecular profiling in a) positive mode and b) negative mode with the nano-DESI IM-MSI platform.

4.3 Results and discussion

Herein, we describe the implementation of the high-resolution nano-DESI MSI on an Agilent 6560 IM-QTOF system. We demonstrate the capabilities of this new platform in combination with IM separation, which enables both m/z - and ion mobility-selected imaging of molecules in tissues. We use mouse uterine tissue on day 4 of pregnancy as a model system, which is a fairly small sample (< 2 mm in diameter) with distinct anatomical features described later in the text and substantial chemical gradients between the different regions of the tissue.³⁴

4.3.1 Nano-DESI imaging of drift time separated ions

Figure 4.3 shows the averaged mass spectra (top) and CCS vs. m/z 2D plots (bottom) of all the species identified in the uterine sections using nano-DESI-IM-MSI experiments in a) positive and b) negative mode. These data were extracted from a line scan corresponding to the central region of the tissue. We observe that phosphatidylcholine (PC) species are abundant in the m/z range of 760-880 in positive mode whereas fatty acid (FA) species in the m/z range of 250-400 are dominant in negative mode. We successfully detected 227 unique species containing 161 lipids

and 66 metabolites. Specifically, 131 species were identified in positive mode, 109 species were identified in negative mode, and 13 species were found in both modes.

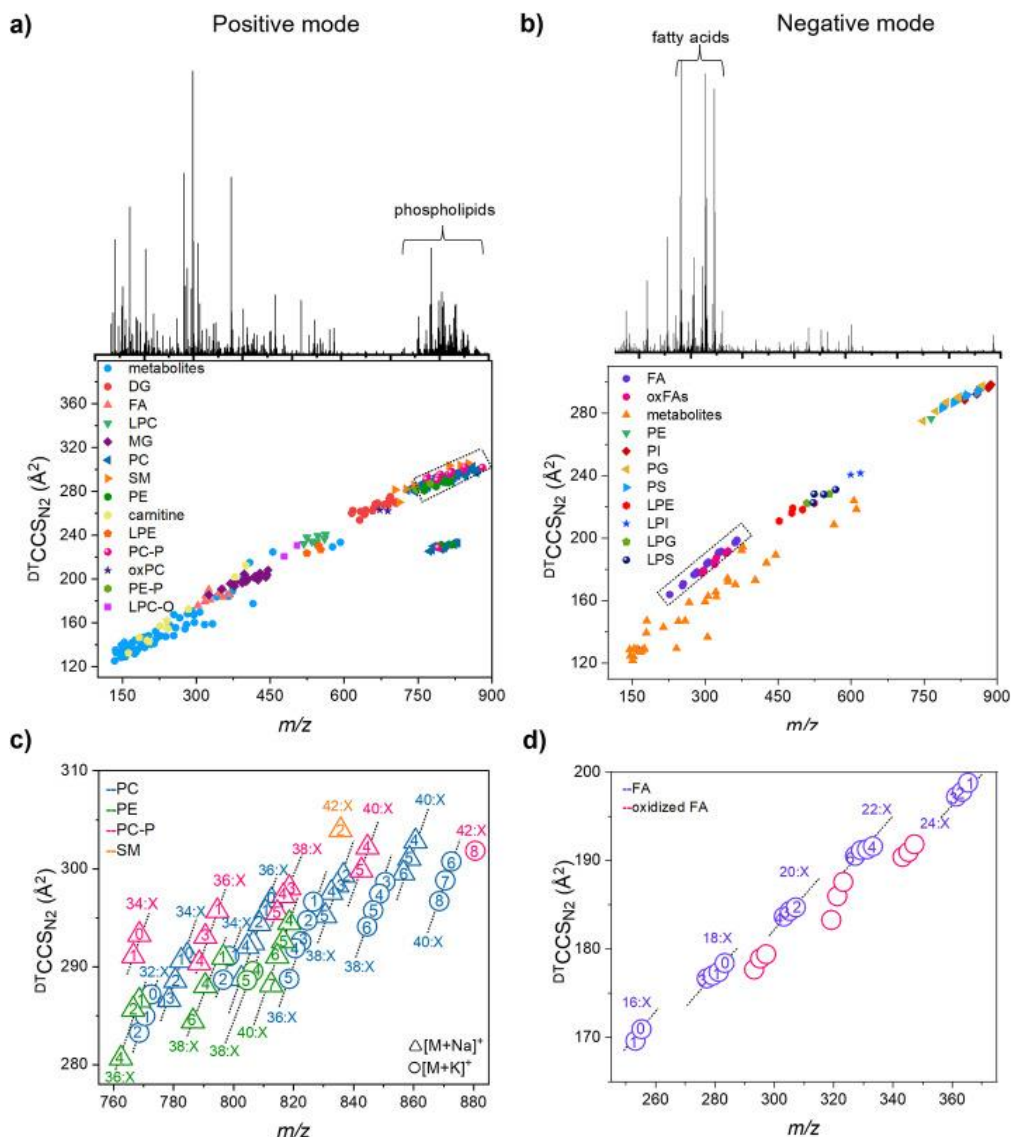


Figure 4.3. Averaged mass spectra and CCS vs. m/z plots of the species identified in the nano-DESI-IM-MSI of a mouse uterine tissue in a) positive mode and b) negative mode. c) Phospholipids separated by drift time in the m/z 720–890 region highlighted with the dashed box in panel a. Triangles and circles denote $[M+Na]^+$ and $[M+K]^+$ ions, respectively, and the symbol colors indicate the lipid class of the molecule as indicated in the legend. The nomenclature used to indicate the individual species is AA:X, where AA denotes the acyl chain length and X denotes the number of double bonds. The dotted lines highlight the series of homologous species differing by the number of double bonds; the number of double bonds for each species is indicated inside the corresponding marker. d) Fatty acids and oxidized fatty acids separated by drift time in the m/z 250–400 region highlighted with the dashed box in panel b. Nomenclature used to indicate individual species is the same as described earlier.

An expanded view of the positive mode CCS vs. m/z plot in the m/z 760-880 range is shown in Figure 4.3c. Phospholipids observed in this region of the spectrum, are grouped into distinct homologous series based on their lipid class-specific CCS-mass correlations. For each adduct type and lipid class indicated by different markers and colors in Figure 2c, the homologous series differing by the number of double bonds follow distinct linear trends in CCS as a function of m/z . Each of these series is highlighted with a dotted line and labeled using the AA:X notation, in which AA indicates the acyl chain length containing X double bonds. The number of double bonds in each species is indicated inside the corresponding marker in the plot. Structural differences pertaining to the lipid class and type of adduct are readily visualized based on their CCS vs. m/z trend lines. For example, it is easy to distinguish different adducts of PC and PE species of varying length of fatty acyl tails. We observe that for the same adduct and length of acyl chains, PE species are characterized by smaller CCS values indicating a better packing efficiency of these molecules in comparison to PC species.¹⁵⁷ Moreover, IM separation highlights structural changes within the same homologous series of species. For example, for the same lipid class, type of adduct, and acyl chain length, the CCS value decreases with an increase in the degree of unsaturation. The addition of a double bond introduces a kink into the acyl chain, which makes the molecule more compact and enables it to travel faster through the drift tube. Similarly, FAs observed in the negative mode CCS vs. m/z plot shown in Figure 4.3d are grouped based on the length of the acyl chain. Interestingly, oxidized FAs (pink circles in Figure 4.3d) display different slopes for different groups of species. This observation likely indicates the presence of different classes of oxidized FAs such as oxo-FAs, hydroperoxides, or epoxides in the tissue sample. Because of the low abundance of these molecules and uninformative fragmentation patterns observed in MS/MS experiments it is difficult to characterize their structures. Nevertheless, their CCS values listed in Table 4.4-4.5 are consistent with their classification as oxidized FAs^{142,158} These observations highlight the power of the CCS measurement for the identification of compounds observed in MSI experiments based on the predictable differences in the trend lines exhibited by every lipid class.

We also took advantage of the measured CCS values to improve the confidence of our metabolite annotations. For example, a feature at m/z 346.0553 could be assigned as the $[M-H]^-$ ion of either adenosine monophosphate (AMP) or deoxyguanosine monophosphate (dGMP), which are isomeric. The collected MS/MS spectrum for m/z 346.0553 (Figure A.1) is dominated by fragments at m/z 78.9596 and 96.9726 corresponding to the loss of the phosphate group.

Because both isomers contain phosphate groups, these fragment ions cannot be used to distinguish between the two structures. Indeed, the METLIN annotation scores are comparable for both structures and are insufficient to distinguish between the isomers (Figure A.1). By using the experimental CCS value of 174.3 \AA^2 as an additional molecular descriptor, we unambiguously identified this molecule as AMP with a reference CCS value of 174.1 \AA^2 .¹⁴² Meanwhile, the CCS value of 169.4 \AA^2 reported for dGMP is substantially lower than the experimentally measured CCS, which allows us to rule out this assignment. Similarly, a feature at m/z 146.0461 could be assigned as the $[M-H]^-$ ion of acetylserine, methylaspartate, or L-glutamate. Upon matching with MS/MS libraries, the highest score is obtained for L-glutamate as shown in Figure A.2. The experimental CCS value of 125.3 \AA^2 allows us to confirm this annotation.

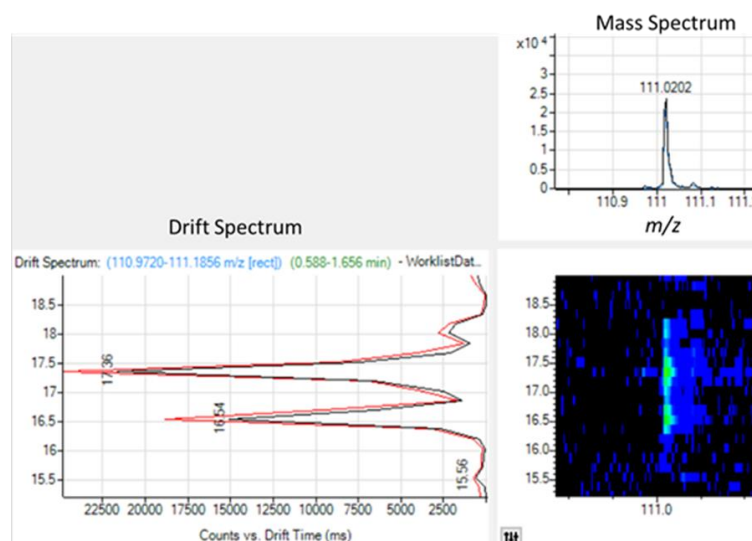


Figure 4.4. A 2D-IM-MS plot obtained for m/z 111.0202.

Finally, we also used CCS values to identify fragments of chemically labile molecules. For example, we found multiple features for m/z 111.0201 at DT 16.54, 17.36 and 18.01 ms as shown in Figure 4.4. Based on the accurate m/z , the peak at m/z 111.0201 could be attributed to uracil. However, the CCS values of 135.9 \AA^2 , 142.6 \AA^2 and 147.8 \AA^2 obtained for the three DT features respectively, largely deviate from the reference value of 113.5 \AA^2 reported for uracil.¹⁴² These results suggest that ions at m/z 111.0201 observed in this experiment are likely fragments of larger molecules such as uridine mono- and di-phosphate, among others. In-source fragmentation is a common process affecting the results of untargeted metabolomics experiments.¹⁵⁹ Our results

indicate that MSI data likely contain a fraction of features produced through in-source fragmentation, which may be mistaken for endogenous molecules. IM separation is particularly advantageous for the identification of such experimental artifacts which is important for quantitative accuracy.

Figure 4.5 displays drift time-separated ion images obtained for molecules in mouse uterine tissues in positive mode (top row) and negative mode (bottom row). Different regions of the uterine tissue sections including myometrium (Myo) which is composed of longitudinal (L) and circular (C) muscle layers, stroma (S), luminal epithelium (LE), and glandular epithelium (GE) are indicated in the optical image. Representative ion images of endogenous molecules highlight different patterns of region-specific molecular distributions observed in uterine tissue sections. For example, ion images corresponding to monoglyceride (MG) 18:1, sphingomyelin (SM) d34:1, phosphatidylglycerol (PG) 34:1 and FA 22:6 display a substantial enhancement in the LE and GE cells. Meanwhile, a complementary distribution is observed for lysoPC 18:0, phosphatidylserine (PS) 40:6 and PC 32:0, which are depleted in both LE and GE. Most metabolites display a less delineated distribution. For example, inosine monophosphate (IMP) is suppressed in both the LE and adjacent stroma cells but is abundant outside of this region. In contrast, AMP is evenly distributed across the stroma. Finally, some molecules such as taurine are evenly distributed across the entire tissue. Identification of these and other biologically lipid molecules in situ is important for understanding uterine biology during pregnancy.

The spatial resolution of $\sim 25\ \mu\text{m}$ was estimated for drift-time separated ion images based on the 20/80 rule.^{34,160} In comparison, spatial resolution of $10\ \mu\text{m}$ has been previously obtained using a similar high-resolution nano-DESI probe.^{32,34} We propose that the spatial resolution in this experiment was limited by the acquisition rate of the mass spectrometer rather than the size of the liquid bridge. In particular, we used the acquisition rate of 1 Hz, which provides good-quality IM-MS data. Based on the scan rate of $20\ \mu\text{m/s}$ used in this experiment, the pixel size along the scan direction is $20\ \mu\text{m}$ at 1 Hz acquisition rate. The spatial resolution can be improved using faster acquisition rates at the expense of sensitivity. For example, in our experiments, the S/N ratio at 782.5655 increases from 915 at 7 Hz to 1699 at 1 Hz due to an increase in the number of mass spectra averaged per pixel. In summary, these results demonstrate the successful implementation of the high-resolution nano-DESI MSI on the IM-QTOF instruments, which provides high-quality ion images of drift time-separated ions. Furthermore, the portable platform constructed in this

study, enables the implementation of nano-DESI MSI on any commercial mass spectrometer. Indeed, we were able to use this platform in combination with an ion trap mass spectrometer in our laboratory.

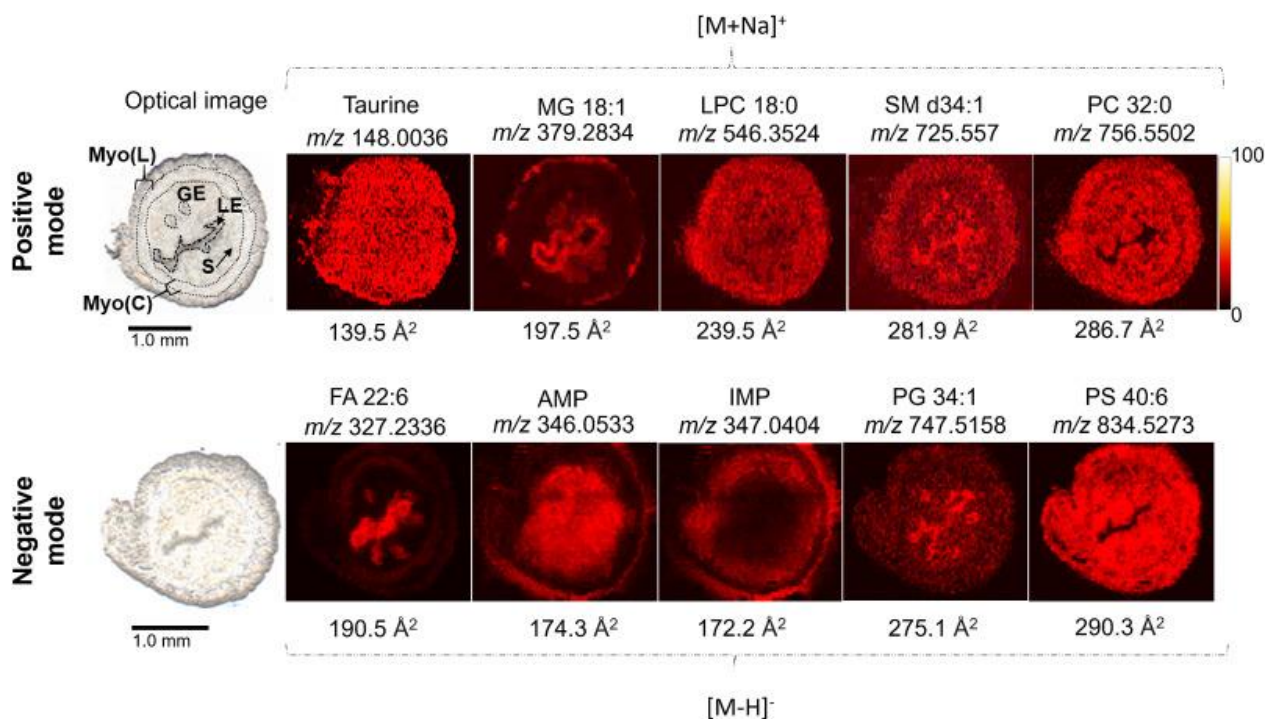


Figure 4.5. Optical images of the mouse uterine tissue sections (left column) highlighting their main components including myometrium (myo) composed of longitudinal (L) and circular (C) muscle layers, stroma (S), luminal epithelium (LE) and glandular epithelium (GE) are included on the left side.

Representative nano-DESI ion images of the tissue sections collected using the new nano-DESI-IM-QTOF platform in positive mode (top row) and negative mode (bottom row) using 1 Hz acquisition rate. The intensity scale changes from black (low) to yellow (high)

4.3.2 Separation of isomeric species

Isomeric separation is a unique capability that greatly enhances chemical coverage of MSI experiments. However, the complexity of lipid isomeric structures makes their drift time separation challenging. It has been demonstrated that the resolving power of greater than 250 is often necessary for the isomeric separation of lipids using IM.¹⁶¹ However, a majority of DTIMS instruments, such as the one used in our experiments, have the IM resolving power of ~60. We identified many unresolved features in the IM-MSI data based on the widths of the

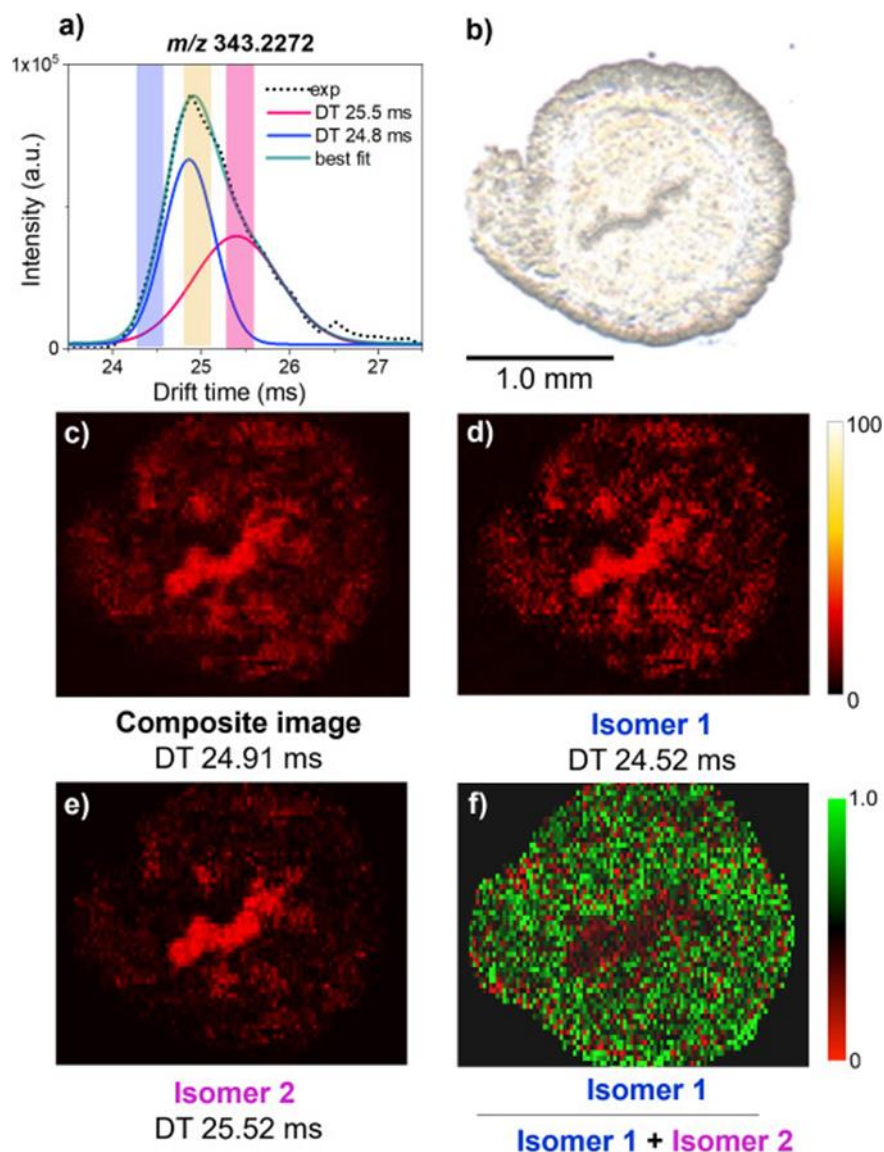


Figure 4.6 a) The experimental and deconvoluted arrival time distribution (ATD) of m/z 343.2272. The experimental ATD (dotted line) is overlaid on top of the best fit profile (solid green line). ATD profiles of isomers 1 and 2 are shown as blue and pink lines, respectively. Colored bars indicate the region selected for image generation. b) An optical image of the mouse uterine tissue section. c) A composite ion image generated at DT 24.91 ms. Ion images of d) isomer 1 at DT 24.52 ms and e) isomer 2 at DT 25.52 ms. d) An FDI image showing that the relative abundance of isomer 1 is decreased in the LE region.

peaks, suggesting the presence of multiple isomeric components. Because our current data analysis tools can only be used to obtain ion images of well-separated features, we performed the analysis of selected unresolved peaks using manual data extraction. Specifically, we used peak fitting to extract the abundance of each isomeric component and generate isomer-specific ion images. Figure 4.6 illustrates this approach. The experimental arrival time distribution of m/z 343.2272 identified

as an oxidized FA is shown as a dotted line in Figure 4.6a. We observe that the peak shape is not symmetrical and shows a shoulder at longer drift times. Without peak deconvolution, our imaging workflow would only select the peak centered at DT 24.91 ms as highlighted by the yellow bar. The optical image is shown in Figure 4.6b whereas the corresponding ion image generated from the region highlighted with a yellow bar is shown in Figure 4.6c. It can be observed that this molecule is enhanced in the GE and LE region of the tissue. Using peak fitting, we identified the presence of at least two isomeric components. The peak of the first isomeric component (blue line) is centered at DT 24.91 ms and the second isomeric component (pink line) is centered at DT 25.52 ms. The spatial distributions of the two isomeric components were obtained by selecting regions of the IM peak where the contribution from the other isomer is small as illustrated in Figures 4.6d and 4.6e. Fractional distribution images (FDI) were obtained by plotting the abundance ratio of the signal obtained for isomer 1 over the total signal of both isomers (Figure 4.6f). Although both isomers of m/z 343.2272 are localized to the same regions of the tissue, the FDI image shows that their relative abundance varies across the tissue. Specifically, isomer 1 is more abundant in myometrium and stroma and suppressed in the LE region in comparison with isomer 2. Similar analysis was performed for other oxidized FAs at m/z 345.2422 and m/z 347.2585 as shown in Figure 4.7, and their FDI distributions are similar to that of m/z 343.2272.

The molecule at m/z 343.2272 was putatively identified based on the accurate m/z measurement as hydroxydocosahexaenoic acid (HDoHE), which is the oxidized form of FA 22:6. It is reasonable to assume that the two isomeric components observed in Figure 4.6a, result from the addition of the OH group to different double bond locations, which generates several isomeric oxidized species observed in the broad drift time distribution. Although the ion signal of these molecules is insufficient to collect MS/MS spectra, their CCS values provide insights into their structures. In particular, the peak centered at DT 24.91 ms has a CCS value of 189.6 \AA^2 , whereas the peak centered at DT 25.52 ms has a CCS value of 194.2 \AA^2 . Upon matching to open CCS databases, these molecules are assigned as 14- HDoHE and 17-HDoHE, respectively.^{142,143} Lipid oxidation may result from the oxidative stress during pregnancy.^{44,162} This inflammatory response increases the concentration of reactive oxygen species, which react with free FAs and cause oxidation. These species are typically present at low concentrations and are difficult to identify using MS/MS. Our results demonstrate the power of IM separation for distinguishing variations in the localization of isomeric species in biological tissues, which cannot be achieved based on the

accurate m/z measurement alone. This capability along with improved identification of molecules based on their CCS values obtained using DTIMS is critical to obtaining accurate imaging and identification of molecules in biological samples in the same experiment. Despite these advantages, the resolving power of DTIMS may be insufficient to fully separate isomeric lipids. This limitation may be partially addressed using advanced data processing approaches. We are currently developing tools that will allow us to extract features from unresolved peaks to further expand the depth of chemical information, which may be obtained using IM-MSI. The resolving power of DTIMS may be further improved using higher-pressure instruments.^{163,164}

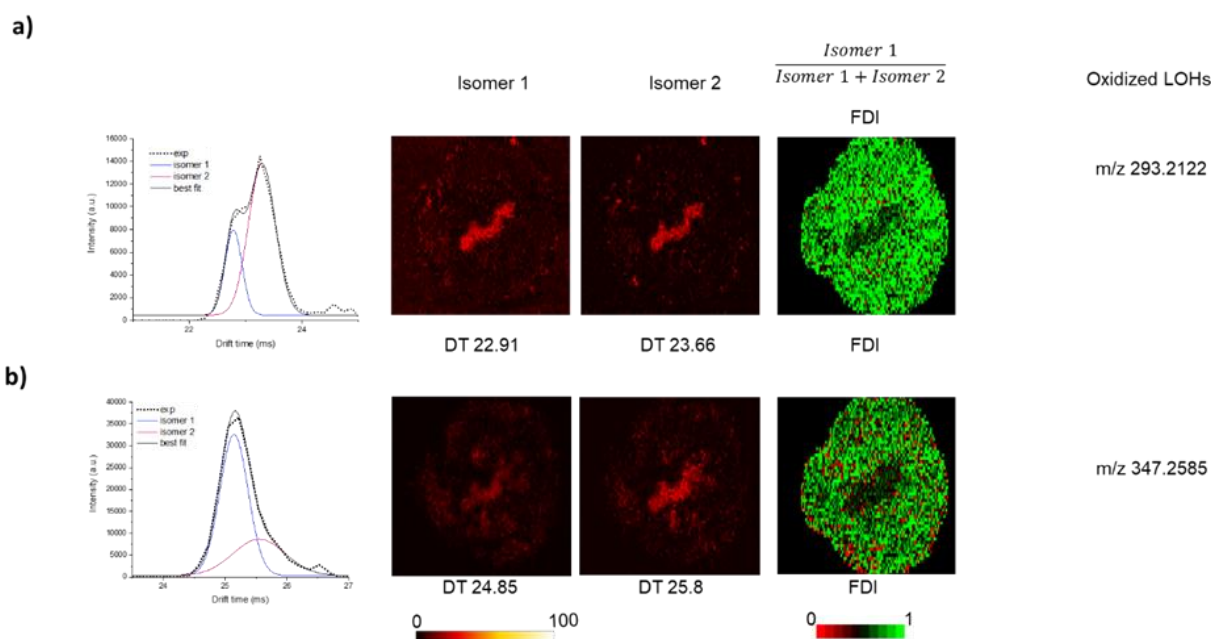


Figure 4.7. Ion images generated from the deconvoluted drift time peak corresponding to a) m/z 345.2422 and b) m/z 347.2585. The FDI images showing the relative abundance of isomer 1 are depicted on the right side

4.3.3 IM-MSI eliminates interferences from isobaric peaks

IM separation in nano-DESI MSI experiments is also a powerful tool for eliminating different types of interferences from imaging data. For example, the monoisotopic peak of glutathione (GSH) contains a contribution from one of the isotopes of the doubly charged oxidized glutathione (GSSG), which may alter the spatial distribution of this important molecule observed in MSI.

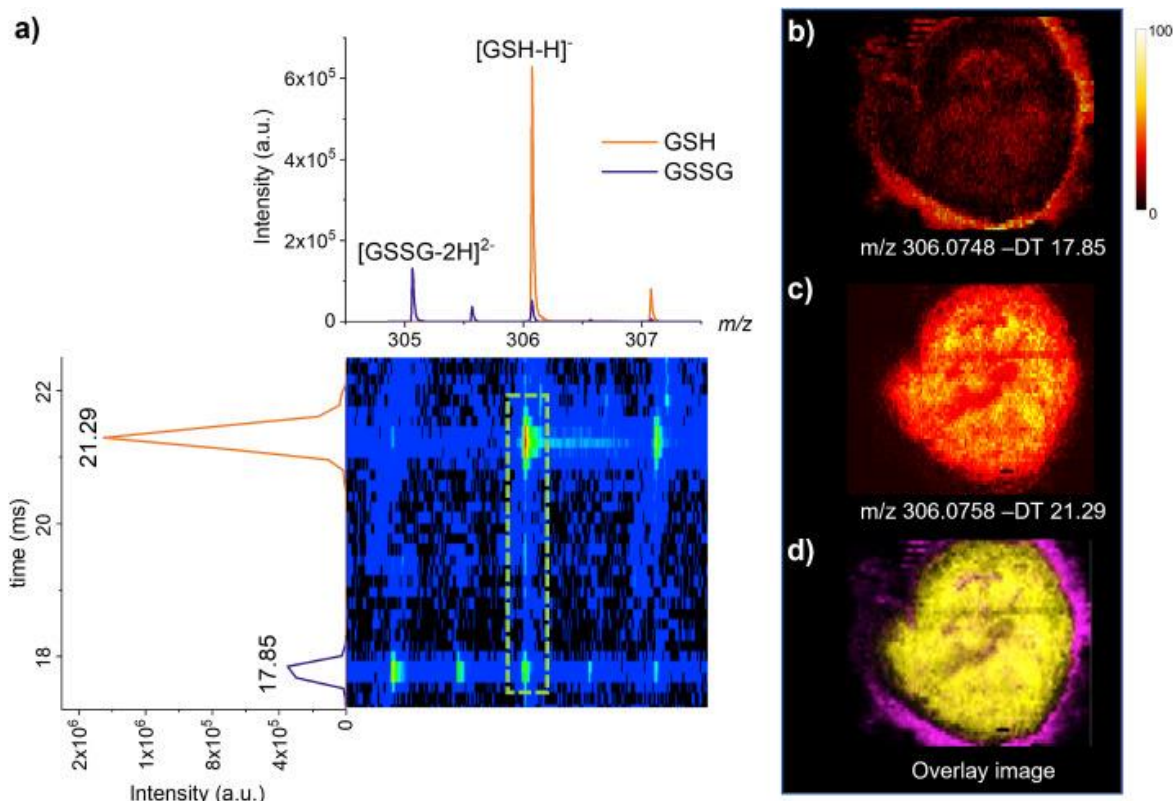


Figure 4.8. a) A 2D-IM-MS plot of the m/z range of 304.5–307.5 showing the isotopic distributions of GSH (orange line) and GSSG (purple line). Ion images of closely-spaced isobaric peaks at b) m/z 306.0748, DT 17.85 ms and c) m/z 306.0758, DT 21.29 ms. d) An ion image obtained without IM separation, in which the contribution of the M+2 isotopic peak of GSSG is indicated in purple and the contribution of the monoisotopic peak of GSH is indicated in yellow.

GSH is a powerful antioxidant tripeptide produced in cells which is comprised of glutamic acid, cysteine, and glycine whereas its oxidized form, GSSG, is comprised of two molecules of GSH linked by a disulfide bridge. IM-MSI experiments reveal that the monoisotopic peak of $[\text{GSH-H}]^-$ at m/z 306.0758 overlaps with the M+2 isotope of $[\text{GSSG-2H}]^{2-}$ at m/z 306.0748. Separation of these two peaks in the m/z domain requires a mass resolving power of $>300,000$ which is challenging even for high mass resolution instruments such as Orbitraps. In contrast, these peaks are readily separated in the drift time domain as shown in Figure 5. Specifically, Figure 4.8a shows the 2D IM-MS map for the m/z range of 304.5–307.5, in which the isotopic distributions for GSH and GSSG are indicated by an orange and purple line, respectively. The two isobaric components at m/z 306 are readily separated in the IM dimension with one peak observed at DT of 17.85 ms and another one at 21.29 ms. Ion images generated for these two components depict distinct spatial localization as shown in Figures 4.8b and 4.8c. The molecule at DT 17.85 ms is

enhanced in the longitudinal muscle layer and stroma whereas the molecule at 21.29 ms is enhanced in the circular muscle layer and stroma. Although the distribution of GSSG can be readily obtained by selecting the monoisotopic peak at m/z 305.0695, the distribution of GSH at m/z 306.0754 is altered by the contribution of the M+2 isotope of GSSG, which cannot be accounted for without IM separation. An overlay of the two peak components is depicted in Figure 4.8d where it can be clearly observed how each of them contributes to the ion image. IM separation is critical to eliminating this type of interference, which may affect biological insights derived from MSI data. For example, the ratio of GSH to GSSG is commonly used to evaluate the oxidative stress within cells with the lower ratio associated with an onset of neurodegenerative diseases.^{165,166} Therefore, accurate measurement of the GSH to GSSG ratio across the tissue may be only obtained using IM-MSI experiments.

Separation of isobaric peaks using IM-MSI is not limited to the overlapping isotopic distributions. Previously, the isobaric differentiation in IM-MSI was used to distinguish between isobaric peptides fragments corresponding to tubulin and ubiquitin.¹⁶⁷ The reconstructed ion images of these proteins showed remarkably different distributions in rat brain tissue sections. In our positive mode data, we observed that some PC and PE species were not separated in the m/z dimension using the extended dynamic range (2 GHz) mode selected in this study. For example, in Figure 4.9 we show two neighboring ions at m/z 818.5637 and 818.6019, which were identified as sodiated PE(40:4) and PC(P-38:3), respectively. Separation of these species with a mass difference of 0.0364 Da corresponding to the difference between CH₄ and O, requires a mass resolving power of 33,000 at m/z 818.6019, which is higher than the mass resolving power of the IM-QTOF in the extended dynamic range mode ($m/\Delta m = 23,500$ at m/z 782.5653). Although the two isobaric peaks are not well-separated in the m/z dimension, they are readily separated in the IM mode. This indicates that IM separation relaxes the constraints imposed on the mass resolving power of a mass spectrometer making it possible to perform MSI experiments using less expensive instrumentation and thereby making it more accessible to the scientific community.

Background solvent peaks are also eliminated as shown in Figure 4.10 which illustrates the separation of LPC(18:2) as a [M+Na]⁺ ion at m/z 542.3208 from an isobaric solvent peak at m/z 542.2983. It can be clearly observed that the spatial distribution of LPC(18:2) is completely masked by the background peak in the MS mode. Meanwhile, a distinct pattern showing that this molecule is depleted in both LE and GE is observed in the IM-MS mode. This capability has been

previously used in MALDI-IMS-MSI experiments to obtain high-quality ion images of endogenous lipids in breast tumor tissue by reducing the interference from matrix ions.¹⁶⁸ Collectively, these results demonstrate the power of IM-MSI for obtaining ion images free of isobaric interferences, which present a challenge to the accurate measurement of concentration gradients and data interpretation.

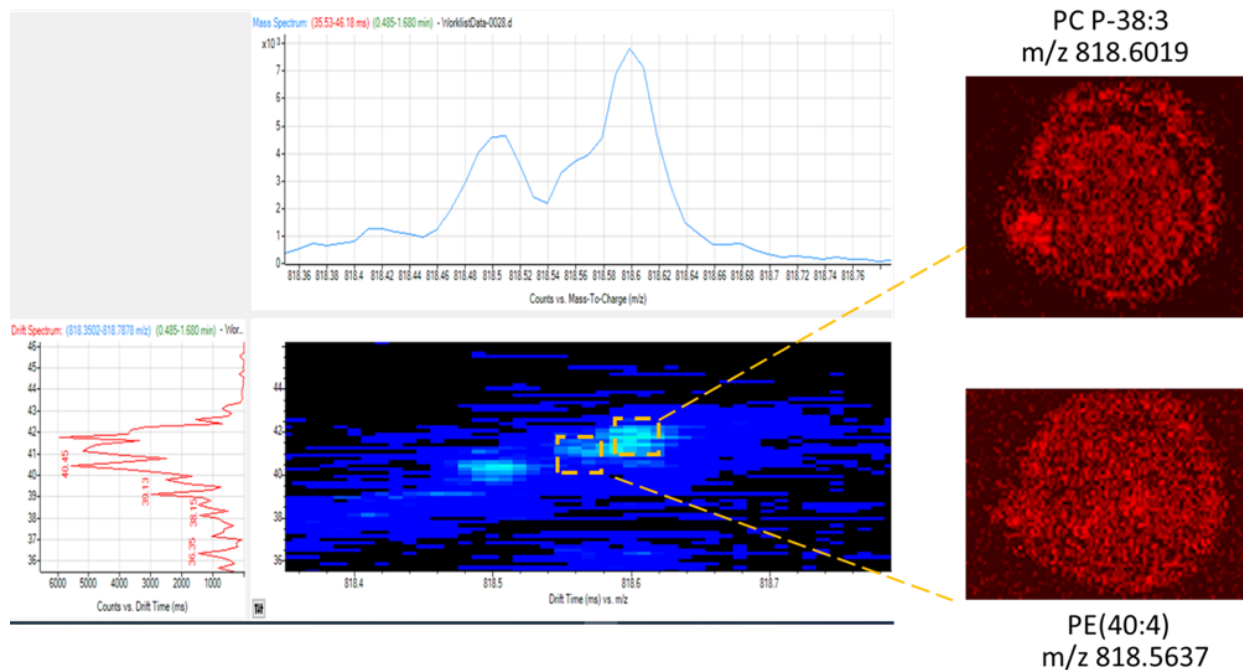


Figure 4.9. Separation of isobaric PE (40:4) from PC (P-38:3) in the 2D IM-MS plot. Drift time-selected ion images generated for each molecule are depicted on the right side.

4.4 Conclusions

In this work, we expanded the analytical capabilities of nano-DESI MSI by successfully coupling it with IM separation, which opens up new opportunities for the spatially-resolved analysis of complex biological samples. An important advantage of our newly developed nano-DESI platform is that it is portable and can be interfaced with any commercial mass spectrometer. Coupling of IM separation with nano-DESI MSI eliminates interferences and enables accurate measurements of concentration gradients of both isomeric and isobaric endogenous molecules extracted from the sample thereby increasing the molecular specificity of MSI. Meanwhile, the CCS values obtained from drift time measurements facilitate the identification of molecules

observed in IM-MSI experiments. Future studies will focus on improving the sensitivity of the IM-MSI experiments to enable the detection of low-abundance species. This may be achieved using multiplexing strategies, which improve the sensitivity of IM experiments at no expense to the throughput. Our first proof-of-concept experiments indicate that the new nano-DESI-IM-MSI platform improves the depth of structural information and accuracy of MSI experiments, which will have a significant impact on biological and clinical research.

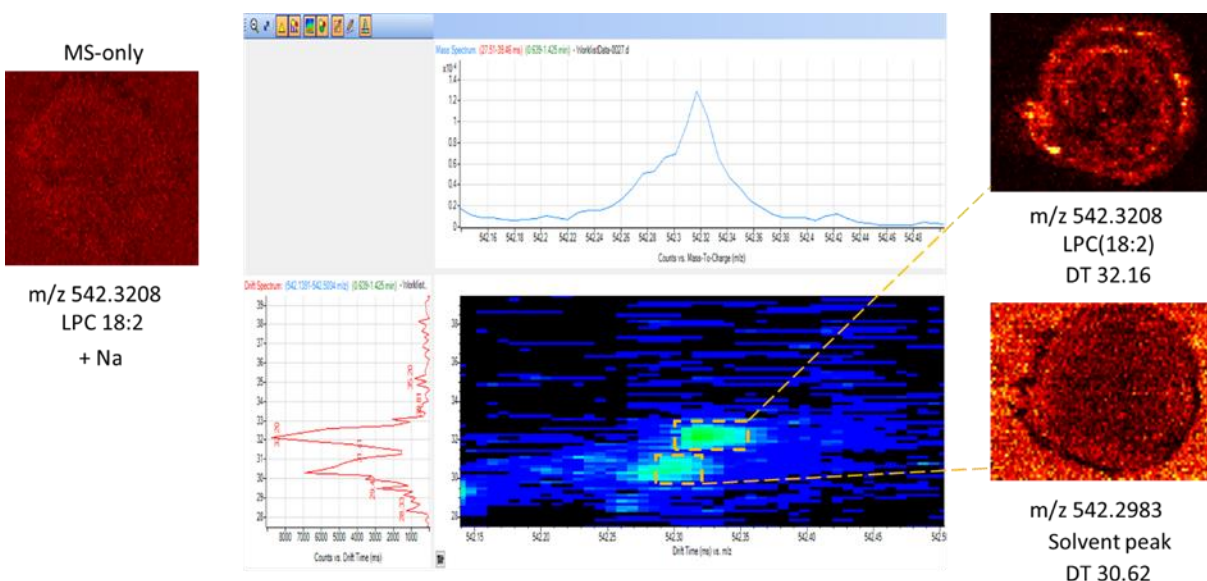


Figure 4.10. 2D IM-MS plot showing the isobaric separation of a solvent peak at DT 30.62 from the endogenous molecule LPC(18:2) at DT 32.16 ms. The ion image corresponding to LPC (18:2) without drift time separation is included on the left side for comparison.

Table 4.4. List of annotations in negative mode nano-DESI-IM-MSI

#	<i>m/z</i> experimental	<i>m/z</i> theoretical	error (ppm)	CCS (Å ²)	Name	Adduct
1	132.0302	132.0302	0.0	120.8	L-Aspartic Acid	-H
2	134.0471	134.0467	-3.1	121.7	Adenine	-H
3	143.0463	143.0468	3.5	141.9	L-4-Hydroxyglutamine	-H
4	145.0621	145.0613	-5.4	128.7	L-Glutamine	-H
5	146.0460	146.0453	-4.6	125.3	L-Glutamate	-H
6	151.0260	151.0250	-6.6	121.8	Xanthine	-H
7	152.9961	152.9953	-5.3	124.3	Propanoyl phosphate	-H
8	154.0622	154.0617	-3.6	129.4	Histidine	-H
9	161.0629	161.0627	-1.2	128.9	FA(10:5)	-H
10	167.0217	167.0205	-7.1	127.3	Uric acid	-H
11	171.0074	171.0059	-9.1	128.4	D-Glycerol 1-phosphate	-H
12	175.0250	175.0240	-5.7	129.4	Ascorbic Acid	-H
13	212.0033	212.0028	-2.4	144.3	indoxyul sulfate	-H
14	214.0484	214.0481	-1.6	143.0	Glycerylphosphorylethanolamine	-H
15	227.2020	227.2017	-1.3	164.0	FA(14:0)	-H
16	241.0130	241.0113	-6.9	129.5	Inositol cyclic phosphate	-H
17	245.0433	245.0426	-2.7	147.0	Phosphatidyl glycerol	-H
18	253.2179	253.2173	-2.4	169.6	FA(16:1)	-H
19	255.2340	255.2330	-3.9	171.0	FA(16:0)	-H
20	259.0230	259.0219	-4.3	147.2	D-Glucose 6-phosphate	-H
21	267.0738	267.0729	-3.2	158.9	Inosine	-H
22	277.2181	277.2173	-2.9	176.7	FA(18:3)	-H
23	279.2336	279.2330	-2.1	177.0	FA(18:2)	-H
24	281.2499	281.2486	-4.6	177.4	FA(18:1)	-H
25	283.2650	283.2643	-2.5	178.4	FA(18:0)	-H
26	293.2122	293.2117	-1.8	176.6	9-OxoODE	-H
27	295.2282	295.2273	-3.0	178.8	(±)9-HODE	-H
28	297.2427	297.2430	0.9	179.5	9-hydroxy-12Z-octadecenoic acid	-H
29	300.0456	300.0484	9.5	159.4	N-Acetyl-α-D-glucosamine 1-phosphate	-H
30	303.2340	303.2330	-3.3	183.7	FA(20:4)	-H
31	305.0695	305.0670	-8.2	136.8	Glutathione, oxidized	-2H
32	305.2493	305.2486	-2.3	184.3	FA(20:3)	-H
33	306.0769	306.0760	-3.0	162.9	Glutathione	-H
34	307.2650	307.2643	-2.3	184.7	FA(20:2)	-H
35	319.2286	319.2273	-4.0	183.3	(±)15-HETE	-H
36	321.2433	321.2430	-1.1	186.0	(±)5-HETrE	-H

Table 4.4 continued

37	322.0452	322.0440	-3.7	165.6	Cytidine 2'-phosphate	-H
38	323.0293	323.0280	-3.9	162.6	Uridine monophosphate (UMP) C ₉ H ₁₃ N ₂ O ₉ P	-H
39	323.2591	323.2586	-1.5	187.6	15(S)-HEDE	-H
40	327.2339	327.2330	-2.8	190.8	FA(22:6)	-H
41	329.2495	329.2486	-2.7	191.4	FA(22:5)	-H
42	331.2652	331.2643	-2.7	191.0	FA(22:4)	-H
43	333.2789	333.2793	1.3	191.7	FA(22:3)	-H
44	343.2285	343.2273	-3.5	190.1	(±)11-HDoHE	-H
45	344.0321	344.0329	2.3	170.1	Cyclic-GMP	-H
46	345.2441	345.2435	-1.7	191.3	FA(22:5)-OH	-H
47	346.0567	346.0553	-4.2	174.3	Adenosine monophosphate	-H
48	347.0431	347.0393	-11.0	172.2	Inosine 5'-monophosphate (IMP)	-H
49	347.2597	347.2592	-1.4	193.9	FA(22:4)-OH	-H
50	357.2805	357.2799	-1.7	198.0	FA(24:5)	-H
51	359.2958	359.2956	-0.6	198.2	FA(24:4)	-H
52	362.0514	362.0502	-3.4	170.5	Guanosine 3'-phosphate	-H
53	363.3278	363.3269	-2.5	197.8	FA(24:2)	-H
54	365.3433	365.3425	-2.2	198.8	FA(24:1)	-H
55	375.2147	375.2171	6.5	192.4	Resolvin D1	-H
56	377.2346	377.2328	-4.8	194.6	C22-PGF4alpha	-H
57	402.9952	402.9944	-2.1	173.2	Uridine diphosphate (UDP)	-H
58	409.2353	409.2361	2.0	201.3	LPA(16:0)	-H
59	426.0236	426.0216	-4.7	184.3	ADP	-H
60	445.0540	445.0526	-3.3	189.4	CDP-ethanolamine	-H
61	452.2827	452.2783	-9.7	211.1	LPE(16:0)	-H
62	478.2946	478.2939	-1.5	216.1	LPE(18:1)	-H
63	480.3110	480.3096	-2.9	219.3	LPE(18:0)	-H
64	500.2797	500.2783	-2.8	218.3	LPE(20:4)	-H
65	509.2906	509.2885	-4.1	222.5	LPG(18:1)	-H
66	522.2817	522.2838	4.0	222.8	LPS(18:1)	-H
67	524.2799	524.2783	-3.1	222.5	LPE(22:6)	-H
68	524.3000	524.2994	-1.1	228.3	LPS(18:0)	-H
69	544.2710	544.2681	-5.3	228.0	LPS(20:4)	-H
70	555.2774	555.2729	-8.1	228.4	LPG(22:6)	-H
71	565.0486	565.0472	-2.5	208.8	UDP-glucose	-H
72	568.2695	568.2681	-2.5	231.2	LPS(22:6)	-H
73	599.3225	599.3202	-3.8	240.7	LPI(18:0)	-H
74	606.0757	606.0737	-3.2	224.1	Uridine diphosphate-N- acetylglucosamine	-H
75	611.1455	611.1441	-2.2	218.6	oxidized glutathione	-H
76	619.2917	619.2889	-4.5	241.6	LPI(20:4)	-H

Table 4.4 continued

77	747.5200	747.5182	-2.4	275.1	PG(34:1)	-H
78	762.5139	762.5079	-7.9	276.6	PE 38:06	-H
79	764.5262	764.5236	-3.4	276.6	PE(38:5)	-H
80	766.5408	766.5392	-2.1	276.9	PE 38:04	-H
81	773.5359	773.5338	-2.7	281.4	PG(36:2)	-H
82	786.5313	786.5291	-2.8	282.7	PS(36:2)	-H
83	788.5476	788.5447	-3.7	284.1	PS(36:1)	-H
84	790.5494	790.5490	-0.5	283.5	PE 40:06	-H
85	793.5103	793.5025	-9.8	285.5	PG(38:6)	-H
86	795.5201	795.5182	-2.4	287.2	PG(38:5)	-H
87	810.5311	810.5291	-2.5	286.4	PS(38:4)	-H
88	812.5446	812.5447	0.1	287.1	PS(38:3)	-H
89	817.5073	817.5025	-5.9	288.7	PG(40:8)	-H
90	819.5215	819.5182	-4.0	289.9	PG(40:7)	-H
91	821.5375	821.5338	-4.5	290.8	PG(40:6)	-H
92	833.5190	833.5186	-0.5	288.5	PI(34:2)	-H
93	834.5318	834.5291	-3.2	290.4	PS(40:6)	-H
94	835.5358	835.5342	-1.9	290.4	PI(34:1)	-H
95	836.5434	836.5447	1.6	290.7	PS(40:5)	-H
96	838.5613	838.5604	-1.1	292.1	PS(40:4)	-H
97	857.5218	857.5186	-3.7	292.3	PI(36:4)	-H
98	858.5253	858.5291	4.4	292.6	PS(42:8)	-H
99	859.5320	859.5342	2.6	292.3	PI(36:3)	-H
100	861.5516	861.5499	-2.0	294.5	PI(36:2)	-H
101	862.5578	862.5604	3.0	295.0	PS(42:6)	-H
102	865.5056	865.5025	-3.6	296.3	PG(44:12)	-H
103	867.5200	867.5182	-2.1	296.9	PG(44:11)	-H
104	869.5410	869.5338	-8.3	297.7	PG(44:10)	-H
105	881.5227	881.5186	-4.7	296.6	PI(38:6)	-H
106	883.5368	883.5342	-2.9	296.5	PI(38:5)	-H
107	885.5534	885.5499	-4.0	298.1	PI(38:4)	-H
108	887.5618	887.5655	4.2	298.4	PI(38:3)	-H

Table 4.5. List of annotations in positive mode nano-DESI-IM-MSI

#	m/z experimental	m/z theoretical	error (ppm)	CCS (\AA^2)	Name	Adduct
1	136.0478	136.0482	2.9	135.1	Creatinine	+ Na
2	140.0679	140.0687	6.0	133.4	valine	+ Na
3	148.0031	148.0039	5.4	139.6	Taurine	+ Na
4	154.0583	154.0592	6.1	137.0	Creatine	+ Na
5	154.083	154.0844	9.0	141.6	L-Leucine	+ Na
6	156.0418	156.0427	5.6	129.0	betaine	+ K
7	160.1325	160.1338	7.8	133.5	3-amino-octanoic acid	+ H
8	162.1119	162.1130	6.8	132.3	Carnitine	+ H
9	166.0852	166.0868	9.6	139.6	L-Phenylalanine	+ H
10	169.0576	169.0584	4.4	132.7	L-Glutamine	+ Na
11	169.9853	169.9855	1.1	141.9	Iminoaspartic acid	+ K
12	170.0319	170.0332	7.5	133.7	Creatine	+ K
13	175.1181	175.1195	8.0	135.4	L-Arginine	+ H
14	176.0656	176.0671	8.7	144.0	Guanidinosuccinic Acid	+ H
15	182.057	182.0583	7.1	136.2	Proline betaine	+ k
16	184.0939	184.0950	5.8	146.7	Carnitine	+ Na
17	188.0678	188.0687	5.0	140.2	L-Phenylalanine	+ Na
18	195.0026	195.0034	4.3	137.4	Glycerol 2-phosphate	+ Na
19	200.0678	200.0689	5.5	144.0	Carnitine	+ K
20	203.0523	203.0526	1.5	148.2	α -D-Glucose	+ Na
21	204.1224	204.1230	2.9	142.7	CAR(2:0)	+ H
22	207.0137	207.0141	1.9	140.1	Phospho-L-serine	+ Na
23	207.9973	207.9987	6.7	141.4	O-Phosphoserine	+ Na
24	219.0259	219.0265	2.9	145.7	α -D-Glucose	+ K
25	226.1051	226.1050	-0.4	157.0	CAR(2:0)	+ Na
26	238.0441	238.0456	6.5	147.4	Glycerylphosphoryleth anolamine	+ Na
27	240.1214	240.1212	-1.0	161.9	Propionyl-L-carnitine	+ Na
28	242.0781	242.0789	3.3	154.9	CAR(2:0)	+ K
29	246.1802	246.1818	6.3	157.6	Lysyl-Valine	+ H
30	254.0181	254.0196	5.8	148.2	Glycerylphosphoryleth anolamine	+ K
31	254.1351	254.1363	4.7	167.5	Butyryl-L-carnitine	+ Na
32	258.1097	258.1106	3.6	155.4	Glycerophosphocholine	+ H
33	266.15	266.1512	4.5	164.5	Lysyl-Proline	+ Na
34	280.0919	280.0926	2.5	158.5	Glycerophosphocholine	+ Na
35	282.1457	282.1430	-9.7	168.1	leucil-glutamine	+ Na

Table 4.5 continued

36	284.1252	284.1264	4.3	172.3	pivaloylcarnitine/ 2-Methylbutyroylcarnitine	+ K
37	291.0695	291.0705	3.6	170.7	Inosine	+ Na
38	296.0657	296.0665	2.8	160.3	Glycerophosphocholine	+ K
39	307.0437	307.0445	2.5	169.7	Inosine	+ K
40	316.9822	316.9803	-5.9	158.3	2-Deoxy-D-ribose 1,5-bisphosphate	+ Na
41	325.2119	325.2143	7.3	190.1	FA 20:5	+ Na
42	327.2278	327.2300	6.6	181.2	FA 20:4	+ Na
43	332.9558	332.9543	-4.6	159.0	2-Deoxy-D-ribose 1,5-bisphosphate	+ K
44	341.2434	341.2456	6.6	183.6	Allopregnanolone	+ Na
45	353.244	353.2451	3.0	183.6	FA 22:5	+ Na
46	355.2584	355.2613	8.1	190.4	FA 22:4	+ Na
47	365.2443	365.2458	4.1	184.1	3-oxo-eicosanoic acid	+ K
48	367.2027	367.2033	1.7	185.7	FA 22:6	+ K
49	367.2587	367.2614	7.5	185.8	3R-hydroxy-eicosanoic acid	+ K
50	369.2392	369.2407	4.1	195.7	MG(16:0)	+ K
51	373.2107	373.2139	8.6	188.9	MG O-18:5	+ K
52	377.2653	377.2668	3.9	193.5	MG(18:2)	+ Na
53	378.2949	378.2984	9.3	201.8	N-palmitoyl valine	+ Na
54	379.2834	379.2824	-2.6	197.5	MG(18:1)	+ Na
55	393.2386	393.2406	5.1	196.3	MG(18:2)	+ K
56	395.2549	395.2564	3.7	198.5	MG(18:1)	+ K
57	395.2762	395.2797	8.8	200.4	15-HETE-G	+ H
58	397.2706	397.2720	3.5	204.4	MG(18:0)	+ K
59	400.3417	400.3421	1.0	212.7	CAR(16:0)	+ H
60	401.2653	401.2668	3.6	197.7	MG(20:4)	+ Na
61	403.281	403.2824	3.5	199.4	MG(20:3)	+ Na
62	408.2867	408.2880	3.1	214.9	Arachidoyl glycine	+ K
63	417.2379	417.2406	6.4	201.3	MG(20:4)	+ K
64	419.2555	419.2562	1.8	202.5	MG(20:3)	+ K
65	425.2634	425.2668	7.9	199.0	MG(22:6)	+ Na
66	427.2796	427.2824	6.6	200.4	MG(22:5)	+ Na
67	429.2966	429.2981	3.4	205.4	MG(22:4)	+ Na
68	441.2349	441.2382	7.4	201.4	MG(22:6)	+ K
69	443.2503	443.2538	8.0	203.9	MG(22:5)	+ K
70	445.2694	445.2719	5.6	207.9	MG(22:4)	+ K
71	457.2344	457.2332	-2.7	203.5	15-HETE-G	+ K
72	518.3212	518.3222	2.0	232.1	LPC 16:0	+ Na

Table 4.5 continued

73	534.2952	534.2962	1.8	234.2	LPC 16:0	+ K
74	542.3208	542.3222	2.7	232.1	LPC 18:2	+ Na
75	544.3391	544.3379	-2.2	234.0	LPC 18:1	+ Na
76	546.3524	546.3535	2.1	239.5	LPC 18:0	+ Na
77	548.274	548.2753	2.4	230.5	LPE 22:6	+ Na
78	562.3261	562.3275	2.5	240.9	LPC 18:0	+ K
79	576.2693	576.2686	-1.3	229.2	Vignatic acid A	+ Na
80	592.2477	592.2425	-8.8	233.4	Vignatic acid A	+ K
81	615.4946	615.4959	2.1	259.9	DG(34:2)	+ Na
82	631.4707	631.4702	-0.7	253.7	DG(34:2)	+ K
83	641.5098	641.5115	2.6	259.0	DG(36:3)	+ Na
84	643.5258	643.5272	2.2	262.9	DG(36:2)	+ Na
85	657.4831	657.4835	0.6	262.2	DG(36:3)	+ K
86	659.4994	659.5011	2.6	264.7	DG(36:2)	+ K
87	663.4943	663.4959	2.4	268.4	DG(38:6)	+ Na
88	665.505	665.5115	9.8	267.4	DG(38:5)	+ Na
89	667.5258	667.5272	2.1	269.4	DG(38:4)	+ Na
90	672.4199	672.4216	2.6	262.9	PC(16:0/9:0(CHO))	+ Na
91	681.4771	681.4835	9.4	267.8	DG(38:5)	+ K
92	683.4941	683.4991	7.4	268.2	DG(38:4)	+ K
93	689.5099	689.5115	2.3	267.5	DG(40:7)	+ Na
94	691.5224	691.5277	7.7	273.1	DG(40:6)	+ Na
95	693.5374	693.5428	7.8	275.0	DG(40:5)	+ Na
96	703.4706	703.4678	-3.9	270.2	DG(40:8)	+ K
97	703.5746	703.5748	0.3	281.4	SM(d34:1)	+ H
98	705.4845	705.4835	-1.4	269.1	DG(40:7)	+ K
99	725.5557	725.5568	1.5	282.0	SM(d34:1)	+ Na
100	728.5189	728.5206	2.3	280.6	PC a 30:0	+ Na
101	741.5279	741.5307	3.8	286.0	SM(d34:1)	+ K
102	742.5666	742.5726	8.1	287.8	PC e 32:0	+ Na
103	744.4967	744.4945	-2.9	279.3	PC a 30:0	+ K
104	746.508	746.5100	2.7	281.6	PE O-36:5	+ Na
105	754.5344	754.5363	2.5	283.4	PC a 32:1	+ Na
106	754.5344	754.5363	2.5	283.4	PC a 34:4	+ H
107	756.5499	756.5519	2.6	286.8	PC a 32:0	+ Na
108	758.5618	758.5694	10.0	285.8	PC a 34:2	+ H
109	760.5833	760.5856	3.0	287.9	PC a 34:1	+ H
110	762.4974	762.5050	9.9	280.6	PE a 36:4	+ Na
111	768.5498	768.5519	2.7	286.6	PE a 36:1	+ Na
112	768.5498	768.5519	2.7	286.6	PE a 38:4	+ H
113	768.5865	768.5883	2.3	293.3	PC P-36:3	+ H
114	770.509	770.5100	1.3	285.0	PC a 32:1	+ K

Table 4.5 continued

115	772.525	772.5257	0.9	287.2	PC a 32:0	+ K
116	774.5352	774.5413	7.9	287.2	PE P-38:4	+ Na
117	778.5358	778.5363	0.6	286.6	PC a 34:3	+ Na
118	778.5358	778.5363	0.6	286.6	PC a 36:6	+ H
119	780.5503	780.5519	2.1	288.6	PC a 34:2	+ Na
120	780.5503	780.5519	2.1	288.6	PC a 36:5	+ H
121	782.5658	782.5676	2.2	290.6	PC a 34:1	+ Na
122	784.5759	784.5832	9.3	291.2	PC a 34:0	+ Na
123	786.4988	786.5049	7.8	284.4	PE a 38:6	+ Na
124	786.5975	786.6013	4.8	293.9	PC a 36:2	+ H
125	788.5591	788.5570	-2.7	290.4	PC(P-36:4)	+ Na
126	790.5339	790.5362	3.0	288.1	PE a 38:4	+ Na
127	790.5688	790.5726	4.8	293.1	PC P-38:6	+ H
128	796.5215	796.5257	5.2	288.7	PC a 34:2	+ K
129	796.5786	796.5832	5.8	291.0	PE 38:1	+ Na
130	798.5397	798.5413	2.0	291.1	PC a 34:1	+ K
131	802.5345	802.5363	2.2	288.8	PC a 38:8	+ H
132	804.488	804.4945	8.1	288.6	PE a 38:5	+ K
133	804.5503	804.5519	2.0	292.1	PC a 38:7	+ H
134	806.5084	806.5102	2.2	288.3	PE a 38:4	+ K
135	806.5633	806.5676	5.3	292.4	PC a 38:6	+ H
136	808.5807	808.5832	3.1	294.4	PC a 38:5	+ H
137	810.5963	810.5988	3.1	295.6	PC a 36:1	+ Na
138	812.5202	812.5206	0.5	288.1	PE a 40:7	+ Na
139	812.5583	812.5571	-1.4	295.8	PC P-38:6	+ Na
140	812.6097	812.6145	5.9	296.8	PC a 36:0	+ Na
141	814.5326	814.5362	4.5	291.1	PE a 40:6	+ Na
142	814.5699	814.5726	3.4	295.5	PC P-38:5	+ Na
143	816.5476	816.5519	5.3	292.6	PE a 40:5	+ Na
144	816.5884	816.5883	-0.1	297.2	PC P-38:4	+ Na
145	816.5884	816.5883	-0.1	297.2	PC P-40:7	+ H
146	818.5097	818.5100	0.4	288.7	PC a 36:5	+ K
147	818.5637	818.5675	4.7	294.5	PE a 40:4	+ Na
148	818.5637	818.5675	4.7	294.5	PE a 42:7	+ H
149	818.6019	818.6039	2.5	298.0	PC P-38:3	+ Na
150	818.6019	818.6039	2.5	298.0	PC P-40:6	+ H
151	820.5236	820.5257	2.5	291.9	PC a 36:4	+ K
152	822.5372	822.5413	5.0	292.6	PC a 36:3	+ K
153	824.5544	824.5570	3.1	294.7	PC a 36:2	+ K
154	826.5699	826.5726	3.3	296.6	PC a 36:1	+ K
155	828.5498	828.5519	2.5	234.5	PC a 38:6	+ Na
156	828.5498	828.5519	2.5	293.9	PC a 40:9	+ H

Table 4.5 continued

157	830.559	830.567	9.6	295.2	PC a 38:5	+ Na
158	832.5802	832.5832	3.6	232.9	PC a 40:7	+ H
159	832.5802	832.5832	3.6	297.5	PC a 38:4	+ Na
160	834.5947	834.5988	5.0	298.3	PC a 40:6	+ H
161	835.6589	835.6663	8.9	304.0	SM(d42:2)	+ Na
162	836.6096	836.6145	5.9	299.3	PC a 40:5	+ H
163	842.5965	842.6034	8.2	299.8	PC P-40:5	+ Na
164	844.5249	844.5257	0.9	294.1	PC a 38:6	+ K
165	844.6162	844.6191	3.4	302.2	PC P-40:4	+ Na
166	844.6162	844.6191	3.4	302.2	PC P-42:7	+ H
167	846.5325	846.541	10.0	295.7	PC a 38:5	+ K
168	848.555	848.5570	2.3	298.1	PC a 38:4	+ K
169	850.5656	850.5726	8.3	298.6	PC a 38:3	+ K
170	856.5757	856.5832	8.8	299.5	PC a 42:9	+ H
171	858.594	858.6007	7.8	301.0	PC a 42:8	+ H
172	860.6103	860.6164	7.1	302.8	PC a 42:7	+ H
173	868.5189	868.5258	8.0	296.7	PC a 40:8	+ K
174	870.536	870.5415	6.3	298.8	PC a 40:7	+ K
175	872.5506	872.5571	7.5	300.7	PC a 40:6	+ K
176	880.5669	880.5622	-5.3	301.8	PC P-42:8	+ K

CHAPTER 5. MULTIMODAL WORKFLOW FOR HIGH-RESOLUTION IMAGING OF INDIVIDUAL SKELETAL MUSCLE FIBERS USING NANO-DESI MSI

5.1 Introduction

Skeletal muscle plays a primary role in human function enabling locomotion, maintenance of posture, metabolic homeostasis, and respiration.¹⁶⁹ The contractile muscle cells also known as muscle fibers, are responsible for the wide array of capabilities that a muscle displays. Muscle fibers are generally classified according to their speed of contraction into two major groups: slow-twitch (type I) and fast-twitch fibers (type II).¹⁷⁰ Type I are fatigue resistant and therefore used in long-lasting activities. In contrast, type II fibers fatigue quickly and therefore are mainly used for sudden bursts of energy. A subtype classification uses myosin as the common molecular motor present in all fiber types to differentiate them based on their shortening velocity. Skeletal muscles in mammals express four major myosin heavy chain (MyHC): type I, type IIa, type IIx and type IIb.¹⁷¹ Another classification of fibers into oxidative/aerobic or glycolytic/anaerobic types accounts for the metabolic pathway through which they generate ATP.¹⁷² The diversity that myofibers display is a result of the combination of different metabolic, contractile and physiological properties. Based on these properties, myofibers are classified as slow-oxidative (type I), fast-oxidative-glycolytic (type IIa), fast-glycolytic (type IIb) and fast-intermediate (type IIX).^{173,174} Understanding of the chemical composition of muscle fibers and how it is linked to their biochemical and contractile properties provides the basis for an optimal design of physical therapies intervention and treatments targeting a wide variety of muscle-related pathologies including sarcopenia,¹⁷⁵ metabolic syndrome¹⁷⁶ among others.

Skeletal muscle fibers are heterogeneously localized in the muscle in a mosaic-like pattern making it difficult to examine their molecular signatures. Metabolic profiling of skeletal muscle fibers typically involves liquid chromatography mass spectrometry (LC-MS) analysis of tissue extracts from a representative muscle enriched in a specific fiber type.^{177,178} However, this approach does not provide information on the chemical gradients in the muscle tissue and fiber-specific molecular markers. Other strategies such as histochemical staining provide localization of some lipid classes but cannot identify individual lipid or metabolite species.

Mass spectrometry imaging (MSI) is a powerful label-free technique that enables the visualization of molecular distributions across biological samples.¹²⁸ In contrast to traditional staining approaches, MSI provides spatial maps of hundreds of compounds in a single experiment. Matrix Assisted Laser Desorption Ionization (MALDI) has been so far the only ionization technique used for imaging of bundles of muscle fibers of different types.^{81,82,176,179,180} Although these studies provided important insights into biochemical processes in muscle metabolism, visualization of individual muscle fibers necessary to address muscle heterogeneity has not been reported. Characterization of myofiber-specific metabolic changes at a single myofiber level requires a spatial resolution of better than 20 μm to differentiate among different fiber types that coexist within the same bundle. In one study, high-resolution MALDI MSI was used for the visualization of individual fibers using a smaller laser spot size at the expense of metabolite signals thereby highlighting challenges associated with molecular characterization of skeletal muscle fibers.¹⁸¹

Nanospray Desorption Electrospray Ionization (nano-DESI) enables imaging of biological tissues with high spatial resolution.²¹ The spatial resolution of nano-DESI MSI experiments is mainly determined by the size of the liquid bridge formed between the nano-DESI probe and sample surface. A spatial resolution of 10 micron has been achieved using a nano-DESI probe composed of two finely pulled capillaries.³⁴ High spatial resolution nano-DESI MSI experiments have been used for imaging of lipids and metabolites in small tissue samples including pancreatic islets ($\sim 100\ \mu\text{m}$ diameter),⁴⁶ lung airways ($\sim 50\ \mu\text{m}$ diameter),³² and mouse uterine tissues ($\sim 1000\ \mu\text{m}$ diameter),^{34,182} which cannot be achieved with moderate spatial resolution.

Herein, we used high resolution nano-DESI MSI for imaging of individual skeletal muscle fibers that have a diameter of $\sim 30\text{-}50\ \mu\text{m}$. Because the fibers are distributed in a mosaic-like pattern and chemical gradients between different fiber types are fairly shallow, this tissue represents one of the most challenging systems for MSI experiments. We used immunofluorescence (IF) imaging to distinguish between different types of fibers in mouse muscle tissues. IF images were subsequently used as roadmaps for identifying molecular signatures of different fiber types based on nano-DESI MSI experiments. Because of the lack of major anatomical or molecular markers in this system, image registration between IF and nano-DESI MSI is particularly challenging. Furthermore, high spatial resolution imposes additional constraints on the accuracy of image registration, which must be performed with $\sim 1\ \mu\text{m}$ accuracy. To address these challenges, we have

developed a robust computational method for image registration and extraction of ion abundances from well-defined regions of interest (ROIs) and performed relative quantification across different fiber types guided by IF imaging data. Using this approach, we identified groups of molecules that are enhanced, but not exclusively present in specific fibers. Our results indicate a relatively shallow variation in chemical gradients across different fiber types from oxidative (type I) to glycolytic fibers (type IIb).

5.2 Materials and methods

5.2.1 Chemicals

LC-MS grade methanol (MeOH) and LC-MS water were purchased from Sigma-Aldrich (St. Louis, MO). Lipid standards lyso-phosphatidylcholine (LPC) 19:0, lyso-phosphatidylethanolamine (LPE) 17:1, lyso-phosphatidylglycerol (LPG) 17:1, lyso-phosphatidylserine (LPS) 17:1 and lyso-phosphatidylinositol (LPI) 17:1 were purchased from Avanti Polar Lipids (Alabaster, AL). Arachidonic Acid (AA)-d8 standard was purchased from Cayman (Ann Arbor, MI).

Primary antibodies used for fiber types staining were purchased from Developmental Studies Hybridoma Bank (DSHB) (Iowa City, IA): Myh7 MyHC-1 (BA-F8) for type I fiber, Myh2 MyHC-2A (2F7) for type IIA fiber, and Myh4 MyHC-2B (10F5) for type IIB fiber. Secondary antibodies used in the staining were purchased from Thermo Fisher Scientific (Waltham, MA): goat anti-mouse IgG1, Alexa Fluor 568 (A-21124); goat anti-mouse IgG2b, Alexa Fluor 647 (A-21242); goat anti-mouse IgM, Alexa Fluor 488 (A-210420).

5.2.2 Tissue sectioning and handling

C57BL/6 mice (X month old) used in this study were originally obtained from Jackson Laboratory (Bar Harbor, ME) and maintained in the animal facility with free access to standard rodent chow and water. All the procedures involving mice were approved by the Purdue University Animal Care and Use Committee (Protocol# 1112000440). Whole gastrocnemius muscle was dissected and frozen immediately in liquid nitrogen. Frozen muscle was fixed on Optimal cutting temperature compound (OCT compound) with 60% of the tissue intact from OCT compound. The muscle was cross-sectioned with a thickness of 12 μm using a Leica CM1850 cryostat.

5.2.3 Immunofluorescence staining

Gastrocnemius sections were directly incubated in a blocking buffer (5% goat serum, 2% bovine serum albumin, 0.1% Triton X-100 and 0.1% sodium azide in PBS) for 1 h at room temperature. Samples were then incubated with primary antibodies diluted in the blocking buffer overnight at 4 °C. After washing with PBS, the samples were incubated with secondary antibodies for 1 h at room temperature. IF images were captured using a Leica DM 6000B microscope with a x 20 objective and merged by Photoshop software.

5.2.4 Nano-DESI experiments

Nano-DESI MSI experiments were carried out on a Q-Exactive HF-X Orbitrap mass spectrometer from Thermo Fisher Scientific (Waltham, MA) using a custom-designed nano-DESI source.^{32,65} The high-resolution nano-DESI probe was assembled by forming a $\sim 90^\circ$ angle between two finely pulled capillaries with o.d. $\sim 20\ \mu\text{m}$: the primary and nanospray capillaries. A third finely pulled capillary was placed next to the nano-DESI probe to serve as a shear force probe. Detailed explanation of the preparation of the primary, nanospray and shear force capillaries and their assembling can be found in our previous work.³⁴ A working nano-DESI solvent of MeOH:H₂O (9:1) (v/v) was used as the extraction solvent and was infused using a syringe pump at $0.5\ \mu\text{L}/\text{min}$. Ionization was achieved by applying a 4 kV potential to the syringe needle. The heated capillary inlet was held at 30 V and 250 °C.

In all the experiments performed in this study, we used a scan rate of $10\ \mu\text{m}/\text{s}$, a step between the lines of $15\ \mu\text{m}$ and an acquisition rate of 7 Hz resulting in an average pixel size of $0.7\ \mu\text{m} \times 15\ \mu\text{m}$. The spatial resolution was calculated to be $6\ \mu\text{m}$ using the 20/80 rule as shown in Figure 5.2. Both positive and negative mode MSI data were acquired for each biological replicate ($n=3$) over a mass range of m/z 133-2000 using a mass resolution of 60,000 at m/z 200. MS/MS data for most of the endogenous species observed in nano-DESI MSI experiments were acquired directly from tissue sections using the data dependent MS/MS mode at a normalized collision energy of 25 V and mass isolation window of $0.5\ m/z$.

5.2.5 Data processing

MS data from nano-DESI experiments were acquired as .RAW files using Xcalibur software (Thermo Electron, Bremen, Germany). To generate ion images, a list of m/z values of interest were firstly selected. Then we used a custom Python script (<https://github.com/LabLaskin/MSI-image-generator>) to generate ion images from .RAW files. We used a mass window of 10 ppm to extract peak intensities and aligned MS signals with respect to the acquisition time. Peak intensities in images were normalized to total ion current (TIC) in corresponding spectrum to compensate the signal fluctuation during the imaging experiments. Ions in the m/z list were annotated by searching against METLIN database (<https://metlin.scripps.edu>) using accurate mass and MS/MS data.

5.2.6 Image registration

Computational image registration was used to correlate the molecular information obtained in MSI experiments with fiber types visualized using immunofluorescence. We used a strategy reported in previous studies.^{183,184} Herein, we regarded the MSI image as a fixed image and immunofluorescence image as a moving image. A linear transformation model was adopted, in which translation and affine transformations were performed in tandem. To optimize the parameters in the transformation model, we selected mutual information as a criterion and adaptive stochastic gradient descent as an optimizer. After the optimal parameters were determined, the linear model was used to transform the moving immunofluorescence image to spatially align to the fixed MSI image. Because the mutual information metric only evaluates intensity correlation between two images with the same dimensions, we converted both MSI and immunofluorescence images into grayscale before registration. For MSI data, we used principal component analysis (PCA) to compress the hyperspectral data into a low-dimensional space while preserving the molecular distribution information in the original high-dimensional data.¹⁸⁴ We further selected 3 PC images to construct a 2D RGB image and converted it into a 2D grayscale image, which reveals the molecular heterogeneity in MSI data. Additional details regarding PCA analysis of nano-DESI MSI data can be found in our previous report.¹⁸⁵

5.2.7 Statistical analysis

Both multivariate and univariate statistics were used for exploratory analysis of muscle biomarkers. Heatmaps of metabolite abundances in different muscle cells were created. MS signals were scaled by a z-score transformation, representing the number of standard deviations from the mean value. To visualize the overall metabolite profile discrepancy (relations) of different muscle cells, a linear discriminant analysis (LDA) was utilized to map mass spectra from muscle cells into a 2D space using registered immunofluorescence images as a guide. In univariate analysis, the difference of metabolite MS signals in distinct muscle cells is analyzed using the volcano plot by plotting a log₂ fold change in abundance versus p-value. Herein, the p-value of one metabolite observed in mass spectra of two types of muscle fibers was calculated using t-test.

5.3 Results

In this study, we performed multimodal imaging of mouse gastrocnemius (GAS) muscle tissues using a combination of IF with nano-DESI MSI to elucidate differences in the chemical composition of different fiber types. Appendix B presents all the annotated species whose identities were confirmed by matching their exact mass with open databases and manual analysis of their MS/MS. GAS muscle tissues contain all four fiber types described earlier (type I, type IIa, type IIx and type IIb) that are not segregated in the tissue making their molecular imaging particularly challenging.

Figure 5.1. shows the results obtained for three biological replicates. For each replicate, we used three adjacent 12 μ m-thick sections: one for IF imaging, one for positive mode, and one for negative mode nano-DESI MSI. Positive and negative mode nano-DESI MSI data are displayed along with the corresponding IF images in Figure 5.1a and 5.1b, respectively. We use IF images as roadmaps of fiber localization as shown in Figure 5.1 and 5.6. A characteristic mosaic pattern of fibers is observed in all the IF images,¹⁸⁶ in which type I fibers are labelled in green, type IIa are labelled in red, type IIx are labelled in black, and type IIb are labelled in blue. As observed in Figure 5.1, GAS tissue displays fiber regionalization in which the greatest proportion of oxidative fibers is found in the deep region closer to the blood supply and glycolytic fibers are mainly found on the edges of the muscle.¹⁸⁷ Despite that, little or no fiber segregation is observed in IF images. The IF data were used to guide nano-DESI experiments to areas where a transition from the deep

region to the surface region of GAS tissue was observed. Representative ion images normalized to the total ion current (TIC) of ions at m/z 856.5830 corresponding to phosphatidylcholine (PC) 40:6 and 622.3716 corresponding to the oxidized PC 22:1;O2 observed in positive and negative mode, respectively, are also shown in Fig. 5.1. These ions correspond to two phospholipids enriched in the deep region of the tissue. It can be observed a good correlation between the pattern observed in the ion images with the IF images. Figure 5.2 shows the calculation of the spatial resolution which is performed by evaluating the chemical gradient of a molecule across a line scan using the 20/80 rule.^{34,160} Our measurements indicate that the spatial resolution of our experiments is about 6 μm , which is the best value reported for nano-DESI MSI so far. High spatial resolution is critical to the visualization of chemical gradients generated by individual muscle fibers.

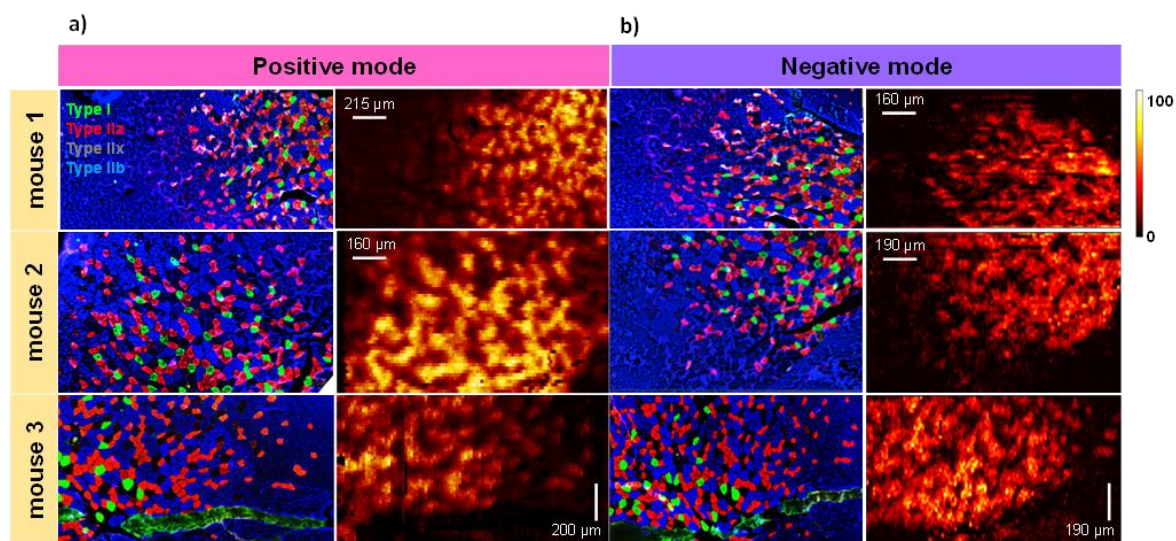


Figure 5.1. Multimodal imaging of skeletal muscle fibers which combines IF imaging with MSI in a) positive mode and b) negative mode. The results are shown for three biological replicates examined in this study. IF images are displayed on the left of ion images showing the distribution of type I (green), type IIa (red), type IIx (black) and type IIb (blue) fibers in GAS. Ion images selected for visualization of fiber patterns are PC 40:6 observed as a $[\text{M}+\text{Na}]^+$ adduct at m/z 856. 5830 and $[\text{M}-\text{H}]^-$ ion of PC 22:1;O2 at m/z 622. 3716 for positive and negative mode nano-DESI MSI, respectively. Scale bars are displayed inside each ion image The color bar is displayed on the right side indicating that the intensity scale changes from black (low) to yellow (high).

Despite the high quality of high-resolution nano-DESI ion images, the complex distribution of muscle fibers observed in Figure 5.1 presents a challenge for feature extraction and image registration to specific fiber types. Although the chemical gradient between the deep region and outer part of the tissue is evident in ion images, the absence of anatomical markers and small

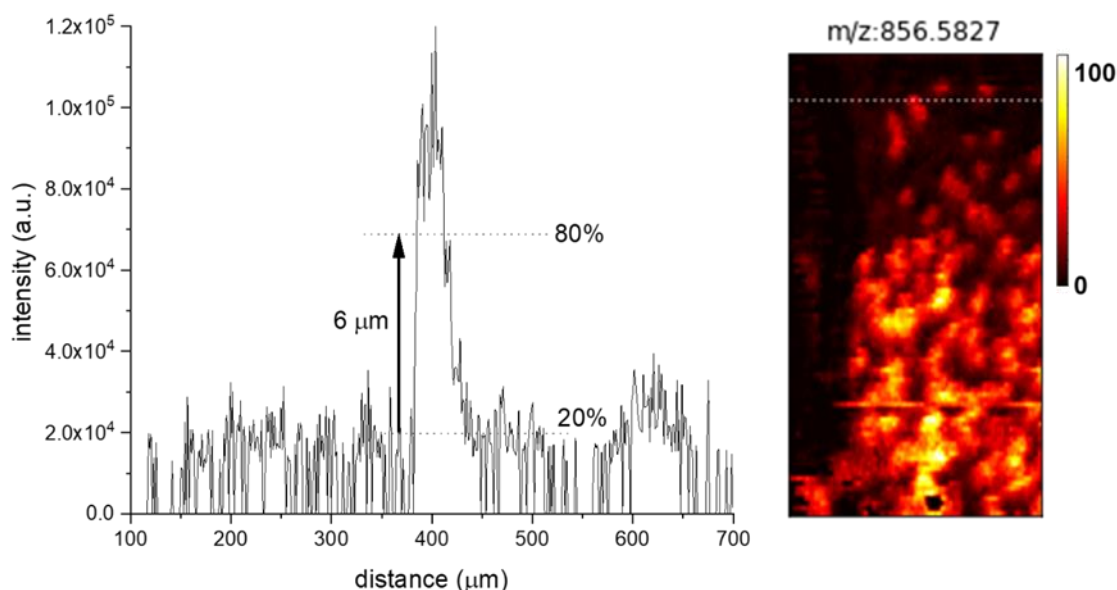


Figure 5.2. Calculation of the spatial registration of the imaging of individual muscle fibers. We use variations on the chemical gradient of a molecule using the 80/20 rule.

dimensions of individual fibers makes it difficult to perform image registration with an accuracy comparable to the spatial resolution of nano-DESI MSI experiments. We solved this problem by developing a robust image registration and segmentation approach which is summarized in Figure 5.3. A yellow box on the optical image of the tissue (Figure 5.3a) marks the region analyzed using nano-DESI MSI. First, the IF image (Figure 5.3b) is cropped to roughly cover the same region. Next, we generate MSI images (Figure 5.3c) using a mass list of peaks. We use principal component analysis (PCA) to reduce data dimensionality of ion images and generate an RGB representation of the chemical gradients in the sample (Figure 5.3d). A grey representation of the IF image is used for the affine registration to the PCA image. Figure 5.4 shows a more detail demonstration of this step in which the IF image is resized and reoriented to align well with the pattern displayed by the PCA image. Next, we perform segmentation of the IF image to obtain fiber type-specific ROIs (Figure 5.3e) using a robust image segmentation approach developed by our group.¹⁸⁵ Finally, the segmented ROI image is registered to the RGB representation image and hence to all the ion images using a stochastic gradient descent algorithm thereby yielding well-defined ROIs specific to each fiber type (Figure 5.3f). A closer view of this step is depicted in Figure 5.5. The segmented ROI image undergoes an erosion process to avoid the extraction of

pixels from fibers located in the vicinity of the fiber of interest (Figure 5.5b). As a result, fiber-specific masks for type I fibers (Figure 5.5c), type IIa fibers (Figure 5.5d), type IIx fibers (Figure 5.5e), and type IIb fibers (Figure 5.5f) are generated which correlate well with the pattern shown by the ion images. The workflow described herein allowed us to extract ion abundances for each fiber type and evaluate differences between their molecular markers (Figure 5.3g).

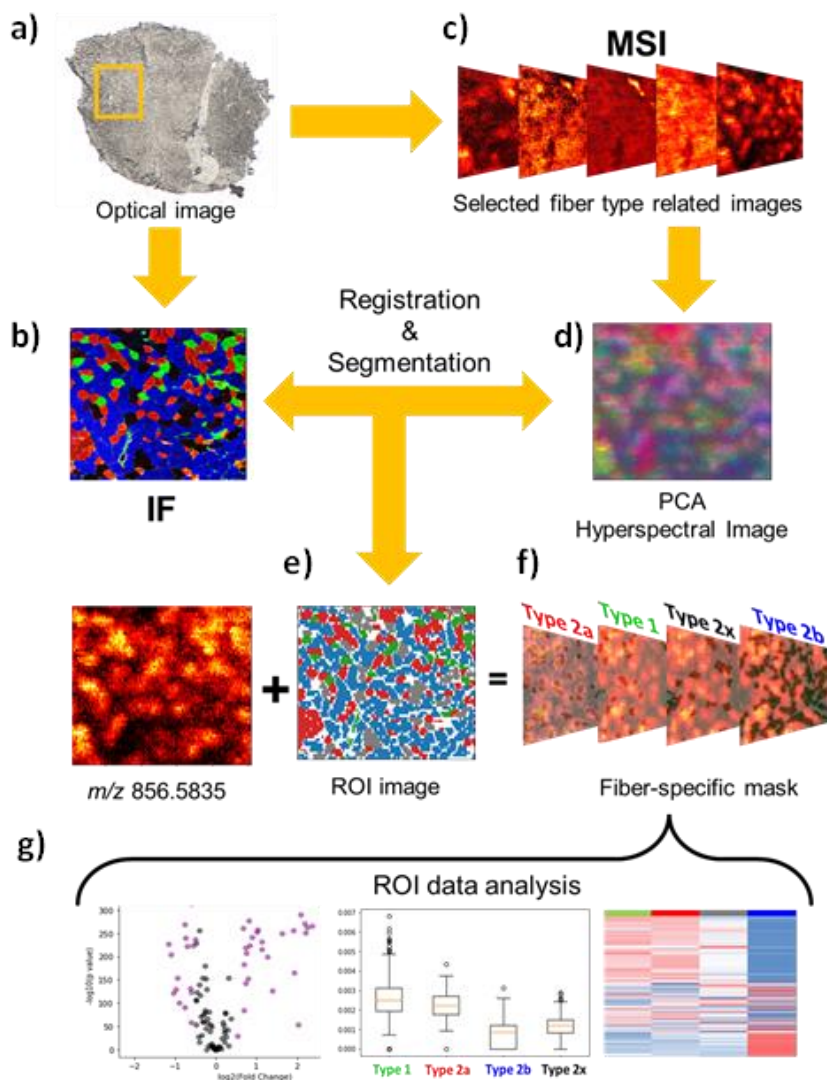


Figure 5.3. Multimodal workflow for nano-DESI MSI of skeletal muscle fibers. a) Optical image of a GAS tissue section. Yellow square indicates the region of the tissue analyzed in the MSI experiment. b) Ion images of tissue-related peaks. c) IF image acquired using an adjacent tissue section cropped to the region analyzed by MSI. d) RGB representation of all ion images using PCA analysis. e) ROI image created from IF segmentation. f) Registration of segmented image to RGB images yields ROI fiber-specific masks that enable feature extraction for each fiber type. g) Data analysis using extracted ion abundances enables comparison of the chemical composition of different fiber types.

Figure 5.6a shows the results of a linear discriminant analysis (LDA) performed on muscle fibers which provided a separation of all the observed m/z features into two big groups. The blue circles corresponding to type IIb fibers are well separated from the rest of the fibers across the LD1 and LD2 axis. In contrast, type I (green circles), type IIa (red circles) and type IIx (black circles) display overlapping regions indicating a greater overlap between the chemical composition of these fibers. These results provide a general overview of all the distribution of the m/z features and their association with specific fiber types.

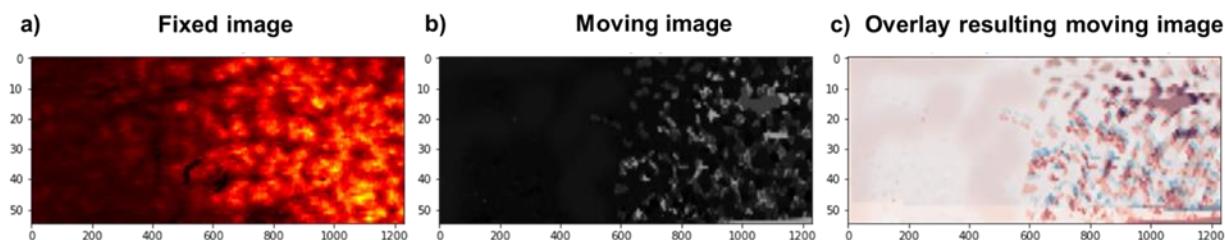


Figure 5.4 Affine registration process. a) Ion image that serves as a fixed image, b) gray scale of an IF image which serves as a moving image. c) The result of the affine registration of the IF image to the ion image.

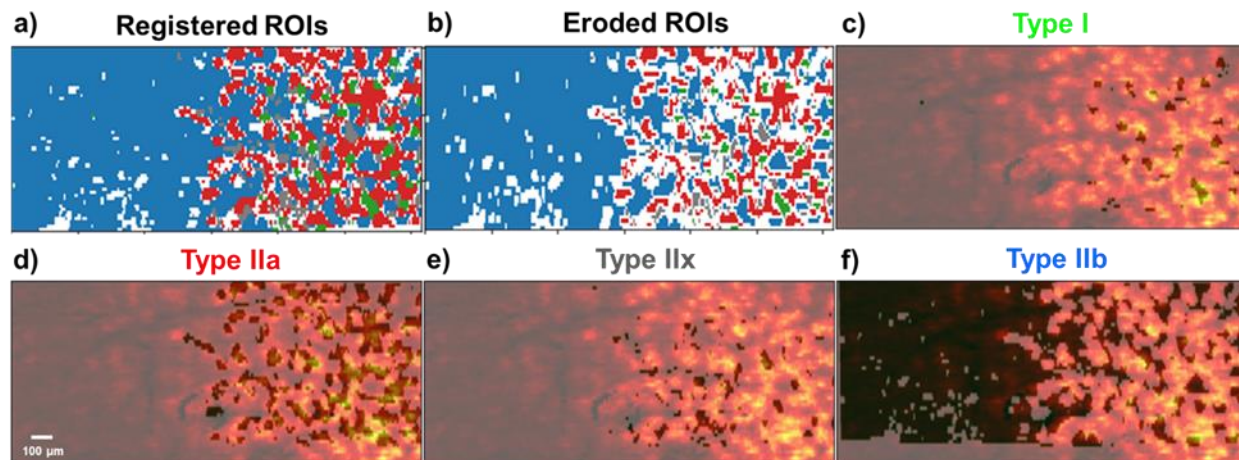


Figure 5.5. a) Segmented IF image. b) Eroded image of a) to eliminate surrounding pixels that might overlap with other fiber types. Fiber-specific mask generated for c) type I, d) type IIa, e) type IIx and f) type IIb are displayed overlapping a representative ion image to show the good match between the mask and fiber pattern.

In this work, we only report molecular markers that were detected in all three replicates and confidently identified using MS/MS. Based on these criteria, we analyzed 140 unique species observed in both positive and negative mode.

For each of these features, we extracted their abundances in all four fiber types and calculated the mean value for each fiber type. Following an approach described in a recent proteomics study where a series of criteria were used to discriminate between specific fiber patterns,¹⁸⁸ we established several criteria for the identification of myofibers based on the high-resolution spatial lipidomics experiments performed in this study. For each feature, we express its mean abundance as a percent of its maximum abundance across the fibers. The relative abundances obtained in this analysis are summarized in Appendix B.

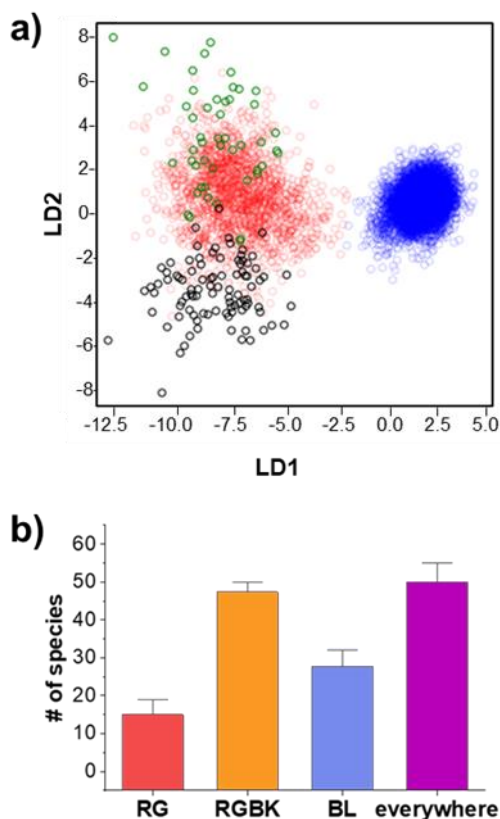


Figure 5.6. a) LDA analysis of all the features identified in GAS tissue in positive mode. Green circles correspond to type I fibers, red circles correspond to type IIa fibers, black circles correspond to type IIx, and blue circles correspond to type IIb fibers. b) Bar graph showing the sorting of species based on their spatial localization. Red-green (RG) corresponds to a molecular distribution enhanced in type I and type IIa fibers. Red-green-black (RGBK) corresponds to a distribution enhanced in type I, type IIa, and type IIx fibers. Blue (BL) corresponds to a distribution enhanced in type IIb fibers. Everywhere pattern indicates a uniform molecular distribution across the tissue.

We then used a series of criteria to discriminate between myofibers. First, we used a fairly stringent criterion for identifying unique fiber-specific markers. We define a unique marker as a species that shows a 2.5-fold change in abundance in one fiber type in comparison with other fibers. This criterion provided only one unique marker of type IIb fibers at m/z 175.0245 corresponding to the $[M-H]^-$ ion of ascorbic acid (Figure 5.7a). Confirmation of the identity of this molecule was performed by comparison with MS/MS reported in the literature.^{189,190} In all three replicates, ion images of m/z 175.0245 show a gradual decrease of the abundance of ascorbate when moving from the more glycolytic region to the more oxidative region of the tissue (Figure 5.7b). No other unique markers for other fiber types have been identified which is consistent with the results of the LDA analysis discussed earlier.

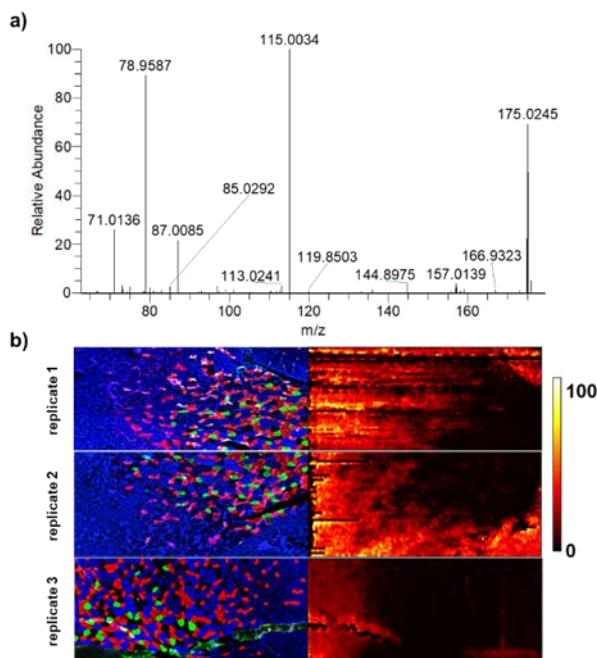


Figure 5.7. a) MS/MS spectrum of m/z 175.0245 identified as ascorbic acid. b) IF and TIC normalized ion images of m/z 175.0245.

Next, we use less stringent criteria to identify groups of molecular markers that display distinct spatial patterns. Based on the most distinct localizations observed in ion images, we identified four patterns that we refer to as red-green (RG), red-green-black (RGBK), blue (BL), and “no pattern”. The RG pattern corresponds to species enhanced in type I and type IIa fibers. Molecules that follow this pattern show a distribution in which their abundance is enhanced by at

least 1.2-fold in type I and IIa fibers in comparison with type IIx and IIb fibers and the intensity ratio between type I and type IIa is less than 1.3. The RGBK pattern describes species enhanced in type I, type IIa, and type IIx fibers. Molecules that were assigned to this pattern have at least 1.2-fold higher abundance in type I, IIa, and IIx fibers in comparison with type IIb fiber and the intensity ratios among type I, IIa, and IIx is less than 1.3. The BL pattern describes species enhanced in type IIb fibers. Because chemical gradients in the glycolytic region are much smoother, we set a criterion that any molecule displaying a higher abundance in type IIb fibers by at least 1.05 in comparison to the other fibers will be assigned to this pattern. Finally, molecules that do not meet any of the criteria described earlier are labelled as ‘everywhere’ indicating that they are uniformly distributed across the tissue. Figure 5.6b shows a bar graph summarizing the results of this analysis. A detailed summary obtained for all the replicates is provided in Appendix B. The RGBK pattern (orange bar) is the most dominant pattern observed for 47 species, followed by the BL (blue bar) with 28 species, and RG (red bar) pattern with 15 species. Interestingly, 50 species (magenta bar) do not display a specific localization across the tissue. None of the molecules observed in nano-DESI MSI data displayed a distinct localization to either type I (green), type IIa (red), or type IIx (black) fibers making it difficult to differentiate between these three fiber types.

We use volcano plots to further uncover significant differences between these fibers by comparing their p-values and their fold-change (FC). The results are shown in Figure 5.8. Using $\log_2(\text{FC})$ of less than -0.5 or greater than 0.5 and $p < 0.05$, we observe the suppression (left side) of sphingomyelin (SM) d36:1, phosphatidylethanolamine (PE) 36:1, phosphatidylcholine (PC) 36:4, PC 30:0 and PC 32:2 and enhancement (right side) of carnitine (CAR) 14:2, CAR 18:2, CAR 18:1, PC O-44:11 and PC 18:0_22:6;O in type I fibers as compared to type IIa fibers (Figure 5.8a). Meanwhile, a comparison between type I and type IIx fibers (Figure 5.8b) provides a larger number of differentially enhanced or suppressed features. In addition to the species listed earlier, we observe the suppression of PC 34:1, PC 34:3, PC 30:0 and PE 38:4 and enhancement of PC 40:4 and PC 38:2 in type I fibers in comparison with type IIx fibers. In contrast, a direct comparison of type IIa vs. type IIx fibers does not indicate any significant differences among these fibers. In an effort to observe more subtle chemical changes, we used a lower $\log_2(\text{FC})$ of less than -0.3 or greater than 0.3 along with the same p-value of < 0.05 (Figure 5.8c). With this relaxed constraint, the only species that are downregulated in type IIa fibers in comparison with type IIx fibers are SM d36:1 and CAR 16:0 whereas the upregulated species are PC 18:0_22:6;O, PC O-44:11,

monoacylglycerol (MG) 22:5 and CAR 18:2. These results indicate a substantial chemical differentiation between type I and type IIx fibers, moderate differentiation between type I and type IIa fibers, and minor differentiation between type IIa and type IIx fibers. The fact that similar molecules are suppressed or enhanced across these fibers suggests a gradual change in their abundance from type I→type IIa→type IIx→ type IIb.

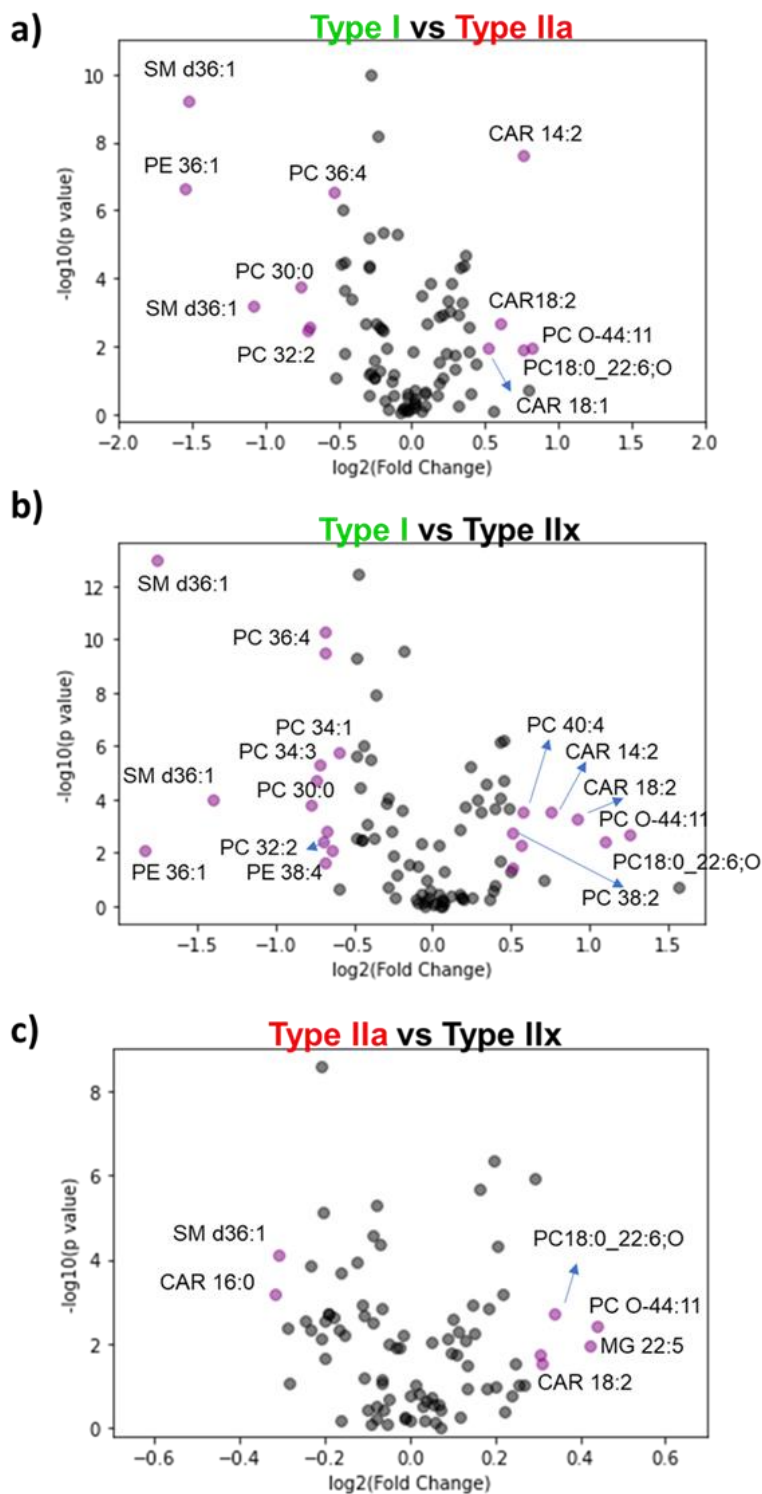


Figure 5.8. Volcano plots showing a direct comparison of a) type I and type IIa fibers, b) type I and type IIa fibers, and c) type IIa and type IIx fibers. Purple circles indicate molecules significantly different displaying a $\log_2(\text{FC})$ less than -0.5 or greater than 0.5 and $p\text{-value} < 0.05$ in a) and b), and $\log_2(\text{FC})$ less than -0.3 or greater than 0.3 and $p\text{-value} < 0.05$ in c).

Figure 5.9 shows a heatmap summarizing the variations in the abundance of species in each fiber type. A z-score is calculated indicating the number of standard deviations from the mean abundance. In this plot, the more positive z-score highlighted in red indicates that the abundance of a molecule in a specific fiber type is higher than the mean abundance across all fibers. Meanwhile, a more negative z-score highlighted in blue indicates an abundance lower than the mean value across the fibers. Finally, a z-score closer to zero shown in white indicates an abundance close to the mean value. All the molecules identified in this study along with their z-scores are provided in Appendix B. Because type IIx fibers are chemically closer to type I and IIa fibers than to type IIb fibers, we classified type I, type IIa, and type IIx as fibers with predominately oxidative metabolism and type IIb as fibers with predominately glycolytic metabolism. We apply this classification to sorting the molecules in Appendix B based on the spatial localization they showed across the three replicates. If a molecule was assigned to either RG or RGBK pattern in more than 2 two replicates, it is considered to correspond to oxidative metabolism. Meanwhile, molecules assigned to the BL pattern in more than two replicates are part of glycolytic metabolism. When extending this classification to the heatmap (Figure 5.9), we observe three distinct blocks depicting different trends: the top block contains all the molecules associated with oxidative metabolism (light yellow), the middle block contains all the molecules associated with mixed metabolism (intermediate yellow), and the bottom block contains the molecules associated with glycolytic metabolism (dark yellow). Regardless of the type of metabolism, it is evident that there is always a gradual transition in molecular abundances from type I/type IIa→type IIx→type IIb across all the replicates (Appendix B). These observations are also confirmed by ion images shown in Figure 5.9. Specifically, the abundance of PC 36:2 (Figure 5.9b) and PE 40:6 (Figure 5.9c) increases from left (glycolytic) to right (oxidative). Meanwhile, PC 34:0 (Figure 5.9d) does not show a specific localization. Lastly, SM d36:1 (Figure 5.9e) and PC 16:0/5:0 (COOH) (Figure 5.9f) display a decreasing chemical gradient from left to right. In summary, these results confirm that the chemical composition across fiber types does not change dramatically but rather undergoes gradual changes especially in the region where all the fiber types coexist such as the deep region of GAS tissue.

The results shown in Figure 5.10 reveal important compositional differences between oxidative and glycolytic fibers. Among the 91 identified phospholipids including isomers with different acyl chain compositions, 52 are more abundant in oxidative fibers, 16 are enhanced in

glycolytic fibers, and 23 are uniformly distributed across the tissue. A majority of phospholipids enhanced in oxidative fibers contain stearic acid (SA), FA 18:0. Meanwhile, a large fraction of phospholipids associated with glycolytic metabolism contain palmitic acid (PA), FA 16:0. Another striking difference is the high abundance of polyunsaturated fatty acids (PUFAs) including docosahexaenoic acid (DHA) FA 22:6, docosapentaenoic acid (DPA) FA 22:5, FA 22:4, and arachidonic acid (AA), FA 20:4, in phospholipids associated with oxidative metabolism in comparison with phospholipids enhanced in glycolytic fibers, which do not contain these acyl chains. The remarkable selectivity towards specific acyl chains in phospholipids characteristic of oxidative and glycolytic fibers indicates the importance of their structures to the function of the fiber.

5.4 Discussion

The results reported in this study provide a global overview of the chemical composition of the four main myofibers identified in mammals: type I, type IIa, type IIx, and type IIb. Our results indicate that although myofibers are classified into discrete categories based on the expression of distinct MyHC isoforms, their chemical composition is not drastically different. Indeed, based on their metabolic composition, myofiber can be considered as a continuous spectrum on fibers where molecular abundances gradually change from type I→type IIa→type IIx→ type IIb. The lack of fiber-specific patterns and prevalence of the ‘everywhere pattern’ (50 species) in Figure 5.6b supports this claim thereby suggesting that a large fraction of lipids and metabolites is present in all myofiber types to support the function of the muscle. The gradual metabolic transition observed between muscle fibers may be related to the inherent plasticity of muscles, which allows them to respond quickly to any environmental and dietary changes.^{170,191} For example, endurance training increases the oxidative capacity of all myofibers types.¹⁹² Since chemical differences are not dramatically different across fibers, it is possible for the muscle to adapt to meet the needs that the new activity demands and in some cases undergo fiber transformation.

Among the four myofiber types analyzed in this study, our results indicate that type IIb fibers are the most differentiated. Type IIb fiber is the only one, for which we identified a specific biomarker. In contrast, type I, type IIa, and type IIx fibers could be differentiated using less stringent criteria that allowed us to identify statistically significant differences in their composition. A major result that we report herein is that although type IIx fibers are more similar to type IIb in

their contractile properties, their chemical composition is more comparable to oxidative fibers: type I and type IIa. This claim is supported by the higher prevalence of the RGBK pattern (47 species) than RG pattern (15 species) (Fig. 3a). We consistently found across all replicates that molecules showing enhancement in type IIx fibers are also enhanced in type I and type IIa fibers as illustrated by the RGBK pattern. These results are different from what is generally reported about type IIx fiber, which is traditionally considered to have a preferred glycolytic metabolism.¹⁹³ Given the complexity of the system and shallow chemical gradients, it may be challenging to unambiguously determine the metabolic profile of type IIx fibers using traditional approaches. Meanwhile, high spatial resolution of nano-DESI MSI allowed us to determine molecular signatures of each fiber type with high specificity. This is particularly advantageous for the characterization of fiber-specific metabolism of muscle tissues with mosaic fiber patterns. Because molecules present in all fiber types are observed in the same experiment, their relative abundances can be compared to uncover variations in the chemical composition of the fibers in the context of the tissue environment. Nano-DESI MSI provides a direct measurement of metabolic signature of myofibers in comparison with a tissue enriched in a specific fiber type, which is traditionally used for studying the metabolomics of myofibers.

5.4.1 Phospholipid acyl chain composition differences in muscle fibers

Phospholipid architecture of biomembranes in skeletal muscles is crucial to their contractile properties and fatigue resistance.^{194,195} Our results show that PA and SA as the two most abundant acyl chains found in the total pool of phospholipids. This result is not surprising as PA is the building block for the synthesis of longer and more unsaturated fatty acids through a series of elongation and desaturation transformations.^{196,197} Since SA can be directly synthesized from PA in one step, it is reasonable to observe the high abundance of SA in phospholipids.

The higher content of phospholipids in oxidative fibers can be explained by the greater number of membrane-bound organelles compared to glycolytic fibers.^{198,199} An example of this difference is the presence of cardiolipins (CL), an essential phospholipid class exclusively located in the mitochondria where oxidative phosphorylation takes place, in oxidative fibers.²⁰⁰ In our experiments, we confidently identified two CL species CL 72:8 and CL 72:7 which displayed a spatial pattern that correlates with the location of oxidative fibers. Several other CL species showing the same pattern were not included in the final count of species due to their low abundance.

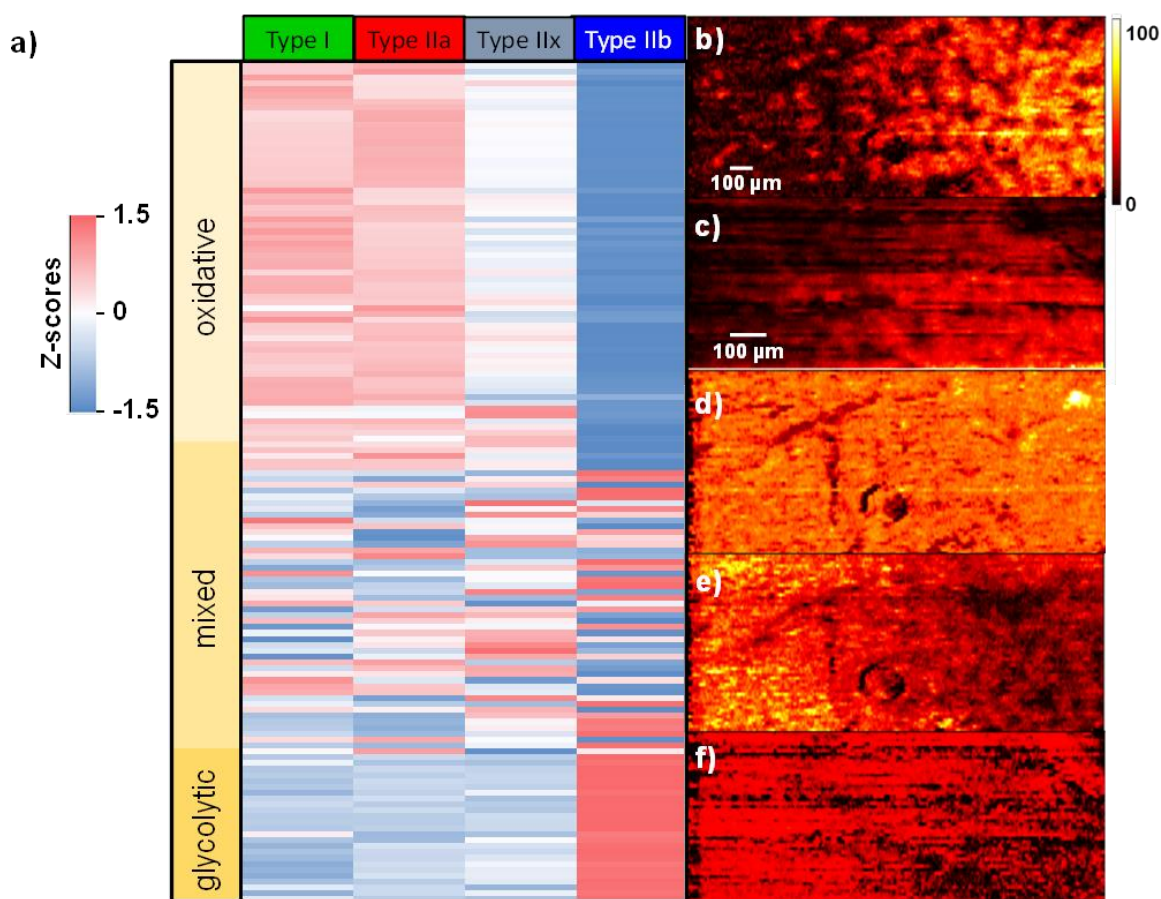


Figure 5.9. a) Heatmap of all the molecules identified in GAS tissue. Abundances are shown in a z-score scale using the blue-white-red color bar which indicates z-values ranging from -1.5 to 1.5. TIC normalized ion images of b) $[M+H]^+$ adduct of PC 36:2 at m/z 786.6007, c) $[M-H]^-$ adduct of PE 40:6 at m/z 790.5787, d) $[M+Na]^+$ adduct of PC 34:0 at m/z 784.5850, e) $[M+Na]^+$ adduct of SM d36:1 at m/z 753.5894 and f) $[M-H]^-$ adduct of PC 16:0_5:0(COOH) at m/z 608.3565. Scale bars are displayed inside each ion image. The color bar is displayed on the right side indicating that the intensity scale changes from black (low) to yellow (high).

The acyl chain distribution depicted in Fig. 5.10 shows a broad range of acyl chain lengths ranging from 12C to 24C. Interestingly, PA was found to be the predominant acyl chain in glycolytic fibers whereas SA was the most abundant acyl chain in oxidative fibers. Furthermore, highly polyunsaturated FAs such as DHA and DPA were exclusively found in oxidative fibers. These results are consistent with findings reported by Macartney et al. who observed an decrease in the concentration of PA and increase in the concentration of DHA with increase in the abundance of fast glycolytic fibers in rat gastrocnemius skeletal muscle tissue.²⁰¹ Considering that all FAs can provide energy via β -oxidation despite differences in their length and degree of unsaturation, the particular acyl chain composition observed per fiber type might be directly

implicated with their role as membrane building blocks instead of as energy source molecules.^{196,202} These FAs dramatically affect the membrane physical properties such as the transition phase: a temperature at which membrane fluidity changes. Longer and more saturated acyl chains increase the packing efficiencies of the membrane phospholipids thereby keeping the membrane more fluid at higher temperatures.²⁰³ Silvius et al. reported a transition temperature of 41 °C for PC 16:0_16:0, -36 °C for PC 16:1_16:1, 6 °C for PC 18:0_18:1 and -2 °C for PC 16:0_18:1.²⁰⁴ Therefore, it is reasonable to believe that such high content of polyunsaturated acyl chains in oxidative fibers, specially DPA and DHA, promotes a more fluid and permeable membrane thus facilitating many membrane processes associated to an endurance phenotype. There are several reports indicating the positive effect of DHA at promoting protein/receptor interactions,²⁰⁵ regulating insulin-mediated glucose disposal,¹⁹⁵ activating multiple transcriptional factors that control the expression of enzymes involved in fatty acid synthesis and β -oxidation²⁰⁶, and modulating Ca^{2+} signaling which improves contractile function and fatigue resistance.²⁰¹ Moreover, several studies about the incorporation of n-6 PUFA to membrane phospholipids through dietary supplementation, reported enhanced insulin sensitivity,^{207–209} better endurance performance and even induced fiber remodelling from glycolytic towards more oxidative fibers.²¹⁰ Following this rationale, the high prevalence of PA in glycolytic fibers and less polyunsaturated species in general, would foster a more rigid membrane thereby constraining molecular movement in the lateral plane of the membrane which might hamper the activation of the oxidative metabolism. For instance, a membrane enriched in PA has been demonstrated to decrease insulin action by altering both insulin binding and insulin-stimulated deoxyglucose uptake.²¹¹ As a result, this type of membrane composition presents a more insulin resistance character which is characteristic of glycolytic fibers.¹⁹⁵ Moreover, the presence of PA has also shown to increase the glycolytic pathway potentially as a result of redox regulation.²¹²

The reactivity of FAs reactive oxygen species (ROS) is also an important factor affecting the properties of cell membranes. Because of the large number of C=C bonds, PUFAs contain several bis-allylic hydrogens, which readily react with radicals resulting in lipid peroxidation. Therefore, phospholipids containing PUFAs are more prone to oxidation than phospholipids containing saturated fatty acids (SFAs) and monounsaturated fatty acids (MUFAs). We observe multiple oxidized species in oxidative fibers including PC 18:0_5:0(COOH) and PC 18:0_4:1(COOH), which are produced through the oxidation of PC 18:0_20:4; PC 18:0_9:0(COOH) and

PC 18:0_12:1;O;COOH, which are produced through the oxidation of PC 18:0_18:2; and PC 18:0_22:6;O, which is produced through the oxidation of PC 18:0_22:6.²¹³ These assignments were manually confirmed with MS/MS as shown in Figure 5.11. Reaction with ROS generated as a by-product of aerobic respiration is one of the major sources of the oxidized species. Oxylipins, another important group of lipid mediators, is also generated through the oxidation of phospholipids containing PUFAs, are also more abundant in oxidative than in glycolytic fibers.²¹⁴ Oxidation of PUFAs through reactions with ROS is prominent in the mitochondria. This organelle is known to generate approximately 90% of cellular ROS. Our results indicate the prevalence of FA 18:2 in CL species, which may be indicative of a selective incorporation of FAs with lower degree of unsaturation into membrane lipids making the membrane more resistant towards oxidative damage caused by ROS.²¹⁵ In summary, our results indicate that the acyl chain composition of membrane phospholipids is strongly linked to the regulation of the contractile and metabolic properties of oxidative and glycolytic skeletal muscle fibers.

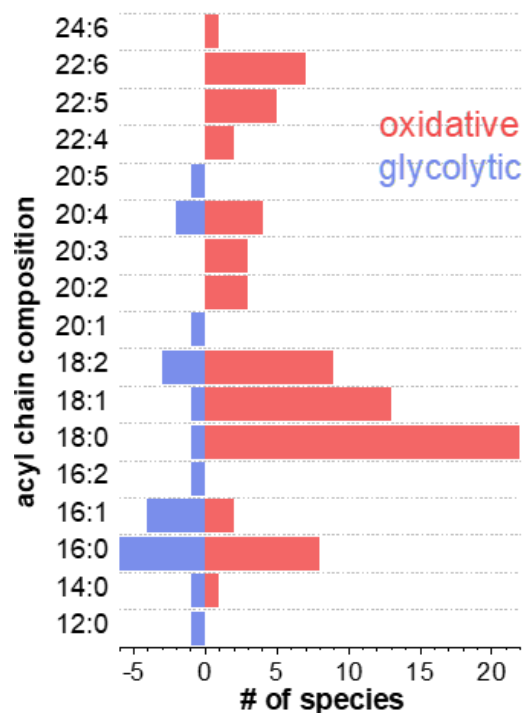


Figure 5.10. Acyl chain composition of all the phospholipids detected in GAS tissue with a carbon length ranging from 12C to 24C. Length of the bars indicates the number of species containing a specific acyl chain. Red bars indicate oxidative species whereas blue bars indicate glycolytic species.

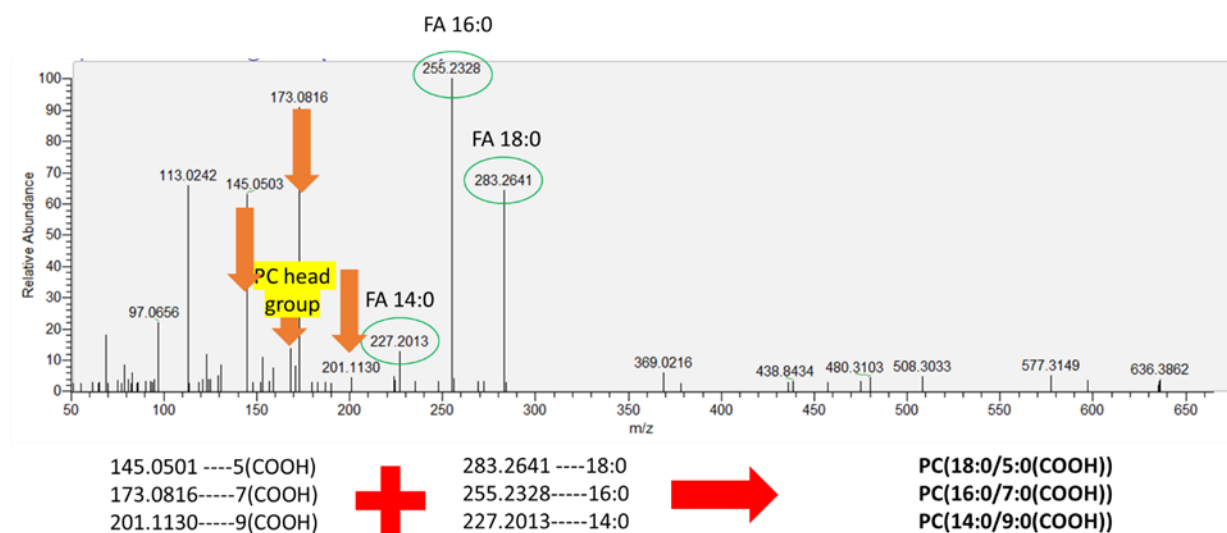


Figure 5.11. MS/MS spectrum of m/z 636.3862 showing the presence of multiple isomers. Orange arrows indicate the truncated oxidized acyl chains whereas the green circles indicate the presence of multiple fatty acid chains.

5.4.2 Metabolomic fingerprints linked to energy metabolism

Substrate-level phosphorylation is the main pathway for the ATP synthesis in fast-glycolytic skeletal muscles. At first, anaerobic degradation of phosphocreatine is used for the immediate phosphorylation of ADP to ATP during sudden bursts of exercise.¹⁷² In our results, we found that creatinine, a direct product of the breakdown of phosphocreatine, was mainly enriched in fast-glycolytic fibers indicating high phosphocreatine utilization in this fiber type. Our findings are in agreement with several studies that reported a higher consumption of the phosphocreatine stores by fast-glycolytic fibers in comparison to slow-oxidative fibers during very intense short-term exercises.^{216,217} With the continuous demand for energy, more ATP is hydrolyzed to ADP and Pi thereby triggering reactions associated with the glycolytic pathway in an effort to keep up with the ATP demand.¹⁷² In anaerobic glycolysis, glycogen is broken down to produce 3 ATP molecules and lactic acid. The build-up of lactic acid causes a drop in the pH thereby promoting muscle fatigue, disrupting phosphocreatine recycling, and causing muscle injury during high intensity exercise.²¹⁸ Therefore, it is not surprising that fast-glycolytic fibers have some mechanisms to protect themselves against oxidatively-induced tissue damage. Our results indicate a higher abundance of histidine-related compounds including histidine, methyl histidine, carnosine and anserine in glycolytic (type ??) fibers. The presence of these molecules is explained by their antioxidant properties which help prevent tissue damage from oxidative stress.²¹⁹ The antioxidant

capability of histidine-related compounds derives from the imidazole ring which efficiently scavenges ROS and harmful α - β -unsaturated aldehydes.^{219,220} Moreover, the presence of the imidazole moiety enhances the buffering capacity of the muscle that helps regulate the acidosis conditions during glycolysis. In particular, carnosine with a $pK_a=6.72$, helps maintain the pH around physiological values thereby delaying the onset of fatigue following short bouts of exercise without affecting its antioxidant performance.²²¹ The acidic environment promoted by glycolysis also facilitates the synthesis of creatinine through the breakdown of phosphocreatine that consumes H^+ for the phosphorylation of ADP.^{222,223}

Oxidative phosphorylation of ADP is the dominant source of energy during physical activity events lasting from minutes to hours. The increased production of ADP with increase in O_2 concentration triggers the mitochondria respiratory chain to generate ATP through the oxidation of fats and carbohydrates.¹⁷² A fingerprint of this dynamic metabolism was found in the distribution of acylcarnitines including CAR 18:2, CAR 18:1, CAR 16:0, and CAR 14:2, which are enhanced in slow-twitch (type I) fibers. These molecules are generated through the conversion of fatty acyl-coAs into acylcarnitines, which subsequently cross the mitochondrial membrane and undergo fatty acid β -oxidation for energy production. Because of the higher content of mitochondria in the oxidative fibers, it is reasonable to observe more β -oxidation activity and therefore higher abundance of acylcarnitines in these fibers. Our findings are in agreement with a higher abundance of acylcarnitines in fibers with oxidative metabolism in a gastrocnemius muscle tissue.⁸² Interestingly, free carnitine and acetylcarnitine, CAR 2:0, did not show a specific pattern in nano-DESI MSI indicating their ubiquitous presence across all the tissue. The fact that carnitine can be readily and enzymatically converted into acetylcarnitine and back, makes these two molecules interchangeable and therefore, it is reasonable to observe that they show a similar spatial distribution. These results highlight another important role of carnitine aside from translocating long-chain fatty acids from the cytosol to mitochondria as described earlier. Indeed, carnitine is also involved in the formation of acetylcarnitine from acetyl-CoA thereby preventing extreme fluctuations in concentrations of acetyl-CoA and free CoA that may be deleterious to cellular function.^{224,225} Based in our results, it is reasonable to conclude that the buffering effect of acetylcarnitine is ubiquitous in all fiber types.

Another marker of oxidative metabolism is observed in the spatial localization of MG 18:2, MG 18:1, and MG 16:0 which are enhanced in oxidative fibers. We hypothesize that these

molecules are traces of intracellular lipid droplets (LDs), which serve as a source of fatty acids for energy metabolism. The abundance of MG species might reflect the lipolysis state of triglycerides (TGs) contained in the LDs, which are broken down to fatty acids via a series of hydrolysis reactions.²²⁶ Several enzymes including adipose triglyceride lipase (ATGL), hormone-sensitive lipase (HSL), and monoacylglycerol lipase (MGL) sequentially hydrolyze TG, DG and MG, respectively, thereby releasing FA in every step.²²⁷ We observe the same acyl chain composition in MG (MG 18:2, MG 18:1 and MG 16:0) and CAR (CAR 18:2, CAR 18:1 and CAR 16:0) species. It is reasonable to assume that FAs released in hydrolysis of MGs are converted into CARs that shuttle through the mitochondrial membrane and undergo β -oxidation. This lipolysis activity is known to be enhanced in oxidative fibers.²²⁸ Moreover, there are several reports indicating high expression of ATG and HSL enzymes in type I fibers which is also consistent with our findings.^{227,229}

5.5 Conclusions

In this study, we demonstrate the power of nano-DESI MSI in combination with IF for identifying molecular signatures of skeletal muscle fibers. The high specificity towards each fiber type allowed us to accurately measure chemical gradients in GAS tissue, especially in regions where multiple myofiber types are present. Our results indicate gradual variations of the chemical composition when transitioning from more oxidative fibers to more glycolytic fibers. These results are supported by the lack of fiber-specific biomarkers which suggest the presence of similar molecules across all fibers, but just in slightly different abundances. The myofiber that is found to be more differentiated is type IIb, which shows a chemical composition characteristic of glycolytic metabolism. Interestingly, type IIx fibers which are generally categorized as glycolytic fibers, have a chemical composition indicative of oxidative metabolism. High-resolution nano-DESI MSI provides unique insights into fiber-specific biochemical pathways, which are important to understanding of the physiology of skeletal muscles. Moreover, this multimodal imaging approach can be extended to the analysis of other highly heterogenous and complex tissues such as pancreatic islets.

CHAPTER 6. CONCLUSIONS AND PERSPECTIVES

The research performed in this thesis has successfully expanded the analytical capabilities of nano-DESI MSI. A major contribution of this work is the capability to perform iMSI of phospholipids, which may be used to uncover the distribution of isomeric C=C lipids in different systems providing unique insights into their role in biological systems. Current efforts to make this methodology quantitative and more sensitive are being pursued. Another important contribution is the addition of ion mobility to nano-DESI experiments. This novel platform enables iMSI of species that can be resolved in a mobility cell, eliminates interferences with background solvent peaks, and improves the specificity and structural characterization of lipids in MSI experiments. The application of nano-DESI to the study of a very complex and heterogenous system such as muscle fibers has motivated the development of registration and segmentation approaches, which can be now applied to other challenging systems. The methods provided herein can also be readily adapted to other liquid extraction techniques.

Despite the development of the nano-DESI technique, assembling of the high resolution nano-DESI probe is still challenging and requires a trained user. A solution to this problem has been recently reported by our lab where an integrated microfluidic probe (iMFP) resembling the shape of the capillary-based nano-DESI probe was developed for imaging of biological samples.²³⁰ The performance of the iMFP is comparable to that of the capillary-based nano-DESI probe in terms of sensitivity, stability, and spatial resolution. Although the iMFP device is fabricated with more sophisticated materials, this development represents a first step towards making nano-DESI more user friendly and accessible to the broader community. Efforts to make the fabrication of the iMFP much simpler are currently underway in our lab.

Similar to other MSI techniques, nano-DESI is typically coupled to high-mass resolution mass spectrometers, which provides good separation of isobaric peaks in complex mixtures. Although in this thesis we improved the characterization of isobaric lipids by coupling nano-DESI with a state-of-the-art ion mobility instrument, there are still some isobaric species that cannot be separated due to very small differences in their masses. Therefore, a more selective MS/MS approach is required to accomplish this goal. The power of nano-DESI MS/MS for the efficient separation and imaging of isobaric and isomeric species has been previously demonstrated.⁸³ Coupling of nano-DESI MSI with a triple quadrupole (QqQ) is a promising approach for the

targeted quantitative imaging and identification of lipids. By exploring different acquisition modalities of a QqQ instrument, imaging experiments may be performed using a less expensive instrument.²³¹ This development will make imaging technologies more accessible to the community and will motivate their incorporation into routine analysis tasks.

In terms of applications, nano-DESI has been largely used for the analysis of lipids and metabolites which are relatively easy to extract in comparison with other biomolecules. Indeed, all the methods developed in this thesis are focused on improving the detection and identification of lipids and metabolites. The utility of nano-DESI for the analysis of protein and protein-derived structures have been demonstrated.^{232–234} The approaches provided in this thesis can be extended to protein imaging with some modifications. For example, solvent systems that mimic native conditions may be used for imaging of intact protein complexes.²³⁵ Coupling of nano-DESI to other ion mobility instruments with better resolving power will provide better separation of overlapping protein signals in the mobility dimension.²³⁶ Moreover, photochemical reactions targeting different functional groups of protein complexes such as S-S bonds can be implemented to aid in their structural characterization.²³⁷ Due to the growing interest of the role of proteins in cellular processes, improvements in coverage and sensitivity are necessary to provide in-depth proteome imaging.

3D imaging is another area of development for MSI in order to provide a full picture of the chemical gradients at the organ level, which is of paramount interest to clinical research. Although there have been preliminary reports demonstrating the feasibility of performing 3D MSI experiments,^{238–241} these are far from routine due to the challenges associated with sample handling and preparation, experimental throughput, and data processing. As a result, 2D imaging is traditionally performed which can only provide molecular snapshots in specific areas of an organ where the tissue was collected. Since most 3D MSI images are generated by mapping sequential tissue sections, advances in the experimental throughput of tissue mapping are critical to these experiments. An immediate solution to this problem will be the use of instruments with faster acquisition rates. Moreover, the development of computational tools for the automated reconstruction of the three-dimensional volume and co-registration to other imaging modalities will dramatically expand its dissemination in the biomedical field. The development of 3D MSI will facilitate the creation of detailed biomolecular atlases of different organs, which is important

to understanding of the intricate molecular networks in the entire organ. This capability will revolutionize tissue-based diagnostics.

Finally, high biological variability still imposes challenges in the adoption of MSI for quantification purposes. Indeed, MSI has been extensively used for relative quantification of small molecules, lipids, and drugs in tissue sections.^{242–247} However, the development of absolute quantification approaches will make MSI a translational technology for providing accurate concentrations of drugs or biomarkers in specific locations of the tissue in support of clinical studies. To accomplish this goal, it is important to obtain a better understanding of matrix effects happening in different biological systems and the develop innovative approaches to compensate for them.

These innovations along with a comprehensive study of the multi-omics information provided by MSI will push the boundaries of MSI technologies and pave the way for their rapid translation into clinical settings.

APPENDIX A. IDENTIFICATION OF METABOLITES USING MS/MS DATABASES

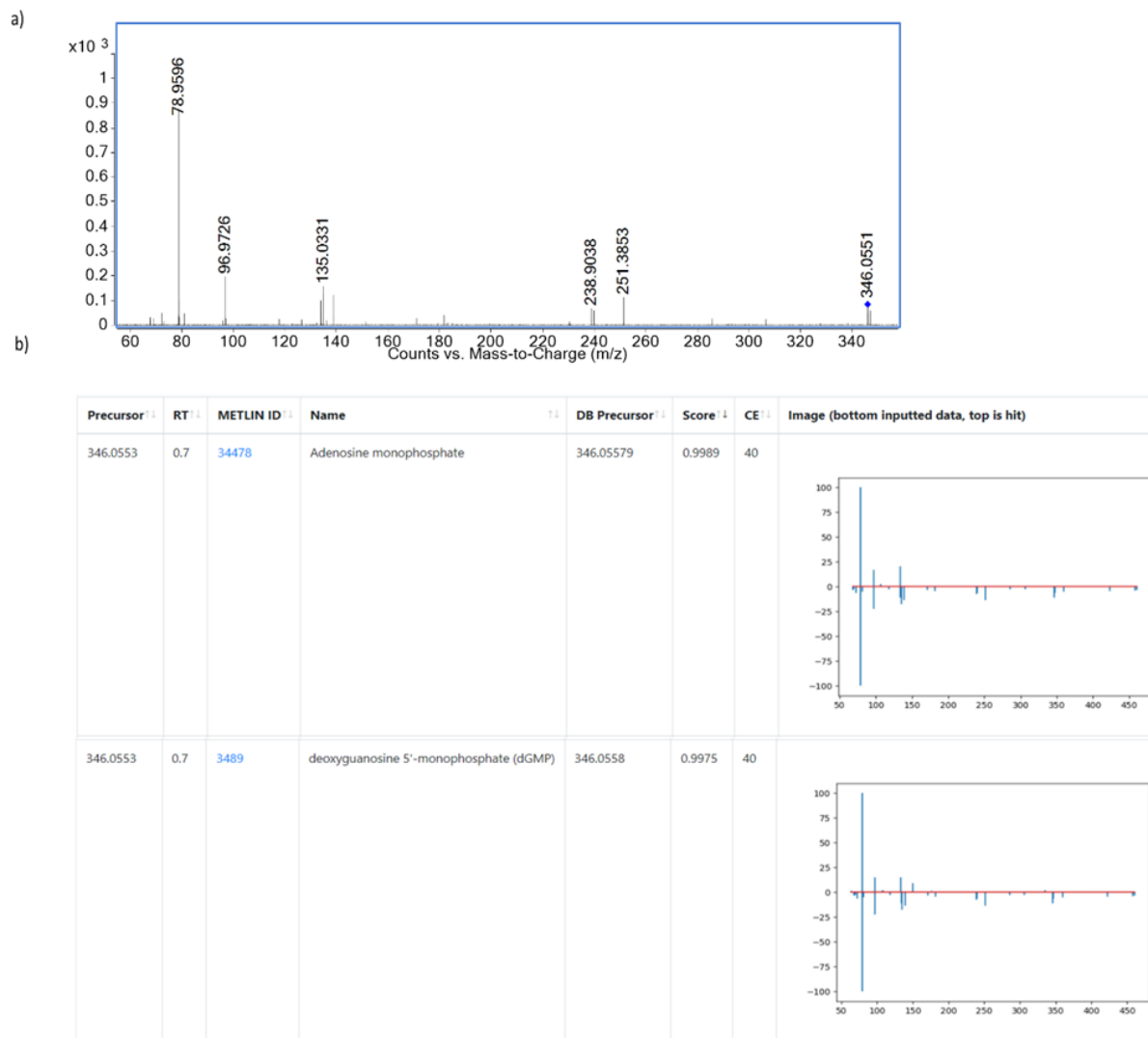


Figure A.1. a) Experimental MS/MS for m/z 346.0553. b) Results from the MS/MS Spectrum scoring search for m/z 346.0553 which renders similar scores of 0.99 for adenosine monophosphate and deoxyguanosine monophosphate.

Precursor	RT	METLIN ID	Name	DB Precursor	Score	CE	Image (bottom inputted data, top is hit)
146.0447	0.7	19	L-Glutamate	146.0459	0.9977	10	
146.0447	0.7	6662	N-Methyl-D-aspartic acid	146.0459	0.6815	10	
146.0447	0.7	96376	N-Acetyl-DL-serine	146.0459	0.0335	10	

Figure A.2. Results from the MS/MS Spectrum scoring search for m/z 146.0459 which facilitates its annotation as L-glutamate with the highest score of 0.99.

APPENDIX B. ANNOTATED SPECIES WITH THEIR RELATIVE ABUNDANCES EXTRACTED PER EACH FIBER TYPE WITH THEIR CLASSIFICATION BASED ON THE PATTERN DISTRIBUTION AND METABOLISM DEPICTED ACROSS ALL THE REPLICATES.

Table B1. Mean abundances and classification of annotated species in mouse 1. R (red) indicate type IIa fibers, G (green) indicate type I fibers, BK (black) indicate type IIx fibers and BL (blue) indicate type IIb fibers. E stands for everywhere pattern.

mouse 1										
<i>m/z</i>	name	ion	R	G	BK	BL	RG	RGBK	BL enriched	E
143.1073	Caprylic acid	-H	93.68	95.35	100.00	95.61	--	--	--	E
145.0614	L-Glutamine	-H	84.48	86.27	88.46	100.00	--	--	BL	--
146.0454	L-Glutamate	-H	99.14	99.60	100.00	72.70	--	RGBK	--	--
149.009	Tartaric acid	-H	99.36	100.00	97.19	84.89	--	--	--	E
151.0257	Xanthine	-H	86.84	97.37	100.00	55.26	--	RGBK	--	--
152.0217	Creatinine	+K	52.8	43.4	64.2	100.0	--	--	BL	--
152.9954	Propanoyl phosphate	-H	96.38	97.32	96.05	100.00	--	--	--	E
154.0617	Histidine	-H	58.76	58.31	62.99	100.00	--	--	BL	--
167.0207	Uric acid	-H	100.00	96.67	95.00	90.00	--	--	--	E
170.0922	1-methylhistidine	+H	65.0	61.0	62.4	100.0	--	--	BL	--
171.1386	FA 10:0	-H	95.45	98.42	100.00	99.08	--	--	--	E
175.0244	Ascorbic acid	-H	10.84	9.49	15.81	100.00	--	--	BL	--
175.1187	L-Arginine	+H	59.0	59.6	62.6	100.0	--	--	BL	--
180.0662	L-Tyrosine	-H	85.37	82.93	87.80	100.00	--	--	BL	--
184.0013	Phospho-L-serine	-H	91.85	100.00	85.19	95.56	--	--	--	E
184.094	Carnitine	+Na	91.2	100.0	98.3	96.4	--	--	--	E
197.1391	Butyrylcholine	+Na	66.7	60.4	65.5	100.0	--	--	BL	--
199.17	FA 12:0	-H	96.79	97.69	100.00	99.16	--	--	--	E
225.1857	FA 14:1	-H	100.00	93.48	89.13	66.85	--	RGBK	--	--
227.1138	Carnosine	+H	55.2	50.7	52.8	100.0	--	--	BL	--
227.2014	FA 14:0	-H	98.90	99.29	100.00	95.78	--	--	--	E
241.1295	Anserine	+H	65.6	61.1	64.2	100.0	--	--	BL	--
245.0426	Phosphatidyl glycerol	-H	95.25	94.58	100.00	79.32	--	--	--	E
251.2013	FA 16:2	-H	100.00	90.32	78.98	25.62	--	RGBK	--	--
253.217	FA 16:1	-H	100.00	96.43	93.69	81.92	--	RGBK	--	--
255.2326	FA 16:0	-H	97.20	97.56	99.55	100.00	--	--	--	E
256.1553	CAR 6:1	-H	92.51	94.12	100.00	97.86	--	--	--	E
258.1706	CAR 6:0	-H	94.39	96.84	97.54	100.00	--	--	--	E

267.0731	Inosine	-H	100.00	99.66	95.40	94.86	--	--	--	E
277.2169	FA 18:3	-H	100.00	91.07	79.57	41.87	--	RGBK	--	--
279.2326	FA 18:2	-H	100.00	90.99	78.11	33.21	--	RGBK	--	--
281.248	FA 18:1	-H	100.00	92.45	82.82	46.70	--	RGBK	--	--
283.2636	FA 18:0	-H	93.26	94.11	96.53	100.00	--	--	--	E
293.2118	9-OxoODE	-H	100.00	81.19	42.32	10.03	RG	--	--	--
295.2272	9-HODE	-H	100.00	90.83	71.69	25.82	--	RGBK	--	--
297.2429	9-hydroxy-12Z-octadecenoic cid	-H	100.00	99.60	99.80	95.00	--	--	--	E
299.2011	FA 20:6	-H	94.08	95.19	97.29	100.00	--	--	--	E
303.2326	FA 20:4	-H	100.00	94.64	83.31	54.07	--	RGBK	--	--
305.2483	FA 20:3	-H	100.00	91.75	77.39	39.15	--	RGBK	--	--
306.0762	Glutathione	-H	82.77	81.59	80.20	100.00	--	--	BL	--
307.2642	FA 20:2	-H	100.00	90.85	77.17	29.40	--	RGBK	--	--
309.2797	FA 20:1	-H	100.00	92.78	79.96	36.88	--	RGBK	--	--
317.2498	Pregnanolone	-H	96.07	97.52	100.00	98.45	--	--	--	E
322.0441	Cytidine 2'-phosphate	-H	99.39	100.00	84.41	34.82	--	RGBK	--	--
323.0281	Uridine monophosphate	-H	99.50	100.00	90.89	48.11	--	RGBK	--	--
327.2325	FA 22:6	-H	100.00	96.99	82.24	48.09	--	RGBK	--	--
329.2483	FA 22:5	-H	100.00	93.39	78.84	37.89	--	RGBK	--	--
331.2643	FA 22:4	-H	100.00	94.68	81.08	41.07	--	RGBK	--	--
332.9569	2-Deoxy-D-ribose 1,5-bisphosphate	+K	83.4	88.5	82.9	100.0	--	--	BL	--
337.311	FA 22:1	-H	100.00	98.42	97.37	92.46	--	--	--	E
339.3264	FA 22:0	-H	85.78	88.47	89.42	100.00	--	--	BL	--
346.0554	Adenosine monophosphate	-H	100.00	99.72	87.24	70.85	--	RGBK	--	--
347.0393	Inosine 5'-monophosphateI MP	-H	100.00	97.97	95.03	94.74	--	--	--	E
347.1825	12-oxo-14,18-dihydroxy-9Z,13E,15Z-octadecatrienoic cid	+Na	81.4	82.5	75.4	100.0	--	--	--	E
351.2202	20-hydroxy LTB4	-H	94.63	96.14	97.65	100.00	--	--	--	E
353.2666	MG 16:0	+Na	86.4	91.7	100.0	80.6	--	--	--	E
362.0503	Guanosine 3'-phosphate	-H	100.00	98.12	91.54	45.18	--	RGBK	--	--
367.3576	FA 24:0	-H	83.69	85.68	89.54	100.00	--	--	--	E
368.2799	CAR 14:2	+H	85.1	100.0	63.5	6.3	RG	--	--	--
377.2653	MG 18:2	+Na	58.9	60.2	100.0	10.2	--	RGBK	--	--
379.2811	MG 18:1	+Na	69.5	76.3	100.0	34.7	--	RGBK	--	--

400.3417	CAR 16:0	+H	92.2	100.0	96.8	29.5	--	RGBK	--	--
426.0217	ADP	-H	83.49	78.42	79.31	100.00	--	--	BL	--
427.2842	MG 22:5	+Na	79.6	90.6	79.3	100.0	--	--	--	E
431.2276	LPA 18:3	-H	94.39	92.86	98.47	100.00	--	--	--	E
440.2779	LPC 12:0	+H	81.0	90.5	82.1	100.0	--	--	BL	--
446.3248	CAR 18:1	+Na	80.9	100.0	70.2	10.0	--	RGBK	--	--
448.3415	CAR 18:2	+Na	78.1	100.0	61.1	6.5	RG	--	--	--
465.2433	LPA 22:6	+H- H ₂ O	52.7	50.3	55.4	100.0	--	--	BL	--
480.3089	LPE 18:0	-H	100.00	97.72	90.18	59.82	--	RGBK	--	--
518.3217	LPC 16:0	+Na	96.6	100.0	96.7	91.8	--	--	--	E
522.3558	LPC 18:0	-H	89.18	89.98	93.80	100.00	--	--	BL	--
524.2777	LPE 22:6	-H	100.00	99.91	86.37	48.95	--	RGBK	--	--
540.0532	cyclic denosine diphosphate ribose	-H	100.00	97.65	93.29	98.03	--	--	--	E
542.3217	LPC 18:2	+Na	91.9	100.0	86.8	41.3	--	RGBK	--	--
546.353	LPC 18:0	+Na	90.3	100.0	79.9	62.4	--	RGBK	--	--
553.3713	Elastin	+H	79.7	81.7	79.8	100.0	--	--	BL	--
557.0907	Cyanidin 3- 3"- malonylglucoside	+Na	83.3	81.9	79.4	100.0	--	--	BL	--
557.2247	Asp Glu Phe Phe	+H	88.0	91.2	87.4	100.0	--	--	BL	--
568.3399	LPC 20:3	+Na	87.2	100.0	80.9	32.8	--	RGBK	--	--
594.3408	PS 22:0	-H	98.14	97.92	100.00	87.73	--	--	--	E
599.3199	LPI 18:0	-H	98.17	100.00	92.55	88.61	--	RGBK	--	--
608.3565	PC 16:0/5:0(COOH)	-H	57.60	54.20	66.55	100.00	--	--	BL	--
622.3716	PC 22:1;O2	-H	100.00	95.88	53.91	19.75	RG	--	--	--
636.3873	PC 18:0/5:0(COOH)	-H	100.00	93.56	94.06	83.66	--	RGBK	--	--
664.4193	PC 16:0/9:0(COOH)	-H	88.87	90.21	100.00	85.99	--	--	--	E
667.4414	PA 34:4	-H	50.90	53.89	71.86	100.00	--	--	BL	--
667.5244	DG 38:4	+Na	93.8	98.4	97.4	100.0	--	--	--	E
669.4563	PA 34:3	-H	96.67	94.33	98.67	100.00	--	--	--	E
673.4264	DG 38:9	+K	100.0	88.1	90.8	76.0	--	RGBK	--	--
688.3922	ox PC 16:0/9:0CHO	+K	97.1	100.0	78.1	91.1	--	--	--	E
723.4783	CL 72:8	-2H	100.00	99.04	70.96	25.32	--	RGBK	--	--
724.4837	CL 72:7	-2H	96.62	100.00	73.34	27.88	--	RGBK	--	--
732.4221	ox PC 18:0/9:0(COOH)	+K	92.6	100.0	85.8	50.1	--	RGBK	--	--
732.4815	PC 30:2;O2	-H	100.00	100.00	27.27	18.18	RG	--	--	--
744.4939	PC 30:0	+K	65.9	53.3	65.6	100.0	--	--	BL	--
745.5025	PG 34:2	-H	100.00	92.94	83.94	31.39	--	RGBK	--	--

747.5188	PG 34:1	-H	100.00	98.45	90.81	62.54	--	RGBK	--	--
748.5216	PC P-36:5	-H	100.00	97.52	90.58	54.77	--	RGBK	--	--
749.5103	PA 38:3	+Na	89.3	100.0	71.3	15.6	RG	--	--	--
754.4783	PE 34:2	+K	87.7	89.3	84.4	100.0	--	--	BL	--
756.5514	PC 32:0	+Na	100.0	94.0	99.3	91.3	--	--	--	E
768.4955	PC 32:2	+K	61.2	53.1	65.8	100.0	--	--	BL	--
768.5537	PE 36:1	+Na	58.6	45.3	66.1	100.0	--	--	BL	--
769.562	SM d36:1	+K	51.2	36.2	58.9	100.0	--	--	BL	--
770.5095	PC 32:1	+K	60.3	54.3	60.6	100.0	--	--	BL	--
774.4499	PE 36:6	+K	85.8	88.7	85.0	100.0	--	--	BL	--
780.5514	PC 34:2	+Na	98.7	94.9	100.0	86.9	--	--	--	E
784.585	PC 34:0	+Na	99.4	100.0	98.3	92.0	--	--	--	E
786.5059	PE 38:6	+Na	100.0	98.5	91.4	88.5	--	--	--	E
794.5096	PC 34:3	+K	78.6	69.9	82.6	100.0	--	--	BL	--
798.5408	PC 34:1	+K	95.6	89.1	95.1	100.0	--	--	--	E
802.5357	PC 36:5	+Na	81.5	72.9	83.1	100.0	--	--	BL	--
806.5117	PE 38:4	+K	96.0	90.6	100.0	98.4	--	--	--	E
810.5056	PE 42:11	+H	100.0	90.5	93.2	55.0	--	RGBK	--	--
810.6007	PC 36:1	+Na	94.5	100.0	83.1	61.3	--	RGBK	--	--
812.6163	PC 36:0	+Na	84.7	100.0	61.3	27.1	RG	--	--	--
816.5485	PE 40:5	+Na	98.4	88.7	100.0	80.8	--	--	--	E
820.5253	PC 36:4	+K	68.9	59.9	73.3	100.0	--	--	BL	--
824.5566	PC 36:2	+K	94.9	100.0	83.7	51.0	--	RGBK	--	--
828.5514	PC 38:6	+Na	91.8	85.6	100.0	77.6	--	--	--	E
830.5096	PE 40:6	+K	100.0	97.3	92.8	63.6	--	RGBK	--	--
832.5827	PC 38:4	+Na	100.0	96.6	94.0	67.2	--	RGBK	--	--
834.5278	PS 40:6	-H	96.75	100.00	85.07	71.59	--	RGBK	--	--
834.5983	PC 38:3	+Na	91.2	100.0	72.0	31.9	--	RGBK	--	--
835.5318	PI 34:1	-H	97.54	100.00	87.45	70.29	--	RGBK	--	--
836.6163	PC 38:2	+Na	90.5	100.0	66.0	15.9	RG	--	--	--
837.5471	PI 34:0	-H	100.00	93.40	74.37	28.92	RG	--	--	--
846.5409	PC 38:5	+K	96.6	88.7	100.0	97.4	--	--	--	E
852.5514	PC 40:8	+Na	100.0	99.1	95.7	54.5	--	RGBK	--	--
854.567	PC 40:7	+Na	100.0	99.5	93.8	60.7	--	RGBK	--	--
856.5827	PC 40:6	+Na	91.1	100.0	69.4	26.2	RG	--	--	--
858.5983	PC 40:5	+Na	91.4	100.0	71.7	27.7	RG	--	--	--
860.6107	PC 40:4	+Na	92.6	100.0	61.1	10.2	RG	--	--	--
861.5483	PI 36:2	-H	91.86	100.00	66.89	26.58	RG	--	--	--
885.5489	PI 38:4	-H	98.43	100.00	92.73	83.22	--	--	--	E

887.5596	PI 38:3	-H	96.65	100.00	87.90	75.68	--	RGBK	--	--
888.554	PC18:0_22:6;O	+K	78.8	100.0	47.8	6.1	RG	--	--	--
904.5596	PC O-44:11	+K	73.5	100.0	44.6	5.6	RG	--	--	--
909.5481	PI 40:6	-H	97.15	100.00	78.82	57.83	--	RGBK	--	--

Table B2. Mean abundances and classification of annotated species in mouse 1. R (red) indicate type IIa fibers, G (green) indicate type I fibers, BK (black) indicate type IIx fibers and BL (blue) indicate type IIb fibers. E indicates for everywhere pattern

mouse 2										
<i>m/z</i>	name	adduct	R	G	BK	BL	RG	RGBK	BL enriched	E
143.1073	Caprylic acid	-H	97.84	99.58	100.00	96.54	--	--	--	E
145.0614	L-Glutamine	-H	97.77	93.40	95.63	100.00	--	--	--	E
146.0454	L-Glutamate	-H	97.86	100.00	89.71	76.69	--	RGBK	--	--
149.009	Tartaric acid	-H	96.54	95.41	100.00	92.45	--	--	--	E
151.0257	Xanthine	-H	100.00	96.07	97.12	70.94	--	RGBK	--	--
152.0217	Creatinine	+K	94.6	84.3	100.0	95.5	--	--	--	E
152.9954	Propanoyl phosphate	-H	98.57	100.00	99.61	94.81	--	--	--	E
154.0617	Histidine	-H	89.94	83.01	90.02	100.00	--	--	BL	--
167.0207	Uric acid	-H	100.00	89.60	95.95	89.02	--	--	--	E
170.0922	1-methylhistidine	+H	69.7	45.9	87.9	100.0	--	--	BL	--
171.1386	FA 10:0	-H	96.89	97.99	100.00	96.53	--	--	--	E
175.0244	Ascorbic acid	-H	26.27	18.63	39.33	100.00	--	--	BL	--
175.1187	L-Arginine	+H	88.6	74.3	94.8	100.0	--	--	BL	--
180.0662	L-Tyrosine	-H	97.29	93.90	96.27	100.00	--	--	--	E
184.0013	Phospho-L-serine	-H	96.59	100.00	78.41	95.45	--	--	--	E
184.094	Carnitine	+Na	97.7	98.7	100.0	99.8	--	--	--	E
197.1391	Butyrylcholine	+Na	72.9	42.5	88.6	100.0	--	--	BL	--
199.17	FA 12:0	-H	97.65	96.83	100.00	96.22	--	--	--	E
225.1857	FA 14:1	-H	96.63	94.23	100.00	69.23	--	RGBK	--	--
227.1138	Carnosine	+H	72.0	53.0	83.4	100.0	--	--	BL	--
227.2014	FA 14:0	-H	99.69	99.11	100.00	95.87	--	--	--	E
241.1295	Anserine	+H	74.5	55.4	86.6	100.0	--	--	BL	--
245.0426	Phosphatidyl glycerol	-H	100.00	95.51	94.23	85.90	--	--	--	E
251.2013	FA 16:2	-H	100.00	85.77	62.92	29.59	RG	--	--	--
253.217	FA 16:1	-H	100.00	97.81	94.29	78.72	--	RGBK	--	--
255.2326	FA 16:0	-H	98.75	100.00	98.59	97.78	--	--	--	E
256.1553	CAR 6:1	-H	95.39	96.93	100.00	99.12	--	--	--	E
258.1706	CAR 6:0	-H	96.70	100.00	97.80	98.53	--	--	--	E
267.0731	Inosine	-H	94.41	91.94	90.43	100.00	--	--	--	E
277.2169	FA 18:3	-H	100.00	91.24	75.48	46.31	--	RGBK	--	--
279.2326	FA 18:2	-H	100.00	92.56	77.59	49.94	--	RGBK	--	--
281.248	FA 18:1	-H	100.00	94.66	86.01	62.14	--	RGBK	--	--
283.2636	FA 18:0	-H	97.65	100.00	98.19	99.01	--	--	--	E

293.2118	9-OxoODE	-H	100.00	90.28	57.92	25.56	RG	--	--	--
295.2272	9-HODE	-H	100.00	91.02	75.93	52.69	--	RGBK	--	--
297.2429	9-hydroxy-12Z-octadecenoic cid	-H	100.00	98.68	93.17	86.31	--	--	--	E
299.2011	FA 20:6	-H	92.21	96.54	100.00	97.62	--	--	--	E
303.2326	FA 20:4	-H	100.00	94.76	95.24	70.52	--	RGBK	--	--
305.2483	FA 20:3	-H	100.00	87.56	83.68	40.16	--	RGBK	--	--
306.0762	Glutathione	-H	86.32	80.59	84.62	100.00	--	--	BL	--
307.2642	FA 20:2	-H	100.00	66.67	53.33	22.67	--	RGBK	--	--
309.2797	FA 20:1	-H	100.00	94.95	81.49	55.61	--	RGBK	--	--
317.2498	Pregnanolone	-H	97.32	100.00	97.68	96.52	--	--	--	E
322.0441	Cytidine 2'-phosphate	-H	94.00	85.45	85.82	100.00	--	--	--	E
323.0281	Uridine monophosphate	-H	97.16	92.34	93.33	100.00	--	--	--	E
327.2325	FA 22:6	-H	100.00	99.53	89.91	68.93	--	RGBK	--	--
329.2483	FA 22:5	-H	100.00	91.33	76.36	42.69	--	RGBK	--	--
331.2643	FA 22:4	-H	97.95	100.00	98.00	79.63	--	RGBK	--	--
332.9569	2-Deoxy-D-ribose 1,5-bisphosphate	+K	89.6	80.1	100.0	93.4	--	--	--	E
337.311	FA 22:1	-H	97.80	100.00	96.02	96.02	--	--	--	E
339.3264	FA 22:0	-H	96.54	97.62	100.00	97.95	--	--	--	E
346.0554	Adenosine monophosphate	-H	98.77	100.00	87.47	77.79	--	RGBK	--	--
347.0393	Inosine 5'-monophosphateIM P	-H	95.21	89.59	90.09	100.00	--	--	BL	--
347.1825	12-oxo-14,18-dihydroxy-9Z,13E,15Z-octadecatrienoic cid	+Na	94.5	83.1	100.0	99.3	--	--	--	E
351.2202	20-hydroxy LTB4	-H	94.76	98.25	100.00	96.83	--	--	--	E
353.2666	MG 16:0	+Na	100.0	80.9	95.4	84.0	--	--	--	E
362.0503	Guanosine 3'-phosphate	-H	100.00	97.42	90.83	79.00	--	RGBK	--	--
367.3576	FA 24:0	-H	92.74	94.40	100.00	95.11	--	--	--	E
368.2799	CAR 14:2	+H	100.0	68.6	47.4	12.0	RG	--	--	--
377.2653	MG 18:2	+Na	100.0	50.0	67.5	14.9	--	RGBK	--	--
379.2811	MG 18:1	+Na	100.0	72.1	80.7	48.9	--	RGBK	--	--
400.3417	CAR 16:0	+H	100.0	79.2	90.3	54.6	--	RGBK	--	--
426.0217	ADP	-H	100.00	94.01	89.70	94.09	--	--	--	E
427.2842	MG 22:5	+Na	90.9	86.6	94.6	100.0	--	--	BL	--
431.2276	LPA 18:3	-H	93.80	100.00	92.25	84.50	--	--	--	E
440.2779	LPC 12:0	+H	91.6	82.5	95.4	100.0	--	--	BL	--
446.3248	CAR 18:1	+Na	100.0	72.5	72.9	29.4	--	RGBK	--	--

448.3415	CAR 18:2	+Na	100.0	79.5	60.9	24.1	RG	--	--	--
465.2433	LPA 22:6	+H-H ₂ O	74.1	66.3	86.1	100.0	--	--	BL	--
480.3089	LPE 18:0	-H	100.00	94.33	73.76	54.96	--	RGBK	--	--
518.3217	LPC 16:0	+Na	100.0	81.2	99.6	92.7	--	--	--	E
522.3558	LPC 18:0	-H	98.36	100.00	97.45	100.00	--	--	--	E
524.2777	LPE 22:6	-H	100.00	96.54	84.58	76.92	--	RGBK	--	--
540.0532	cyclic denosine diphosphate ribose	-H	79.37	73.38	79.61	100.00	--	--	BL	--
542.3217	LPC 18:2	+Na	100.0	80.7	63.5	36.8	RG	--	--	--
546.353	LPC 18:0	+Na	100.0	81.6	71.5	60.8	--	RGBK	--	--
553.3713	Elastin	+H	91.8	82.9	95.3	100.0	--	--	BL	--
557.0907	Cyanidin 3- 3"-malonylglucoside	+Na	93.8	88.1	95.6	100.0	--	--	BL	--
557.2247	Asp Glu Phe Phe	+H	100.0	72.6	73.9	47.4	--	RGBK	--	--
568.3399	LPC 20:3	+Na	95.2	84.8	100.0	99.3	--	--	--	E
594.3408	PS 22:0	-H	100.00	96.53	97.98	83.54	--	--	--	E
599.3199	LPI 18:0	-H	93.56	100.00	88.26	75.00	--	RGBK	--	--
608.3565	PC 16:0/5:0(COOH)	-H	89.53	78.65	100.00	100.00	--	--	--	E
622.3716	PC 22:1;O2	-H	96.67	100.00	55.75	29.00	RG	--	--	--
636.3873	PC 18:0/5:0(COOH)	-H	100.00	95.12	87.32	68.94	--	RGBK	--	--
664.4193	PC 16:0/9:0(COOH)	-H	94.32	100.00	94.51	77.86	--	RGBK	--	--
667.4414	PA 34:4	-H	80.43	97.83	100.00	100.00	--	--	--	E
667.5244	DG 38:4	+Na	87.8	47.3	100.0	29.7	--	RGBK	--	--
669.4563	PA 34:3	-H	88.79	91.93	100.00	92.83	--	--	--	E
673.4264	DG 38:9	+K	100.0	74.1	97.2	80.6	--	--	--	E
688.3922	ox PC 16:0/9:0CHO	+K	81.4	100.0	75.2	74.1	--	--	--	E
723.4783	CL 72:8	-2H	100.00	72.55	64.71	25.49	--	RGBK	--	--
724.4837	CL 72:7	-2H	100.00	66.67	55.56	33.33	--	RGBK	--	--
732.4221	ox PC 18:0/9:0(COOH)	+K	51.9	55.6	74.1	100.0	--	--	BL	--
732.4815	PC 30:2;O2	-H	73.68	100.00	36.84	15.79	RG	--	--	--
744.4939	PC 30:0	+K	40.4	19.1	85.4	100.0	--	--	BL	--
745.5025	PG 34:2	-H	100.00	76.74	55.81	34.88	RG	--	--	--
747.5188	PG 34:1	-H	100.00	92.03	91.59	70.72	--	RGBK	--	--
748.5216	PC P-36:5	-H	100.00	82.35	90.76	57.98	--	RGBK	--	--
749.5103	PA 38:3	+Na	100.0	55.0	30.0	15.0	RG	--	--	--
754.4783	PE 34:2	+K	92.1	93.9	94.3	100.0	--	--	BL	--
756.5514	PC 32:0	+Na	94.7	86.0	100.0	98.7	--	--	--	E
768.4955	PC 32:2	+K	44.0	38.0	58.0	100.0	--	--	BL	--
768.5537	PE 36:1	+Na	36.8	33.0	94.3	100.0	--	--	BL	--

769.562	SM d36:1	+K	45.5	19.6	100.0	99.1	--	--	BL	--
770.5095	PC 32:1	+K	66.7	59.3	88.4	100.0	--	--	BL	--
774.4499	PE 36:6	+K	100.0	98.1	99.9	94.4	--	--	--	E
780.5514	PC 34:2	+Na	100.0	86.2	96.5	80.2	--	--	--	E
784.585	PC 34:0	+Na	94.2	100.0	85.5	78.4	--	--	--	E
786.5059	PE 38:6	+Na	100.0	87.2	76.0	84.7	--	--	--	E
794.5096	PC 34:3	+K	70.9	42.9	97.3	100.0	--	--	BL	--
798.5408	PC 34:1	+K	90.8	82.6	100.0	87.1	--	--	--	E
802.5357	PC 36:5	+Na	99.7	80.7	97.5	100.0	--	--	--	E
806.5117	PE 38:4	+K	73.0	67.0	100.0	79.1	--	--	--	E
810.5056	PE 42:11	+H	100.0	88.7	91.8	67.0	--	RGBK	--	--
810.6007	PC 36:1	+Na	85.3	100.0	33.6	11.2	RG	--	--	--
812.6163	PC 36:0	+Na	100.0	96.4	97.9	75.7	--	RGBK	--	--
816.5485	PE 40:5	+Na	100.0	94.8	83.1	84.7	--	--	--	E
820.5253	PC 36:4	+K	77.6	61.9	95.3	100.0	--	--	BL	--
824.5566	PC 36:2	+K	100.0	83.0	70.2	40.8	--	RGBK	--	--
828.5514	PC 38:6	+Na	93.0	76.7	99.3	100.0	--	--	--	E
830.5096	PE 40:6	+K	100.0	83.7	85.4	67.9	--	RGBK	--	--
832.5827	PC 38:4	+Na	100.0	79.9	81.8	67.4	--	RGBK	--	--
834.5278	PS 40:6	-H	100.00	95.97	94.90	93.42	--	--	--	E
834.5983	PC 38:3	+Na	100.0	79.2	62.8	44.1	RG	--	--	--
835.5318	PI 34:1	-H	100.00	83.12	99.58	79.75	--	RGBK	--	--
836.6163	PC 38:2	+Na	100.0	86.0	26.9	12.9	RG	--	--	--
837.5471	PI 34:0	-H	100.00	70.19	54.81	25.00	RG	--	--	--
846.5409	PC 38:5	+K	86.5	68.1	100.0	92.9	--	--	--	E
852.5514	PC 40:8	+Na	100.0	81.1	77.2	62.9	--	RGBK	--	--
854.567	PC 40:7	+Na	100.0	80.9	71.4	48.5	--	RGBK	--	--
856.5827	PC 40:6	+Na	100.0	82.8	55.6	35.8	RG	--	--	--
858.5983	PC 40:5	+Na	100.0	82.4	54.7	33.7	RG	--	--	--
860.6107	PC 40:4	+Na	100.0	99.3	22.1	11.0	RG	--	--	--
861.5483	PI 36:2	-H	61.96	100.00	55.43	16.85	RG	--	--	--
885.5489	PI 38:4	-H	95.52	85.90	100.00	97.68	--	--	--	E
887.5596	PI 38:3	-H	88.48	76.04	100.00	85.71	--	--	--	E
888.554	PC18:0_22:6;O	+K	100.0	82.6	21.1	6.4	RG	--	--	--
904.5596	PC O-44:11	+K	100.0	54.1	26.8	7.1	RG	--	--	--
909.5481	PI 40:6	-H	100.00	90.41	93.15	71.23	--	RGBK	--	--

Table B3. Mean abundances and classification of annotated species in mouse 1. R (red) indicate type IIa fibers, G (green) indicate type I fibers, BK (black) indicate type IIx fibers and BL (blue) indicate type IIb fibers. E indicates for everywhere pattern.

mouse 3										
<i>m/z</i>	name	adduct	R	G	BK	BL	RG	RGBK	BL enriched	E
143.1073	Caprylic acid	-H	99.00	97.86	97.79	100.00	--	--	--	E
145.0614	L-Glutamine	-H	91.61	100.00	91.38	87.79	--	--	--	E
146.0454	L-Glutamate	-H	90.38	100.00	90.98	81.74	--	RGBK	--	--
149.009	Tartaric acid	-H	99.13	92.25	98.35	100.00	--	--	--	E
151.0257	Xanthine	-H	67.39	100.00	74.13	51.09	--	RGBK	--	--
152.0217	Creatinine	+K	86.7	76.9	81.5	100.0	--	--	BL	--
152.9954	Propanoyl phosphate	-H	100.00	95.31	97.28	89.38	--	--	--	E
154.0617	Histidine	-H	87.59	84.30	86.08	100.00	--	--	BL	--
167.0207	Uric acid	-H	83.93	100.00	91.07	73.21	--	--	--	E
170.0922	1-methylhistidine	+H	82.6	57.4	83.0	100.0	--	--	BL	--
171.1386	FA 10:0	-H	99.57	98.69	98.64	100.00	--	--	--	E
175.0244	Ascorbic acid	-H	26.78	23.93	28.20	100.00	--	--	BL	--
175.1187	L-Arginine	+H	98.3	90.3	100.0	91.2	--	--	--	E
180.0662	L-Tyrosine	-H	92.18	100.00	88.48	90.95	--	--	--	E
184.0013	Phospho-L-serine	-H	98.93	99.23	98.62	100.00	--	--	--	E
184.094	Carnitine	+Na	78.1	92.2	82.8	100.0	--	--	BL	--
197.1391	Butyrylcholine	+Na	80.9	51.0	80.4	100.0	--	--	BL	--
199.17	FA 12:0	-H	99.83	99.46	99.21	100.00	--	--	--	E
225.1857	FA 14:1	-H	100.00	99.02	99.91	98.84	--	--	--	E
227.1138	Carnosine	+H	77.2	52.8	77.2	100.0	--	--	BL	--
227.2014	FA 14:0	-H	99.62	99.80	100.00	98.78	--	--	--	E
241.1295	Anserine	+H	82.8	61.1	82.5	100.0	--	--	BL	--
245.0426	Phosphatidyl glycerol	-H	77.42	100.00	69.35	67.74	--	--	--	E
251.2013	FA 16:2	-H	100.00	90.34	86.29	52.58	--	RGBK	--	--
253.217	FA 16:1	-H	99.06	97.12	100.00	81.20	--	RGBK	--	--
255.2326	FA 16:0	-H	99.17	97.08	99.35	100.00	--	--	--	E
256.1553	CAR 6:1	-H	95.53	100.00	94.97	98.32	--	--	--	E
258.1706	CAR 6:0	-H	95.57	100.00	93.26	94.99	--	--	--	E
267.0731	Inosine	-H	100.00	95.11	98.49	98.34	--	--	--	E
277.2169	FA 18:3	-H	100.00	89.86	88.40	59.65	--	RGBK	--	--
279.2326	FA 18:2	-H	100.00	90.86	86.44	56.38	--	RGBK	--	--
281.248	FA 18:1	-H	100.00	93.56	93.49	76.73	--	RGBK	--	--
283.2636	FA 18:0	-H	97.76	98.80	98.67	100.00	--	--	--	E
293.2118	9-OxoODE	-H	100.00	75.37	76.38	36.76	--	RGBK	--	--

295.2272	9-HODE	-H	100.00	79.86	80.42	51.73	--	RGBK	--	--
297.2429	9-hydroxy-12Z-octadecenoic cid	-H	100.00	95.44	97.35	89.40	--	--	--	E
299.2011	FA 20:6	-H	97.41	93.92	98.65	100.00	--	--	--	E
303.2326	FA 20:4	-H	96.15	100.00	88.56	69.94	--	RGBK	--	--
305.2483	FA 20:3	-H	100.00	77.27	64.46	35.54	--	RGBK	--	--
306.0762	Glutathione	-H	87.88	85.65	89.79	100.00	--	--	BL	--
307.2642	FA 20:2	-H	100.00	81.96	73.33	50.59	--	RGBK	--	--
309.2797	FA 20:1	-H	100.00	90.71	84.61	65.63	--	RGBK	--	--
317.2498	Pregnanolone	-H	97.40	100.00	93.40	92.40	--	--	--	E
322.0441	Cytidine 2'-phosphate	-H	100.00	88.58	97.26	96.35	--	--	--	E
323.0281	Uridine monophosphate	-H	99.85	100.00	98.71	95.06	--	--	--	E
327.2325	FA 22:6	-H	100.00	88.95	74.47	43.95	--	RGBK	--	--
329.2483	FA 22:5	-H	100.00	82.76	53.45	27.01	RG	--	--	--
331.2643	FA 22:4	-H	100.00	96.07	89.70	68.40	--	RGBK	--	--
332.9569	2-Deoxy-D-ribose 1,5-bisphosphate	+K	86.5	86.2	80.0	100.0	--	--	BL	--
337.311	FA 22:1	-H	100.00	96.25	100.00	99.32	--	--	--	E
339.3264	FA 22:0	-H	97.32	100.00	97.70	98.85	--	--	--	E
346.0554	Adenosine monophosphate	-H	87.66	100.00	87.00	65.06	--	RGBK	--	--
347.0393	Inosine 5'-monophosphateIM P	-H	100.00	97.56	99.97	98.56	--	--	--	E
347.1825	12-oxo-14,18-dihydroxy-9Z,13E,15Z-octadecatrienoic cid	+Na	98.8	100.0	93.6	96.8	--	--	--	E
351.2202	20-hydroxy LTB4	-H	97.91	99.83	99.65	100.00	--	--	--	E
353.2666	MG 16:0	+Na	100.0	98.6	96.0	78.8	--	--	--	E
362.0503	Guanosine 3'-phosphate	-H	93.75	100.00	93.19	80.13	--	RGBK	--	--
367.3576	FA 24:0	-H	97.92	99.13	99.19	100.00	--	--	--	E
368.2799	CAR 14:2	+H	100.0	90.0	77.1	29.0	--	RGBK	--	--
377.2653	MG 18:2	+Na	71.7	100.0	71.9	18.5	--	RGBK	--	--
379.2811	MG 18:1	+Na	85.2	100.0	76.5	42.8	--	RGBK	--	--
400.3417	CAR 16:0	+H	99.4	100.0	98.7	65.8	--	RGBK	--	--
426.0217	ADP	-H	94.33	100.00	92.39	75.37	--	RGBK	--	--
427.2842	MG 22:5	+Na	96.2	88.8	90.2	100.0	--	--	--	E
431.2276	LPA 18:3	-H	98.79	100.00	96.13	95.83	--	--	--	E
440.2779	LPC 12:0	+H	85.1	93.9	86.5	100.0	--	--	BL	--
446.3248	CAR 18:1	+Na	100.0	63.7	89.0	30.2	--	RGBK	--	--
448.3415	CAR 18:2	+Na	100.0	68.9	77.8	28.9	--	RGBK	--	--

465.2433	LPA 22:6	[+H-H ₂ O]	91.7	80.8	87.5	100.0	--	--	BL	--
480.3089	LPE 18:0	-H	100.00	93.96	85.23	47.65	--	RGBK	--	--
518.3217	LPC 16:0	+Na	100.0	96.7	96.5	93.8	--	--	--	E
522.3558	LPC 18:0	-H	96.20	98.91	97.98	100.00	--	--	--	E
524.2777	LPE 22:6	-H	100.00	96.39	72.89	43.37	--	RGBK	--	--
540.0532	cyclic adenosine diphosphate ribose	-H	45.10	25.49	48.04	100.00	--	--	BL	--
542.3217	LPC 18:2	+Na	100.0	79.8	90.8	32.8	--	RGBK	--	--
546.353	LPC 18:0	+Na	100.0	97.3	87.7	49.1	--	RGBK	--	--
553.3713	Elastin	+H	92.8	88.8	91.6	100.0	--	--	BL	--
557.0907	Cyanidin 3- 3"-malonylglucoside	+Na	77.5	67.6	74.5	100.0	--	--	BL	--
557.2247	Asp Glu Phe Phe	+H	95.5	95.1	96.5	100.0	--	--	--	E
568.3399	LPC 20:3	+Na	100.0	92.9	82.1	76.4	--	RGBK	--	--
594.3408	PS 22:0	-H	100.00	91.92	96.15	87.42	--	--	--	E
599.3199	LPI 18:0	-H	97.23	98.29	100.00	93.60	--	--	--	E
608.3565	PC 16:0/5:0(COOH)	-H	77.60	69.96	84.21	100.00	--	--	BL	--
622.3716	PC 22:1;O2	-H	100.00	83.21	53.68	30.19	RG	--	--	--
636.3873	PC 18:0/5:0(COOH)	-H	100.00	91.29	87.36	71.35	--	RGBK	--	--
664.4193	PC 16:0/9:0(COOH)	-H	90.22	93.19	100.00	76.76	--	--	--	E
667.4414	PA 34:4	-H	84.40	90.83	89.91	100.00	--	--	BL	--
667.5244	DG 38:4	+Na	80.4	96.4	100.0	87.1	--	--	--	E
669.4563	PA 34:3	-H	98.28	100.00	99.46	98.91	--	--	--	E
673.4264	DG 38:9	+K	97.9	92.2	100.0	82.4	--	RGBK	--	--
688.3922	ox PC 16:0/9:0CHO	+K	89.4	63.8	100.0	64.9	--	--	--	E
723.4783	CL 72:8	-2H	100.00	62.28	76.05	15.57	--	RGBK	--	--
724.4837	CL 72:7	-2H	100.00	57.63	77.97	16.95	--	RGBK	--	--
732.4221	ox PC 18:0/9:0(COOH)	+K	100.0	71.2	92.7	46.3	--	RGBK	--	--
732.4815	PC 30:2;O2	-H	100.00	52.63	73.68	15.79	--	RGBK	--	--
744.4939	PC 30:0	+K	67.2	42.1	62.1	100.0	--	--	BL	--
745.5025	PG 34:2	-H	100.00	77.58	85.45	24.24	--	RGBK	--	--
747.5188	PG 34:1	-H	100.00	87.36	93.56	56.62	--	RGBK	--	--
748.5216	PC P-36:5	-H	100.00	74.30	90.36	38.96	--	RGBK	--	--
749.5103	PA 38:3	+Na	100.0	89.4	71.2	49.0	RG	--	--	--
754.4783	PE 34:2	+K	86.4	67.1	73.7	100.0	--	--	BL	--
756.5514	PC 32:0	+Na	98.1	100.0	96.2	90.3	--	--	--	E
768.4955	PC 32:2	+K	87.7	77.8	86.2	100.0	--	--	BL	--
768.5537	PE 36:1	+Na	74.1	88.9	81.5	100.0	--	--	BL	--
769.562	SM d36:1	+K	68.0	57.8	66.0	100.0	--	--	BL	--

770.5095	PC 32:1	+K	77.1	64.6	76.3	100.0	--	--	BL	--
774.4499	PE 36:6	+K	94.9	94.0	92.5	100.0	--	--	BL	--
780.5514	PC 34:2	+Na	92.6	97.0	100.0	78.4	--	--	--	E
784.585	PC 34:0	+Na	95.8	97.1	100.0	85.7	--	--	--	E
786.5059	PE 38:6	+Na	73.7	100.0	52.6	82.9	--	--	--	E
794.5096	PC 34:3	+K	88.9	78.0	81.5	100.0	--	--	BL	--
798.5408	PC 34:1	+K	100.0	92.8	99.3	97.4	--	--	--	E
802.5357	PC 36:5	+Na	75.8	73.4	79.2	100.0	--	--	BL	--
806.5117	PE 38:4	+K	96.0	62.2	100.0	83.6	--	--	--	E
810.5056	PE 42:11	+H	92.9	84.3	100.0	44.1	--	RGBK	--	--
810.6007	PC 36:1	+Na	100.0	89.6	93.7	63.3	--	RGBK	--	--
812.6163	PC 36:0	+Na	100.0	72.4	80.3	31.9	--	RGBK	--	--
816.5485	PE 40:5	+Na	84.5	100.0	91.5	69.0	--	RGBK	--	--
820.5253	PC 36:4	+K	72.6	62.1	73.9	100.0	--	--	BL	--
824.5566	PC 36:2	+K	100.0	87.7	86.7	40.1	--	RGBK	--	--
828.5514	PC 38:6	+Na	100.0	99.7	96.6	96.1	--	--	--	E
830.5096	PE 40:6	+K	100.0	76.7	86.9	59.5	--	RGBK	--	--
832.5827	PC 38:4	+Na	100.0	91.2	92.5	64.0	--	RGBK	--	--
834.5278	PS 40:6	-H	100.00	93.16	91.73	80.76	--	RGBK	--	--
834.5983	PC 38:3	+Na	100.0	85.6	73.6	38.0	--	RGBK	--	--
835.5318	PI 34:1	-H	100.00	87.08	91.08	59.38	--	RGBK	--	--
836.6163	PC 38:2	+Na	100.0	82.7	66.5	25.7	RG	--	--	--
837.5471	PI 34:0	-H	100.00	76.30	50.79	14.29	RG	--	--	--
846.5409	PC 38:5	+K	99.6	88.9	91.7	100.0	--	--	--	E
852.5514	PC 40:8	+Na	100.0	90.9	87.4	54.3	--	RGBK	--	--
854.567	PC 40:7	+Na	100.0	86.6	86.0	57.9	--	RGBK	--	--
856.5827	PC 40:6	+Na	100.0	82.9	67.7	31.2	RG	--	--	--
858.5983	PC 40:5	+Na	100.0	82.8	65.3	26.5	RG	--	--	--
860.6107	PC 40:4	+Na	100.0	62.5	47.3	18.8	RG	--	--	--
861.5483	PI 36:2	-H	92.93	100.00	65.15	15.15	RG	--	--	--
885.5489	PI 38:4	-H	100.00	95.06	99.62	88.81	--	--	--	E
887.5596	PI 38:3	-H	100.00	88.84	92.78	78.56	--	--	--	E
888.554	PC18:0_22:6;O	+K	87.5	100.0	40.6	21.9	RG	--	--	--
904.5596	PC O-44:11	+K	76.7	100.0	50.9	16.6	RG	--	--	--
909.5481	PI 40:6	-H	100.00	75.38	63.08	61.54	--	--	--	E

REFERENCES

- (1) Fenn, J. B.; Mann, M.; Meng, C. K.; Wong, S. F.; Whitehouse, C. M. Electrospray Ionization—Principles and Practice. *Mass Spectrom. Rev.* **1990**, 9 (1), 37–70.
- (2) Hillenkamp, F.; Karas, M.; Beavis, R. C.; Chait, B. T. Matrix-Assisted Laser Desorption/Ionization Mass Spectrometry of Biopolymers. *Anal. Chem.* **1991**, 63 (24), 1193A–1203A.
- (3) Norris, J. L.; Caprioli, R. M. Analysis of Tissue Specimens by Matrix-Assisted Laser Desorption/Ionization Imaging Mass Spectrometry in Biological and Clinical Research. *Chem. Rev.* **2013**, 113 (4), 2309–2342.
- (4) Wu, C.; Dill, A. L.; Eberlin, L. S.; Cooks, R. G.; Ifa, D. R. Mass Spectrometry Imaging under Ambient Conditions. *Mass Spectrom. Rev.* **2013**, 32 (3), 218–243.
- (5) Watrous, J. D.; Dorrestein, P. C. Imaging Mass Spectrometry in Microbiology. *Nat. Rev. Microbiol.* **2011**, 9 (9), 683–694.
- (6) Swales, J. G.; Hamm, G.; Clench, M. R.; Goodwin, R. J. A. Mass Spectrometry Imaging and Its Application in Pharmaceutical Research and Development: A Concise Review. *Int. J. Mass Spectrom.* **2019**, 437, 99–112.
- (7) Buchberger, A. R.; DeLaney, K.; Johnson, J.; Li, L. Mass Spectrometry Imaging: A Review of Emerging Advancements and Future Insights. *Anal. Chem.* **2018**, 90 (1), 240–265.
- (8) Rubakhin, S. S.; Jurchen, J. C.; Monroe, E. B.; Sweedler, J. V. Imaging Mass Spectrometry: Fundamentals and Applications to Drug Discovery. *Drug Discov. Today* **2005**, 10 (12), 823–837.
- (9) McDonnell, L. A.; Heeren, R. M. A. Imaging Mass Spectrometry. *Mass Spectrom. Rev.* **2007**, 26 (4), 606–643.
- (10) Caprioli, R. M.; Farmer, T. B.; Gile, J. Molecular Imaging of Biological Samples: Localization of Peptides and Proteins Using MALDI-TOF MS. *Anal. Chem.* **1997**, 69 (23), 4751–4760.
- (11) Cornett, D. S.; Reyzer, M. L.; Chaurand, P.; Caprioli, R. M. MALDI Imaging Mass Spectrometry: Molecular Snapshots of Biochemical Systems. *Nat. Methods* **2007**, 4, 828–833.
- (12) Walch, A.; Rauser, S.; Deininger, S. O.; Höfler, H. MALDI Imaging Mass Spectrometry for Direct Tissue Analysis: A New Frontier for Molecular Histology. *Histochem. Cell Biol.* **2008**, 130 (3), 421–434.

- (13) Chen, H.; Gamez, G.; Zenobi, R. What Can We Learn from Ambient Ionization Techniques? *J. Am. Soc. Mass Spectrom.* **2009**, *20* (11), 1947–1963.
- (14) Laskin, J.; Lanekoff, I. Ambient Mass Spectrometry Imaging Using Direct Liquid Extraction Techniques. *Anal. Chem.* **2016**, *88* (1), 52–73.
- (15) Ifa, D. R.; Wu, C.; Ouyang, Z.; Cooks, R. G. Desorption Electrospray Ionization and Other Ambient Ionization Methods: Current Progress and Preview. *Analyst* **2010**, *135* (4), 669–681.
- (16) Venter, A. R.; Douglass, K. A.; Shelley, J. T.; Hasman, G.; Honarvar, E. Mechanisms of Real-Time, Proximal Sample Processing during Ambient Ionization Mass Spectrometry. *Anal. Chem.* **2014**, *86* (1), 233–249.
- (17) Nemes, P.; Vertes, A. Laser Ablation Electrospray Ionization for Atmospheric Pressure, in Vivo, and Imaging Mass Spectrometry. *Anal. Chem.* **2007**, *79* (21), 8098–8106.
- (18) Sampson, J. S.; Hawkrige, A. M.; Muddiman, D. C. Generation and Detection of Multiply-Charged Peptides and Proteins by Matrix-Assisted Laser Desorption Electrospray Ionization (MALDESI) Fourier Transform Ion Cyclotron Resonance Mass Spectrometry. *J. Am. Soc. Mass Spectrom.* **2006**, *17* (12), 1712–1716.
- (19) Takáts, Z.; Wiseman, J. M.; Gologan, B.; Cooks, R. G. Mass Spectrometry Sampling under Ambient Conditions with Desorption Electrospray Ionization. *Science* (80-.). **2004**, *306* (5695), 471–473.
- (20) Wiseman, J. M.; Ifa, D. R.; Zhu, Y.; Kissinger, C. B.; Manicke, N. E.; Kissinger, P. T.; Cooks, R. G. Desorption Electrospray Ionization Mass Spectrometry: Imaging Drugs and Metabolites in Tissues. *Proc. Natl. Acad. Sci. U. S. A.* **2008**, *105* (47), 18120–18125.
- (21) Roach, P. J.; Laskin, J.; Laskin, A. Nanospray Desorption Electrospray Ionization: An Ambient Method for Liquid-Extraction Surface Sampling in Mass Spectrometry. *Analyst* **2010**, *135*, 2233–2236.
- (22) Van Berkel, G. J.; Sanchez, A. D.; Martin Quirke, J. E. Thin Layer Chromatography Coupled to Mass Spectrometry. In *Handbook of Thin Layer Chromatography*; Sherma. *Fresenius J. Anal. Chem* **1992**, *856* (1), 6216–6223.
- (23) Kertesz, V.; Van Berkel, G. J. Fully Automated Liquid Extraction-Based Surface Sampling and Ionization Using a Chip-Based Robotic Nanoelectrospray Platform. *J. Mass Spectrom.* **2010**, *45* (3), 252–260.
- (24) Laskin, J.; Heath, B. S.; Roach, P. J.; Cazares, L.; Semmes, O. J. Tissue Imaging Using Nanospray Desorption Electrospray Ionization Mass Spectrometry. *Anal. Chem.* **2012**, *84* (1), 141–148.

- (25) Nguyen, S. N.; Kyle, J. E.; Dautel, S. E.; Sontag, R.; Luders, T.; Corley, R.; Ansong, C.; Carson, J.; Laskin, J. Lipid Coverage in Nanospray Desorption Electrospray Ionization Mass Spectrometry Imaging of Mouse Lung Tissues. *Anal. Chem.* **2019**, *91* (18), 11629–11635.
- (26) Laskin, J.; A. Eckert, P.; J. Roach, P.; S. Heath, B.; A. Nizkorodov, S.; Laskin, A. Chemical Analysis of Complex Organic Mixtures Using Reactive Nanospray Desorption Electrospray Ionization Mass Spectrometry. *Anal. Chem.* **2012**, *84* (16), 7179–7187.
- (27) Duncan, K. D.; Fang, R.; Yuan, J.; Chu, R. K.; Dey, S. K.; Burnum-Johnson, K. E.; Lanekoff, I. Quantitative Mass Spectrometry Imaging of Prostaglandins as Silver Ion Adducts with Nanospray Desorption Electrospray Ionization. *Anal. Chem.* **2018**, *90* (12), 7246–7252.
- (28) Weigand, M. R.; Yang, M.; Hu, H.; Zensho, C.; Laskin, J. Enhancement of Lipid Signals with Ammonium Fluoride in Negative Mode Nano-DESI Mass Spectrometry Imaging. *Int. J. Mass Spectrom.* **2022**, *478*, 116859.
- (29) Lanekoff, I.; Stevens, S. L.; Stenzel-Poore, M. P.; Laskin, J. Matrix Effects in Biological Mass Spectrometry Imaging: Identification and Compensation. *Analyst* **2014**, *139* (14), 3528–3532.
- (30) Lanekoff, I.; S. Heath, B.; Liyu, A.; Thomas, M.; P. Carson, J.; Laskin, J. Automated Platform for High-Resolution Tissue Imaging Using Nanospray Desorption Electrospray Ionization Mass Spectrometry. *Anal. Chem.* **2012**, *84* (19), 8351–8356.
- (31) Nguyen, S. N.; Liyu, A. V.; Chu, R. K.; Anderton, C. R.; Laskin, J. Constant-Distance Mode Nanospray Desorption Electrospray Ionization Mass Spectrometry Imaging of Biological Samples with Complex Topography. *Anal. Chem.* **2017**, *89* (2), 1131–1137.
- (32) Nguyen, S. N.; Sontag, R. L.; Carson, J. P.; Corley, R. A.; Ansong, C.; Laskin, J. Towards High-Resolution Tissue Imaging Using Nanospray Desorption Electrospray Ionization Mass Spectrometry Coupled to Shear Force Microscopy. *J. Am. Soc. Mass Spectrom.* **2018**, *29* (2), 316–322.
- (33) Duncan, K. D.; Lanekoff, I. Oversampling To Improve Spatial Resolution for Liquid Extraction Mass Spectrometry Imaging. *Anal. Chem.* **2018**, *90*, 32.
- (34) Yin, R.; Burnum-Johnson, K. E.; Sun, X.; Dey, S. K.; Laskin, J. High Spatial Resolution Imaging of Biological Tissues Using Nanospray Desorption Electrospray Ionization Mass Spectrometry. *Nat. Protoc.* **2019**, *14* (12), 3445–3470.
- (35) Laskin, J.; Eckert, P. A.; Roach, P. J.; Heath, B. S.; Nizkorodov, S. A.; Laskin, A. Chemical Analysis of Complex Organic Mixtures Using Reactive Nanospray Desorption Electrospray Ionization Mass Spectrometry. *Anal. Chem.* **2012**.

- (36) O'Brien, R. E.; Nguyen, T. B.; Laskin, A.; Laskin, J.; Hayes, P. L.; Liu, S.; Jimenez, J. L.; Russell, L. M.; Nizkorodov, S. A.; Goldstein, A. H.; O'Brien, C. ; Nguyen, T. B.; Laskin, A.; Laskin, J.; Hayes, P. L.; Liu, S.; Jimenez, J. L.; Russell, L. M.; Nizkorodov, S. A.; Goldstein, A. H. Probing Molecular Associations of Field-Collected and Laboratory-Generated SOA with Nano-DESI High-Resolution Mass Spectrometry. *J. Geophys. Res. Atmos.* **2013**, *118* (2), 1042–1051.
- (37) Eckert, P. A.; Roach, P. J.; Laskin, A.; Laskin, J. Chemical Characterization of Crude Petroleum Using Nanospray Desorption Electrospray Ionization Coupled with High-Resolution Mass Spectrometry. *Anal. Chem.* **2012**.
- (38) Lanekoff, I.; Geydebekht, O.; Pinchuk, G. E.; Konopka, A. E.; Laskin, J. Spatially Resolved Analysis of Glycolipids and Metabolites in Living *Synechococcus* Sp. PCC 7002 Using Nanospray Desorption Electrospray Ionization. *Analyst* **2013**, *138* (7), 1971–1978.
- (39) Heath, B. S.; Marshall, M. J.; Laskin, J. The Characterization of Living Bacterial Colonies Using Nanospray Desorption Electrospray Ionization Mass Spectrometry. *Methods Mol. Biol.* **2014**, *1151*, 199–208.
- (40) Watrous, J.; Roach, P.; Alexandrov, T.; Heath, B. S.; Yang, J. Y.; Kersten, R. D.; Van Der Voort, M.; Pogliano, K.; Gross, H.; Raaijmakers, J. M.; Moore, B. S.; Laskin, J.; Bandeira, N.; Dorrestein, P. C. Mass Spectral Molecular Networking of Living Microbial Colonies. *Proc. Natl. Acad. Sci. U. S. A.* **2012**, *109* (26).
- (41) Watrous, J.; Roach, P.; Heath, B.; Alexandrov, T.; Laskin, J.; Dorrestein, P. C. Metabolic Profiling Directly from the Petri Dish Using Nanospray Desorption Electrospray Ionization Imaging Mass Spectrometry. *Anal. Chem.* **2013**, *85* (21), 10385–10391.
- (42) Bergman, H. M.; Lindfors, L.; Palm, F.; Kihlberg, J.; Lanekoff, I. Metabolite Aberrations in Early Diabetes Detected in Rat Kidney Using Mass Spectrometry Imaging. *Anal. Bioanal. Chem.* **2019**.
- (43) Dautel, S. E.; Kyle, J. E.; Clair, G.; Sontag, R. L.; Weitz, K. K.; Shukla, A. K.; Nguyen, S. N.; Kim, Y. M.; Zink, E. M.; Luders, T.; Frevert, C. W.; Gharib, S. A.; Laskin, J.; Carson, J. P.; Metz, T. O.; Corley, R. A.; Ansong, C. Lipidomics Reveals Dramatic Lipid Compositional Changes in the Maturing Postnatal Lung. *Sci. Rep.* **2017**, *7*, 40555.
- (44) Lanekoff, I.; Cha, J.; Kyle, J. E.; Dey, S. K.; Laskin, J.; Burnum-Johnson, K. E. Trp53 Deficient Mice Predisposed to Preterm Birth Display Region-Specific Lipid Alterations at the Embryo Implantation Site. *Sci. Rep.* **2016**, *6*, 33023.
- (45) Piehowski, P. D.; Zhu, Y.; Bramer, L. M.; Stratton, K. G.; Zhao, R.; Orton, D. J.; Moore, R. J.; Yuan, J.; Mitchell, H. D.; Gao, Y.; Webb-Robertson, B. J. M.; Dey, S. K.; Kelly, R. T.; Burnum-Johnson, K. E. Automated Mass Spectrometry Imaging of over 2000 Proteins from Tissue Sections at 100-Mm Spatial Resolution. *Nat. Commun.* **2020**, *11* (1), 8.

- (46) Yin, R.; Kyle, J.; Burnum-Johnson, K.; Bloodsworth, K. J.; Sussel, L.; Ansong, C.; Laskin, J. High Spatial Resolution Imaging of Mouse Pancreatic Islets Using Nanospray Desorption Electrospray Ionization Mass Spectrometry. *Anal. Chem.* **2018**, *90* (11), 6548–6555.
- (47) Bergman, H. M.; Lanekoff, I. Profiling and Quantifying Endogenous Molecules in Single Cells Using Nano-DESI MS. *Analyst* **2017**, *142* (19), 3639–3647.
- (48) Muro, E.; Atilla-Gokcumen, G. E.; Eggert, U. S. Lipids in Cell Biology: How Can We Understand Them Better? *Mol. Biol. Cell* **2014**.
- (49) Cajka, T.; Fiehn, O. Toward Merging Untargeted and Targeted Methods in Mass Spectrometry-Based Metabolomics and Lipidomics. *Analytical Chemistry*. 2016.
- (50) Rustam, Y. H.; Reid, G. E. Analytical Challenges and Recent Advances in Mass Spectrometry Based Lipidomics. *Analytical Chemistry*. 2018.
- (51) Han, X.; Gross, R. W. Shotgun Lipidomics: Electrospray Ionization Mass Spectrometric Analysis and Quantitation of Cellular Lipidomes Directly from Crude Extracts of Biological Samples. *Mass Spectrom. Rev.* **2005**.
- (52) Vvedenskaya, O.; Wang, Y.; Ackerman, J. M.; Knittelfelder, O.; Shevchenko, A. Analytical Challenges in Human Plasma Lipidomics: A Winding Path towards the Truth. *TrAC - Trends in Analytical Chemistry*. 2018.
- (53) Han, X. Lipidomics for Studying Metabolism. *Nature Reviews Endocrinology*. 2016.
- (54) Norris, J. L.; Caprioli, R. M. Imaging Mass Spectrometry: A New Tool for Pathology in a Molecular Age. *Proteomics - Clin. Appl.* **2013**.
- (55) Gode, D.; Volmer, D. A. Lipid Imaging by Mass Spectrometry-a Review. *Analyst* **2013**, *138* (5), 1289–1315.
- (56) Zemski Berry, K. A.; Hankin, J. A.; Barkley, R. M.; Spraggins, J. M.; Caprioli, R. M.; Murphy, R. C. MALDI Imaging of Lipid Biochemistry in Tissues by Mass Spectrometry. *Chemical Reviews*. 2011.
- (57) Javanshad, R.; Venter, A. R. Ambient Ionization Mass Spectrometry: Real-Time, Proximal Sample Processing and Ionization. *Analytical Methods*. 2017.
- (58) Perez, C. J.; Bagga, A. K.; Prova, S. S.; Yousefi Taemeh, M.; Ifa, D. R. Review and Perspectives on the Applications of Mass Spectrometry Imaging under Ambient Conditions. *Rapid Communications in Mass Spectrometry*. 2018.
- (59) Eberlin, L. S.; Norton, I.; Dill, A. L.; Golby, A. J.; Ligon, K. L.; Santagata, S.; Graham Cooks, R.; Agar, N. Y. R. Classifying Human Brain Tumors by Lipid Imaging with Mass Spectrometry. *Cancer Res.* **2012**.

- (60) Zhang, J.; Yu, W.; Ryu, S. W.; Lin, J.; Buentello, G.; Tibshirani, R.; Suliburk, J.; Eberlin, L. S. Cardiolipins Are Biomarkers of Mitochondria-Rich Thyroid Oncocytic Tumors. *Cancer Res.* **2016**.
- (61) Javanshad, R.; Honarvar, E.; Venter, A. R. Addition of Serine Enhances Protein Analysis by DESI-MS. *J. Am. Soc. Mass Spectrom.* **2019**.
- (62) Lostun, D.; Perez, C. J.; Licence, P.; Barrett, D. A.; Ifa, D. R. Reactive DESI-MS Imaging of Biological Tissues with Dicationic Ion-Pairing Compounds. *Anal. Chem.* **2015**, 87 (6), 3286–3293.
- (63) Manicke, N. E.; Wiseman, J. M.; Ifa, D. R.; Cooks, R. G. Desorption Electrospray Ionization (DESI) Mass Spectrometry and Tandem Mass Spectrometry (MS/MS) of Phospholipids and Sphingolipids: Ionization, Adduct Formation, and Fragmentation. *J. Am. Soc. Mass Spectrom.* **2008**.
- (64) Eberlin, L. S.; Ferreira, C. R.; Dill, A. L.; Ifa, D. R.; Cheng, L.; Cooks, R. G. Nondestructive, Histologically Compatible Tissue Imaging by Desorption Electrospray Ionization Mass Spectrometry. *ChemBioChem* **2011**, 12 (14), 2129–2132.
- (65) Lanekoff, I.; Heath, B. S.; Liyu, A.; Thomas, M.; Carson, J. P.; Laskin, J. Automated Platform for High-Resolution Tissue Imaging Using Nanospray Desorption Electrospray Ionization Mass Spectrometry. *Anal. Chem.* **2012**, 84 (19), 8351–8356.
- (66) S.N. Nguyen, J.E. Kyle, S.E. Dautel, R. Sontang, T. Luders, R. Corley, C. Ansong, J. Carson, J. Laskin. Lipids Extraction Study of Lung Tissue by Nano-DESI MS Imaging and LC-MS/MS Lipidomic. *Anal. Chem.* **2019**, submitted.
- (67) J. Berg, J. Tymoczko, L. S. *Biochemistry*, 5th ed.; W.H. Freeman: New York, 2002.
- (68) Lettner, A.; Roden, M. Ectopic Fat and Insulin Resistance. *Current Diabetes Reports.* 2008.
- (69) Schweiger, M.; Lass, A.; Zimmermann, R.; Eichmann, T. O.; Zechner, R. Neutral Lipid Storage Disease: Genetic Disorders Caused by Mutations in Adipose Triglyceride Lipase/PNPLA2 or CGI-58 / ABHD5 . *Am. J. Physiol. Metab.* **2009**.
- (70) Romeo, S.; Kozlitina, J.; Xing, C.; Pertsemlidis, A.; Cox, D.; Pennacchio, L. A.; Boerwinkle, E.; Cohen, J. C.; Hobbs, H. H. Genetic Variation in PNPLA3 Confers Susceptibility to Nonalcoholic Fatty Liver Disease. *Nat. Genet.* **2008**.
- (71) Gerbig, S.; Takáts, Z. Analysis of Triglycerides in Food Items by Desorption Electrospray Ionization Mass Spectrometry. *Rapid Commun. Mass Spectrom.* **2010**.
- (72) Jackson, A. U.; Shum, T.; Sokol, E.; Dill, A.; Cooks, R. G. Enhanced Detection of Olefins Using Ambient Ionization Mass Spectrometry: Ag⁺ Adducts of Biologically Relevant Alkenes. *Anal. Bioanal. Chem.* **2011**.

- (73) Wang, C.; Yue, F.; Kuang, S. Muscle Histology Characterization Using H&E Staining and Muscle Fiber Type Classification Using Immunofluorescence Staining. *BIO-PROTOCOL* **2017**.
- (74) Cequier-Sánchez, E.; Rodríguez, C.; Ravelo, Á. G.; Zárate, R. Dichloromethane as a Solvent for Lipid Extraction and Assessment of Lipid Classes and Fatty Acids from Samples of Different Natures. *J. Agric. Food Chem.* **2008**.
- (75) Watrous, J.; Roach, P.; Heath, B.; Alexandrov, T.; Laskin, J.; Dorrestein, P. C. Metabolic Profiling Directly from the Petri Dish Using Nanospray Desorption Electrospray Ionization Imaging Mass Spectrometry. *Anal. Chem.* **2013**.
- (76) Cech, N. B.; Enke, C. G. Practical Implications of Some Recent Studies in Electrospray Ionization Fundamentals. *Mass Spectrom. Rev.* **2001**.
- (77) Gaiser, R. A.; Pessia, A.; Ateeb, Z.; Davanian, H.; Fernández Moro, C.; Alkharaan, H.; Healy, K.; Ghazi, S.; Arnelo, U.; Valente, R.; Velagapudi, V.; Sällberg Chen, M.; Del Chiaro, M. Integrated Targeted Metabolomic and Lipidomic Analysis: A Novel Approach to Classifying Early Cystic Precursors to Invasive Pancreatic Cancer. *Sci. Rep.* **2019**, 9 (1), 10208.
- (78) Contrepois, K.; Mahmoudi, S.; Ubhi, B. K.; Papsdorf, K.; Hornburg, D.; Brunet, A.; Snyder, M. Cross-Platform Comparison of Untargeted and Targeted Lipidomics Approaches on Aging Mouse Plasma. *Sci. Rep.* **2018**.
- (79) Wu, C.; Ifa, D. R.; Manicke, N. E.; Cooks, R. G. Rapid, Direct Analysis of Cholesterol by Charge Labeling in Reactive Desorption Electrospray Ionization. *Anal. Chem.* **2009**, 81 (18), 7618–7624.
- (80) Girod, M.; Moyano, E.; Campbell, D. I.; Cooks, R. G. Accelerated Bimolecular Reactions in Microdroplets Studied by Desorption Electrospray Ionization Mass Spectrometry. *Chem. Sci.* **2011**, 2 (3), 501–510.
- (81) Goto-Inoue, N.; Morisasa, M.; Machida, K.; Furuichi, Y.; Fujii, N. L.; Miura, S.; Mori, T. Characterization of Myofiber-Type-Specific Molecules Using Mass Spectrometry Imaging. *Rapid Commun. Mass Spectrom.* **2019**.
- (82) Tsai, Y. H.; Garrett, T. J.; Carter, C. S.; Yost, R. A. Metabolomic Analysis of Oxidative and Glycolytic Skeletal Muscles by Matrix-Assisted Laser Desorption/Ionizationmass Spectrometric Imaging (MALDI MSI). *J. Am. Soc. Mass Spectrom.* **2015**.
- (83) Lanekoff, I.; Burnum-Johnson, K.; Thomas, M.; Short, J.; Carson, J. P.; Cha, J.; Dey, S. K.; Yang, P.; Prieto Conaway, M. C.; Laskin, J. High-Speed Tandem Mass Spectrometric in Situ Imaging by Nanospray Desorption Electrospray Ionization Mass Spectrometry. *Anal. Chem.* **2013**, 85 (20), 9596–9603.

- (84) Duffin, K. L.; Henion, J. D.; Shieh, J. J. Electrospray and Tandem Mass Spectrometry Characterization of Acylglycerol Mixtures That Are Dissolved in Nonpolar Solvents. *Anal. Chem.* **1991**.
- (85) Harayama, T.; Riezman, H. Understanding the Diversity of Membrane Lipid Composition. *Nat. Rev. Mol. Cell Biol.* **2018**, *19* (5), 281–296.
- (86) Fahy, E.; Cotter, D.; Sud, M.; Subramaniam, S. Lipid Classification, Structures and Tools. *Biochim. Biophys. Acta - Mol. Cell Biol. Lipids* **2011**, *1811* (11), 637–647.
- (87) Han, X.; Gross, R. W. Shotgun Lipidomics: Electrospray Ionization Mass Spectrometric Analysis and Quantitation of Cellular Lipidomes Directly from Crude Extracts of Biological Samples. *Mass Spectrom. Rev.* **2005**, *24* (3), 367–412.
- (88) Porta Siegel, T.; Ekroos, K.; Ellis, S. R. Reshaping Lipid Biochemistry by Pushing Barriers in Structural Lipidomics. *Angewandte Chemie - International Edition*. 2019, pp 6492–6501.
- (89) Bonney, J. R.; Prentice, B. M. Perspective on Emerging Mass Spectrometry Technologies for Comprehensive Lipid Structural Elucidation. *Anal. Chem.* **2021**, *93* (16).
- (90) Claes, B. S. R.; Takeo, E.; Fukusaki, E.; Shimma, S.; Heeren, R. M. A. Imaging Isomers on a Biological Surface: A Review. *Mass Spectrometry*. 2019.
- (91) Young, R. S. E.; Claes, B. S. R.; Bowman, A. P.; Williams, E. D.; Shepherd, B.; Perren, A.; Poad, B. L. J.; Ellis, S. R.; Heeren, R. M. A.; Sadowski, M. C.; Blanksby, S. J. Isomer-Resolved Imaging of Prostate Cancer Tissues Reveals Specific Lipid Unsaturation Profiles Associated With Lymphocytes and Abnormal Prostate Epithelia. *Front. Endocrinol. (Lausanne)*. **2021**, *12*.
- (92) A. Macias, L.; S. Brodbelt, J. Enhanced Characterization of Cardiolipins via Hybrid 193 Nm Ultraviolet Photodissociation Mass Spectrometry. *Anal. Chem.* **2022**, *0* (0).
- (93) Lin, Q.; Li, P.; Fang, M.; Zhang, D.; Xia, Y. Deep Profiling of Aminophospholipids Reveals a Dysregulated Desaturation Pattern in Breast Cancer Cell Lines. *Anal. Chem.* **2021**, *94* (2), 820–828.
- (94) J. Swiner, D.; S. Kulyk, D.; Osae, H.; R. Durisek III, G.; K. Badu-Tawiah, A. Reactive Thread Spray Mass Spectrometry for Localization of C=C Bonds in Free Fatty Acids: Applications for Obesity Diagnosis. *Anal. Chem.* **2022**, *94* (5), 2358–2365.
- (95) Sansone, A.; Tolika, E.; Louka, M.; Sunda, V.; Deplano, S.; Melchiorre, M.; Anagnostopoulos, D.; Chatgililoglu, C.; Formisano, C.; Di Micco, R.; Mennella, M. R. F.; Ferreri, C. Hexadecenoic Fatty Acid Isomers in Human Blood Lipids and Their Relevance for the Interpretation of Lipidomic Profiles. *PLoS One* **2016**, *11* (4).
- (96) Zhang, W.; Zhang, D.; Chen, Q.; Wu, J.; Ouyang, Z.; Xia, Y. Online Photochemical Derivatization Enables Comprehensive Mass Spectrometric Analysis of Unsaturated Phospholipid Isomers. *Nat. Commun.* **2019**, *10* (1).

- (97) Huynh, K.; Lim, W. L. F.; Giles, C.; Jayawardana, K. S.; Salim, A.; Mellett, N. A.; Smith, A. A. T.; Olshansky, G.; Drew, B. G.; Chatterjee, P.; Martins, I.; Laws, S. M.; Bush, A. I.; Rowe, C. C.; Villemagne, V. L.; Ames, D.; Masters, C. L.; Arnold, M.; Nho, K.; Saykin, A. J.; Baillie, R.; Han, X.; Kaddurah-Daouk, R.; Martins, R. N.; Meikle, P. J. Concordant Peripheral Lipidome Signatures in Two Large Clinical Studies of Alzheimer's Disease. *Nat. Commun.* **2020**, *11* (1).
- (98) Ma, X.; Xia, Y. Pinpointing Double Bonds in Lipids by Paternò-Büchi Reactions and Mass Spectrometry. *Angew. Chemie - Int. Ed.* **2014**, *53* (10), 2592–2596.
- (99) Harris, R. A.; May, J. C.; Stinson, C. A.; Xia, Y.; McLean, J. A. Determining Double Bond Position in Lipids Using Online Ozonolysis Coupled to Liquid Chromatography and Ion Mobility-Mass Spectrometry. *Anal. Chem.* **2018**, *90* (3), 1915–1924.
- (100) Tang, S.; Cheng, H.; Yan, X. On-Demand Electrochemical Epoxidation in Nano-Electrospray Ionization Mass Spectrometry to Locate Carbon–Carbon Double Bonds. *Angew. Chemie - Int. Ed.* **2020**, *59* (1), 209–214.
- (101) Adhikari, S.; Zhang, W.; Xie, X.; Chen, Q.; Xia, Y. Shotgun Analysis of Diacylglycerols Enabled by Thiol-Ene Click Chemistry. *Anal. Chem.* **2018**, *90* (8), 5239–5246.
- (102) Kuo, T. H.; Chung, H. H.; Chang, H. Y.; Lin, C. W.; Wang, M. Y.; Shen, T. L.; Hsu, C. C. Deep Lipidomics and Molecular Imaging of Unsaturated Lipid Isomers: A Universal Strategy Initiated by MCPBA Epoxidation. *Anal. Chem.* **2019**, *91* (18), 11905–11915.
- (103) Bednařík, A.; Bölsker, S.; Soltwisch, J.; Dreisewerd, K. An On-Tissue Paternò-Büchi Reaction for Localization of Carbon–Carbon Double Bonds in Phospholipids and Glycolipids by Matrix-Assisted Laser-Desorption–Ionization Mass-Spectrometry Imaging. *Angew. Chemie - Int. Ed.* **2018**, *57* (37), 12092–12096.
- (104) Wäldchen, F.; Spengler, B.; Heiles, S. Reactive Matrix-Assisted Laser Desorption/Ionization Mass Spectrometry Imaging Using an Intrinsically Photoreactive Paternò-Büchi Matrix for Double-Bond Localization in Isomeric Phospholipids. *J. Am. Chem. Soc.* **2019**, *141* (30), 11816–11820.
- (105) Williams, P. E.; Klein, D. R.; Greer, S. M.; Brodbelt, J. S. Pinpointing Double Bond and Sn-Positions in Glycerophospholipids via Hybrid 193 Nm Ultraviolet Photodissociation (UVPD) Mass Spectrometry. *J. Am. Chem. Soc.* **2017**, *139* (44).
- (106) Marshall, D. L.; Criscuolo, A.; Young, R. S. E.; Poad, B. L. J.; Zeller, M.; Reid, G. E.; Mitchell, T. W.; Blanksby, S. J. Mapping Unsaturation in Human Plasma Lipids by Data-Independent Ozone-Induced Dissociation. *J. Am. Soc. Mass Spectrom.* **2019**, *30* (9), 1621–1630.
- (107) Randolph, C. E.; Blanksby, S. J.; McLuckey, S. A. Toward Complete Structure Elucidation of Glycerophospholipids in the Gas Phase through Charge Inversion Ion/Ion Chemistry. *Anal. Chem.* **2020**, *92* (1).

- (108) Feider, C. L.; MacIas, L. A.; Brodbelt, J. S.; Eberlin, L. S. Double Bond Characterization of Free Fatty Acids Directly from Biological Tissues by Ultraviolet Photodissociation. *Anal. Chem.* **2020**, 92 (12), 8386–8395.
- (109) Paine, M. R. L.; Poad, B. L. J.; Eijkel, G. B.; Marshall, D. L.; Blanksby, S. J.; Heeren, R. M. A.; Ellis, S. R. Mass Spectrometry Imaging with Isomeric Resolution Enabled by Ozone-Induced Dissociation. *Angew. Chemie - Int. Ed.* **2018**, 57 (33), 10530–10534.
- (110) Specker, J. T.; Van Orden, S. L.; Ridgeway, M. E.; Prentice, B. M. Identification of Phosphatidylcholine Isomers in Imaging Mass Spectrometry Using Gas-Phase Charge Inversion Ion/Ion Reactions. *Anal. Chem.* **2020**, 92 (19).
- (111) Girotti, A. W. Photosensitized Oxidation of Membrane Lipids: Reaction Pathways, Cytotoxic Effects, and Cytoprotective Mechanisms. *J. Photochem. Photobiol. B Biol.* **2001**, 63 (1–3), 103–113.
- (112) Bacellar, I. O. L.; Baptista, M. S. Mechanisms of Photosensitized Lipid Oxidation and Membrane Permeabilization. *ACS Omega* **2019**, 4 (26), 21636–21646.
- (113) Kato, S.; Nakagawa, K.; Suzuki, Y.; Asai, A.; Nagao, M.; Nagashima, K.; Oikawa, S.; Miyazawa, T. Liquid Chromatography-Tandem Mass Spectrometry Determination of Human Plasma 1-Palmitoyl-2-Hydroperoxyoctadecadienoyl-Phosphatidylcholine Isomers via Promotion of Sodium Adduct Formation. *Anal. Biochem.* **2015**, 471, 51–60.
- (114) Ito, J.; Mizuochi, S.; Nakagawa, K.; Kato, S.; Miyazawa, T. Tandem Mass Spectrometry Analysis of Linoleic and Arachidonic Acid Hydroperoxides via Promotion of Alkali Metal Adduct Formation. *Anal. Chem.* **2015**, 87 (9), 4980–4987.
- (115) Kato, S.; Shimizu, N.; Hanzawa, Y.; Otoki, Y.; Ito, J.; Kimura, F.; Takekoshi, S.; Sakaino, M.; Sano, T.; Eitsuka, T.; Miyazawa, T.; Nakagawa, K. Determination of Triacylglycerol Oxidation Mechanisms in Canola Oil Using Liquid Chromatography–Tandem Mass Spectrometry. *Sci. Food* **2018**, 2 (1).
- (116) DeRosa, M. C.; Crutchley, R. J. Photosensitized Singlet Oxygen and Its Applications. *Coordination Chemistry Reviews.* 2002, pp 351–371.
- (117) Klein, D. R.; Feider, C. L.; Garza, K. Y.; Lin, J. Q.; Eberlin, L. S.; Brodbelt, J. S. Desorption Electrospray Ionization Coupled with Ultraviolet Photodissociation for Characterization of Phospholipid Isomers in Tissue Sections. *Anal. Chem.* **2018**, 90 (17), 10100–10104.
- (118) Stoekli, M.; Chaurand, P.; Hallahan, D. E.; Caprioli, R. M. Imaging Mass Spectrometry: A New Technology for the Analysis of Protein Expression in Mammalian Tissues. *Nat. Med.* **2001**, 7, 493–496.
- (119) Nilsson, A.; Goodwin, R. J. A.; Shariatgorji, M.; Vallianatou, T.; Webbhorn, P. J. H.; Andrén, P. E. Mass Spectrometry Imaging in Drug Development. *Anal. Chem.* **2015**, 87, 1437–1455.

- (120) Lanni, E. J.; Rubakhin, S. S.; Sweedler, J. V. Mass Spectrometry Imaging and Profiling of Single Cells. *J. Proteomics* **2012**, 75 (16), 5036–5051.
- (121) Tsubata, Y.; Hayashi, M.; Tanino, R.; Aikawa, H.; Ohuchi, M.; Tamura, K.; Fujiwara, Y.; Isobe, T.; Hamada, A. Evaluation of the Heterogeneous Tissue Distribution of Erlotinib in Lung Cancer Using Matrix-Assisted Laser Desorption Ionization Mass Spectrometry Imaging. *Sci. Rep.* **2017**, 7, 12622.
- (122) Jarmusch, A. K.; Pirro, V.; Baird, Z.; Hattab, E. M.; Cohen-Gadol, A. A.; Cooks, R. G. Lipid and Metabolite Profiles of Human Brain Tumors by Desorption Electrospray Ionization-MS. *Proc. Natl. Acad. Sci. U. S. A.* **2016**, 113 (6), 1486–1491.
- (123) Garikapati, V.; Karnati, S.; Bhandari, D. R.; Baumgart-Vogt, E.; Spengler, B. High-Resolution Atmospheric-Pressure MALDI Mass Spectrometry Imaging Workflow for Lipidomic Analysis of Late Fetal Mouse Lungs. *Sci. Rep.* **2019**, 9, 3192.
- (124) Bruinen, A. L.; Van Oevelen, C.; Eijkel, G. B.; Van Heerden, M.; Cuyckens, F.; Heeren, R. M. A. Mass Spectrometry Imaging of Drug Related Crystal-Like Structures in Formalin-Fixed Frozen and Paraffin-Embedded Rabbit Kidney Tissue Sections. *J. Am. Soc. Mass Spectrom.* **2016**, 27 (1), 117–123.
- (125) Rao, T.; Shao, Y.; Hamada, N.; Li, Y.; Ye, H.; Kang, D.; Shen, B.; Li, X.; Yin, X.; Zhu, Z.; Li, H.; Xie, L.; Wang, G.; Liang, Y. Pharmacokinetic Study Based on a Matrix-Assisted Laser Desorption/Ionization Quadrupole Ion Trap Time-of-Flight Imaging Mass Microscope Combined with a Novel Relative Exposure Approach: A Case of Octreotide in Mouse Target Tissues. *Anal. Chim. Acta* **2017**, 952, 71–80.
- (126) Hamilton, B. R.; Marshall, D. L.; Casewell, N. R.; Harrison, R. A.; Blanksby, S. J.; Undheim, E. A. B. Mapping Enzyme Activity on Tissue by Functional Mass Spectrometry Imaging. *Angew. Chemie - Int. Ed.* **2020**, 59, 3855–3858.
- (127) Eberlin, L. S.; Ferreira, C. R.; Dill, A. L.; Ifa, D. R.; Cooks, R. G. Desorption Electrospray Ionization Mass Spectrometry for Lipid Characterization and Biological Tissue Imaging. *Biochim. Biophys. Acta - Mol. Cell Biol. Lipids* **2011**, 1811 (11), 946–960.
- (128) Spengler, B. Mass Spectrometry Imaging of Biomolecular Information. *Anal. Chem.* **2015**, 87 (1), 64–82.
- (129) Bergman, H.-M.; Lundin, E.; Andersson, M.; Lanekoff, I. Quantitative Mass Spectrometry Imaging of Small-Molecule Neurotransmitters in Rat Brain Tissue Sections Using Nanospray Desorption Electrospray Ionization. *Analyst* **2016**, 141 (12), 3686–3695.
- (130) Lanekoff, I.; Thomas, M.; Carson, J. P.; Smith, J. N.; Timchalk, C.; Laskin, J. Imaging Nicotine in Rat Brain Tissue by Use of Nanospray Desorption Electrospray Ionization Mass Spectrometry. *Anal. Chem.* **2013**, 85 (2), 882–889.

- (131) Burnum, K. E.; Cornett, D. S.; Puolitaival, S. M.; Milne, S. B.; Myers, D. S.; Tranguch, S.; Brown, H. A.; Dey, S. K.; Caprioli, R. M. Spatial and Temporal Alterations of Phospholipids Determined by Mass Spectrometry during Mouse Embryo Implantation. *J. Lipid Res.* **2009**, *50* (11), 2290–2298.
- (132) Unsihuay, D.; Su, P.; Hu, H.; Qiu, J.; Kuang, S.; Li, Y.; Sun, X.; Dey, S. K.; Laskin, J. Inside Cover: Imaging and Analysis of Isomeric Unsaturated Lipids through Online Photochemical Derivatization of Carbon–Carbon Double Bonds (Angew. Chem. Int. Ed. 14/2021). *Angew. Chemie Int. Ed.* **2021**, *60* (14), 7450–7450.
- (133) Bednařík, A.; Preisler, J.; Bezdeková, D.; Machálková, M.; Hendrych, M.; Navrátilová, J.; Knopfová, L.; Moskovets, E.; Soltwisch, J.; Dreisewerd, K. Ozonization of Tissue Sections for MALDI MS Imaging of Carbon–Carbon Double Bond Positional Isomers of Phospholipids. *Anal. Chem.* **2020**, *92* (9), 6245–6250.
- (134) Paglia, G.; Astarita, G. Metabolomics and Lipidomics Using Traveling-Wave Ion Mobility Mass Spectrometry. *Nat. Protoc.* **2017**, *12*, 797–813.
- (135) Dodds, J. N.; Baker, E. S. Ion Mobility Spectrometry: Fundamental Concepts, Instrumentation, Applications, and the Road Ahead. *J. Am. Soc. Mass Spectrom.* **2019**, *30* (11), 2185–2195.
- (136) Kiss, A.; Heeren, R. M. A. Size, Weight and Position: Ion Mobility Spectrometry and Imaging MS Combined. *Anal. Bioanal. Chem.* **2011**, *399*, 2623–2634.
- (137) Sans, M.; Feider, C. L.; Eberlin, L. S. Advances in Mass Spectrometry Imaging Coupled to Ion Mobility Spectrometry for Enhanced Imaging of Biological Tissues. *Curr. Opin. Chem. Biol.* **2018**, *42*, 138–146.
- (138) May, J. C.; Goodwin, C. R.; Lareau, N. M.; Leaptrot, K. L.; Morris, C. B.; Kurulugama, R. T.; Mordehai, A.; Klein, C.; Barry, W.; Darland, E.; Overney, G.; Imatani, K.; Stafford, G. C.; Fjeldsted, J. C.; McLean, J. A. Conformational Ordering of Biomolecules in the Gas Phase: Nitrogen Collision Cross Sections Measured on a Prototype High Resolution Drift Tube Ion Mobility-Mass Spectrometer. *Anal. Chem.* **2014**, *86* (4), 2107–2116.
- (139) Bowers, M. T. Ion Mobility Spectrometry: A Personal View of Its Development at UCSB. *Int. J. Mass Spectrom.* **2014**, *370*, 75–95.
- (140) Bohrer, B. C.; Merenbloom, S. I.; Koeniger, S. L.; Hilderbrand, A. E.; Clemmer, D. E. Biomolecule Analysis by Ion Mobility Spectrometry. *Annu. Rev. Anal. Chem.* **2008**, *1*, 293–327.
- (141) Stow, S. M.; Causon, T. J.; Zheng, X.; Kurulugama, R. T.; Mairinger, T.; May, J. C.; Rennie, E. E.; Baker, E. S.; Smith, R. D.; McLean, J. A.; Hann, S.; Fjeldsted, J. C. An Interlaboratory Evaluation of Drift Tube Ion Mobility-Mass Spectrometry Collision Cross Section Measurements. *Anal. Chem.* **2017**, *89* (17), 9048–9055.

- (142) Picache, J. A.; Rose, B. S.; Balinski, A.; Leaptrot, K. L.; Sherrod, S. D.; May, J. C.; McLean, J. A. Collision Cross Section Compendium to Annotate and Predict Multi-Omic Compound Identities. *Chem. Sci.* **2019**, *10*, 983–993.
- (143) Zheng, X.; Aly, N. A.; Zhou, Y.; Dupuis, K. T.; Bilbao, A.; Paurus, V. L.; Orton, D. J.; Wilson, R.; Payne, S. H.; Smith, R. D.; Baker, E. S. A Structural Examination and Collision Cross Section Database for over 500 Metabolites and Xenobiotics Using Drift Tube Ion Mobility Spectrometry. *Chem. Sci.* **2017**, *8*, 7724–7736.
- (144) Plante, P. L.; Francovic-Fontaine, É.; May, J. C.; McLean, J. A.; Baker, E. S.; Laviolette, F.; Marchand, M.; Corbeil, J. Predicting Ion Mobility Collision Cross-Sections Using a Deep Neural Network: DeepCCS. *Anal. Chem.* **2019**, *91* (8), 5191–5199.
- (145) Jackson, S. N.; Ugarov, M.; Egan, T.; Post, J. D.; Langlais, D.; Schultz, J. A.; Woods, A. S. MALDI-Ion Mobility-TOFMS Imaging of Lipids in Rat Brain Tissue. *J. Mass Spectrom.* **2007**, *42* (8), 1093–1098.
- (146) Spraggins, J. M.; Djambazova, K. V.; Rivera, E. S.; Migas, L. G.; Neumann, E. K.; Fuetterer, A.; Suetering, J.; Goedecke, N.; Ly, A.; Van De Plas, R.; Caprioli, R. M. High-Performance Molecular Imaging with MALDI Trapped Ion-Mobility Time-of-Flight (TimsTOF) Mass Spectrometry. *Anal. Chem.* **2019**, *91* (22), 14552–14560.
- (147) Feider, C. L.; Elizondo, N.; Eberlin, L. S. Ambient Ionization and FAIMS Mass Spectrometry for Enhanced Imaging of Multiply Charged Molecular Ions in Biological Tissues. *Anal. Chem.* **2016**, *88* (23), 11533–11541.
- (148) Bennett, R. V.; Gamage, C. M.; Galhena, A. S.; Fernández, F. M. Contrast-Enhanced Differential Mobility-Desorption Electrospray Ionization-Mass Spectrometry Imaging of Biological Tissues. *Anal. Chem.* **2014**, *86* (8), 3756–3763.
- (149) Griffiths, R. L.; Hughes, J. W.; Abbatiello, S. E.; Belford, M. W.; Styles, I. B.; Cooper, H. J. Comprehensive LESA Mass Spectrometry Imaging of Intact Proteins by Integration of Cylindrical FAIMS. *Anal. Chem.* **2020**, *92* (4), 2885–2890.
- (150) Shrestha, B.; Vertes, A. High-Throughput Cell and Tissue Analysis with Enhanced Molecular Coverage by Laser Ablation Electrospray Ionization Mass Spectrometry Using Ion Mobility Separation. *Anal. Chem.* **2014**, *86* (9), 4308–4315.
- (151) Ekelöf, M.; Dodds, J.; Khodjaniyazova, S.; Garrard, K. P.; Baker, E. S.; Muddiman, D. C. Coupling IR-MALDESI with Drift Tube Ion Mobility-Mass Spectrometry for High-Throughput Screening and Imaging Applications. *J. Am. Soc. Mass Spectrom.* **2020**, *31* (3), 642–650.
- (152) Sans, M.; Feider, C. L.; Eberlin, L. S. Advances in Mass Spectrometry Imaging Coupled to Ion Mobility Spectrometry for Enhanced Imaging of Biological Tissues. *Curr. Opin. Chem. Biol.* **2018**, *42*, 138–146.

- (153) Lanekoff, I.; Thomas, M.; Laskin, J. Shotgun Approach for Quantitative Imaging of Phospholipids Using Nanospray Desorption Electrospray Ionization Mass Spectrometry. *Anal. Chem.* **2014**, *86* (3), 1872–1880.
- (154) Lanekoff, I.; Burnum-Johnson, K.; Thomas, M.; Cha, J.; Dey, S. K.; Yang, P.; Prieto Conaway, M. C.; Laskin, J. Three-Dimensional Imaging of Lipids and Metabolites in Tissues by Nanospray Desorption Electrospray Ionization Mass Spectrometry. *Anal. Bioanal. Chem.* **2015**, *407* (8), 2063–2071.
- (155) Mesa Sanchez, D.; Creger, S.; Singla, V.; Kurulugama, R. T.; Fjeldsted, J. C.; Laskin, J. An Ion Mobility-Mass Spectrometry Imaging Workflow. *J. Am. Soc. Mass Spectrom.* **2020**, *0* (0).
- (156) MacLean, B.; Tomazela, D. M.; Shulman, N.; Chambers, M.; Finney, G. L.; Frewen, B.; Kern, R.; Tabb, D. L.; Liebler, D. C.; MacCoss, M. J. Skyline: An Open Source Document Editor for Creating and Analyzing Targeted Proteomics Experiments. *Bioinformatics* **2010**, *26* (7), 966–968.
- (157) Hines, K. M.; Herron, J.; Xu, L. Assessment of Altered Lipid Homeostasis by HILIC-Ion Mobility-Mass Spectrometry-Based Lipidomics. *J. Lipid Res.* **2017**, *58* (4), 809–819.
- (158) Kyle, J. E.; Aly, N.; Zheng, X.; Burnum-Johnson, K. E.; Smith, R. D.; Baker, E. S. Evaluating Lipid Mediator Structural Complexity Using Ion Mobility Spectrometry Combined with Mass Spectrometry. *Bioanalysis* **2018**, *10* (5).
- (159) Domingo-Almenara, X.; Rafael Montenegro-Burke, J.; Guijas, C.; L.-W. Majumder, E.; Paul Benton, H.; Siuzdak, G. Autonomous METLIN-Guided In-Source Fragment Annotation for Untargeted Metabolomics. *Anal. Chem.* **2019**, *91* (5), 3246–3253.
- (160) Luxembourg, S. L.; Mize, T. H.; McDonnell, L. A.; Heeren, R. M. A. High-Spatial Resolution Mass Spectrometric Imaging of Peptide and Protein Distributions on a Surface. *Anal. Chem.* **2004**, *76* (18), 5339–5344.
- (161) Djambazova, K. V.; Klein, D. R.; Migas, L. G.; Neumann, E. K.; Rivera, E. S.; Van De Plas, R.; Caprioli, R. M.; Spraggins, J. M. Resolving the Complexity of Spatial Lipidomics Using MALDI TIMS Imaging Mass Spectrometry. *Anal. Chem.* **2020**, *92* (19), 13290–13297.
- (162) Chiarello, D. I.; Abad, C.; Rojas, D.; Toledo, F.; Vázquez, C. M.; Mate, A.; Sobrevia, L.; Marín, R. Oxidative Stress: Normal Pregnancy versus Preeclampsia. *Biochimica et Biophysica Acta - Molecular Basis of Disease*. 2020.
- (163) Groessl, M.; Graf, S.; Knochenmuss, R. High Resolution Ion Mobility-Mass Spectrometry for Separation and Identification of Isomeric Lipids. *Analyst* **2015**, *140* (20), 6904–6911.
- (164) N. Dodds, J.; C. May, J.; A. McLean, J. Correlating Resolving Power, Resolution, and Collision Cross Section: Unifying Cross-Platform Assessment of Separation Efficiency in Ion Mobility Spectrometry. *Anal. Chem.* **2017**, *89* (22), 12176–12184.

- (165) Owen, J. B.; Allan Butterfiel, D. Measurement of Oxidized/Reduced Glutathione Ratio. In *Methods in Molecular Biology*; 2010; Vol. 648, pp 269–277.
- (166) Zitka, O.; Skalickova, S.; Gumulec, J.; Masarik, M.; Adam, V.; Hubalek, J.; Trnkova, L.; Kruseova, J.; Eckschlager, T.; Kizek, R. Redox Status Expressed as GSH:GSSG Ratio as a Marker for Oxidative Stress in Paediatric Tumour Patients. *Oncol. Lett.* **2012**, 4 (6), 1247–1253.
- (167) Stauber, J.; MacAleese, L.; Franck, J.; Claude, E.; Snel, M.; Kaletas, B. K.; Wiel, I. M. V. D.; Wisztorski, M.; Fournier, I.; Heeren, R. M. A. On-Tissue Protein Identification and Imaging by MALDI-Ion Mobility Mass Spectrometry. *J. Am. Soc. Mass Spectrom.* **2010**, 21 (3), 338–347.
- (168) Chughtai, K.; Jiang, L.; Greenwood, T. R.; Glunde, K.; Heeren, R. M. A. Mass Spectrometry Images Acylcarnitines, Phosphatidylcholines, and Sphingomyelin in MDA-MB-231 Breast Tumor Models. *J. Lipid Res.* **2013**, 54 (2), 333–344.
- (169) Mukund, K.; Subramaniam, S. Skeletal Muscle: A Review of Molecular Structure and Function, in Health and Disease. *Wiley Interdisciplinary Reviews: Systems Biology and Medicine*. Wiley-Blackwell January 1, 2020, p e1462.
- (170) Schiaffino, S.; Reggiani, C. Fiber Types in Mammalian Skeletal Muscles. *Physiol. Rev.* **2011**, 91 (4), 1447–1531.
- (171) Schiaffino, S. Muscle Fiber Type Diversity Revealed by Anti-Myosin Heavy Chain Antibodies. *FEBS Journal*. Blackwell Publishing Ltd October 1, 2018, pp 3688–3694.
- (172) Hargreaves, M.; Spriet, L. L. Skeletal Muscle Energy Metabolism during Exercise. *Nat. Metab.*
- (173) Scott, W.; Stevens, J.; Binder-Macleod, S. A. Human Skeletal Muscle Fiber Type Classifications. *Phys. Ther.* **2001**, 81 (11), 1810–1816.
- (174) Schiaffino, S.; Reggiani, C. Fiber Types in Mammalian Skeletal Muscles. *Physiol. Rev.* **2011**.
- (175) Mo, C.; Du, Y.; O’Connell, T. M. Applications of Lipidomics to Age-Related Musculoskeletal Disorders. *Curr. Osteoporos. Rep.* **2021**, 19 (2), 151–157.
- (176) Gueugneau, M.; Coudy-Gandilhon, C.; Théron, L.; Meunier, B.; Barboiron, C.; Combaret, L.; Taillandier, D.; Polge, C.; Attaix, D.; Picard, B.; Verney, J.; Roche, F.; Féasson, L.; Barthélémy, J. C.; Béchet, D. Skeletal Muscle Lipid Content and Oxidative Activity in Relation to Muscle Fiber Type in Aging and Metabolic Syndrome. *Journals Gerontol. - Ser. A Biol. Sci. Med. Sci.* **2015**, 70 (5), 566–576.
- (177) Uchitomi, R.; Hatazawa, Y.; Senoo, N.; Yoshioka, K.; Fujita, M.; Shimizu, T.; Miura, S.; Ono, Y.; Kamei, Y. Metabolomic Analysis of Skeletal Muscle in Aged Mice. *Sci. Rep.* **2019**, 9 (1), 1–11.

- (178) Goto-Inoue, N.; Yamada, K.; Inagaki, A.; Furuichi, Y.; Ogino, S.; Manabe, Y.; Setou, M.; Fujii, N. L. Lipidomics Analysis Revealed the Phospholipid Compositional Changes in Muscle by Chronic Exercise and High-Fat Diet. *Sci. Rep.* **2013**, 3 (1), 1–9.
- (179) Furuichi, Y.; Goto-Inoue, N.; Manabe, Y.; Setou, M.; Masuda, K.; Fujii, N. L. Imaging Mass Spectrometry Reveals Fiber-Specific Distribution of Acetylcarnitine and Contraction-Induced Carnitine Dynamics in Rat Skeletal Muscles. *Biochim. Biophys. Acta - Bioenerg.* **2014**, 1837 (10), 1699–1706.
- (180) Goto-Inoue, N.; Manabe, Y.; Miyatake, S.; Ogino, S.; Morishita, A.; Hayasaka, T.; Masaki, N.; Setou, M.; Fujii, N. L. Visualization of Dynamic Change in Contraction-Induced Lipid Composition in Mouse Skeletal Muscle by Matrix-Assisted Laser Desorption/Ionization Imaging Mass Spectrometry. In *Analytical and Bioanalytical Chemistry*; Anal Bioanal Chem, 2012; Vol. 403, pp 1863–1871.
- (181) Tsai, Y. H.; Bhandari, D. R.; Garrett, T. J.; Carter, C. S.; Spengler, B.; Yost, R. A. Skeletal Muscle Fiber Analysis by Atmospheric Pressure Scanning Microprobe Matrix-Assisted Laser Desorption/Ionization Mass Spectrometric Imaging at High Mass and High Spatial Resolution. *Proteomics* **2016**, 16 (11–12), 1822–1824.
- (182) Unsihuay, D.; Yin, R.; Sanchez, D. M.; Yang, M.; Li, Y.; Sun, X.; Dey, S. K.; Laskin, J. High-Resolution Imaging and Identification of Biomolecules Using Nano-DESI Coupled to Ion Mobility Spectrometry. *Anal. Chim. Acta* **2021**, 1186, 339085.
- (183) Abdelmoula, W. M.; Škrášková, K.; Balluff, B.; Carreira, R. J.; Tolner, E. A.; Lelieveldt, B. P. F.; Van Der Maaten, L.; Morreau, H.; Van Den Maagdenberg, A. M. J. M.; Heeren, R. M. A.; McDonnell, L. A.; Dijkstra, J. Automatic Generic Registration of Mass Spectrometry Imaging Data to Histology Using Nonlinear Stochastic Embedding. *Anal. Chem.* **2014**, 86 (18), 9204–9211.
- (184) Verbeeck, N.; Spraggins, J. M.; Murphy, M. J. M.; Wang, H. dong; Deutch, A. Y.; Caprioli, R. M.; Van de Plas, R. Connecting Imaging Mass Spectrometry and Magnetic Resonance Imaging-Based Anatomical Atlases for Automated Anatomical Interpretation and Differential Analysis. *Biochim. Biophys. Acta - Proteins Proteomics* **2017**, 1865 (7), 967–977.
- (185) Hu, H.; Yin, R.; Brown, H. M.; Laskin, J. Spatial Segmentation of Mass Spectrometry Imaging Data by Combining Multivariate Clustering and Univariate Thresholding. *Anal. Chem.* **2021**, 93 (7), 3477–3485.
- (186) Sánchez-Gutiérrez, D.; Sáez, A.; Gómez-Gálvez, P.; Paradas, C.; Escudero, L. M. Rules of Tissue Packing Involving Different Cell Types: Human Muscle Organization. *Nat. Publ. Gr.* **2016**.
- (187) Sher, J.; Cardasis, C. Skeletal Muscle Fiber Types in the Adult Mouse. *Acta Neurol. Scand.* **1976**, 54 (1), 45–56.

- (188) Murgia, M.; Nogara, L.; Baraldo, M.; Reggiani, C.; Mann, M.; Schiaffino, S. Protein Profile of Fiber Types in Human Skeletal Muscle: A Single-Fiber Proteomics Study. *Skelet. Muscle* **2021**, *11* (1), 1–19.
- (189) Lavoie, J. C.; Chessex, P.; Rouleau, T.; Migneault, D.; Comte, B. Light-Induced Byproducts of Vitamin C in Multivitamin Solutions. *Clin. Chem.* **2004**, *50* (1), 135–140.
- (190) Fenoll, J.; Martínez, A.; Hellín, P.; Flores, P. Simultaneous Determination of Ascorbic and Dehydroascorbic Acids in Vegetables and Fruits by Liquid Chromatography with Tandem-Mass Spectrometry. *Food Chem.* **2011**, *127* (1), 340–344.
- (191) Flück, M.; Hoppeler, H. Molecular Basis of Skeletal Muscle Plasticity--from Gene to Form and Function. *Rev. Physiol. Biochem. Pharmacol.* **2003**, *146*, 159–216.
- (192) Henriksson, J. Effects of Physical Training on the Metabolism of Skeletal Muscle. In *Diabetes Care*; Diabetes Care, 1992; Vol. 15, pp 1701–1711.
- (193) Toniolo, L.; Maccatrozzo, L.; Patruno, M.; Caliaro, F.; Mascarello, F.; Reggiani, C. Expression of Eight Distinct MHC Isoforms in Bovine Striated Muscles: Evidence for MHC-2B Presence Only in Extraocular Muscles. *J. Exp. Biol.* **2005**, *208* (22), 4243–4253.
- (194) Andersson, A.; Sjödin, A.; Hedman, A.; Olsson, R.; Vessby, B. Fatty Acid Profile of Skeletal Muscle Phospholipids in Trained and Untrained Young Men. *Am. J. Physiol. - Endocrinol. Metab.* **2000**, *279* (4), 42–44.
- (195) Kriketos, A. D.; Pan, D. A.; Sutton, J. R.; Hoh, J. F. Y.; Baur, L. A.; Cooney, G. J.; Jenkins, A. B.; Storlien, L. H. Relationships between Muscle Membrane Lipids, Fiber Type, and Enzyme Activities in Sedentary and Exercised Rats. *Am. J. Physiol. - Regul. Integr. Comp. Physiol.* **1995**, *269* (5), 38–5.
- (196) Hulbert, A. J.; Kelly, M. A.; Abbott, S. K. Polyunsaturated Fats, Membrane Lipids and Animal Longevity. *Journal of Comparative Physiology B: Biochemical, Systemic, and Environmental Physiology*. 2014, pp 149–166.
- (197) Carta, G.; Murru, E.; Banni, S.; Manca, C. Palmitic Acid: Physiological Role, Metabolism and Nutritional Implications. *Frontiers in Physiology*. 2017.
- (198) De Smet, S.; Raes, K.; Demeyer, D. Meat Fatty Acid Composition as Affected by Fatness and Genetic Factors: A Review. *Animal Research*. 2004, pp 81–98.
- (199) Hergenreder, J. E.; Legako, J. F.; Dinh, T. T. N.; Broadway, P. R.; Spivey, K. S.; Baggerman, J. O.; Hutcheson, J. P.; Corrigan, M. E.; Johnson, B. J. Zilpaterol Hydrochloride Affects Cellular Muscle Metabolism and Lipid Components of 10 Different Muscles in Feedlot Heifers. *Meat Muscle Biol.* **2017**, *1* (1).
- (200) Stefanyk, L. E.; Coverdale, N.; Roy, B. D.; Peters, S. J.; Leblanc, P. J. Skeletal Muscle Type Comparison of Subsarcolemmal Mitochondrial Membrane Phospholipid Fatty Acid Composition in Rat. *J. Membr. Biol.* **2010**, *234* (3), 207–215.

- (201) Macartney, M. J.; Peoples, G. E.; Treweek, T. M.; McLennan, P. L. Docosaehaenoic Acid Varies in Rat Skeletal Muscle Membranes According to Fibre Type and Provision of Dietary Fish Oil. *Prostaglandins Leukot. Essent. Fat. Acids* **2019**, *151*, 37–44.
- (202) Leyton, J.; Drury, P. J.; Crawford, M. A. Differential Oxidation of Saturated and Unsaturated Fatty Acids in Vivo in the Rat. *Br. J. Nutr.* **51** (1987), 383–393.
- (203) Ballweg, S.; Sezgin, E.; Doktorova, M.; Covino, R.; Reinhard, J.; Wunnicke, D.; Hänelt, I.; Levental, I.; Hummer, G.; Ernst, R. Regulation of Lipid Saturation without Sensing Membrane Fluidity. *Nat. Commun.* **2020**, *11* (1).
- (204) Silvius, J. R. Thermotropic Phase Transitions of Pure Lipids in Model Membranes and Their Modification by Membrane Proteins. In *Lipid-Protein Interactions*; Jost, P. C., Griffith, O. H., Eds.; John Wiley and Sons Inc.: New York, 1982; Vol. 2, pp 239–281.
- (205) Weber, J.-M. The Physiology of Long-Distance Migration: Extending the Limits of Endurance Metabolism. *J. Exp. Biol.* **2009**.
- (206) DeMar, J. C.; DiMartino, C.; Baca, A. W.; Lefkowitz, W.; Salem, N. Effect of Dietary Docosaehaenoic Acid on Biosynthesis of Docosaehaenoic Acid from Alpha-Linolenic Acid in Young Rats. *J. Lipid Res.* **2008**, *49* (9), 1963–1980.
- (207) Kunz, H. E.; Dasari, S.; Lanza, I. R. EPA and DHA Elicit Distinct Transcriptional Responses to High-Fat Feeding in Skeletal Muscle and Liver. *Am. J. Physiol. - Endocrinol. Metab.* **2019**, *317* (3), E460–E472.
- (208) Baur, L. A.; O'Connor, J.; Pan, D. A.; Kriketos, A. D.; Storlien, L. H. The Fatty Acid Composition of Skeletal Muscle Membrane Phospholipid: Its Relationship with the Type of Feeding and Plasma Glucose Levels in Young Children. *Metab. - Clin. Exp.* **1998**, *47* (1), 106–112.
- (209) Storlien, L. H.; Jenkins, A. B.; Chisholm, D. J.; Pascoe, W. S.; Khouri, S.; Kraegen, E. W. Influence of Dietary Fat Composition on Development of Insulin Resistance in Rats: Relationship to Muscle Triglyceride and ω -3 Fatty Acids in Muscle Phospholipid. *Diabetes* **1991**, *40* (2), 280–289.
- (210) Chen, W.; Chen, Y.; Wu, R.; Guo, G.; Liu, Y.; Zeng, B.; Liao, X.; Wang, Y.; Wang, X. DHA Alleviates Diet-Induced Skeletal Muscle Fiber Remodeling via FTO/M6A/DDIT4/PGC1 α Signaling. *BMC Biol.* **2022**, *20* (1), 39.
- (211) Grunfeld, C.; Baird, K. L.; Kahn, C. R. Maintenance of 3T3-L1 Cells in Culture Media Containing Saturated Fatty Acids Decreases Insulin Binding and Insulin Action. *Biochem. Biophys. Res. Commun.* **1981**, *103* (1), 219–226.
- (212) Kakimoto, P. A.; Serna, J. D. C.; de Miranda Ramos, V.; Zorzano, A.; Kowaltowski, A. J. Increased Glycolysis Is an Early Consequence of Palmitate Lipotoxicity Mediated by Redox Signaling. *Redox Biol.* **2021**, *45*, 102026.

- (213) Matsuoka, Y.; Takahashi, M.; Sugiura, Y.; Izumi, Y.; Nishiyama, K.; Nishida, M.; Suematsu, M.; Bamba, T.; Yamada, K. ichi. Structural Library and Visualization of Endogenously Oxidized Phosphatidylcholines Using Mass Spectrometry-Based Techniques. *Nat. Commun.* **2021**, *12* (1), 1–12.
- (214) Penner, A. L.; Waytt, V.; Winter, T.; Leng, S.; Duhamel, T. A.; Aukema, H. M. Oxylipin Profiles and Levels Vary by Skeletal Muscle Type, Dietary Fat and Sex in Young Rats. *Appl. Physiol. Nutr. Metab.* **2021**, *46* (11), 1378–1388.
- (215) Tsalouhidou, S.; Argyrou, C.; Theofilidis, G.; Karaoglanidis, D.; Orfanidou, E.; Nikolaidis, M. G.; Petridou, A.; Mougios, V. Mitochondrial Phospholipids of Rat Skeletal Muscle Are Less Polyunsaturated than Whole Tissue Phospholipids: Implications for Protection against Oxidative Stress. *J. Anim. Sci.* **2006**, *84* (10), 2818–2825.
- (216) Kohlmeier, M. Amino Acids and Nitrogen Compounds. In *Nutrient Metabolism*; 2015; pp 265–477.
- (217) Rehunen, S.; Karli, P.; Härkönen, M. High-Energy Phosphate Compounds in Slow-Twitch and Fast-Twitch Muscle Fibres. Changes during Exercise in Some Neuromuscular Diseases. *J. Neurol. Sci.* **1985**, *67* (3), 299–306.
- (218) Wan, J. J.; Qin, Z.; Wang, P. Y.; Sun, Y.; Liu, X. Muscle Fatigue: General Understanding and Treatment. *Exp. Mol. Med.* **2017**, *49* (10), e384.
- (219) Kohen, R.; Yamamoto, Y.; Cundy, K. C.; Ames, B. N. Antioxidant Activity of Carnosine, Homocarnosine, and Anserine Present in Muscle and Brain. *Proc. Natl. Acad. Sci. U. S. A.* **1988**, *85* (9), 3175–3179.
- (220) Powers, S. K.; Deminice, R.; Ozdemir, M.; Yoshihara, T.; Bomkamp, M. P.; Hyatt, H. Exercise-Induced Oxidative Stress: Friend or Foe? *Journal of Sport and Health Science*. 2020, pp 415–425.
- (221) Doğru-Abbasoğlu, S.; Koçak-Toker, N.; Uysal, M. Carnosine as a Putative Antioxidant in Usage Against Liver Disease. In *The Liver: Oxidative Stress and Dietary Antioxidants*; 2018; pp 295–304.
- (222) Wyss, M.; Kaddurah-Daouk, R. Creatine and Creatinine Metabolism. *Physiological Reviews*. 2000, pp 1107–1213.
- (223) Casey, A.; Greenhaff, P. L. Does Dietary Creatine Supplementation Play a Role in Skeletal Muscle Metabolism and Performance? In *American Journal of Clinical Nutrition*; 2000; Vol. 72.
- (224) Bruls, Y. M.; de Ligt, M.; Lindeboom, L.; Phielix, E.; Havekes, B.; Schaart, G.; Kornips, E.; Wildberger, J. E.; Hesselink, M. K.; Muoio, D.; Schrauwen, P.; Schrauwen-Hinderling, V. B. Carnitine Supplementation Improves Metabolic Flexibility and Skeletal Muscle Acetylcarnitine Formation in Volunteers with Impaired Glucose Tolerance: A Randomised Controlled Trial. *EBioMedicine* **2019**, *49*, 318–330.

- (225) McCann, M. R.; De la Rosa, M. V. G.; Rosania, G. R.; Stringer, K. A. L-Carnitine and Acylcarnitines: Mitochondrial Biomarkers for Precision Medicine. *Metabolites*. Metabolites January 1, 2021, pp 1–21.
- (226) Morales, P. E.; Bucarey, J. L.; Espinosa, A. Muscle Lipid Metabolism: Role of Lipid Droplets and Perilipins. *J. Diabetes Res.* **2017**, 2017, 1789395.
- (227) Watt, M. J.; Van Denderen, B. J. W.; Castelli, L. A.; Bruce, C. R.; Hoy, A. J.; Kraegen, E. W.; Macaulay, L.; Kemp, B. E. Adipose Triglyceride Lipase Regulation of Skeletal Muscle Lipid Metabolism and Insulin Responsiveness. *Mol. Endocrinol.* **2008**, 22 (5), 1200–1212.
- (228) Watt, M. J.; Hoy, A. J. Lipid Metabolism in Skeletal Muscle: Generation of Adaptive and Maladaptive Intracellular Signals for Cellular Function. *American Journal of Physiology - Endocrinology and Metabolism*. American Physiological Society Bethesda, MD June 1, 2012, pp 1315–1328.
- (229) Phua, W. W. T.; Wong, M. X. Y.; Liao, Z.; Tan, N. S. An Apparent Functional Consequence in Skeletal Muscle Physiology via Peroxisome Proliferator-Activated Receptors. *International Journal of Molecular Sciences*. Int J Mol Sci May 10, 2018.
- (230) Li, X.; Yin, R.; Hu, H.; Li, Y.; Sun, X.; Dey, S. K.; Laskin, J. An Integrated Microfluidic Probe for Mass Spectrometry Imaging of Biological Samples**. *Angew. Chemie - Int. Ed.* **2020**, 59 (50), 22388–22391.
- (231) Lamont, L.; Eijkel, G. B.; Jones, E. A.; Flinders, B.; Ellis, S. R.; Porta Siegel, T.; Heeren, R. M. A.; Vreeken, R. J. Targeted Drug and Metabolite Imaging: Desorption Electrospray Ionization Combined with Triple Quadrupole Mass Spectrometry. *Anal. Chem.* **2018**, 90 (22), 13229–13235.
- (232) Yang, M.; Hu, H.; Su, P.; Thomas, P. M.; Camarillo, J. M.; Greer, J. B.; Early, B. P.; Fellers, R. T.; Kelleher, N. L.; Laskin, J. Proteoform-Selective Imaging of Tissues Using Mass Spectrometry**. *Angew. Chemie Int. Ed.* **2022**, e202200721.
- (233) Cooper, H. J.; Hale, O. J. Native Mass Spectrometry Imaging of Proteins and Protein Complexes by Nano-Desi. *Anal. Chem.* **2021**, 93 (10), 4619–4627.
- (234) Hsu, C.-C.; Chou, P.-T.; N. Zare, R. Imaging of Proteins in Tissue Samples Using Nanospray Desorption Electrospray Ionization Mass Spectrometry. *Anal. Chem.* **2015**, 87 (22), 11171–11175.
- (235) Sisley, E. K.; Hale, O. J.; Styles, I. B.; Cooper, H. J. Native Ambient Mass Spectrometry Imaging of Ligand-Bound and Metal-Bound Proteins in Rat Brain. *J. Am. Chem. Soc.* **2022**, 144 (5), 2120–2128.
- (236) Hale, O. J.; Hughes, J. W.; Cooper, H. J. Simultaneous Spatial, Conformational, and Mass Analysis of Intact Proteins and Protein Assemblies by Nano-DESI Travelling Wave Ion Mobility Mass Spectrometry Imaging. *Int. J. Mass Spectrom.* **2021**, 468, 116656.

- (237) Yang, X.; Zhang, L.; Xia, Y. Photochemical Disulfide–Ene Modification Enhances Protein Sequencing and Disulfide Mapping by Mass Spectrometry. *Anal. Chem.* **2021**, *93* (46), 15231–15235.
- (238) Giordano, S.; Morosi, L.; Veglianesi, P.; Licandro, S. A.; Frapolli, R.; Zucchetti, M.; Cappelletti, G.; Falciola, L.; Pifferi, V.; Visentin, S.; D’Incalci, M.; Davoli, E. 3D Mass Spectrometry Imaging Reveals a Very Heterogeneous Drug Distribution in Tumors. *Sci. Rep.* **2016**, *6*, 37027.
- (239) Seeley, E. H.; Caprioli, R. M. 3D Imaging by Mass Spectrometry: A New Frontier. *Anal. Chem.* **2012**, *84* (5), 2105–2110.
- (240) Crecelius, A.; Caprioli, R.; Williams, B.; Dawant, B.; Bodenheimer, B. Three-Dimensional Visualization of Protein Expression in Mouse Brain Structures Using Imaging Mass Spectrometry. *J. Am. Soc. Mass Spectrom.* **2005**, *16* (7), 1093–1099.
- (241) Eberlin, L. S.; Ifa, D. R.; Wu, C.; Cooks, R. G. Three-Dimensional Visualization of Mouse Brain by Lipid Analysis Using Ambient Ionization Mass Spectrometry. *Angew. Chemie* **2010**, *122* (5), 885–888.
- (242) Swales, J. G.; Dexter, A.; Hamm, G.; Nilsson, A.; Strittmatter, N.; Michopoulos, F.; Hardy, C.; Morentin-Gutierrez, P.; Mellor, M.; Andren, P. E.; Clench, M. R.; Bunch, J.; Critchlow, S. E.; Goodwin, R. J. A. Quantitation of Endogenous Metabolites in Mouse Tumors Using Mass-Spectrometry Imaging. *Anal. Chem.* **2018**, *90* (10), 6051–6058.
- (243) Lanekoff, I.; Laskin, J. Quantitative Mass Spectrometry Imaging of Molecules in Biological Systems. In *Advances in Chromatography*; Grushka, E., Grinberg, N., Eds.; CRC Press: Boca Raton, 2018; Vol. 54, pp 43–72.
- (244) Porta, T.; Lesur, A.; Varesio, E.; Hopfgartner, G. Quantification in MALDI-MS Imaging: What Can We Learn from MALDI-Selected Reaction Monitoring and What Can We Expect for Imaging? *Anal. Bioanal. Chem.* **2015**, *407* (8), 2177–2187.
- (245) Lanekoff, I.; Thomas, M.; Laskin, J. Shotgun Approach for Quantitative Imaging of Phospholipids Using Nanospray Desorption Electrospray Ionization Mass Spectrometry. *Anal. Chem.* **2014**, *86* (3), 1872–1880.
- (246) Ellis, S. R.; Bruinen, A. L.; Heeren, R. M. A. A Critical Evaluation of the Current State-of-the-Art in Quantitative Imaging Mass Spectrometry. *Anal. Bioanal. Chem.* **2014**, *406* (5), 1275–1289.
- (247) Vismeh, R.; Waldon, D. J.; Teffera, Y.; Zhao, Z. Localization and Quantification of Drugs in Animal Tissues by Use of Desorption Electrospray Ionization Mass Spectrometry Imaging. *Anal. Chem.* **2012**, *84* (12), 5439–5445.

VITA

Daisy M. Unsihuay Vila was born in 1992 in Lima, Peru. She went to school at San Benito de Palermo, where she graduated in 2009. During high school, Daisy developed a great interest for fundamental science including Biology, Chemistry and Physics. In August 2010, Daisy was accepted to National University of Engineering (UNI), Lima, Peru, from which she received her BS in Chemistry in December 2015. During her undergraduate studies, Daisy carried out research under the supervision of Prof. Gino Picasso Escobar in the area of heterogenous catalysis. Her research involved the synthesis and characterization of metal oxides for the oxidative dehydrogenation of ethane. The results of this work were published at the Peruvian Chemical Society Journal. Daisy made a research internship at the University of Navarra (Spain) in the Microbiology and Parasitology lab as part of the Research Experience for Peruvian Undergraduates (REPU) program. There, she worked under the guidance of Prof. Carlos Gamazo de la Rasilla in the development of an oral vaccine against Shigellosis. The results of this work were published in 2015 at the *International Journal of Pharmaceutics*. In 2015, Daisy was accepted to be part of the Vanderbilt International Research Academy (VISRA) program at Vanderbilt University, USA. In this internship, Daisy worked on the characterization of a small molecule '921 as potential antimicrobial against *Staphylococcus aureus*. This research was conducted at the Skaar Lab and was published in 2021 at the *MBio* Journal. In July 2017, Daisy defended her undergraduate thesis which was approved with excellence.

Daisy started her PhD studies at the Department of Chemistry at Purdue University in August 2017. She joined the Julia Laskin lab where she worked on developing new approaches for mass spectrometry imaging using the nanospray desorption electrospray ionization (nano-DESI). During her graduate studies, Daisy was awarded the Women Chemists Committee (WCC) Merck Research Award, Thomas W. Keough Graduate Fellowship, Bilsland Dissertation Fellowship, ASMS Graduate Student Travel Award, Best Applied Student Paper Award of International Journal of Mass Spectrometry, Purdue Graduate Student Center (PGSG) and the Women in Science Program (WISP) travel awards.

Daisy has been involved in numerous science outreach and mentoring activities. During her undergraduate studies, she has served as the head of the student group AEDICI where she organized a series of chemistry workshops for undergraduate students. Daisy has also served as an

Einstein fellow at the MiniAcademy of Science and Technology to provide science workshops to Peruvian woman schoolers. During her time at Purdue, she served as the head of thinkUNI, an event that gathers Peruvian graduate students around the world to provide advice about graduate student life. She also served as part of the outreach committee of the Iota Sigma Pi Plutonium Chapter, where she organized the National Chemistry Week and Girls Scout Days in the Lafayette area. Finally, Daisy is currently serving as the head of the Chemistry branch of the REPU program which provides a research internship to Peruvian undergraduates to gain experience in the best institutions in the world.

Daisy will continue her postdoctoral training as a Clinical Chemistry fellow at a joint program of the Hospital of University of Pennsylvania (HUP) and the Children's Hospital of Philadelphia (CHOP).

LIST OF PUBLICATIONS

- (1) **Unsihuay, D.**, Hu H., Latorre-Palomino A., Yang M., Qiu J., Kuang S., Ruichuan Y., Laskin J. Multimodal workflow for high-resolution imaging of individual skeletal muscle fibers using nano-DESI MSI (in progress).
- (2) **Unsihuay, D.**; Yin, R.; Sanchez, D. M.; Yang, M.; Li, Y.; Sun, X.; Dey, S. K.; Laskin, J. High-Resolution Imaging and Identification of Biomolecules Using Nano-DESI Coupled to Ion Mobility Spectrometry. *Anal. Chim. Acta* **2021**, 1186, 339085.
- (3) **Unsihuay, D.**; Su, P.; Hu, H.; Qiu, J.; Kuang, S.; Li, Y.; Sun, X.; Dey, S. K.; Laskin, J. Innentitelbild: Imaging and Analysis of Isomeric Unsaturated Lipids through Online Photochemical Derivatization of Carbon–Carbon Double Bonds. *Angew. Chemie Int. Ed.* **2021**, 133 (14).
- (4) **Unsihuay, D.**; Mesa Sanchez, D.; Laskin, J. Quantitative Mass Spectrometry Imaging of Biological Systems. *Annu. Rev. Phys. Chem.* **2021**, 72, 307–329.
- (5) Juttukonda, L. J.; Beavers, W. N.; **Unsihuay, D.**; Kim, K.; Pishchany, G.; Horning, K. J.; Weiss, A.; Al-Tameemi, H.; Boyd, J. M.; Sulikowski, G. A.; Bowman, A. B.; Skaara, E. P. A Small-Molecule Modulator of Metal Homeostasis in Gram-Positive Pathogens. *MBio* **2020**, 11 (5), 1–22.
- (6) Su, P.; Hu, H.; **Unsihuay, D.**; Zhang, D.; Dainese, T.; Diaz, R. E.; Lee, J.; Gunaratne, D. K.; Wang, H.; Maran, F.; Mei, J.; Laskin, J. Preparative Mass Spectrometry Using a Rotating-Wall Mass Analyzer. *Angew. Chemie Int. Ed.* **2020**, 59 (20), 7711–7716.
- (7) **Unsihuay, D.**; Qiu, J.; Swaroop, S.; Nagornov, K. O.; Kozhinov, A. N.; Tsybin, Y. O.; Kuang, S.; Laskin, J. Imaging of Triglycerides in Tissues Using Nanospray Desorption Electrospray Ionization (Nano-DESI) Mass Spectrometry. *Int. J. Mass Spectrom.* **2020**, 448, 116269.